THE UNIVERSITY OF CHICAGO

TARGETED DELIVERY OF THERAPEUTIC PEPTIDES USING SUPRAMOLECULAR NANOMATERIALS TO DRUG INTRACELLULAR PROTEIN-PROTEIN INTERACTIONS IN CANCER

A DISSERTATION SUBMITTED TO
THE FACULTY OF THE DIVISION OF THE BIOLOGICAL SCIENCES
AND THE PRITZKER SCHOOL OF MEDICINE
IN CANDIDACY FOR THE DEGREE OF
DOCTOR OF PHILOSOPHY

INTERDISCIPLINARY SCIENTIST TRAINING PROGRAM:
MOLECULAR ENGINEERING

BY
MATHEW RYAN SCHNORENBERG

CHICAGO, ILLINOIS
DECEMBER 2020

To my parents, Sandi and Gary Schnorenberg.

Thank you for your constant support and encouragement.

"The important thing is not to stop questioning. Curiosity has its own reason for existence. One cannot help but be in awe when he contemplates the mysteries of eternity, of life, of the marvelous structure of reality. It is enough if one tries merely to comprehend a little of this mystery each day."

- Albert Einstein

May 2nd, 1955

TABLE OF CONTENTS

LIST OF FIGURES

ACKNOWLEDGMENTS

There are many people to whom I would like to give my sincere thanks and gratitude for supporting me throughout my PhD training.

First, I would like to thank my PIs, Professors Matthew Tirrell and James LaBelle. Matt and James have been invaluable advisors, mentors, and role models to me. Their support and encouragement have been unwavering – always supporting me and challenging me to pursue my ideas and at times believing in me more than I believed in myself. I'm grateful to have had the opportunity to be co-mentored by Matt and James. It truly feels like having 2x the mentorship and support. Their guidance and examples have made me a better scientist, colleague, mentor, leader, friend, and future physician-scientist, and for these things I'll always be grateful.

I am also grateful to Professors Jeffrey Hubbell and Jun Huang, who have also been invaluable mentors and role models in my training. Jeff and Jun have always been supportive while also offering their deep scientific expertise and guidance, both formally, as members of my thesis committee, and informally. With Jeff, I also had the opportunity to TA in his classes to grow as a teacher, rotate in his lab to grow as a scientist, learn from him in a grant-writing class to grow as a writer, and finally to collaborate and work deeply with his lab on a critical part of my thesis work. I'll always be thankful to Jeff and Jun for being integral mentors in my training.

There are many people I would like to thank from the MSTP, PME, Pediatrics, and elsewhere in the University for helping me in countless ways, including Marcus Clark, Lucy Godley, Ken Onel, Elise Covic, Alison Anastasio, Kristin McCann, Shay McAllister, Sarah Laloggia, Marisa Davis, Hafsah Mohammed, Diana Morgan, Maria Rubio, LaKesha Lloyd, Amanda Dennis, Lindsay Bartolomei, Andre Walker, Sharon Dunn, and Kerri Pride-Fair.

As a member of two labs, I have had the chance to become friends, colleagues, mentee, and mentor with a set of people as innumerable as my gratitude. Thank you for everything, to all of my fellow labmates whom I've had the opportunity to learn from, become friends with,

and enjoy the ups and downs of graduate school with, especially: Handan Acar, Katrina Maxcy, Lindsey Ludwig, Rosy Liao, Alex Marras, Jeff Ting, Yu Tian, Amanda Marciel, Ravand Samaeekia, Abbas Hadji, Rachel Eclov, Greta Schmitt, Eun Ji Chung, Lorraine Leon, Jeff Vieregg, John Barrett, Sam Srivastava, Blair Brettmann, Michael Lueckheide, Lu Li, Hao Wu, Jelena Dinic, Whitney Fowler, Angelika Neitzel, Guilhem De Hoe, Ed Jiang, Carlos Medina Jimenez, Yan Fang, Dean Mastropietro, Michael Mellas, Siqi Meng, Harrison Paul, Kaden Stevens, Ge Zhang, Tara Suntum, Amir Siddiqui, Michele Nassin, Sean Mao, Qiming He, Wei Chen, Logan Leak, Alex Yoo, Isadora Kucera, Luqiong Wang, Julie Chael, Christina Stebbins, Dawson Mills, and others.

Thank you also to my classmates and friends I have made along the way. My MSTP cohort has been a constant source of friendship and camaraderie from Day 1 at U of C: Alyson Yee, Michael Clark, Blake Flood, Katie Long, Kaitlin McLean, Victoria Okuneye, Frank Wen, and Phil Hsu. Elyse Watkins was my first friend in PME and now a close lifelong friend, and I'm glad we got the chance to collaborate in our research. To all my other colleagues, friends, and classmates, thank you for making this training experience enjoyable, manageable, and fruitful.

Finally, thank you to my greatest source of support of all, my family. Thank you to my parents Sandi and Gary, my brother Kevin, and my extended family for their never-ending support, encouragement, and love. Thank you to Emily, my wife, better half, best friend, and source of infinite support. I don't know how I would've made it through my PhD without your support. And last, but certainly not least, thank you to the most valuable "lab"-mate of all, our dog Kato. He adopted us as his humans at the very beginning of grad school, and nothing can compare to his unwavering love, enthusiasm, and support, in good times and hard times alike.

ABSTRACT

The overall goal of my thesis work was to develop supramolecular nanocarriers to deliver therapeutic peptides to and into diseased cells. I primarily applied this to therapeutic peptides that inhibit protein-protein interactions (PPIs) cancer cells rely on to avoid therapeutic-induced cell death.

In Chapter 1, I introduce the importance of PPIs as therapeutic targets in cancer, why they are commonly considered "undruggable" targets, and how supramolecular nanomaterials can be used to deliver peptide therapeutics to and into cancer cells to overcome these obstacles.

In Chapter 2, we used a peptide amphiphile micelle nanocarrier to deliver a BIM BH3 peptide into cells to reactivate apoptosis. While the peptide alone is cell impermeable and therefore therapeutically inert, attaching it to a lipid tail facilitated its cellular uptake, and an endosome-cleavable linker facilitated the peptide's release after uptake to drive intracellular accumulation and pro-apoptotic efficacy.

In Chapter 3, I present our work identifying the synthesis and purification conditions in which ester-containing peptide amphiphiles are stable, including an optimized synthesis and purification strategy that avoids ester hydrolysis byproducts. This optimized synthesis and purification strategy is then used to create stapled peptide amphiphile micelles designed to reactivate p53, and their biological efficacy is evaluated.

In Chapter 4, we used CD19-targeted polymersomes to deliver an MCL-1 inhibiting stapled peptide to and into DLBCL cells to reactivate cell death. Using this platform for targeted, intracellular delivery, the efficacy of stapled peptides could be greatly enhanced, and we used this to target the synergistic combination of p53 reactivation and MCL-1 inhibition.

In Chapter 5, I discuss the relative strengths, weaknesses, and contributions of our nanocarriers for intracellular delivery of peptide therapeutics. Lastly, future directions are described that could advance these lines of research toward clinical applicability.

CHAPTER 1

INTRODUCTION

Protein-protein interactions (PPIs) have long been considered "undruggable" targets using traditional therapeutic approaches. In this chapter, I introduce the the biomedical importance of PPIs in cancer, including two PPI networks actively being targeted for cancer therapy (i.e. the BCL-2 family of proteins, p53-inactivation). I then discuss the classes of therapeutics in development as PPI inhibitors and their relative strengths and weaknesses. We ultimately aim to capitalize on the strengths of therapeutic peptides as PPI inhibitors and overcome their relative weaknesses using nanocarrier delivery vehicles. The types of peptide nanocarriers discussed in this thesis are then outlined in the context of their existing literature. Finally, I describe the main model disease in which I have studied these questions, diffuse large B-cell lymphoma (DLBCL).[1]

1.1 Protein-Protein Interactions (PPIs): an Elusive Class of Therapeutic Targets in Cancer

Intracellular PPIs are critical regulators of cellular function and critical therapeutic targets. There are an estimated 650,000 PPIs in the human interactome [2], and the deregulation of many of these PPIs is known to cause diseases, including cancer [3]. Despite their known biomedical importance, intracellular PPIs have largely been considered an "undruggable" class of targets due to their intractability using traditional, drug-like molecules. In fact, only one drug targeting an intracellular PPI has been successfully approved by the U.S. Food and Drug Administration (FDA) [4], despite an enormous amount of effort from researchers and pharmaceutical companies.

1. Parts of this chapter were adapted from my F30 fellowship proposal [1] – A potent and specific approach to targeting B-cell lymphoma: Disrupting malignant protein-protein interactions using CD19-targeted stapled peptide amphiphile nanoparticles. National Cancer Institute, National Institutes of Health, 5F30CA221250, July 2017.

The "undruggable" reputation of intracellular PPIs comes primarily from their large surface areas combined with their intracellular location. The traditional, drug-like, therapeutic molecules that can enter cells (i.e. "small molecules") are generally too small to block PPIs. Most PPI interfaces are mediated by many key residues spanning surface areas of at least 1,500 - 3,000 $Å^2$, while small molecule therapeutics can only bind surface areas of 300 - 1,000 $Å^2$. This size discrepency prevents small molecules from effectively blocking PPI interfaces with sufficient specificity [5–9]. Another widely successful category of therapeutics is biologics (e.g. proteins, peptides). These large, polar molecules are able to bind very large surface areas with high affinity and specificity, but they are cell-impermeable and therefore unable to reach intracellular PPIs [10]. The size of PPI interfaces, combined with the pharmacologic trade-offs between size, specificity, solubility, and cellular uptake, leaves intracellular PPIs nearly untouched by traditional therapeutic approaches [11].

Despite an ever-increasing pool of knowledge about PPIs that drive diseases, and therefore known PPIs that are ideal drug targets, drugging these targets remains a monumental, unmet biomedical need. It is not a lack of biological knowledge that has inhibited success in this area, but a lack of tools and paradigms to drug new types of targets such as these. Some of the therapeutics currently being explored to drug intracellular PPIs are discussed in Section 1.2.

1.1.1 The Gatekeepers of Cell Death: the BCL-2 Family of Proteins

One of the most infamous examples of pathologic PPIs in cancer is the inactivation of programmed cell death (i.e. apoptosis), and "resisting cell death" is one of the hallmarks of cancer [12, 13]. Apoptosis is critically important in the development and maintenance of healthy tissues, and much is now known about its mechanisms and regulation. Cancer cells must find a way to avoid apoptosis to become malignant, and most cancer therapies function by ultimately forcing cancer cells to reactivate their molecular machinery for apoptosis.

Apoptosis is regulated by the BCL-2 family of proteins, which comprises a network of

PPIs that integrates pro- and anti-apoptotic signals to determine cell fate by either blocking or initiating apoptosis at the level of the mitochondrion [14–17]. The BCL-2 family consists of three types of proteins: (1) the effectors of apoptosis (i.e. BAX and BAK), (2) the anti-apoptotic proteins that bind to and inactivate the effectors (e.g. BCL-2, MCL-1, BCL-XL, BCL-W, BFL-1 (the human homolog of murine protein A1)), and (3) the the pro-apoptotic sensitizers (a.k.a. "BH3-only" proteins) that bind to and inhibit the inactivators or activate the effectors (e.g. BIM, PUMA, NOXA, BID, BAD, BMF, HRK, BIK). The balance of pro- and anti-apoptotic PPIs between all these proteins controls a cell's fate to live or die. When pro-apoptotic PPIs dominate and BAX and BAK are sufficiently activated, they oligomerize to form pores in the outer mitochondrial membrane (mitochondrial outer membrane permeabilization (MOMP)). MOMP is the point-of-no-return that triggers the feed-forward process of apoptosis by releasing cytochrome C from the mitochondria, activating the apoptosome, and activating caspases. Cancer therapies often act to activate this apoptotic process, while cancers act to turn off this process.

Apoptosis is commonly divided into two distinct yet related pathways: the extrinsic pathway, in which a cell initiates cell death in response to extracellular signals (e.g. Fas-FasL signaling from immune cells, TNF-receptor stimulation), and the intrinsic pathway, in which a cell initiates cell death in response to intracellular signals (e.g. DNA damage, cellular stress). Both the extrinsic and (especially) the intrinsic pathways of apoptosis are controlled primarily by the BCL-2 family of proteins and their PPIs.

Apoptosis is a feed-forward, threshold event, and any one cell can be closer to or farther from the apoptotic threshold depending on the balance of pro- and anti-apoptotic PPIs within the BCL-2 family. This concept is often called "apoptotic priming." Many cancer cells are often "primed to die" due to cellular stresses, and this is the molecular basis of the therapeutic window for many cancer chemotherapies. When cancer cells are more "primed to die" than healthy cells, a non-specific, cytotoxic chemotherapeutic can push the cancer cells over the apoptotic threshold without killing most of the healthy cells. Conversely, cancers

can exploit the BCL-2 family's PPIs to push themselves away from the apoptotic threshold to develop chemoresistance. Cancers can achieve this by upregulating anti-apoptotic PPIs, for example by genetic translocation (e.g. *BCL-2* next to the $E\mu$ immunoglobulin enhancer), copy number amplification (e.g. *MCL-1*), or over-expression (e.g. MCL-1 protein) [18]. Meanwhile, cancers often down-regulate pro-apoptotic PPIs through mechanisms such as genomic loss (e.g. *BIM* deletion), epigenetic silencing (e.g. *PUMA*), or mutation (e.g. *BAX*) [18]. When cancer manipulates the BCL-2 family to avoid cell death, this often makes it impossible to therapeutically kill the cancer cells without also killing other cells, and this is one of the molecular bases for many relapsed and refractory cancers.

While cancer chemotherapies essentially function as upstream activators of apoptosis, direct manipulation of the BCL-2 family would provide fewer upstream opportunities for cancers to develop chemoresistance. To that end, an emerging paradigm in cancer treatment is the direct, therapeutic manipulation of the BCL-2 family using BH3-mimetics [19]. The proteins in the BCL-2 family share four BCL-2 homology (BH) domains (BH1 - BH4), of which the BH3 domain primarily mediates the functional PPIs in the network. The pro-apoptotic sensitizer proteins are often called "BH3-only" proteins because they contain only the BH3 domain, and this BH3 domain is what binds to and inhibits the anti-apoptotic proteins or activates the effectors of apoptosis. Therapeutics are being developed to mimic these BH3 domains (appropriately called "BH3-mimetics") to therapeutically inhibit the anti-apoptotic members of the BCL-2 family and activate apoptosis in cancer. BH3 mimetics, both small molecules and peptide therapeutics, are discussed in more detail in Section 1.2.

1.1.2 p53 Inactivation: Sequestering the Guardian of the Genome

Tumor suppressor protein p53, nicknamed "the guardian of the genome" [20], is involved in another common example of cancer-driving PPIs. p53 is responsible for maintaining the genomic integrity of cells by initiating cell-cycle-arrest or apoptosis in response to cellular damage. In healthy cells, p53 is bound and inactivated by proteins such as HDM2 and HDMX

(the human homologs of murine MDM2 and MDMX), which hold p53 inactive and, in the case of HDM2, facilitate p53's ubiquitination and degradation. In response to DNA damage and cellular stress signals, p53 becomes activated, is released from its inhibitory binding partners HDM2 and HDMX, and translocates to the nucleus to function as a transcription factor for genes that arrest the cell cycle and activate DNA repair. As a "backup" to cellular repair, p53 transcription also primes cells for apoptosis by up-regulating pro-apoptotic members of the BCL-2 family and down-regulating anti-apoptotic members. This way, if a cell with damaged DNA fails to repair itself, p53 can activate apoptosis rather than allowing the damaged cell to progress through the cell cycle, thus preventing damaged DNA from being incorporated into the genome as mutations.

In cancer, p53 can be inactivated either by mutation of the *TP53* gene itself or through PPIs that inactivate the p53 protein. Different types of cancers have a different prevalence of each inactivation mechanism, but in some types of cancer (e.g. DLBCL (see Section 1.4)), up to 80% of cases have wildtype *TP53* with the p53 protein presumably inactivated by aberrant up-regulation of HDM2 and HDMX [21–28]. While these binding partners of p53 are crucial in the functioning of healthy cells, their up-regulation can functionally inactivate p53 in cancer. In fact, across all cancers, p53's inhibitory binding partner HDM2 is one of the most frequently amplified genes in terms of somatic copy number alterations (CNAs), while HDM2's negative regulator, p14ARF (coded for by the *CDKN2A* gene) is one of the most frequently deleted [29]. While mutated *TP53* is associated with poorer clinical outcomes, we do not yet have the tools to fix mutated genes in a therapeutic context (though perhaps with gene editing and replacement technology, it may be on the distant horizon). However, for cancers with wildtype but inactivated p53, these PPIs represent an attractive and impactful therapeutic target that we might drug and disrupt to reactivate cell death. In Section 1.2, I discuss therapeutics currently in development for reactivating p53 by binding HDM2 and HDMX to disrupt their inhibitory PPIs with p53.

1.2 Therapeutic Disruption of PPIs: BH3 Mimetics and p53-Reactivation

To drug "undruggable" PPIs, people are developing entirely new concepts and tools for drugs and drug discovery. Despite the disadvantages small molecules face in targeting PPIs generally, some relatively large small molecules have had some success against smaller PPI interfaces, including some in the BCL-2 family (see Section 1.2.1). Meanwhile, other therapeutic approaches are also being envisioned to drug intracellular PPIs. Rather than traditionally drug-like small molecules, people are harnessing the ability of biologic therapeutics (i.e. peptides and proteins) to block large PPI interfaces and finding ways to enhance their intracellular access. In other approaches, rather than simply orthosterically blocking an intracellular PPI, investigators have found ways to eliminate the problematic protein altogether, by either triggering its degradation at the protein level or blocking the protein's expression at the level of DNA or mRNA. Many therapeutics ultimately modulate disease-driving PPIs from far upstream in a pathway by drugging more "druggable" targets (e.g. by drugging upstream kinases), but by developing PPI inhibitors, we and many others seek a more precise way to modulate disease-driving PPIs.

1.2.1 Small Molecule PPI Inhibitors

For drugging intracellular targets, small molecule therapeutics have been the most clinically successful class of therapeutics. While their successes have primarily come from targets that are much smaller than PPIs (e.g. small, enzymatic active sites), it is not surprising that this class of therapeutics has received the most attention and effort from the pharmaceutical industry's attempts to drug PPIs. Though small molecules are generally too small to specifically disrupt relatively large PPI interfaces (see page 1 for details), there have been some hard-won successes for small molecule PPI inhibitors against key PPI disease targets, especially against anti-apoptotic proteins in the BCL-2 family.

The first and only FDA-approved inhibitor of an intracellular PPI is venetoclax (a.k.a. ABT-199), a relatively large small molecule (868 Da) that specifically binds and inhibits the anti-apoptotic protein BCL-2 (see Section 1.1.1 on BCL-2). The development and 2016 FDA approval of venetoclax was not fast or easy. The *BCL-2* gene was first identified in 1984 as a gene on chromosome 18 that was commonly translocated next to the Ig heavy chain locus on chromosome 14 in the t(14:18) chromosomal translocation commonly seen in neoplastic B cells [30]. In 1988, *BCL-2* was deemed a candidate oncogene when its pro-survival function was discovered [31]. The first FDA approval of venetoclax to inhibit BCL-2 in 2016 came 32 years after the discovery of the *BCL-2* gene and 28 years after the designation of *BCL-2* as a candidate oncogene.

In those 32-years as an "undruggable" target, much was learned about the biology, structures, and interactions of the BCL-2 family of proteins and how they regulate apoptosis [32], while the quest for a BCL-2 inhibitor struggled onward [33]. A few putative (at that time) BCL-2 family inhibitors emerged in the forms of antisense oligonucleotides (e.g. oblimersen, G3139 [34–36]) and natural products (e.g. R-(-)-gossypol, or AT-101 [37–39]), but all ultimately failed to achieve efficacy in clinical trials [33].

The first "drug-like" small molecule inhibitor of the BCL-2 family, ABT-737, was first reported in 2005 [40]. The development of ABT-737 required a new approach to drug discovery. Rather than using the traditional approach for small-molecule drug discovery, namely high-throughput screening of as many compounds as possible, the scientists at Abbot Laboratories (before the 2013 split into Abbott and AbbVie) used a fragment-based NMR screening approach [40, 41]. Using the structures of BCL-2, BCL-XL, and BCL-W each bound to BAK, one of their shared shared pro-apoptotic binding partners, they screened for fragment molecules that could mimic each of the key binding residues of BAK in its interface with BCL-2, BCL-XL, or BCL-W. They then designed and synthesized a molecule (ABT-737) in which they linked each of those key fragments together into a single, drug-like molecule. ABT-737 is large for a "small" molecule drug (813 Da) and would not have

been available for discovery by simply using high-throughput screening libraries. Instead, the concept of fragment-based drug discovery enabled this first "drug-like" inhibitor of the BCL-2 family of proteins.

In 2008, they then published an orally bioavailable analog (ABT-263, a.k.a. navitoclax) that simultaneously inhibited BCL-2, BCL-XL, and BCL-W [42], which was then used in clinical trials. Due to the dependence of platelets on BCL-XL for survival [43], navitoclax ultimately caused a dose-limiting thrombocytopenia in both pre-clinical and clinical trials and was unable to achieve efficacious dosages and therefore FDA-approval as a single-agent therapy [44–47]. Today, navitoclax continues to be evaluated in synergistic combinations with other therapeutics to enhance its anti-cancer effects at lower, non-toxic doses, and some of these trials have shown clinical promise [48].

Meanwhile, scientists at Abbott/AbbVie iterated on this therapeutic yet again, seeking to generate a drug that would bind only to BCL-2 and not BCL-XL, thereby avoiding dose-limiting thrombocytopenia in hopes of achieving efficacious anti-tumor effects. The binding interfaces of BCL-2 and BCL-XL with navitoclax are very similar, but not identical. Using co-crystal structures of navitoclax with each of the proteins, they modified navitoclax via a rational design approach to generate a BCL-2-specific, BCL-XL-sparing therapeutic, venetoclax (a.k.a. ABT-199) in 2013 [47]. Venetoclax then received breakthrough therapy designation from the FDA in 2015 and was rapidly approved by the FDA in 2016 to become the first efficacious and FDA-approved inhibitor of an intracellular PPI.

The development and approval of venetoclax as a BCL-2 inhibitor in 2016 required decades of work, numerous dead-end clinical trials, multiple iterations on its molecular structure, and new paradigms for small molecule drug discovery (i.e. fragment-based screening and rational design). Venetoclax has already had profound effects on clinical outcomes [49], but more generally, the drug discovery approaches that were used to develop venetoclax have been and are being used to design small molecule inhibitors of other PPIs. While none have yet achieved FDA-approval, many are showing great promise in both pre-clinical and clinical

trials.

For BCL-2 family drug targets, one on-going, aspirational goal is to design single-protein-specific inhibitors, analogous to venetoclax for BCL-2. Such highly specific inhibitors would provide ultimate control in drugging the anti-apoptotic weaknesses of specific cancers while limiting on-target toxicities in other tissues. Multiple such drugs are on the horizon, currently in pre-clinical and clinical development, including MCL-1 inhibitors [50] (e.g. S63845 [51], S64315/MIK665 [52–54], AZD5991 [55, 56], AMG-176 [57], AMG-397 [58], A-1210477 [59]) and BCL-XL inhibitors (e.g. A-1155463 [60, 61], A-1331852 [61], WEHI-539 [62]).

For drugging the PPIs that inactivate p53 (see page 4, Section 1.1.2), small molecules have likewise been developed and tested, but so far none have succeeded in demonstrating clinical efficacy and gaining FDA approval. The "nutlin" family of drugs (primarily nutlin-3a [63]) is perhaps the most well-known class of small-molecule p53-reactivators, but they are able to inhibit only p53:HDM2 interactions and not p53:HDM4 interactions [64]. For p53 reactivation, hydrocarbon stapled peptides (i.e. ALRN-6924) are another approach that is currently showing success in clinical trials (discussed on page 12).

The development story and success of venetoclax is a leap forward for drugging "undruggable" intracellular PPIs. The fragment-based screening and rational design approaches used to develop venetoclax could also likely succeed in drugging other relatively small PPI interface disease targets with high specificity and potency. However, for drugging PPIs more broadly, unaddressed questions remain. How can we drug much larger PPI interfaces, with key binding residues that span surface areas larger than any existing small molecule therapeutics? How can we drug PPIs that diseased cells rely on but healthy tissues rely on too (e.g. BCL-XL is critical in both platelets and cancers)? These obstacles are unlikely to be overcome by developing new methods of small molecule drug discovery and will likely require developing and applying entirely new therapeutic modalities.

1.2.2 Peptides and Stapled Peptides as PPI Inhibitors

Peptides, in contrast to small molecule therapeutics, can span large surface areas to simultaneously bind the many key residues of a PPI interface with high affinity and specificity [65, 66]. Synthetic peptide PPI inhibitors can also be rationally designed quite readily by mimicking one of the binding partners in a native PPI interface to create a competitive inhibitor [67, 68].

While peptides are a promising tool for disrupting PPIs at the molecular level, important barriers remain for their in vivo and clinical translation. First, circulating peptides have short plasma half-lives due to clearance and hydrolysis, and they can fail to reach the target cell in an efficacious dosage. Second, peptides are almost never cell permeable, and therefore almost all peptide therapeutics that enter clinical trials are designed to bind extracellular targets [10]. The exception to this cell-permeability rule is a class of cell-penetrating peptides (CPPs), which are often highly cationic, α-helical, and/or amphiphilic, and often mimic domains of proteins that microorganisms use to infect cells. CPPs have proven quite useful in pre-clinical research for getting therapeutics into a cell (see Section 1.3), but therapeutic peptides that mimic an intracellular PPI interface are not intrinsically cell-permeable and therefore need assistance entering cells. Finally, while peptides may be designed to mimic the sequence of a protein, that peptide loses its secondary structure outside of the context of the rest of the protein, and this loss of structure can greatly inhibit the peptide's affinity for its target protein [67]. Multiple strategies are currently being researched to harness the strengths of peptides as PPI inhibitors while seeking to overcome these weaknesses.

PPI interfaces rely not only on the sequences of the two proteins (primary structure), but also on the proteins' secondary structures and tertiary structures. When a peptide is synthesized to mimic a small piece of a PPI interface, the sequence is easily mimicked, but outside the context of the entire protein, the structure is lost. Although unstructured peptides can sometimes bind to a protein target via induced fit [69, 70], peptide:protein binding typically relies on stabilizing the secondary structure. To better mimic α-helical

secondary structures commonly seen at PPI interfaces, many chemistry strategies have been developed to stabilize small, synthetic peptides into stabilized α-helices [71, 72]. These helix-stabilizing modifications can be synthetically installed either on side chains of the peptide or within the backbone of the alpha helix (i.e. hydrogen-bond surrogates) [71]. These synthetic stabilization strategies are often referred to as "stapling" to generate "stapled" peptides. To date, the most widely utilized type of stapled peptides, and the only stapled peptides to enter clinical trials, are all-hydrocarbon stapled peptides.

All-hydrocarbon stapled peptides are synthesized by incorporating into the peptide sequence non-natural amino acids with olefin-tether side chains, usually one or two α-helical turns apart, then closing the "staple" using ruthenium-catalyzed ring closing metathesis (RCM) to lock the peptide into an α-helical secondary structure. This allows a synthetic peptide to more accurately mimic an α-helix of a native protein to bind and modulate PPIs, thus expanding the collection of PPIs targetable by therapeutic peptides. All-hydrocarbon stapling also imparts multiple beneficial, drug-like properties to an otherwise inert peptide, including (1) higher affinity and specificity for its PPI-interface target [73], (2) resistance to degradation [73–75], and (3) cellular uptake in some cases [73, 76].

The history of all-hydrocarbon stapled peptides was well summarized in a 2014 publication by Walensky and Bird [77], and I only summarize the landmark events here. The first synthesis of macrocyclic peptides by RCM was reported in 1998 by Blackwell and Grubbs [78]. Then in 2000, Schafmeister, Po, and Verdine used the same RCM cross-linking chemistry with Grubbs catalyst to synthesize α-α-disubstituted all-hydrocarbon stapled peptides on solid-phase (the same synthesis strategy now widely used for synthesizing all-hydrocarbon stapled peptides) [74, 79, 80]. Importantly, they demonstrated that this stapling strategy enhanced the peptide's α-helicity and shielded the amide backbone from proteolysis [74]. Meanwhile, in the field of apoptosis research, Letai et al. (including Walensky and others in the Korsmeyer group) found that peptides mimicking the BH3 domains of pro-apoptotic members of the BCL-2 family (see Section 1.1.1) could activate apoptosis. This seemed like a

promising potential cancer therapeutic, but those first unstructured BH3 peptides (1) could not get into cells and (2) lost their α-helical secondary structure when removed from the context of the rest of the protein [69]. In 2004, Walensky et al. (bridging the expertise of the Verdine and Korsmeyer groups) made hydrocarbon-stapled BH3 peptides, which could enter cells and activate apoptosis without needing to artificially permeabilize the cell membrane. This was the first demonstration of cellular uptake of an all-hydrocarbon stapled peptide and thereby biomedical applicability for intracellular PPI modulation. Since this work in 2004, all-hydrocarbon stapled peptides have been increasingly used, by the Walensky group and by many others, for therapeutically modulating PPIs in a variety of diseases [77, 81, 82].

In 2013, the first stapled peptide entered and completed a phase I clinical trial demonstrating safety. ALRN-5281, a stapled peptide mimetic of human growth hormone releasing hormone, was developed by Aileron Therapeutics and completed a phase I safety trial in 32 healthy volunteers [83]. In the trial, there were no adverse events, toxicities, or withdrawals noted [77]. Since the completion of this safety trial, Aileron has stopped pushing this peptide forward for now and has instead begun and focused on clinical trials for another stapled peptide, ALRN-6924, which is now in many phase I and phase II clinical trials for cancer [84–91].

ALRN-6924 is a stapled peptide that re-activates p53 by blocking p53's inhibitory binding partners, HDM2 and HDMX, to prevent p53 sequestration and degradation (see Section 1.1.2). The first published iteration of this stapled peptide was SAH-p53-8, which was modeled after an α-helix of p53's binding domain with HDM2/HDMX with a few intentional amino acid changes to the make the peptide cell-permeable [92, 93]. While SAH-p53-8 had high binding affinity for its targets HDM2 and HDMX, its therapeutic activity was almost completely eliminated by the presence of serum proteins, and all in vitro treatments were therefore done in the absence of FBS. The biopharmaceutical company Aileron Therapeutics then further optimized the peptide to create the next iteration, ATSP-7041 [28], which was inhibited by serum to a lesser degree and could be used therapeutically not only in vitro

in the presence of serum, but also in vivo. ATSP-7041 has been used in vitro in many publications, but only in a few publications has it been used in vivo [28, 94, 95].

Of note, each of the publications with in vivo applications alludes to a formulation method involving amphiphilic DSPE-PEG. The reasoning for this formulation strategy and the methods by which it was done have not been thoroughly described in any of these publications and remain a trade secret. The presumptive reasoning is that this DSPE-PEG formulation increases the solubility of ATSP-7041 sufficiently for intravenous injection and/or improves its pharmacokinetics via micelle encapsulation.

Aileron then further optimized ATSP-7041 to create ALRN-6924, the stapled peptide ultimately used in clinical trials. After extensive iteration and optimization, ALRN-6924 achieved the perfect balance of high binding affinity/specificity for its targets, cellular uptake, and aqueous solubility to become the first stapled peptide to definitively show clinical efficacy. The sequence/structure of ALRN-6924 is still undisclosed, and therefore the most clinically relevant peptide we can use in our research is its preclinical predecessor, ATSP-7041.

In an interesting new application, ALRN-6924 is being used not only for inducing cell death in WTp53 cancer cells (see Section 1.1.2), it is also being used in a clinical trial for myelopreservation during topotecan chemotherapy in cancers with mutant p53 [86]. Topotecan inhibits topoisomerase I during DNA replication, causing double-stranded DNA breaks in replicating cells. As a chemotherapeutic, topotecan damages rapidly dividing cancer cells but also rapidly dividing healthy cells, including crucial cell types in the bone marrow (e.g. red blood cells, white blood cells, platelets). This causes severe toxicities commonly seen with chemotherapeutics such as topotecan. The goal of this myelopreservation clinical trial is to use ALRN-6924 to activate p53 in healthy cells to arrest their cell cycle and avoid healthy cell DNA damage while topotecan is used to kill cancer cells with mutated p53 that continue to rapidly divide despite the presence of ALRN-6924. This has shown some successful myelopreservation in pre-clinical work [96], and the clinical trial is still ongoing [86].

While ALRN-6924 has been highly optimized to strike a balance between cellular uptake

and solubility, the principles that govern the cellular uptake of stapled peptides are only beginning to be understood [76, 77, 97–101], and cell-permeable candidates are still found qualitatively through empirical screening and fluorescence microscopy. While stapled peptides can be made unquestionably more cell-permeable than non-stapled peptides, even the most highly optimized, cell-permeable stapled peptides still require 100 - 10,000 times higher concentrations for efficacy in cellular assays when the cell membrane is intact than when the cell membrane is permeabilized or absent. For example, ATSP-7041, the pre-clinical precursor of ALRN-6924, is reported to bind its targets, HDM2 and HDMX, with kD values of 0.91 and 2.31 nM ex vitro, respectively, while it kills SJSA-1, a highly HDM2-dependent osteosarcoma, with a much higher EC50 value of 0.6 μM in vitro [28]. As a second example, a qualitatively cell-permeable MCL-1 inhibitor, SAH-MS1-18, binds MCL-1 with high specificity at 25 nM ex vitro, but kills MCL-1-dependent cancer cells at 5 μM in vitro, and when the cell membrane is permeabilized prior to an identical treatment, induces mitochondrial depolarization (a proxy for cell death) at 0.45 - 18 nM [102]. As a third example, BIM SAHB, a pan-inhibitor of the BCL-2 family's anti-apoptotic proteins, binds its protein targets in the 1-11 nM range ex vitro [103], but kills cancer cells at 1,000-fold higher concentrations in vitro and only when administered in the absence of FBS [104]. While hydrocarbon-stapled peptides are one of the most promising classes of PPI-inhibitors to-date, these numbers suggest that only a small fraction of the treatments successfully reach their intracellular protein targets to exert their therapeutic effect in vitro.

The delivery obstacles for stapled peptides are further exacerbated in vivo. Most research-grade stapled peptides are sequestered and completely inhibited by serum proteins [27, 28, 105, 106]. Currently, there is also no existing strategy to deliver these therapeutics into specific cell types via receptor-mediated endocytosis (RME), as is possible for small molecules using antibody-drug conjugates (ADCs). This makes it currently impossible to target intracellular PPIs that cancer cells and healthy cells both rely on without on-target toxicities in healthy tissues. While stapled peptides are highly potent PPI-inhibitors as molecular tools,

their delivery to and into diseased cells remains a major set of obstacles to their in vivo applicability and clinical translation.

We believe that nanomedicine delivery platforms can capitalize on the strengths of therapeutic peptides while improving upon their weaknesses to facilitate in vivo efficacy and clinical translation. The traditional drug paradigm, in which one therapeutic molecule single-handedly overcomes each obstacle on its journey from administration to intracellular target, can be made to succeed for hydrocarbon stapled peptides, as is now evidenced by the clinical success of ALRN-6924. However, the design properties (admittedly only beginning to be understood [76]) that influence a peptide's cellular uptake, membrane toxicity, aqueous solubility, and pharmacokinetics are fundamentally at odds with each other and largely unrelated to the peptide's ability to bind its protein target and disrupt a PPI. Meanwhile, the dawn of supramolecular nanomedicine (see Section 1.3.1) is now beginning to make it possible to decouple a therapeutic molecule's function at the molecular level from its "drug-like" properties at the cellular, tissue, and organismal levels. As a case in point, in 2018 the FDA approved for clinical use the first nanomedicine (patisiran) that delivers to the cytoplasm an otherwise non-cell-permeable biologic therapeutic (siRNA). The obstacles facing stapled peptides are precisely the obstacles that countless nanomedicines are being designed to overcome and that are now becoming clinically applicable. The research fields of stapled peptide therapeutics and nanomedicine are complementary, and we believe their combination can make a positive impact in the clinical treatment of otherwise "undruggable" disease targets.

By delivering stapled peptides with nanocarriers, our research aims to (1) overcome the obstacles facing stapled peptides for in vivo and clinical translation and (2) decouple a peptide's ability to disrupt a PPI at the molecular level from its requirements for drug-like characteristics. Developing such a platform (or platforms) will require a coordinated combination of chemistry, physics, and biology from the fields of chemical biology and nanomedicine. In Section 1.3, I introduce the nanocarrier platforms I have used in my thesis research toward

these goals.

1.2.3 Other Approaches

The approaches described above for therapeutic PPI disruption are currently the most widely used and clinically relevant. However, other important strategies are also being developed and are worth highlighting.

In one interesting approach, therapeutics are being developed not only to orthosterically block a PPI, but to trigger proteasomal degradation of a problematic protein. These molecules are often referred to as proteolysis targeting chimeras (PROTACs). They are two-headed molecules joined by a linker; one head binds the target protein of interest, and the other binds an E3 ubiquitin ligase (e.g. cereblon, VHL, MDM2). This recruits the E3 ubiquitin ligase to the target protein in a ternary complex to cause ubiquitination and ultimately proteasomal degradation of the target protein. This is useful if, for example, a small molecule ligand is available to the target protein but that small molecule alone does not block the PPI binding site. Moreover, rather than one drug molecule inhibiting one protein, PROTACs have been shown to catalytically facilitate protein degradation. This is beneficial because smaller amounts of drug can be used to cause greater therapeutic effect. However, this also means that doses can be used that are too high, if both protein binding partners become saturated in binary drug:protein interactions rather than the ternary complexes required for protein degradation. This is likely more of an in vitro assay consideration rather than an in vivo therapeutic concern, thanks to drug clearance and pharmacokinetics.

In addition to knocking down a protein, a disease-driving protein in a PPI can be knocked down at the DNA (e.g. CRISPR) or RNA (e.g. siRNA, miRNA) levels. There are many interesting lines of research using these approaches, but they are not directly related to the research presented here and are not elaborated upon further.

1.3 Nanocarriers for Intracellular Delivery of Therapeutic Peptides

Peptides and other biologic therapeutics show great promise for drugging targets that are otherwise considered "undruggable" (e.g. PPIs) by classically "drug-like" therapeutics (i.e. small molecules). However, for intracellular targets, cell-specific delivery and cellular uptake remain two of their primary obstacles [107]. We and others are using nanocarriers to facilitate the cellular uptake of peptide therapeutics and other biologics to capitalize on their therapeutic potential.

In this section, I discuss the current state of nanomedicine for biologic therapeutics in the clinic, then I introduce the nanomaterials relevant to my thesis work. First, peptide amphiphile (PA) micelles (Section 1.3.2) were the nanodelivery platform used in Chapter 2 for the intracellular delivery of a therapeutic BIM BH3 peptide. In Chapter 3, I further refined the synthesis and purification strategies for PAs similar to those used in Chapter 2. Next, I briefly introduce liposomes as a nanocarrier. Liposomes have been the most successful nanomedicine in the clinic so far, and much pre-clinical work has been done towards developing ligand-targeted liposomes for DLBCL chemotherapy. While my research has not involved liposomes, these literature examples strongly informed our own nanomedicine designs in Chapter 4 using polymersomes. Lastly, I introduce polymersomes, the type of nanocarrier used in Chapter 4, which are vesicular nanostructures designed to expand the chemical and physical capabilities of already widely successful liposomes.

1.3.1 The State of Nanomedicine for Biologic Therapeutics

Cancer nanomedicine is a broad field, both in terms of the nanoparticles being used for delivery and in terms of the therapeutics being delivered [108, 109]. In general, the goal of nanomedicines is to improve in one or more ways the drug-like properties of a particular therapeutic. For drugs against intracellular targets, nanoparticles have been shown to enhance

the efficacy of drugs at multiples stages of delivery, including (1) protecting the drug before it reaches the diseased cells, such as by preventing degradation, clearance, and phagocytosis to improve pharmacokinetics, (2) helping the drug reach the diseased cells and lessening accumulation in healthy tissues, for example via the enhanced permeability and retention (EPR) effect into solid tumors or active targeting, and finally (3) helping the drug enter the diseased cells [108, 110]. For small molecule therapeutics, these steps enhance efficacy and minimize toxicity relative to the drug administered alone. For biologic therapeutics, however, another critical step is required, namely endosomal escape [111].

Nanomedicines are typically taken into cells via active, endocytic processes, which leaves therapeutics trapped in an endosome, compartmentalized away from the cytoplasm or other subcellular location where it would exert its therapeutic effect [112]. After endocytosis, early endosomes are sorted to either be recycled back out of the cell (i.e. exocytosis) or to become late endosomes and fuse with lysosomes to ultimately breakdown its contents [112, 113]. Small molecule therapeutics are often unharmed by this process after endocytosis for two reasons. First, they often lack lysosome-degradable bonds and thus are more resistant to degradation than biologic therapeutics, and second, they are usually able to rapidly cross the endosomal membrane and escape when released from their carrier. For biologic therapeutics, however, endosomal escape is critical to protect the therapeutic payload from lysosomal degradation before it can reach the cytoplasm or other subcellular compartment [107]. As such, nanomedicines for cytoplasmic delivery of biologics must include some mechanism for endosomal escape.

Mechanisms for endosomal escape usually exploit the unique chemistry of endosomes, which is slightly different from the extracellular environment in multiple ways. First, while the extracellular space is a relatively oxidizing environment, the endosome is a relatively reducing environment, and some materials are designed to respond to this difference in redox potentials to trigger chemical changes in the materials and thereby facilitate endosomal escape. Second, endosomes become relatively acidic as they mature, and some nanomedicines

are designed to be pH responsive to facilitate therapeutic release and endosomal escape in response to this change in pH. In a third approach, some therapeutics capitalize on the sequence preferences of proteases during lysosomal degradation for protease-triggered release of the therapeutic and/or endosomal escape. People have used many approaches in designing endosome-responsive materials for therapeutic release and endosomal escape of nanomedicine cargoes. For non-membrane-permeable cargoes such as biologic therapeutics, endosomal escape is a non-trivial and indispensable step for cytoplasmic delivery.

There are now numerous examples of nanomedicines that have been successfully approved for clinical use, as detailed extensively in a recent review by Anselmo and Mitragotri [114, 115]. The vast majority of FDA-approved cancer nanomedicines are liposome-based nanoparticles encapsulating small molecule chemotherapeutics [115]. Before 2018, all FDA-approved cancer nanomedicines were relatively simple nanoparticles with no targeting elements, stimulus-responsive materials, or endosome escape functionalities. Most effects from cancer nanomedicine were optimized in terms of the particles' size, shape, and surface charge, and much has been learned about how those particle characteristics influence nanoparticle distributions and accumulations [109]. Without more complex functionalities, the only clinically successful cargoes were small molecule therapeutics, which could enter cells on their own but still benefited from the enhanced pharmacokinetics, tumor accumulation, and reduced toxicity provided by nanocarriers. Meanwhile, pre-clinical research was developing far more complicated (and capable) nanomaterials, for both small molecule and biologic cargoes. For biologic therapeutics, however, the only way forward to clinical translation will likely be with more complicated, comprehensive, and rationally designed delivery systems that can account for and overcome each and every delivery barrier. In 2018, the FDA-approval of patisiran (Onpattro) was a major first-in-class milestone not only for siRNA therapy and biologic therapeutics, but for the field of nanomedicine [116].

Patisiran is the first clinically approved nanomedicine for cytoplasmic delivery of a biologic therapeutic. It is used to treat a rare but fatal disease, hereditary transthyretin amy-

loidosis, by delivering an siRNA into hepatocytes to knock down expression of the causative mutant protein. This siRNA nanocarrier is precisely designed to overcome each barrier to cytoplasmic delivery of siRNAs [116]. Patisiran consists of a therapeutic siRNA complexed with cationic lipids to form highly stable, lipid-based, PEGylated nanoparticles for intracellular siRNA delivery. The resulting nanoparticles are highly stable with a solid core. A PEG shell is adsorbed to the particle using a short C_{14} chain attached to the PEG. This PEG shell stabilizes the particles during processing and storage but rapidly dissociates from the particles in the plasma in the presence of lipid sink conditions. This then allows native ApoE proteins from the plasma to adsorb to the particle's surface to facilitate targeting to and endocytosis by hepatocytes, the targeted cell type for this therapy. The important next step, endosomal escape, is facilitated by a precisely designed ionizable lipid with a pKa of 6.4. Complexation with the siRNA is done in the lipid's cationic state at low pH, but then at physiological pH, the particle is relatively uncharged while the solid-state of the core maintains the particle's stability. After endocytosis, as the pH begins to decrease, the ionizable lipid becomes positively charged to become a cationic lipid and facilitate endosomal escape. Whereas many cationic lipids are highly toxic, this formulation has the benefit of being membrane-lytic only at endosomal pH and highly biocompatible at physiological pH. This new nanomedicine has greatly impacted treatment for this rare and life-threatening disease [117], but beyond that, it has stoked the hope and enthusiasm for using nanomedicines for the intracellular delivery of biologic therapeutics in the clinic.

For nanomedicines to succeed clinically in the intracellular delivery of biologic therapeutics, they will need to meet certain requirements, which are all exemplified in the success of patisiran. First, each successful nanomedicine must overcome each biological barrier to cytoplasmic delivery (as described above), including the often overlooked step of endosomal escape [118]. Currently, these capabilities are being rationally designed into nanomedicines in a low throughput manner [114], though in the future they could conceivably be found through screening, computational modeling, or artificial intelligence capabilities. Second, as a nano-

excipient, successful materials will be highly biocompatible, non-toxic, non-immunogenic (unless immunogenicity is favored for a particular application), and demonstrably capable of being cleared from the body [119]. Third, successful nanomedicines must be scalable in their synthesis and stable in transportation, distribution, and storage [114]. These ideas and considerations have come to guide the design principles and progression of the nanomedicine platforms I present in my own work in this thesis.

1.3.2 Peptide Amphiphile Micelles for Intracellular Peptide Delivery

Peptide amphiphiles (PAs) are one delivery system that we and others have used for the delivery of therapeutic peptides and are the platform used in Chapters 2 and 3. PAs are formed by conjugating a hydrophobic "tail" domain to one end of a therapeutic peptide [120, 121]. PAs have been used in countless applications beyond intracellular peptide delivery, including drug delivery, regenerative medicine, diagnostics, and vaccines [122].

For our applications of intracellular peptide delivery, the amphiphilic nature of a PA is used to drive the self-assembly of micellar nanoparticles. PA micelles are of optimal size to slow clearance from circulation [118], but the PA unimers are non-toxic and can be cleared through the kidneys [123]. Their micellar structure also helps prevent hydrolysis and proteolysis of the therapeutic peptide during circulation [124]. When a PA micelle reaches its target cell, its non-covalent supramolecular assembly allows unimers to dissociate from the nanoparticle, and the amphiphilic tail facilitates peptide internalization [125–127]. Moreover, targeting moieties can be conjugated to these nanoparticles for active targeting to specific cell types [128–140]. Finally, the ability to co-assemble multiple PAs into one nanoparticle by simple mixing provides the potential for combination therapy applications.

When I joined the Tirrell and LaBelle groups in 2015, it was previously established that PAs could facilitate the uptake of otherwise cell-impermeable peptides [125–127], though the peptides still remained trapped in endosomes and unable to exert a therapeutic effect [125]. Obstacles and strategies to overcome endosomal escape are discussed more broadly

on page 18. In my first laboratory work as a PhD student, I was trained by and worked with Dr. Handan Acar in her work on incorporating a cathepsin-cleavable linker between the peptide and lipid domains of a PA to short-circuit lipid-driven exocytosis/recycling of PAs and enhance their intracellular accumulation [141]. After Dr. Acar studied the mechanisms by which a cathepsin-cleavable PA could enhance the intracellular accumulation of a peptide [141], we then applied this platform to the intracellular delivery of a BIM BH3 peptide designed to activate apoptosis via the BCL-2 family of proteins (Chapter 2) [142].

Using the PA platform, we had achieved peptide uptake and intracellular accumulation, though endosomal escape was still an unconquered obstacle. In Chapter 2, a BIM BH3 peptide, delivered intracellularly as a cathepsin-cleavable PA, was able to exert a therapeutic effect, however we still do not understand how the therapeutic peptide was able to escape the endosome after release from the lipid tail [142]. The peptide alone is not cell permeable, and it does not have any obvious properties that should make it able to escape the endosome. Yet, by some unknown means, the peptide was able to escape the endosome to reach its cytoplasmic and mitochondrial targets to activate apoptosis. We are currently still exploring strategies to intentionally facilitate the endosomal escape of therapeutic peptides after release from a lipid tail after endocytosis.

PAs can be synthesized in multiple ways. They can have one or two or more lipid tails, and those lipids can be attached by various types of bonds, most commonly amides or esters. Sometimes a PEG spacer is also added to the tail domain (e.g. DSPE-PEG has two C18 lipid tails with a PEG spacer) to increase the size of the hydrophilic head group. Importantly, changing the chemical structure of the lipid domain of a PA changes the packing parameter (which can roughly be said to describe the "shape") of the PA unimer, which changes the shape of the supramolecular structure into which it will assemble [143]. For our applications we sought to use spherical micelles, which can be assembled from PAs with a large hydrophilic headgroup, and DSPE-PEG was a useful PEGylated lipid to synthesize such PAs [110]. DSPE-PEG also has two lipid tails instead of one, and having two lipid tails has been shown

to facilitate greater cellular uptake compared to one lipid tail [125]. Finally, the esters in DSPE-PEG do not impart any directional hydrogen bonding effects, which is ideal for the formation of spheres rather than more one-dimensional, worm-like micelles, which can be promoted by more directional amide bonds.

The PEGylated lipid DSPE-PEG was a useful tool for forming spherical micelles and for facilitating intracellular peptide uptake [110], but we found that its ester bonds were susceptible to hydrolysis under conditions commonly employed during peptide and PA synthesis and purification (Chapter 3) [121]. Hydrolysis of these esters often went undetected due to the dispersity of the PEG domain hiding the relatively small changes in the molecular weight of the PA. By developing a strategy to detect these ester hydrolysis byproducts via ESI-MS fragmentation, we optimized conditions under which DSPE-PEG PAs could reliably be synthesized and purified. After publishing our initial work on this [121], we made further improvements to the synthesis and purification process that have not yet been published (page 88).

Other Therapeutic Applications of Self-Assembled Peptide-Conjugates

In addition to applications in intracellular peptide delivery, peptide-conjugate self-assemblies have also been used for other applications in nanomedicine.[2]

Numerous examples of targeting peptides have been incorporated into PAs to deliver therapeutics to specific cell populations. RGD peptides are a popular example that preferentially bind $\alpha V\beta 3$ integrin overexpressed by some tumors [144]. Saraf et al. used RGD PA self-assembly to make micelles that preferentially bound melanoma cells and were internalized in vitro [145]. They then loaded a hydrophobic small-molecule anti-cancer drug called paclitaxel into the hydrophobic core, and the targeted micelles preferentially killed melanoma tumors in an in vivo mouse model.

2. This section was adapted from [122]: Handan Acar, Samanvaya Srivastava, Eun Ji Chung, Mathew R. Schnorenberg, John C.Barrett, James L. LaBelle, and Matthew Tirrell. Self-assembling peptide-based building blocks in medical applications. Advanced Drug Delivery Reviews, 110-111:65–79, February 2017.

While small molecule drugs can be loaded into the hydrophobic core of a micelle, a peptide-conjugate's peptide domain can itself be therapeutic. Zha et al. coupled a peptide domain from an anti-angiogenic protein, maspin, to an alkyl tail to form nanorods [146]. The maspin peptide domain interacts with endothelial cells to upregulate their adhesion, down-regulate their migration, and thereby inhibit angiogenesis during tumor growth [147–149]. They found that their maspin-mimetic nanorods inhibited angiogenesis in vivo and at far lower doses than when peptide was administered alone [146].

In addition to aiding in the delivery of therapeutics, a supramolecular nanoparticle's physical structure can also be harnessed as a therapeutic. Morgan et al. showed that circulating nanofibers can be actively targeted to accumulate at the site of blood vessel disruption to control hemorrhage and minimize blood loss [150]. They conjugated a peptide targeted against tissue factor to a beta-sheet forming peptide domain and an alkyl tail to form stabilized nanofibers. The nanofibers normally circulated without binding anything and were naturally cleared from the body. However, upon blood vessel disruption by injury, the nanofibers encountered and bound tissue factor in the intravascular space where they accumulated to stop blood flow from the wound.

The peptide domain of a peptide conjugate can also be used to control the stability of a micelle in the circulation and thereby control pharmacokinetics. For example, Dong et al. coupled a peptide domain, designed to form a 3-helix coiled coil, to a hydrophobic tail to form 15 nm spherical micelles that circulated in the bloodstream for at least 48 h with minimal cargo leakage [151]. In the context of actively-targeted micelles, this degree of stability could be important to ensure that the micelles reach their targets before releasing their payloads.

1.3.3 Liposomes

Liposomes, nanoparticle vesicles comprised of a lipid bilayer, have been the most clinically successful class of nanoparticles for drug delivery [114, 152–155]. Though my work has not used liposomes, their clinical success and the principles established using liposomal

nanomedicines make them crucial to discuss.

So far, clinically approved liposomes deliver small molecule therapeutics but not biologics (e.g. proteins, peptides). While small molecule cargoes are typically cell-permeable by themselves, they still benefit from liposome delivery via reduced toxicity, improved pharmacokinetics, and in cancer, preferential accumulation in solid tumors via the enhanced permeability and retention (EPR) effect [114, 154]. Each of the clinically-approved liposomes are relatively simple nanoparticles with no targeting elements, responsive materials, or endosome-escape domains, despite the now common appearance of these advanced functionalities in successful pre-clinical liposome formulations. For more on the current state of clinical nanomedicines, including liposomes, see page 19.

For intracellular delivery of biologics, however, these more complex functionalities will be required for successful clinical translation. The pre-clinical applications using more advanced liposomes have been granularly reviewed by others in recent review [107, 154–161].

Many of our key conceptual understandings about supramolecular nanomedicines have come from applications in liposomes. Others have recently reviewed the important parameters and design considerations for liposomes and their effects on biological efficacy [154, 162].

The motivating benefits of liposomal encapsulation for protein and peptide delivery are primarily (1) improved pharmacokinetics, (2) the ability to incorporate the cargo without modification, and (3) a long-standing precedent of safety and biocompatibility of liposomes [154]. The major obstacles and weaknesses to liposomal delivery, meanwhile, include (1) rapid clearance from circulation (although improved compared to non-encapsulated protein or peptide), (2) lack of cellular uptake, and (3) after cellular uptake, endosomal entrapment [154, 156].

Many people have sought strategies to improve upon the stability and circulation times of liposomes. First, by changing the composition of the lipids, the stability of the lipid bilayer can be greatly improved [154]. Second, introducing a PEG coating to the surface of liposomes has widely been shown to increase the circulation times of liposomes [163]. This improved cir-

culation time has been widely thought to be due to a PEG coating preventing serum proteins from adsorbing to the surface, thus minimizing phagocytosis and clearance from circulation. Of note, however, liposomes can typically not be more than ∼5-10% PEGylated without the PEG chains starting to repel each other and disrupting the liposomal bilayer [163–166]. In contrast to the commonly-accepted notion about PEGylation preventing adsorption, it has been shown that at 5% liposome PEGylation, serum protein adsorption is actually not inhibited at all [167]. Rather, these low amounts of PEGylation limit liposomal aggregation, and the authors show that this decreased aggregation, not decreased protein adsorption, is the primary reason for improved circulation times of PEGylated liposomes [167]. In other recent work, Lee and Larson have shown that in order for a PEG layer to repel protein adsorption, the PEG density must be high enough to achieve an extended brush-like conformation, rather than being sparsely spaced out such that each PEG chain is in a "mushroom" conformation, which serum proteins can overcome to still adsorb [168]. However, the same steric crowding of a dense PEG brush that repels protein adsorption is precisely what causes PEGylated lipids to desorb from the liposome, resulting in the approximately ∼10% limit on surface PEGylation. This low upper limit on the PEG density achievable for liposomes is limiting to their pharmacokinetics. Unlike liposomes, which are limited by the characteristics of lipids, polymersomes (introduced in Section 1.3.4) can be designed with completely synthetic block copolymers to intentionally overcome these weaknesses and form "tough"er vesicular nanocarriers [169]. Due to their increased stability, polymersomes can also be 100% PEGylated with a dense PEG brush, to better resist protein adsorption and phagocytosis to achieve longer circulation times than liposomes [170]. While many attempts have been made to improve the limiting stability and pharmacokinetics of liposomes, these characteristics can be remarkably improved by abandoning the limiting characteristics of lipids altogether and using synthetic block copolymers in polymersomes (introduced in Section 1.3.4).

The second obstacle facing liposomes for intracellular delivery of peptides and proteins is cellular uptake. Cellular uptake of liposomes is often facilitated by attaching a targeting lig-

and (e.g. antibodies, proteins, peptides, nucleic acid aptamers, other ligands) to the surface of the liposome to facilitate RME, and targeted liposome applications have been granularly reviewed by others [108, 158, 161]. While targeting endocytic receptors can mitigate the problem of uptake, the problem of endosomal escape remains.

For liposomal delivery of proteins and peptides, endosomal escape is one of the primary factors limiting efficacy. For liposomes, endosomal escape is typically achieved in one of two ways. In one strategy, cationic lipids are incorporated into the liposome's structure. The primary concerns with this approach are non-specific delivery into off-target cells and toxicity of highly cationic lipids. To ameliorate these concerns, much work has been done to develop ionizable lipids that have a precise pKa slightly below physiological pH. The goal is for the lipids to be neutrally charged outside of the cell but become protonated and cationic inside the endosome as the endosome matures and starts to acidify. The cationic lipids then facilitate endosomal escape, after which they should be buffered back to a neutral pH and uncharged state. The second set of strategies for endosomal escape involves attaching endosome-escape ligands to the surface of the liposome, such as cell-penetrating peptides (CPPs). With this approach, non-specific cellular uptake is again a concern. One way around this is to add a PEG layer to the liposome to sterically shield the CPPs until the PEG layer is removed in response to some cue, for example in the acidic endosome (to facilitate endosomal escape) or acidic tumor microenvironment (to facilitate uptake and endosomal escape). Sheddable-layer strategies have been reviewed by Romberg et al. [171].

Liposomes now have a long-standing precedent of success in clinical translation for the delivery of small molecule therapeutics. For cytoplasmic delivery of biologics, such as peptides and proteins, cellular uptake and endosomal escape remain additional obstacles. The 2018 approval of patisiran (as described on page 19) for cytoplasmic delivery of siRNA has set a new precedent for the use of ionizable lipids in facilitating the endosomal escape of biologic therapeutics in the clinic. Perhaps this success will facilitate the clinical translation of next generation lipid-based nanomedicines for cytoplasmic delivery of peptides and proteins.

While protein cargoes have been commonly employed in literature examples of intracellular liposome delivery [107, 154–161], peptide therapeutic cargoes have been used only rarely. Liposomes are often decorated with peptides on the surface to impart various functionalities, but rarely are they used as the therapeutic cargo itself, intended for intracellular delivery. Others have reviewed specific literature examples of pre-clinical therapeutic peptides intended for intracellular delivery [107, 172].

While pre-clinical liposomal peptide therapeutics are rare, clinically-approved formulations are non-existent. There is one clinically-approved formulation of a peptide-containing-liposome in Europe, called mifamurtide, which is used for treating osteosarcoma, but it failed to gain FDA approval in the US due to insufficient efficacy data. This liposomal formulation encapsulates an immunostimulatory lipopeptide that mimics muramyl dipeptide on the surface of bacteria to bind the NOD2 receptor of innate immune cells, activate an innate immune response and cytokine secretion, and improve the anti-cancer immune response as an adjunct to chemotherapy. The NOD2 receptor is predominantly found in the cytoplasm of innate immune cells [173], and the lipid domain of this immunostimulatory lipopeptide likely facilitates its endosomal escape and cytoplasmic access to reach its target.

While we have not used liposomes, and liposomes have not been used specifically for intracellular delivery of therapeutic peptides, many key lessons have been learned using liposomes about how to design and apply supramolecular nanomedicines.

1.3.4 Polymersomes

Polymersomes are highly-stable, polymeric vesicles that are analogous to liposomes but expand upon their useful chemical and physical properties [169, 174]. In 1999, Discher et al. first reported on "Polymersomes: Tough Vesicles Made from Diblock Copolymers" in *Science* [169]. At that point in time, liposomes had been in use since the 1960s and had proven extremely useful as nanocarriers. While liposomes are primarily limited by the sizes and characteristics of natural lipids, polymersomes can be self-assembled from fully synthetic,

amphiphilic block copolymers that can be much larger and more synthetically customizable than lipids. In this first report, they demonstrated that their polymersomes were "tough"er than liposomes, resisting an order of magnitude greater strain while being an order of magnitude less permeable to water. Their synthetic, amphiphilic block polymers were much larger than lipids and generated vesicles with a thicker membrane than liposomes. Since this 1999 report, polymersomes as a class of nanomaterials have now greatly expanded upon the chemical and physical properties of liposomes, capitalizing on their strengths and improving upon their weaknesses.

In Section 1.3.3, I discussed two key weaknesses of liposomes as nanomedicines, namely their stability and degree of PEGylation. First, while liposomes can be made more stable by varying the lipid composition, polymersome stability can be infinitely tuned, including making them far more stable than liposomes, by changing the synthetic polymer building blocks. Second, while liposomes can be PEGylated, they can only achieve 5-10% PEGylation before the PEG-lipids start to disrupt the liposome structure [163–166]. This 5-10% PEGylation is not enough PEG to achieve a dense PEG brush and significantly prevent protein adsorption to the surface of liposomes [167, 168], and the resulting protein adsorption is the first step to premature phagocytic clearance of nanoparticles from the body. Polymersomes, meanwhile, can routinely be made 100% PEGylated without affecting their structure, thus better preventing protein adsorption and premature clearance when compared to liposomes [170].

Another key weakness of liposomes-as-nanocarriers that I discussed in Section 1.3.3 is their endosomal entrapment. Due to the chemical versatility of polymers, polymersomes can be designed to undergo chemical and physical changes in response to stimuli. Messager et al. have summarized many of the key ways in which polymersomes have expanded upon the chemical versatility of liposomes [174]. Importantly for endosomal escape, a key requirement of intracellular delivery of peptides and proteins, polymers can be designed to respond to the unique chemical cues of early endosomes (e.g. a reducing environment [175–181]), of ma-

turing endosomes (e.g. decreasing pH [182, 183]), or of the unique endosomes of phagocytic immune cells (e.g. an oxidizing environment [184–187]).

1.3.5 PEG-SS-PPS Polymersomes

In Chapter 4, we sought to use a supramolecular nanostructure to encapsulate hydrocarbon stapled peptides, target them specifically to DLBCL cells, and facilitate their cellular uptake and endosomal escape. A polymersome platform previously developed by the Hubbell lab seemed to have all the characteristics of an ideal nanocarrier for this application. We used an amphiphilic block copolymer composed of a hydrophilic poly(ethylene glycol) (PEG) block and a hydrophobic poly(propylene sulfide) (PPS) block with a disulfide bond between the two blocks (PEG-SS-PPS) [181]. This block copolymer and its similar counterparts have previously been shown to have characteristics of an ideal nanocarrier for this application.

First, the stability of PEG-PPS polymersomes should protect stapled peptides in circulation and allow for attachment of targeting ligands for RME. The Hubbell lab has previously characterized the physical properties of PEG-PPS polymersomes [188]. While PEG-PPS block copolymers can form highly stable polymersomes, PPS has a low glass transition temperature (T_g) of around 230 K (-43 °C), which means these polymersomes can be easily assembled at room temperature, without the need for heat or co-solvents. This allows for assembly by a variety of methods, including thin film formation, inverse direct dissolution [189], or flash nanoprecipitation [190, 191]. For cargo that we do not expect to be able to diffuse across a PPS vesicle layer, such as a stapled peptide, a low T_g polymer is ideal for ease of assembly and more rapid responses to physiological chemical cues. For hydrophobic small molecule drugs, or applications in which we would require a more solid-like vesicle, we would perhaps need to use a polymer with a higher T_g for more stable encapsulation to avoid drug leakage.

In addition to the PPS layer of polymersomes being both stable but non-glassy, the PPS backbone is also susceptible to oxidation, from poly(propylene sulfide) to poly(propylene sul-

foxide) then poly(propylene sulphone) [192]. This oxidation makes the PPS block relatively hydrophilic, causing polymersomes to disassemble through various intermediate structures and ultimately into soluble unimers [192, 193]. For a nanomedicine, this is major benefit, because it facilitates the eventual clearance of the polymersome building blocks through simple renal filtration. PEG-PPS polymersomes have recently been shown to be non-toxic in high doses in both mice and non-human primates [191], and the ability of the individual polymers to be processed and cleared from the body should presumably contribute to this complete lack of toxicity.

This susceptibility to oxidation of PPS has been shown to be a useful nanocarrier release mechanism in response to inflamed tissues [192] for extracellular release, or intracellularly after phagocytosis by certain immune cell types with oxidative phagosomes for immune modulation and antigen presentation [194–196]. However, we primarily aim to harness the oxidation-susceptibility of PPS for its non-toxic clearance rather than for polymersome disruption, which we seek to achieve through a different mechanism.

By adding a disulfide bond between the the PEG and PPS blocks, Cerritelli et al. made reduction-sensitive PEG-SS-PPS polymersomes [181]. This allowed for rapid cleavage of the block copolymer (PEG-SS-PPS) in the reducing environment of the endosome [175–181], which disrupted the polymersomes and facilitated endosomal escape and intracellular accumulation of a model cargo, presumably due to the freed hydrophobic PPS block interacting with the endosomal membrane [181]. For cytoplasmic delivery of peptide therapeutics, we aim to facilitate endosomal escape as early after endocytosis as possible, and the PEG-SS-PPS block copolymer should be ideal for facilitating rapid and early endosomal escape in many cell types with reducing endosomes, including DLBCL.

Another important feature of PEG-PPS polymersomes as nanocarriers is their dense PEGylation. While liposomes can only achieve 5-10% PEGylation before their structure is disrupted (see Section 1.3.3) [163–166], polymersomes with a PEG block copolymer are 100% PEG functionalized on the polymersome surface, which resists protein-adsorption that would

otherwise lead to non-specific uptake and clearance from the body. In a direct comparison between polymersomes and liposomes, Photos et al. showed that polymersomes, which are more stable and more highly PEGylated compared to liposomes, were better able to resist opsonization and phagocytosis [170].

For encapsulating hydrocarbon stapled peptides, PEG-PPS polymersomes seemed like a particularly promising encapsulation vehicle. PEG-PPS nanocarriers have been shown to successfully encapsulate both hydrophilic cargoes in the aqueous lumen and hydrophobic cargoes in the PPS phase [181, 189, 196–198]. We hypothesized this dual hydrophobic/hydrophilic loading capability would allow for successful encapsulation of hydrocarbon-stapled peptides, which have both a hydrophilic peptide domain and a hydrophobic all-hydrocarbon staple. It might otherwise prove difficult to encapsulate a cargo with both hydrophilic and hydrophobic domains, but with PEG-PPS polymersomes, the hydrophilic-hydrophobic boundary in the core is likely an ideal interface for hydrocarbon-stapled peptides.

Together, these characteristics of PEG-SS-PPS polymersomes describe a theoretically ideal nanocarrier for cytoplasmic delivery of hydrocarbon stapled peptides to and into a targeted cell type. In Chapter 4, we build upon this previous literature on PEG-PPS and PEG-SS-PPS polymersomes. To move beyond passive targeting to phagocytic cell types, we modified the distal end of the PEG chain with an azide handle to attach targeting elements to specifically bind and trigger uptake into B cells via CD19.

1.3.6 Ligand-Targeted Nanoparticles

In Chapter 4, the design of our CD19-targeted Fab-polymersome nanocarriers builds on important design considerations from a breadth of work from Dr. Theresa Allen and colleagues on ligand-targeted nanoparticles. Most notably, work on CD19-targeted liposomes for small molecule delivery has previously highlighted the utility of CD19-targeted, internalized nanocarriers for enhancing therapeutic efficacy in DLBCL and minimizing on-target

toxicities [199–204].

One of the design parameters they identified as important was the choice of antibody fragment used for nanoparticle targeting, for which they compared IgG, F(ab') fragments, and scFv fragments from an anti-CD19 antibody [203]. They found that full IgGs accelerated the premature clearance of nanoparticles from circulation, presumably by immune recognition of the Fc domain of IgG being recognized by immune cells' Fc receptors in the liver and spleen. However, the scFv fragments also decreased the circulation time of nanoparticles, presumably due to the inclusion of potentially immunogenic tags on the scFv for identification and purification. When the tags were excluded from the scFv, less of the targeted nanoparticles accumulated in the liver. F(ab') fragments, meanwhile, allowed for the most efficacious formulations of their doxorubicin-loaded nanoparticles, as F(ab') fragments have no Fc domain and also require no affinity tags for identification and purification.

Despite the advantages of F(ab') fragments relative IgG or scFvs, as of 2010 the authors still preferred scFvs as the antibody fragment of choice for ligand-targeted nanoparticles [204]. Their reasoning was primarily due to (1) the ability to engineer site-specific linkers into the scFvs, and (2) the ability to recombinantly produce scFvs, while F(ab') fragments were produced through low-throughput and tedious digestion of IgG. To that end, many people have sought ways to understand and improve upon the primary weaknesses of scFvs, which are (1) their lack of stability in solution and (2) difficulty in reliably expressing soluble protein [203–206].

Importantly, F(ab') fragments are far more stable than scFvs. In fact, simply converting an unstable scFv sequence into a Fab format can improve its stability and in vivo efficacy [207]. Our collaborators in the Hubbell lab sought to capitalize on the strengths of Fab fragments and find a way to recombinantly express Fabs instead of digest IgGs. In doing so, they have developed a platform for scalable expression of engineered Fab fragments with the potential for site-specific modifications. Their engineered Fabs are often solubly expressed, correctly folded, and functional on the first try, as was the case with our αCD19 targeting

Fabs used in Chapter 4. With this platform, they have developed a platform that capitalizes on the strengths of Fabs as targeting antibody fragments, while routinely being solubly expressed in high yields and secreted from mammalian cells.

1.4 Diffuse Large B-Cell Lymphoma (DLBCL) as a Clinically Relevant and Impactful Model for Ligand-Targeted Drug Delivery, Chemoresistance, and Protein-Protein Interactions

As our primary therapeutic application in Chapter 4, we chose to target the p53 and MCL-1 pathways in diffuse large B-cell lymphoma (DLBCL). DLBCL as a disease exemplifies both the clinical need and potential for novel PPI-inhibiting drugs, particularly for the current state-of-the-art stapled peptide PPI inhibitors. As a disease of B cells, it also represents an opportunity for drugging PPIs with ligand-targeted nanoparticles as a precise delivery vehicle. The primary obstacles for stapled peptides as PPI inhibitors are their in vivo activity, cell-specific delivery, and cellular uptake (see Section 1.2.2), and DLBCL is a clinically relevant model in which to address these weaknesses with ligand-targeted nanoparticles to capitalize on the strengths of stapled peptides as PPI inhibitors.

DLBCL is the most common form of lymphoma, and 60% of patients present with advanced stage III or IV disease [208, 209]. Despite major advances in first line therapies, 63% of DLBCL cases will be refractory to treatment and/or relapse [210]. For patients with relapsed DLBCL, 73% will not survive five years [211].

Despite their chemoresistance, more than 80% of DLBCL cases have wildtype *TP53*, with the p53 protein presumably inactivated by its PPI binding partners, HDM2 and HDMX [23, 212, 213]. Inactivating p53 PPIs are one of the most well known examples of cancer-driving, "undruggable" PPIs (see Section 1.1.2). The most clinically relevant stapled peptide, ALRN-6924, is a p53-reactivating stapled peptide that is currently advancing through clinical trials (see Section 1.2.2). The sequence of ALRN-6924, and most clinical and pre-clinical

data from its use, are proprietary and unpublished. The preclinical predecessor to ALRN-6924, however, is ATSP-7041, and this research-grade stapled peptide has been synthesized, used, and studied by numerous research groups. This well-studied, p53-reactivating stapled peptide has been highly optimized to be cell-permeable, non-toxic, and active in vivo. ATSP-7041 has not yet been studied and used in DLBCL, but as a cancer in which the majority of cases have wildtype *TP53*, DLBCL is a highly relevant form of cancer in which utilize ATSP-7041 and therapeutic p53 reactivation. In Chapter 4, we studied the effects of ATSP-7041 in DLBCL by looking at p53-mediated changes in the BCL-2 family of proteins, its effects in priming the mitochondria for apoptosis, and ultimately its therapeutic synergy with MCL-1 inhibitors for reactivating cancer cell death.

Acquiring resistance to cell death is a well-known hallmark of cancer [12, 13], and like other cancers, DLBCL resists cell death by deregulating PPIs in the BCL-2 family of proteins to inactivate apoptosis [214] (for more on the BCL-2 family, see Section 1.1.1). While venetoclax, a BCL-2 inhibitor, has dramatically changed the treatment of some cancers (see Section 1.2.1), a Phase I study suggests it has a minimal effect on chemoresistant and chemorefractory DLBCL [215].

Another key anti-apoptotic member of the BCL-2 family, MCL-1, is one of the most commonly upregulated genes that cancers rely on for survival [29], including DLBCL [216, 217]. MCL-1 upregulation in DLBCL is associated with poorer clinical outcomes [218], and it is implicated in resistance to therapeutic cell death [219, 220]. Inhibition of MCL-1, meanwhile, can reactivate cell death and overcome chemoresistance in DLBCL [221–223]. MCL-1 is an important therapeutic target in many kinds of cancers, and DLBCL is no exception.

However, systemic inhibition of MCL-1 has the potential for on-target toxicities due to the critical function of MCL-1 in maintaining the viability of many healthy tissues [224–230]. For this reason, a targeted delivery vehicle could potentially greatly improve the efficacy and translational potential of MCL-1 inhibitors for cancer therapy. While MCL-1 inhibition in

DLBCL is a clinically relevant first target, a successful nanoparticle delivery platform for stapled peptides would be relevant in a variety of cancers for targeting a variety of PPIs.

In Chapter 4, we developed a DLBCL-targeted nanoparticle for intracellular delivery of a stapled peptide. We chose as our model peptide SAH-MS1-18, which has been shown to specifically inhibit MCL-1 [102]. SAH-MS1-18 binds MCL-1 tightly with high affinity, and it does so specifically, without also binding and inhibiting the other structurally-similar anti-apoptotic proteins in the BCL-2 family. Meanwhile, the authors were able to iteratively optimize the peptide to be both cell permeable (qualitatively, by fluorescence microscopy with a FITC-labeled peptide) and non-toxic. Ultimately, SAH-MS1-18 was able to induce cell death in MCL-1 dependent cancers in a highly MCL-1-dependent manner. This peptide was also not inhibited by the presence of serum proteins during treatments (e.g. 10% FBS during in vitro treatments), which is a common problem for many research-grade stapled peptides. This paper highlights the strengths of stapled peptides for designing inhibitors of PPIs that are notoriously difficult to drug with both potency and specificity.

However, SAH-MS1-18 also exemplifies one of the greatest areas for improvement for stapled peptides, namely their marginal and poorly understood cell permeability (see page 13 for more examples). SAH-MS1-18 binds MCL-1 with high specificity at 25 nM ex vitro, but kills MCL-1-dependent cancer cells at 5 μM in vitro. When the cell membrane is permeabilized prior to treatment, SAH-MS1-18 induces mitochondrial depolarization (a proxy for cell death) at 0.45 - 18 nM [102]. While there may be other factors contributing to these differences in effective doses, the presence of a cell membrane clearly inhibits the efficacy of this stapled peptide, even though it has been optimized for cell permeability.

Our goal is to develop a targeted nanocarrier to facilitate the cell-specific, intracellular delivery of stapled peptides for PPI inhibition. The p53 and BCL-2-family pathways represent two highly relevant, disease-driving PPI examples in cancer, and they are particularly relevant in DLBCL. The stapled peptide research community (and now pharmaceutical industry) have been developing stapled peptides to target p53-reactivation (e.g. ALRN-6924,

ATSP-7041, SAH-p53-8, among others) and MCL-1 inhibition (e.g. SAH-MS1-18). With the confluence of these factors, we think that DLBCL represents a clinically-relevant model system in which to develop a cell-targeted nanoparticle for intracellular delivery of stapled peptides.

CHAPTER 2

ACTIVATING THE INTRINSIC PATHWAY OF APOPTOSIS USING BIM BH3 PEPTIDES DELIVERED BY PEPTIDE AMPHIPHILES WITH ENDOSOMAL RELEASE

This chapter is presented as published [142] in Materials 2019, 12(16), 2567.

2.1 Abstract

Therapeutic manipulation of the BCL-2 family using BH3 mimetics is an emerging paradigm in cancer treatment and immune modulation. For example, peptides mimicking the BIM BH3 helix can directly target the full complement of anti- and pro-apoptotic BCL-2 proteins to trigger apoptosis. This study has incorporated the potent BH3 α-helical death domain of BIM into peptide amphiphile (PA) nanostructures designed to facilitate cellular uptake and induce cell death. This study shows that these PA nanostructures are quickly incorporated into cells, are able to specifically bind BCL-2 proteins, are stable at physiologic temperatures and pH, and induce dose-dependent apoptosis in cells. The incorporation of a cathepsin B cleavable linker between the BIM BH3 peptide and the hydrophobic tail resulted in increased intracellular accumulation and mitochondrial co-localization of the BIM BH3 peptide while also improving BCL-2 family member binding and apoptotic reactivation. This PA platform represents a promising new strategy for intracellular therapeutic peptide delivery for the disruption of intracellular protein:protein interactions.

2.2 Introduction

The BCL-2 family of proteins forms a complex protein-protein interaction (PPI) network that regulates cellular life and death decisions, which contributes to organismal development, cancer ontogeny and chemoresistance, hematopoiesis, and immune regulation [14, 231–233].

Members of the BCL-2 family known as BH3-only proteins (e.g., BIM, BID, PUMA, NOXA) serve as cellular stress sentinels and can trigger irreversible activation of apoptosis through their α-helical BH3 death domains. These pro-apoptotic signals are normally held in check by the multidomain anti-apoptotic family members (e.g., BCL-XL, BCL-2, BCL-W, MCL-1) through sequestering PPIs. However, when pro-apoptotic signals outweigh anti-apoptotic signals, the multidomain pro-apoptotic effectors, BAX and BAK, are activated and trigger the cell death cascade by oligomerizing in the mitochondrial membrane, leading to mitochondrial outer membrane permeabilization (MOMP), cytochrome c release, apoptosome formation, and effector caspase activation [14].

The BCL-2 family's PPIs have emerged as an impactful set of therapeutic targets [18]. Cancer cells often push the BCL-2 family's PPI balance toward an anti-apoptotic state to avoid cell death despite cellular stress and damage, for example by upregulating anti-apoptotic members or downregulating pro-apoptotic members [18, 19]. As most chemotherapies function by ultimately inducing apoptosis, cancers often acquire chemotherapeutic resistance by manipulating the homeostatic balance of BCL-2 family members [19]. BH3-mimetics are a powerful way to therapeutically interrupt this balance and reactivate cell death, particularly in cancers that are "primed for death" with upregulated anti-apoptotic proteins [234].

While intracellular PPIs are commonly deemed undruggable targets, peptides can effectively mimic the PPI interface domains of proteins and thus disrupt PPIs with high specificity and affinity. However, because peptides are typically not cell permeable, chemical poration of the cell membrane is required for peptides to reach their intracellular targets, making many potential peptides irrelevant for therapeutic applications. Hydrocarbon-stapled peptides are a noteworthy exception in which an all-hydrocarbon staple is installed across helical turns of a peptide. These stapled peptides have enhanced α-helicity, resist proteolysis, and, with empirical screening, can be made cell-permeable [76, 77, 235].

Recent work has shown that peptide amphiphiles (PAs), or peptides linked to a hydropho-

bic, lipid-like tail, can also impart cellular uptake for otherwise cell-impermeable peptides [125–127]. Moreover, these PAs can spontaneously self-assemble into micellar nanostructures in aqueous solution. Supramolecular peptide delivery provides several advantages compared to peptides alone: single micelles can (1) deliver high concentrations of peptides into cells; (2) stabilize peptide secondary structure(s); (3) protect peptides from proteolysis in the blood stream; (4) increase circulation half-lives; and (5) simultaneously deliver multiple therapeutics targeting non-redundant, synergistic cellular pathways [110]. We have also previously shown that PA micelles can be actively targeted to specific cell types in vivo, where a targeting PA can successfully carry non-targeted cargo to a target receptor simply through their supramolecular co-assembly [128, 131].

While the exact mechanism of PA cellular uptake remains unproven, recent work has shown that PAs interact with the cell membrane and traffic through endosomes and lysosomes [125–127, 236]. However, facile intracellular delivery and the release from endosomal/lysosomal compartments have been significant limitations to using PAs for intracellular delivery of biofunctional peptides. We recently showed that incorporating an endosomally-cleavable linker between the peptide cargo and lipid tail enhances intracellular accumulation and minimizes lipid-driven recycling out of the cell [141].

Here, this study develops and biochemically characterizes novel PAs able to intracellularly deliver an α-helical peptide mimicking the BH3 death domain of BIM previously shown to bind BCL-2 family members and potently reactivate apoptosis in resistant malignancies [103, 237–239]. In so doing, these PAs overcome membrane sequestration, plasma membrane recycling, and lysosomal degradation limitations known to decrease the potency of first-generation PAs. Using native peptides, which by themselves are cell-impermeable, the BIM BH3 domain was attached to hydrophobic tails and thereby incorporated into spherical micelles, which are ideal for in vivo delivery and trafficking [118]. Lastly, intracellular organelle sequestration of the biofunctional peptide was overcome through the incorporation of a cathepsin-cleavable linker between the peptide and hydrophobic tail.

2.3 Results

2.3.1 Peptide Amphiphile Design

To test our PA delivery strategy for therapeutic peptides, we constructed a set of PAs to mimic the BH3 death domain of BIM (BIM_A BH3; Figure 2.1). However, this peptide sequence is sparingly soluble in water, so five C-terminal lysines were added to increase the charge and solubility of the peptide ($BIM_{A,K}$) (Figure 2.1a). This peptide was attached to two different lipid-based tails, both of which our group and others have previously used to deliver peptides into cells, to form $BIM_{A,K}PA_1$ and $BIM_{A,K}PA_2$ (Figure 2.1b, Figures 2.7 and 2.8). The lipid tails were attached to the side chain of the C-terminal lysine of the BIM BH3 peptides. Finally, a cathepsin-cleavable linker was incorporated between the therapeutic peptide and the C-terminal lysines to form a cathepsin-cleavable PA, $BIM_{A,cath,K}PA_2$, which we hypothesized would allow for release of the peptide cargo following PA uptake into the cell.

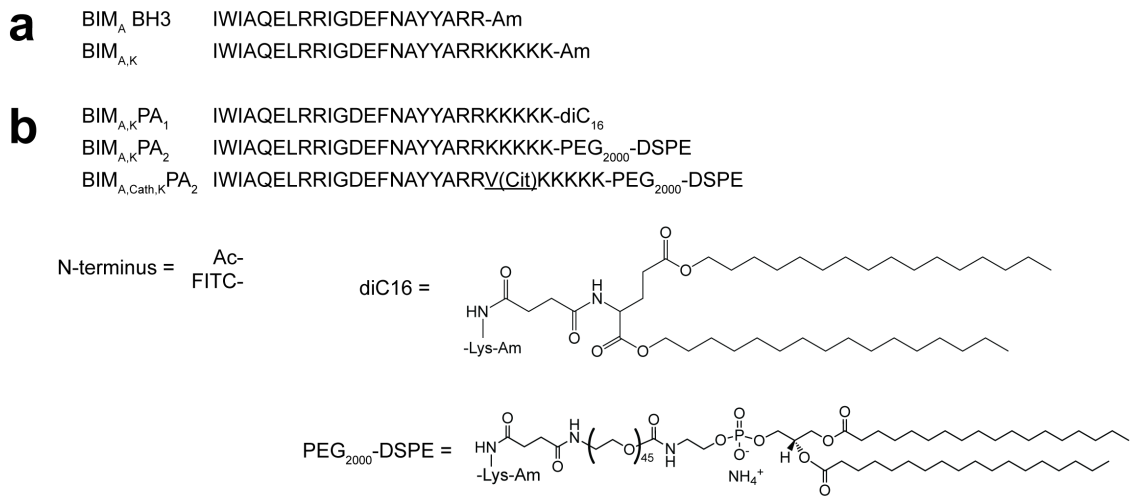

Figure 2.1: Sequences and structures of BIM BH3 PAs. (a) BIM_A BH3 mimics the BH3 death domain of BIM. To enhance its charge and aqueous solubility, five lysines were added to the C-terminus to create $BIM_{A,K}$. (b) To the $BIM_{A,K}$ peptide, a diC16 lipid tail was added to form $BIM_{A,K}PA_1$, and a DSPE-PEG lipid tail was added to form $BIM_{A,K}PA_2$. A cathepsin-cleavable linker was also incorporated into $BIM_{A,K}PA_2$ between the BIM_A sequence and the C-terminal lysines and lipid tail to form $BIM_{A,cath,K}PA_2$.

2.3.2 PAs Enhance Cellular Uptake Without Non-Specific Membrane Disruption

The ability of the PAs to deliver the BIM_A BH3 peptide into cells was tested next, as these lipid tails have previously been shown to facilitate cellular internalization [125–127]. To determine the extent of intracellular localization, HeLa cells were incubated in the presence of FITC-labeled peptides or PAs for 2 h followed by imaging using live cell confocal microscopy. Prior to imaging, the cells were washed to remove non-cell associated PAs. $BIM_{A,K}$ peptide alone was not taken up into cells, but the addition of a diC16 tail ($BIM_{A,K}PA_1$) or a DSPE-PEG tail ($BIM_{A,K}PA_2$) enabled cell uptake of the otherwise cell-impermeable peptide (Figure 2.2a). The DSPE-PEG PA, $BIM_{A,K}PA_2$, was more localized to the cellular membrane at this time point, while the diC16 PA, $BIM_{A,K}PA_1$, had a more diffuse intracellular presence. Importantly, both $BIM_{A,K}PA_2$ and $BIM_{A,cath,K}PA_2$ had greater presence at the membrane and in punctate organelles when compared to $BIM_{A,K}PA_1$, suggesting poorer penetrating ability of the DSPE-PEG tail compared to the diC16 tail. Incorporation of a hydrophilic PEG domain has previously been shown to affect membrane interactions and uptake mechanisms [127], with a PEG spacer causing cellular internalization more dependent upon the active uptake mechanisms. Interestingly, when a cathepsin-cleavable linker was added between the peptide and DSPE-PEG tail domain in $BIM_{A,cath,K}PA_2$, the intracellular peptide more quickly became diffuse and co-localized with mitochondria, the site of action of the BCL-2 family of proteins (Figure 2.9). This localization of $BIM_{A,cath,K}PA_2$ was observed to be time dependent (Figure 2.10).

As the proposed mechanism(s) of PA uptake involves interactions of the lipid domains with the cell membrane, it is critical to test for non-specific membrane disruption and cytotoxicity caused by the lipid tails [238]. To rule out non-specific membrane disruption, the release of cytoplasmic LDH from cells treated with PAs was measured 1 h following treatment (Figure 2.2b). $BIM_{A,K}PA_1$, which readily entered the cells, caused dose-dependent LDH release, indicating some degree of non-specific lipid-associated membrane disruption.

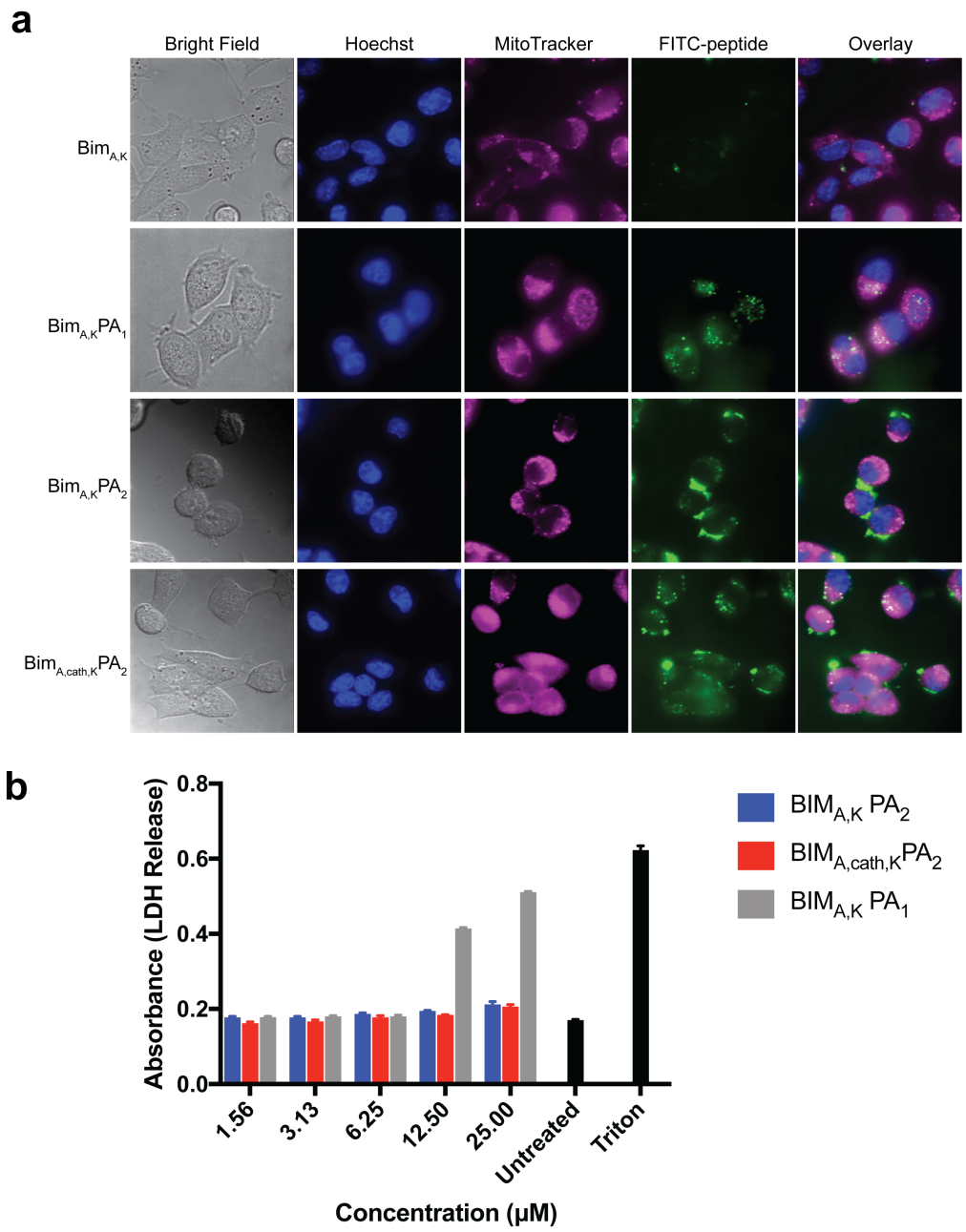

Figure 2.2: Addition of lipid tails imparts cell uptake to an otherwise cell-impermeable BIM BH3 peptide. (a) Live cell confocal microscopy of HeLa cells treated with fluorescein isothiocyanate (FITC)-labeled $BIM_{A,K}$ peptide, $BIM_{A,K}PA_1$, $BIM_{A,K}PA_2$, or $BIM_{A,cath,K}PA_2$ for 2 h followed by washing. $BIM_{A,K}PA_1$ and $BIM_{A,cath,K}PA_2$ resulted in diffuse intracellular localization of the BIM BH3 peptide. (b) $BIM_{A,K}PA_1$ caused non-specific membrane disruption and LDH release in a dose-dependent manner while $BIM_{A,K}PA_2$ and $BIM_{A,cath,K}PA_2$ did not. Values plotted are the mean ± S.E.M.

The DSPE-PEG tail of $BIM_{A,K}PA_2$, however, caused no measurable LDH release, with or without the cathepsin-cleavable linker (Figure 2.2b). Based upon its facile intracellular penetration, lack of non-specific cellular membrane disruption, and ability to diffusely disseminate the BIM BH3 peptide, $BIM_{A,cath,K}PA_2$ appeared to be a logical candidate PA for further structural, target binding, and efficacy testing compared to $BIM_{A,K}PA_2$.

2.3.3 Biophysical Characterization of Micelles

The critical micelle concentration (CMC) was 1.04 μM and 1.54 μM for $BIM_{A,K}PA_2$ and $BIM_{A,cath,K}PA_2$, respectively (Figure 2.3a). Dynamic light scattering (DLS) was used to measure the mean hydrodynamic radii (Rh) of the micelles, which were 53.7 nm ($\pm$8.1 nm) for $BIM_{A,K}PA_2$ and 85.4 nm ($\pm$10.0 nm) for $BIM_{A,cath,K}PA_2$ (Figure 2.3b). Imaging the micelles with negative-stain TEM confirmed the micelles were spherical, as expected for DSPE-PEG micelles, and the sizes agreed with the DLS measurements (Figure 2.3c). Incorporation of a peptide into a micelle has been shown to increase its natural α-helical structure formation [240–242], so we next used circular dichroism (CD) to measure the alpha helicity of $BIM_{A,K}$ after incorporation into micelles. BIM BH3 peptides within both PAs had similar degrees of alpha helicity, which were constant at temperatures ranging from 25 to 50 °C and after heating to 70 °C followed by cooling to 37 °C (Figure 2.3d).

2.3.4 Target Protein Binding

Specific apoptosis induction within cells requires selective binding of the BIM BH3 peptide to hydrophobic grooves formed by selective helical domains of anti-apoptotic and pro-apoptotic BCL-2 family target proteins [103, 238, 239, 243]. The addition of a large lipid tail, while facilitating intracellular delivery of $BIM_{A,K}PA_2$ and $BIM_{A,cath,K}PA_2$, may sterically inhibit the BIM BH3 peptide binding to its cognate target binding region. To test this, fluorescence polarization (FP) was used to measure the binding of FITC-labeled BIM BH3 peptides and PAs to recombinant antiapoptotic BCL-2 family proteins [103]. Indeed, the addition of a

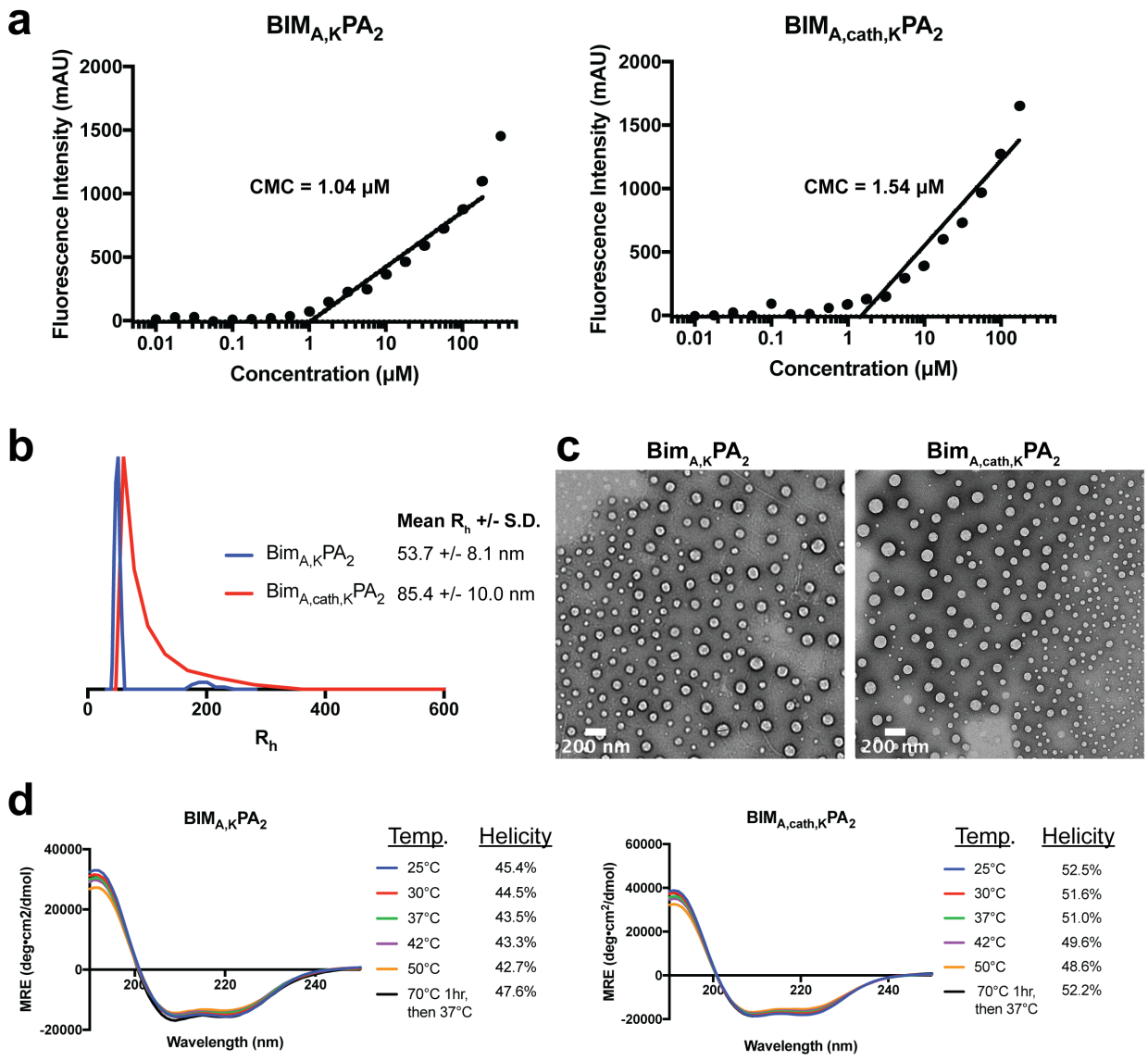

Figure 2.3: Biophysical characterization of peptide amphiphile (PA) self-assembly into micelles. (a) The critical micelle concentration (CMC) of $\mathrm{BIM_{A,K}PA_2}$ and $\mathrm{BIM_{A,cath,K}PA_2}$ as measured using 1,6-diphenyl-1,3,5-hexatriene (DPH) incorporation assay. (b) Dynamic light scattering (DLS) measurements of the hydrodynamic radii of $\mathrm{BIM_{A,K}PA_2}$ and $\mathrm{BIM_{A,cath,K}PA_2}$ indicated uniform micelle formation. (c) Negative-stained TEM confirmed that $\mathrm{BIM_{A,K}PA_2}$ and $\mathrm{BIM_{A,cath,K}PA_2}$ micelles were spherical and of equivalent sizes as measured by DLS. (d) Circular dichroism (CD) of the BIM BH3 peptide secondary structure within $\mathrm{BIM_{A,K}PA_2}$ and $\mathrm{BIM_{A,cath,K}PA_2}$ micelles revealed stable α-helicity of the $\mathrm{BIM_A}$ peptides independent of temperature.

DSPE-PEG tail inhibited $BIM_{A,K}$'s ability to bind to BCL-2, BCL-W, BCL-XL, and MCL-1 (Figure 2.4a). The $BIM_{A,K}$ peptide alone bound each protein with double-digit nanomolar affinity. However, the addition of the DSPE-PEG tail decreased these affinities by ∼2–5 fold (Figure 2.4a). Of note, $BIM_{A,K}$ bound with affinities between 76–99 nM while BIM_A peptide (lacking the C-terminal lysines) is known to bind these same antiapoptotic targets with ∼10x fold higher affinities, indicating that the addition of the lysines also likely dampened cognate target protein binding [103, 238, 244].

Based upon the intact PA:target protein binding affinities, we next aimed to determine if the release of the BIM BH3 peptide from both the C-terminal lysines and DSPE-PEG lipid tail could improve binding to BCL-2 family antiapoptotic protein targets. To do this, $BIM_{A,cath,K}PA_2$ was preincubated with recombinant cathepsin B enzyme prior to incubation with anti-apoptotic BCL-2 family proteins. Cathepsin pre-incubation resulted in time dependent increased affinities to BCL-XL plateauing between 15–30 min (Figure 2.4b). Incubation of $BIM_{A,cath,K}PA_2$ with recombinant cathepsin for 30 min led to increased BIM BH3 peptide affinity for BCL-XL and MCL-1 (Figure 2.4c). In fact, following the cleavage of the BIM BH3 native peptide from the C-terminal lysines and lipid tail, peptide affinity increased 6–10 fold compared to $BIM_{A,K}$, presumably due to release from the C-terminal lysines (87 nM to 14 nM for BCL-XL and 99 nM to 10 nM for MCL-1) (Figure 2.4c). These binding profiles reflect previously published reports of affinities of the BIM_A peptide for these proteins [103, 238]. These data suggest that following intracellular delivery of intact PAs, removing the lipid tail and C-terminal lysines from BIM_A is critical not only for the intracellular trafficking of the therapeutic peptide, but also for its ability to bind to its target proteins.

2.3.5 Cathepsin Dependence for Intracellular Accumulation

We next tested whether or not $BIM_{A,cath,K}PA_2$'s diffuse intracellular trafficking (Figure 2.2a) depended on cathepsin cleavage of the BIM_A peptide from the DSPE-PEG tail by using

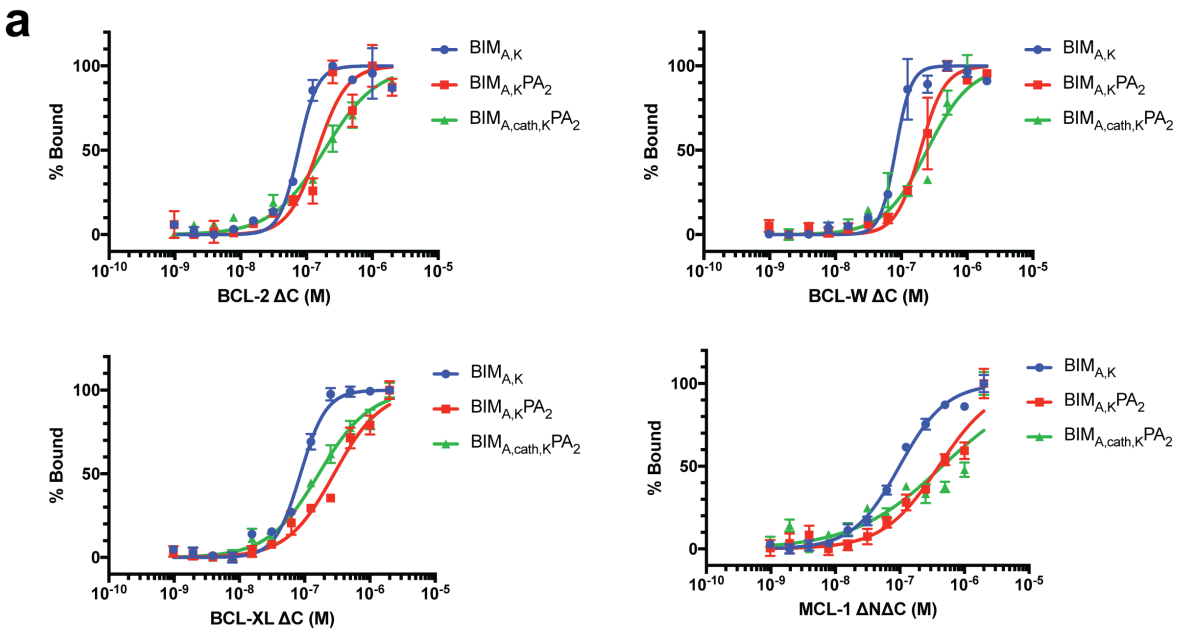

	BCL-2 ΔC	BCL-W ΔC	BCL-XL ΔC	MCL-1 ΔNΔC
Bim$_{A,K}$	76 ± 5 nM	82 ± 5 nM	87 ± 4 nM	99 ± 5 nM
Bim$_{A,K}$PA$_2$	147 ± 20 nM	195 ± 16 nM	283 ± 23 nM	400 ± 46 nM
Bim$_{A,cath,K}$PA$_2$	187 ± 18 nM	247 ± 26 nM	165 ± 12 nM	453 ± 89 nM

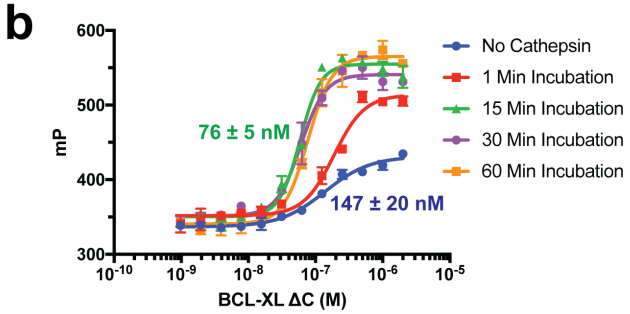

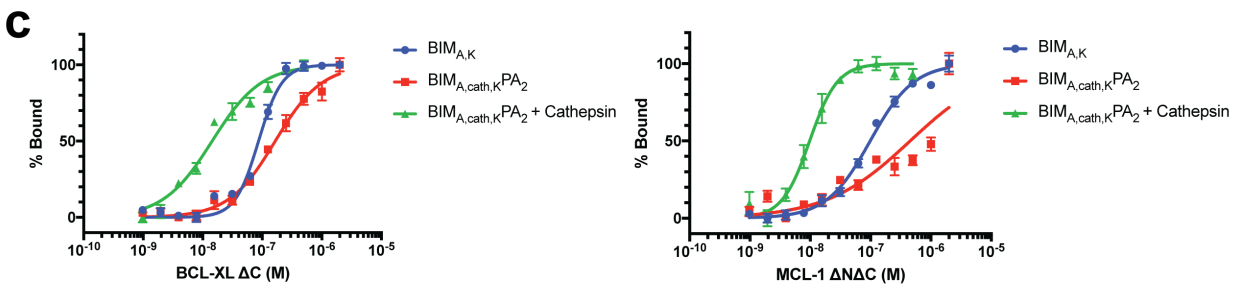

	BCL-XL ΔC	MCL-1 ΔNΔC
Bim$_{A,K}$	87 ± 4 nM	99 ± 5 nM
Bim$_{A,cath,K}$PA$_2$	165 ± 12 nM	453 ± 89 nM
Bim$_{A,cath,K}$PA$_2$ + Cathepsin	14 ± 1 nM	10 ± 1 nM

Figure 2.4: Removal of the C-terminal lipid tail and lysines of BIM$_{A,cath,K}$PA$_2$ enhances binding to antiapoptotic BCL-2 family targets. (Continued on the following page.)

Figure 2.4, continued: Removal of the C-terminal lipid tail and lysines of $BIM_{A,cath,K}PA_2$ enhances binding to antiapoptotic BCL-2 family targets. (a) FITC-labeled peptide and PAs were incubated with serial dilutions of recombinant BCL-2, BCL-XL, BCL-W, and MCL-1, and affinity profiles were measured by fluorescence polarization (FP). Kd values are listed as the mean of replicates ± S.E.M. (b) $BIM_{A,cath,K}PA_2$ pre-incubated with recombinant cathepsin B improved binding to recombinant BCL-XL in a time-dependent manner. (c) $BIM_{A,cath,K}PA_2$ pre-incubated with cathepsin B followed by enzyme-inactivation resulted in increased BIM_A peptide affinities to recombinant BCL-XL ΔC and MCL-1 ΔN ΔC. Plotted data and Kd values are the mean of replicates ± S.E.M.

cathepsin inhibitor CA-074Me. The cathepsin inhibitory effect of CA-074Me was first tested in vitro using recombinant cathepsin B added to a cathepsin-substrate linker that becomes fluorescent upon cathepsin cleavage (Figure 2.11). Cathepsin B caused a time-dependent increase in fluorescence while the addition of CA-074Me blocked reporter substrate cleavage.

To determine the importance of cathepsin cleavage on intracellular localization and trafficking of the BIM_A peptide, WT mouse embryonic fibroblasts (MEFs) were pre-treated with CA-074Me or a DMSO control for 1 h followed by incubation with 10 μM $BIM_{A,cath,K}PA_2$. In contrast to the more rapid intracellular localization of FITC-$BIM_{A,cath,K}PA_2$ in control-treated WT MEFs, those pre-treated with CA-074Me showed FITC-$BIM_{A,cath,K}PA_2$ localized primarily near the cell surface after 1 h (Figure 2.12). However, 2 h following treatment with $BIM_{A,cath,K}PA_2$, FITC-BIM_A was located more diffusely throughout the cells (Figure 2.5), as was previously measured in identically treated HeLa cells (Figure 2.2). Interestingly, the nuclei of these cells appeared fragmented, and bright field imaging revealed anoikic, rounded cells with membrane blebbing, classical hallmarks of apoptosis (Figure 2.5). Meanwhile, WT MEFs pre-incubated with CA-074Me showed diminished FITC-BIM_A association that was confined to puncta near the edges of the cell membrane and lacked signs of apoptosis (Figure 2.5). These data suggest that the earlier diffuse intracellular accumulation of the FITC-BIM_A peptide after delivery by the cleavable DSPE-PEG tail depended to some degree on cathepsin cleavage of the linker.

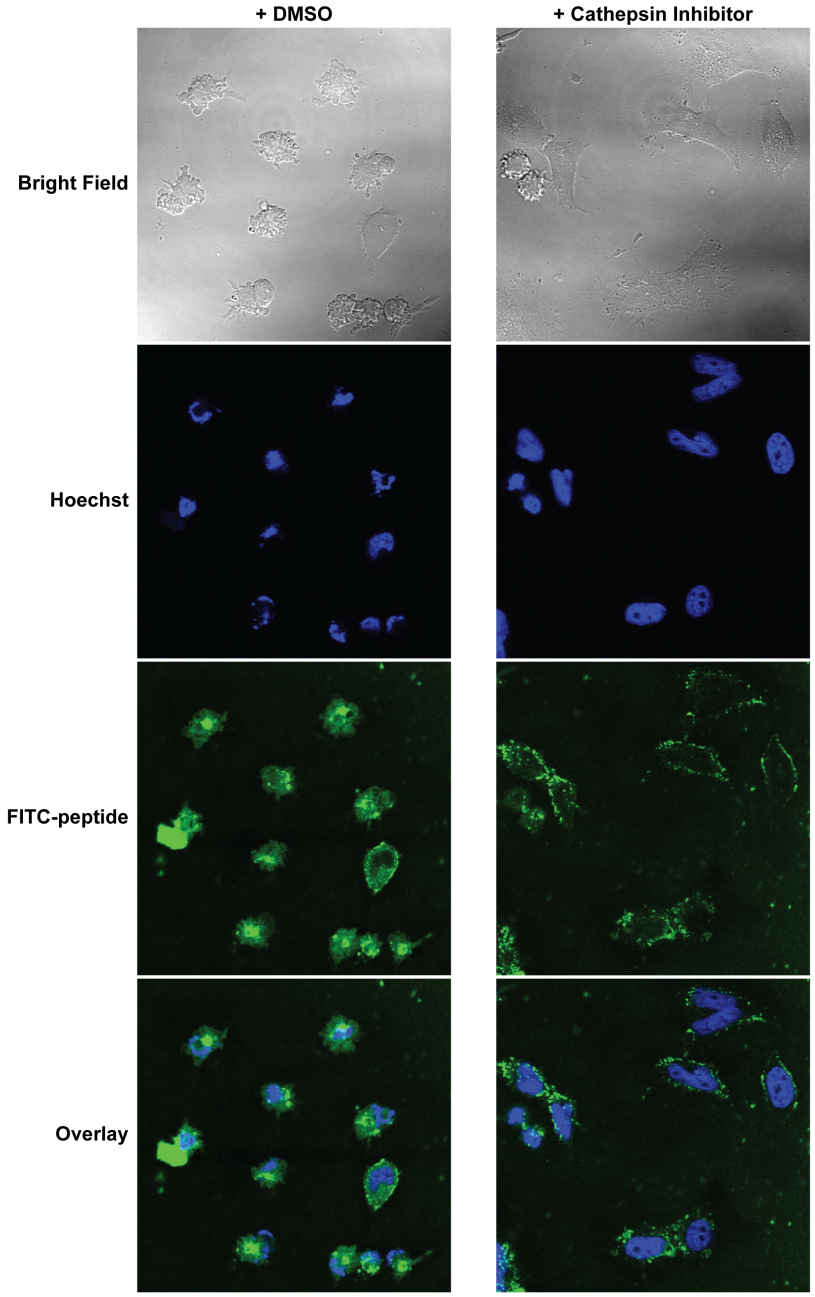

Figure 2.5: Cathepsin inhibition inhibits cellular uptake and therapeutic function of $BIM_{A,cath,K}PA_2$. Mouse embryonic fibroblasts (MEFs) were pre-incubated with either 5 μM CA-074Me or 0.1% (v/v) DMSO control in complete media for 1 h. The cells were then washed and treated with 10 μM FITC-$BIM_{A,cath,K}PA_2$ for 2 h before washing, fixation, staining with Hoechst, and confocal imaging. In the DMSO control, the FITC-BIM_A signal was located diffusely throughout the MEFs. Their nuclei appeared fragmented, and their cellular membranes appeared blebbed, consistent with secondary signs of apoptosis. MEFs pre-treated with CA-074Me showed FITC-BIM_A localized to the cell membrane and appeared otherwise morphologically normal.

2.3.6 Apoptotic Cell Death Induction

Given there were early signs suggestive of apoptosis in MEFs treated with $BIM_{A,cath,K}PA_2$, we next determined if treatment with $BIM_{A,cath,K}PA_2$ induced dose- and time-dependent cell death in these same cells. $BIM_{A,cath,K}PA_2$ induced progressive dose- and time-dependent cell death and corresponding caspase-3/7 activation in WT MEFs (Figure 2.6a). The non-cleavable $BIM_{A,K}PA_2$ induced a lesser degree of cell death by 72 h with corresponding caspase activation (Figure 2.6b). The $BIM_{A,K}$ peptide alone, however, which was unable to enter cells (Figure 2.2a), did not induce measurable cell death or caspase-3/7 activation (Figure 2.6c). An inert BIM BH3 peptide (BIM_B-MRPEIWIAQELRRIGDFNAKKKKK) was used as a peptide control in these studies. Importantly, $BIM_{A,cath,K}PA_2$ was unable to induce caspase-3/7 activation in MEFs lacking the pro-apoptotic effector proteins BAK and BAX (BAX-/-BAK-/- MEFs), indicating specific activation of the intrinsic pathway of apoptosis rather than non-specific mitochondrial outer membrane disruption by either the BIM_A peptide or the DSPE-PEG tail (Figure 2.6d). $BIM_{A,cath,K}PA_2$ and, to a lesser extent, $BIM_{A,K}PA_2$ also induced corresponding PARP cleavage in WT MEFs, another hallmark of apoptotic cell death (Figure 2.6e).

2.4 Discussion

Intracellular PPIs remain a great challenge to therapeutically target and are often therefore described as "undruggable" [245]. There is a new resurgence in research exploring how to effectively drug these challenging interfaces through orthosteric inhibition. PPIs are particularly challenging to drug using small molecules as the contact interfaces between proteins are usually distributed along geographically large surface areas and consist of a complex topographical interplay of polar and hydrophobic interactions. However, there has been some success in this area using relatively large small molecules such as the first in class BCL-2 inhibitor venetoclax, which recently gained FDA approval for use in patients with a number of

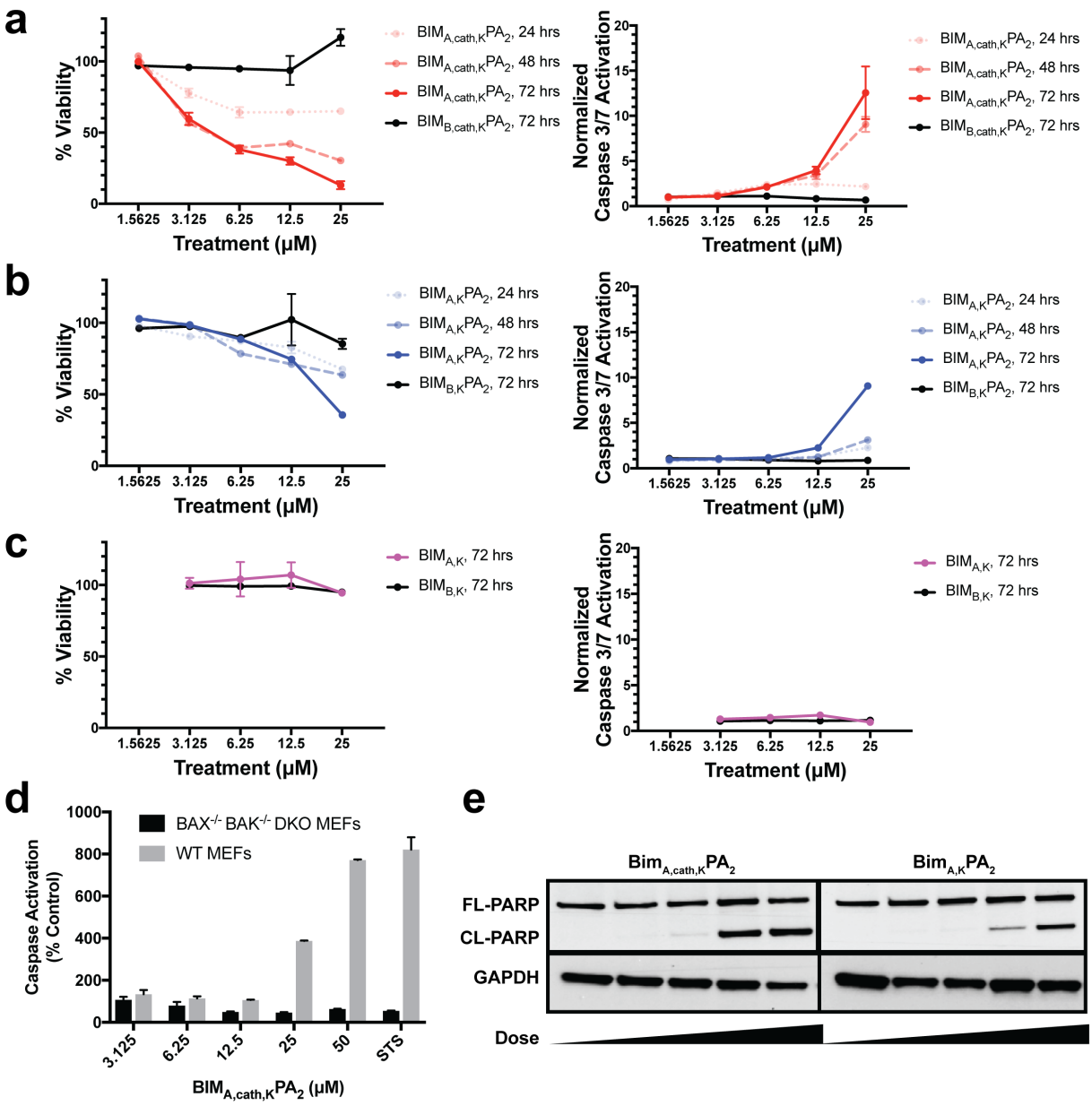

Figure 2.6: BIM$_A$ PAs induce dose- and time-dependent apoptotic cell death. (Continued on the following page.)

Figure 2.6, continued: BIM_A PAs induce dose- and time-dependent apoptotic cell death. WT MEFs were treated with (a) $BIM_{A,cath,K}PA_2$, (b) $BIM_{A,K}PA_2$, or (c) $BIM_{A,K}$ for 24, 48 and 72 h with serial dilutions of peptide or PA followed by measurement of cell viability (left column) and caspase-3/7 activation (right column). The corresponding, inactive BIM_B peptides were used as negative controls. The cathepsin-cleavable $BIM_{A,cath,K}PA_2$ induced potent cell death and corresponding caspase-3/7 activation within 24 h. The non-cleavable $BIM_{A,K}PA_2$ induced a lesser degree of cell death with corresponding caspase-3/7 activation by 72 h. The $BIM_{A,K}$ peptide alone induced no measurable cell death or caspase-3/7 activation. (d) $BIM_{A,cath,K}PA_2$ induction of caspase-3/7 activation was absent in BAX-/-BAK-/-MEFs indicating on-target specificity of the BIM_A peptide. Staurosporine (STS; 1 μM) was used as a positive control for caspase activation. (e) BIM_A PAs induced dose-dependent PARP cleavage, another hallmark of apoptosis, as measured by Western blot analysis. FL = full length, CL = cleaved.

hematological malignancies [4]. Peptides, on the other hand, have long been used as research tools to mimic fragments of proteins and disrupt PPIs. However, an enormous obstacle to their therapeutic relevance is their lack of intracellular accessibility. One strategy that has been quite successful at facilitating peptides' cell uptake is hydrocarbon-stapling of naturally α-helical peptides, and multiple clinical trials are now underway using a stapled peptide that therapeutically reactivates WT p53 in cancerous cells [89–91]. Nanomaterials, such as PAs, are also being widely explored for building delivery vehicles to carry unmodified therapeutic peptides into cells while at the same time protecting them from extracellular degradation [110].

PAs have been used to build supramolecular nanomaterials for numerous biomedical applications including therapeutics, diagnostics, regenerative medicine, and vaccines [122]. Most of these applications involve cell-material interactions occurring at the cellular surface. However, our group and others have also found that unimer PAs can use their lipid tails to directly interact with the cell membrane and trigger cell uptake [125–127, 236]. We have since studied the mechanisms by which a number of lipid tails facilitate such cellular penetration [127]. We have also determined that following lipid-mediated trafficking into endosomes, removal of the tail prevents lipid-mediated ejection and recycling of the peptide-laden PA back out of the cell and facilitates intracellular accumulation of the therapeutic peptide

[141]. The current study expands upon these works by using cleavable PAs to deliver the bioactive BIM BH3 death domain into cells to induce apoptosis. The BIM BH3 domain is well known to potently induce apoptosis by manipulating the BCL-2 family of proteins' PPIs through induced-fit binding of both pro- and anti-apoptotic proteins, but only when the cell membrane is chemically permeabilized [69, 246]. Additionally, although stapled peptides are able to enter the cells, their potency can be greatly enhanced through outer cell membrane permeabilization [102].

Two similar PAs were tested, one with a PEG spacer ($BIM_{A,K}PA_2$) and one without ($BIM_{A,K}PA_1$), both with dialkyl lipid tails, for their ability to carry a BIM BH3 peptide into cells without non-specific disruption of the cell membrane. Although the diC16 PA ($BIM_{A,K}PA_1$) lacking the PEG spacer readily delivered the BIM_A peptide into cells, it also caused non-specific membrane disruption, a problematic, often not tested, off-target cytotoxic effect. Inclusion of a hydrophilic PEG spacer with a DSPE-PEG tail ($BIM_{A,K}PA_2$), meanwhile, eliminated membrane disruption. However, this addition led to inefficient intracellular localization of the peptide as cargo was seen primarily on or near the cell membrane surface. It is unclear if this was from tempered membrane crossing or from rapid endosomal recycling as our group has measured in other PA systems [127, 141]. However, the incorporation of the endosomally-cleavable valine-citrulline cathepsin-substrate linker into the DSPE-PEG PA ($BIM_{A,cath,K}PA_2$) amplified the peptide's intracellular accumulation, while still avoiding non-specific membrane disruption. It is likely the cathepsin linker allows for quick release of the BIM_A peptide and that the peptide was able to escape, to some extent, late endosomal/lysosomal trafficking and enter the cytoplasm. We have previously measured similar discrepancies in therapeutic peptide intracellular accumulation using a similar cleavage system between a peptide cargo and lipid tail carrier, indicating that the increased intracellular localization measured here is not a unique feature of the BIM_A peptide [122].

Removal of the lipid tail following cellular uptake proved to be important not only for intracellular trafficking and accumulation, but also for the peptide's ability to bind its target

protein(s) and exert its therapeutic effect. As may be expected, addition of the DSPE-PEG tail inhibited the ability of the BIM BH3 peptide to bind to all antiapoptotic proteins tested (BCL-2, BCL-W, BCL-XL, and MCL-1). While $BIM_{A,K}PA_2$ and $BIM_{A,cath,K}PA_2$ were able to bind their target proteins, they did so with 2–3 fold lower affinity compared to the parent $BIM_{A,K}$ peptide alone. It is important to note that the concentration of PAs used in the binding assays (50 nM) was well below their critical micellar concentrations (¿1 μM). Thereby, the differences in binding affinity were likely not due to supramolecular self-assembly, but rather due to steric hinderance within each unimer imparted by the DSPE-PEG tail. Cleavage of this tail, and the C-terminal lysines, greatly improved binding affinities of the BIM_A peptide to its target proteins, which translated to increased efficacy.

Finally, we measured the PAs' abilities to induce apoptosis after intracellular delivery. Both $BIM_{A,K}PA_2$ and $BIM_{A,cath,K}PA_2$ were able to enter cells and bind their target proteins, though the cathepsin-cleavable PA performed better at both cell uptake and target protein binding. It is possible that $BIM_{A,K}PA_2$ primarily resided in early/late endosomes near the cell surface and then rapidly recycled back to the cell membrane. While this may have also occurred to some extent with $BIM_{A,cath,K}PA_2$, some PA unimers may have been able to be cleaved upon transitioning to late endosomes upon acidification of these compartments and activation of cathepsin B. This transition and cleavage was largely blocked by cathepsin inhibition. As anticipated, the PAs' abilities to induce apoptosis correlated with these prerequisites. Both PAs were able to induce apoptosis, however, the cathepsin-cleavable PA did so with faster kinetics and at lower doses. Given that the peptides were not structurally reinforced (e.g., hydrocarbon stapled), it is unclear how much of the delivered peptide was able to escape the endosomal/lysosomal network. Studies evaluating the efficiency of intact delivery of native peptides into the cytoplasm of cells are currently underway and beyond the scope of the present study.

$BIM_{A,cath,K}PA_2$ was designed to release the peptide from the tail in the endosome, but this study did not intentionally include any mechanisms to facilitate endosomal escape. By

an unknown mechanism, the released peptide was able to escape the endosome, reach the mitochondria, and activate apoptosis. In addition to cellular uptake, endosomal escape of nanoparticles and biofunctional warheads is another monumental obstacle to intracellular delivery of biologic therapeutics [118]. More work is needed to understand how otherwise cell-impermeable peptides are able to escape the endosome following internalization. The overall secondary structure and charge of the peptide is likely to be critical to organelle escape once internalized into the cell [76, 247].

This study expands on our explorations of how PA nanoparticles interact with cells and facilitate a therapeutic peptide's intracellular uptake and dissemination. While a lipid tail can improve a peptide's cellular uptake, our work supports the importance of removing the tail after uptake, not only to prevent recycling back out of the cell, but to prevent the tail from inhibiting the peptide's binding to its target and thereby dampening its therapeutic efficacy. Endosomal entrapment and lack of cytoplasmic access, as well as stability in circulation (i.e., binding to serum proteins) remain formidable and poorly understood obstacles in the clinical translation of lipid-based carrier nanoparticles [110, 122]. This study demonstrates, as proof-of-concept, that cathepsin-cleavable PAs can be used to deliver therapeutic peptides into cells to exert a biomedical effect. More research is warranted to understand the mechanisms behind membrane trafficking and endosomal escape in order to fully unlock the therapeutic potential of such peptide-based protein mimetics.

2.5 Materials and Methods

2.5.1 Micelle Synthesis

Two overlapping but functionally non-equivalent sequences of the BCL-2 binding motif of the BIM protein (BIM_A: IWIAQELRRIGDEFNAYYARR [103], and BIM_B: MRPEIWIAQELRRIGDEFNA [69, 246]) were synthesized on 0.25 mmoles of rink amide resin (Novabiochem) through standard Fmoc-mediated solid phase peptide synthesis methods using an automated

PS3 Benchtop Peptide Synthesizer (Protein Technologies, Tucson, AZ, USA). Amino acids were used in 4X excess. Each coupling began with Fmoc-deprotection of the resin using 20% piperidine in dimethylformamide (DMF), followed by amino acid activation with N,N,N',N'-Tetramethyl-O-(1H-benzotriazol-1-yl)uronium hexafluorophosphate (HBTU) and 0.4 M N-methylmorpholine in DMF before adding the activated amino acid to the resin. Five lysines were added at the C-termini of both sequences to make them more charged and water-soluble. After splitting each batch of the peptides in half, one half was acetylated with acetic anhydride in DMF, while the other half was labeled with fluorescein isothiocyanate (FITC; Molecular Probes) at their N-termini. The acetylated and FITC-labeled peptides were again each divided in half. One half was conjugated at the ε-amine of C-terminal lysine to dipalmitoylglutamic acid, or diC16, as described previously [120, 141] to form Ac-BIM-PA1 or FITC-BIM-PA1. The other half was coupled with 1,2-distearoyl-sn-glycero-3-phosphoethanolamine-N-[succinyl(polyethylene glycol)-2000], or DSPE-PEG(2000)-succinyl (Avanti Polar Lipids, Alabaster, AL, USA), using equal molar equivalent of peptide to lipid in a 1:1 mixture of DMF:DCM and named Ac-BIM-PA2 or FITC-BIM-PA2. The same peptides were re-synthesized with a cathepsin cleavage sequence—Valine, Citrulline (VCit)—incorporated between the BIM sequences and the five C-terminal lysines, and the modified PAs were named Ac-BIMcath,KPA2 or FITC-BIMcath,KPA2. Peptide amphiphiles were then cleaved with 82.5:5:5:2.5 by volume trifluoroacetic acid: H2O: phenol: thioanisole: 1,2-ethanedithiol. They were precipitated and washed with cold diethyl ether, dried under nitrogen, and dissolved in water. Reverse-phase HPLC (Prominence, Shimadzu, Columbia, MD, USA) on a C8 column (Waters, Milford, MA, USA) at 40 °C was employed to purify soluble peptides using a gradient method and acetonitrile/water solvents containing 0.1% formic acid. The fractions were mass-characterized by MALDI-TOF mass spectral analysis (Biflex III, Bruker, Billerica, MA, USA) and the confirmed fractions were aliquoted, lyophilized, and stored as powders at -20 °C (Figures 2.7,2.8). The exact concentrations of the aliquots were determined by amino acid analysis (AAA). To fabricate BIM micelles, the

lyophilized powders were reconstituted, sonicated for 1 h at room temperature, incubated in 70 °C water bath for 1 h, and left at room temperature for at least 2 h to cool down and equilibrate.

2.5.2 Critical Micelle Concentration (CMC)

To measure the CMC of PA micelles, 1,6-diphenyl-1,3,5-hexatriene (DPH) was first dissolved in tetrahydrofuran and then diluted in water to 1 μM final concentration. A range of PA solutions (from 512 μM to 0.01 μM in serial one-half dilutions) were prepared in a 1 μM DPH solution and left to equilibrate for 1 h at room temperature. These solutions were plated in triplicates in a 96-well plate, and their fluorescence intensity was measured using a Tecan Infinite 200 plate reader (Mannedorf, Switzerland). DPH was excited at 350 nm, and fluorescence emission was measured at 428 nm. The concentration values were log transformed, and the data were fit with a trend line for the increasing intensity measurements. The CMC relies on the partitioning of DPH from the aqueous solution into the hydrophobic core of intact PA micelles, resulting in a sharp increase in fluorescence intensity. The CMC was calculated as the inflection point where the fluorescence intensity began to increase.

2.5.3 Dynamic Light Scattering (DLS)

Stock solutions of 0.5 mM BIM PAs were prepared as mentioned above, and DLS measurements were performed at a 90° angle with a 637 nm laser using a Brookhaven Instruments (Holtzville, NY, USA) system with a BI-9000AT autocorrelator. Hydrodynamic radii were determined via the Stokes-Einstein equation using the diffusion coefficient determined from the auto correlation function.

2.5.4 Transmission Electron Microscopy (TEM)

Ultrathin carbon type-A 400 mesh copper grids (Ted Pella, Redding, CA, USA) were loaded with 1 μL of BIM PAs and allowed to dry. The grids were washed with several drops of water and then negatively stained with 1% aqueous phosphotungstic acid for 1 min. The excess solution was then removed and grids were left to dry. All the grids were imaged on a FEI Tecnai 12 TEM (Hillsboro, OR, USA) using an accelerating voltage of 120 kV.

2.5.5 Circular Dichroism

A quartz cuvette with a 0.1 cm pathlength was loaded with 200 μL of 50 μM solutions of BIM PAs. Measurements were done at 25, 37, 42 and 50 °C with a Jasco J-815 Circular Dichroism Spectropolarimeter (Easton, MD, USA). Each sample was scanned five times from 250 to 190 nm, and the data were averaged. Mean residue ellipticity $[\theta]$ was calculated using equation 2.1:

$$[\theta] = \text{millidegree/molar concentration/amino acid residues} \tag{2.1}$$

with units degree x cm^2 x dmol^{-1} x residue^{-1}. Percent α-helicity was then calculated from the value of $[\theta]$ at 222 nm using equations 2.2 and 2.3:

$$\%\ \text{Helicity} = 100 \times \frac{[\theta]_{222}}{[\theta]_{222}^{\max}} \tag{2.2}$$

$$[\theta]_{222}^{\max} = -40,000 \times [1 - \frac{2.5}{\text{amino acid residues}}] + 100 \times T \tag{2.3}$$

with T measured in °C [81, 248].

2.5.6 Lactate Dehydrogenase Release Assay

Mouse embryonic fibroblasts (MEFs) were cultured in a 96-well plate (5000 cells per well) and allowed to adhere overnight. A serial dilution of the BIM PAs (25, 12.5, 6.25, 3.125, and 1.563 μM) as well as 1% triton were prepared in treatment media (Advanced DMEM, 1% FBS, 0.1% penicillin/streptomycin), and the cells' media was replaced with the treatment dilutions to a final volume of 100 μL in each well. After incubation at 37 °C for 1 h, 50 μL of the treatment media was removed carefully from each well, transferred to a new plate, and mixed with 50 μL of lactate dehydrogenase (LDH) reagent (Roche) for 30 min while shaking, and absorbance was then measured at 492 nm on a microplate reader (SpectraMax M5 Microplate Reader, Molecular Devices, San Jose, CA, USA).

2.5.7 Protein Production

Recombinant and tagless BCL-XLΔC, MCL-1ΔNΔC, BCL-2ΔC and BCL-WΔC were produced and purified as described previously [103]. Briefly, glutathione-S-transferase fusion proteins were expressed in Escherichia coli BL21 (DE3) using pGEX2T (Pharmacia Biotech) constructs. Bacterial cells were cultured in ampicillin-containing Luria Broth, and protein expression was induced with 0.5 mM isopropyl β-D-1-thiogalactopyranoside. The bacterial pellet was resuspended in PBS containing 1 mg/mL lysozyme, SigmaFAST protease inhibitor tablet (Sigma-Aldrich, St. Louis, MO, USA), and 1% (v/v) Triton X-100. Bacteria were lysed by sonication at 4 °C, and, after centrifugation at 16,000 g for 30 min, the supernatant was applied to a glutathione-agarose (Sigma-Aldrich, St. Louis, MO, USA) column and washed with PBS. Tagless protein was obtained by overnight on-bead digestion with 50 units of thrombin (GE Healthcare, Pittsburgh, PA, USA) in 3 mL PBS at room temperature. The cleaved proteins were purified by size exclusion chromatography using 150 mM NaCl and 50 mM Tris (pH 7.4) buffer conditions on a Superdex-75 gel filtration column (GE Healthcare, Pittsburgh, PA, USA).

2.5.8 Fluorescence Polarization (FP) Binding Assay

FP binding assays were performed as previously described [103, 249]. FITC-labeled peptides and peptide amphiphiles (50 nM) were incubated with serial dilutions of recombinant protein in FP binding buffer (50 mM Tris, 100 mM NaCl, pH 8.0) until equilibrium was reached. FP was measured using a SpectraMax M5 microplate reader (Molecular Devices, San Jose, CA, USA). To calculate Kd values, the data were fitted to normalized sigmoidal curves with a variable slope using nonlinear regression analysis in Graphpad Prism.

2.5.9 Cathepsin B Cleavage FP and Fluorogenic Assays

Cathepsin B purified from human liver (Sigma-Aldrich, St. Louis, MO, USA) was diluted 1:40 in cathepsin B activation buffer (25 mM HEPES, 25 mM DTT, pH 5.0) and incubated at room temperature for 15 min to activate the enzyme. FITC- $BIM_{A,cath,K}PA_2$ was added to activated enzyme to achieve a final peptide amphiphile concentration of 50 μM and incubated at room temperature for 30 min. The reaction was stopped by diluting the reaction mixture 1:100 in FP binding buffer (50 mM Tris, 100 mM NaCl, pH 8.0). The enzyme-treated peptide amphiphile (50 nM) was then incubated with serial dilutions of recombinant protein in FP binding buffer until equilibrium was reached. FP was measured using a SpectraMax M5 microplate reader (Molecular Devices, San Jose, CA, USA), and Kd values were calculated as described above. The fluorogenic cathepsin-cleavage assay was done as previously described [141] using the cathepsin B cleavage substrate Z-Arg-Arg-7-amido-4-methylcoumarin hydrochloride (Z-RR-AMC; Sigma-Aldrich, St. Louis, MO, USA) and human cathepsin B with or without the cathepsin inhibitor CA-074Me (EMD Millipore, Burlington, MA, USA).

2.5.10 Cell Culture

Mouse embryonic fibroblasts (MEFs) and HeLa cells were maintained in DMEM (Invitrogen, Carlsbad, CA, USA) supplemented with 10% FBS, 100 U/mL penicillin/streptomycin, 2 mM L-glutamine, and 0.1 mM MEM nonessential amino acids.

2.5.11 Live Cell Confocal Microscopy

HeLa cells were incubated with 10 μM FITC-labeled peptides or PAs for the indicated time in Advanced DMEM (Invitrogen, Carlsbad, CA, USA) supplemented with 1% FBS. The media was then removed, and the cells were washed and then incubated in prewarmed Opti-MEM (Invitrogen, Carlsbad, CA, USA) containing 250 nM MitoTracker Red (Invitrogen, Carlsbad, CA, USA) and 5 μg/mL Hoechst 33342 (Invitrogen, Carlsbad, CA, USA) for 30 min. The cells were then washed and incubated in Opti-MEM media lacking phenol red (Invitrogen, Carlsbad, CA, USA). Confocal images were collected on an Olympus DSU spinning disk confocal system (Olympus, Carlsbad, CA, USA) with a heated platform and a humidified chamber with 5% CO2. Excitation of the 3 fluorophores was performed sequentially using 405-nm, 488-nm, and 561-nm lasers. Images were acquired using a 100 Plan Apo objective lens with a Hamamatsu EM-CCD camera (Andor Technology, Belfast, UK). Acquisition parameters, shutters, filter positions, and focus were controlled by Slidebook 6 software (Intelligent Imaging Innovations, Denver, CO, USA).

2.5.12 Cell Viability Assay

MEF cells were aliquoted (2.5 x 103, 100 μL) in 96-well opaque plates in complete DMEM media, and, 24 h later (at 75%–90% cellular confluence), the media was removed. The indicated doses of peptides or PAs were then added in Advanced DMEM (Invitrogen, Carlsbad, CA, USA) supplemented with 1% FBS, and after 6 h of treatment, 10% FBS was added back to the media. Cell viability was measured at the indicated time points by the addition

of CellTiter-Glo chemiluminescence reagent in accordance with the manufacture's protocol (Promega, Madison, WI, USA). Luminescence was detected by a Synergy 2 microplate reader (BioTek Instruments, Inc., Winooski, VT, USA).

2.5.13 Caspase-3/7 Activation Assay

Cells were treated as described above for the cell viability assays, and caspase-3/7 activation was measured at indicated time points by addition of the Caspase-Glo 3/7 chemiluminescence reagent in accordance with the manufacturer's protocol (Promega, Madison, WI, USA). Luminescence was detected by a Synergy 2 microplate reader (BioTek Instruments, Inc., Winooski, VT, USA). Caspase-3/7 activation per living cells was determined by the ratio of Caspase-Glo luminescence to the percent viability from the corresponding CellTiter-Glo assay from identical experiments plated simultaneously, as previously described [250].

2.5.14 Western Blotting

Treated MEFs were collected and lysed in lysis buffer (50 mM Tris, 150 mM NaCl, 1 mM EDTA, 1 mM DTT, 1% (v/v) Triton X-100, complete protease inhibitor tablet (Roche), pH 7.4; PBST), and the protein content of each lysate was quantified using BCA kit (Thermo-Fischer Scientific, Waltham, MA, USA). Further, 5 μg of total protein from each lysate was loaded and separated on a 12% SDS-PAGE gel, transferred onto a PVDF membrane, and blocked with 5% skim milk in PBST for 45 min. The membranes were probed with primary antibody overnight at 4 °C with antibodies against PARP (Cell Signaling, Danvers, MA, USA; 1:1000) and GAPDH (Santa Cruz, Dallas, TX, USA; 1:1000), followed by 1 h of incubation at room temperature with HRP-conjugated secondary antibody (Santa Cruz, Dallas, TX, USA; 1:8000). Immuno-reactivity was visualized with a chemiluminescent detection kit (Amersham, Little Chalfont, UK).

2.5.15 Confocal Imaging after Cathepsin Inhibition

MEFs were cultured on coverslips inside 6-well plates overnight. They were then pre-treated with either 5 μM CA-074Me (cathepsin inhibitor) or 0.1% DMSO in complete DMEM for 1 h. The media was replaced with Advanced DMEM (Invitrogen, Carlsbad, CA, USA) supplemented with 1% FBS and 10 μM FITC-labeled PAs, and the cells were incubated for 2 h. Hoechst (5 μg/mL) was added to the media 30 min before the end of the PA incubation. The treatment media was then removed, and the cells were washed and fixed immediately with 4% paraformaldehyde in PBS for 10 min at room temperature. The fixed cells were then washed, and the coverslips were mounted on glass slides before imaging. Confocal images were collected on Leica TCS SP2 AOBS Laser Scanning Confocal microscope. The acquisition parameters, shutters, filter positions, and focus were controlled by LCS Leica confocal software LASAF 2.7.3.9723 (Leica, Wetzlar, Germany).

2.6 Author Contributions

Conceptualization and methodology, J.L.L., M.V.T. and J.A.B.; investigation and formal analysis, J.A.B., R.S. and H.A.; writing—original draft preparation, M.R.S. and J.L.L.; writing—review and editing, M.R.S., M.V.T. and J.L.L.; supervision and funding acquisition, J.L.L., M.V.T.

2.7 Funding

M.S. was supported by the National Institutes of Health (NIH) as an F30 fellow (F30CA221250) and by the University of Chicago MSTP training grant (T32GM007281). This work was also supported by a Hoogland Lymphoma Research Award (J.L.).

2.8 Acknowledgments

We would like to acknowledge the University of Chicago's Advanced Electron Microscopy Core Facility where the TEM images were acquired. Confocal microscopy images were acquired at the Universtiy of Chicago's Integrated Light Microscopy Core Facility, funded by the Cancer Center Support Grant P30CA014599. We would also like to thank the University of Chicago's Mass Spectrometry Core Facility, where the MALDI-TOF spectra were acquired, with support from the National Science Foundation (NSF) instrumentation grant CHE-1048528.

2.9 Conflicts of Interest

The authors declare no conflict of interest.

2.10 Supplementary Materials

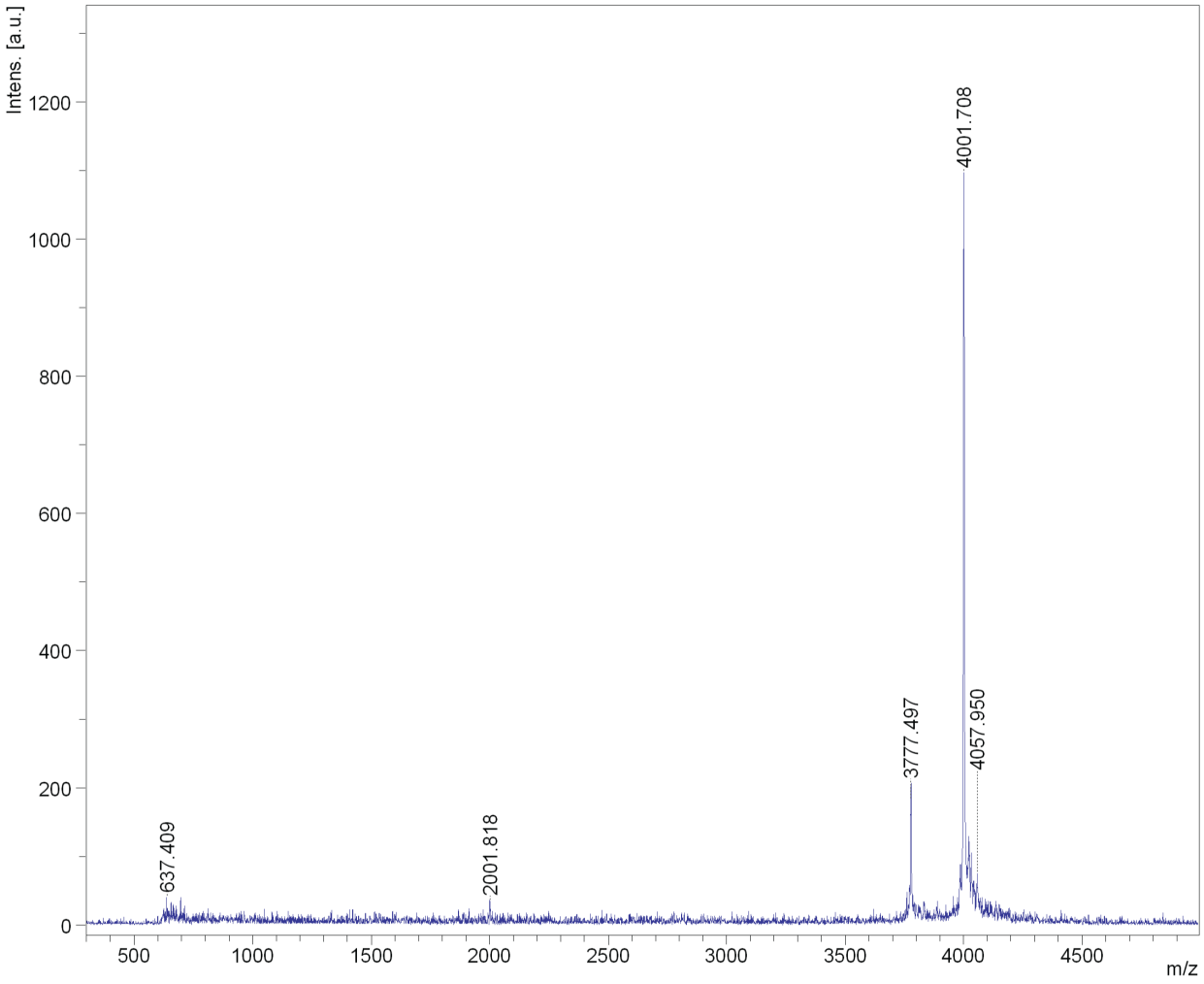

Figure 2.7: MALDI-TOF spectrum of $BIM_{A,K}PA_1$. Expected molecular weight is 4001 Da.

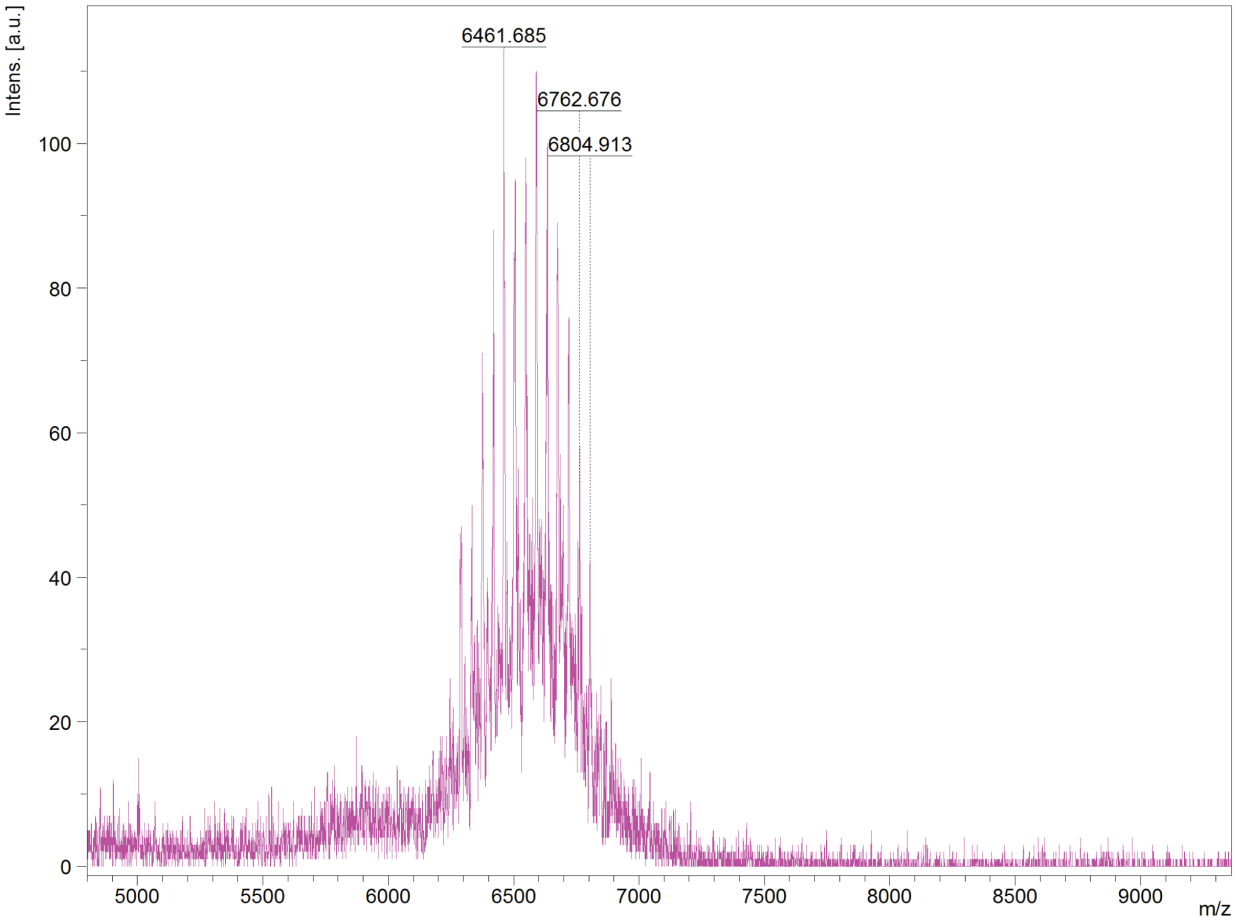

Figure 2.8: MALDI-TOF spectrum of $BIM_{A,cath,K}PA_2$. The expected average molecular weight is ∼6452 Da, with polydispersity due to the PEG spacer in the tail.

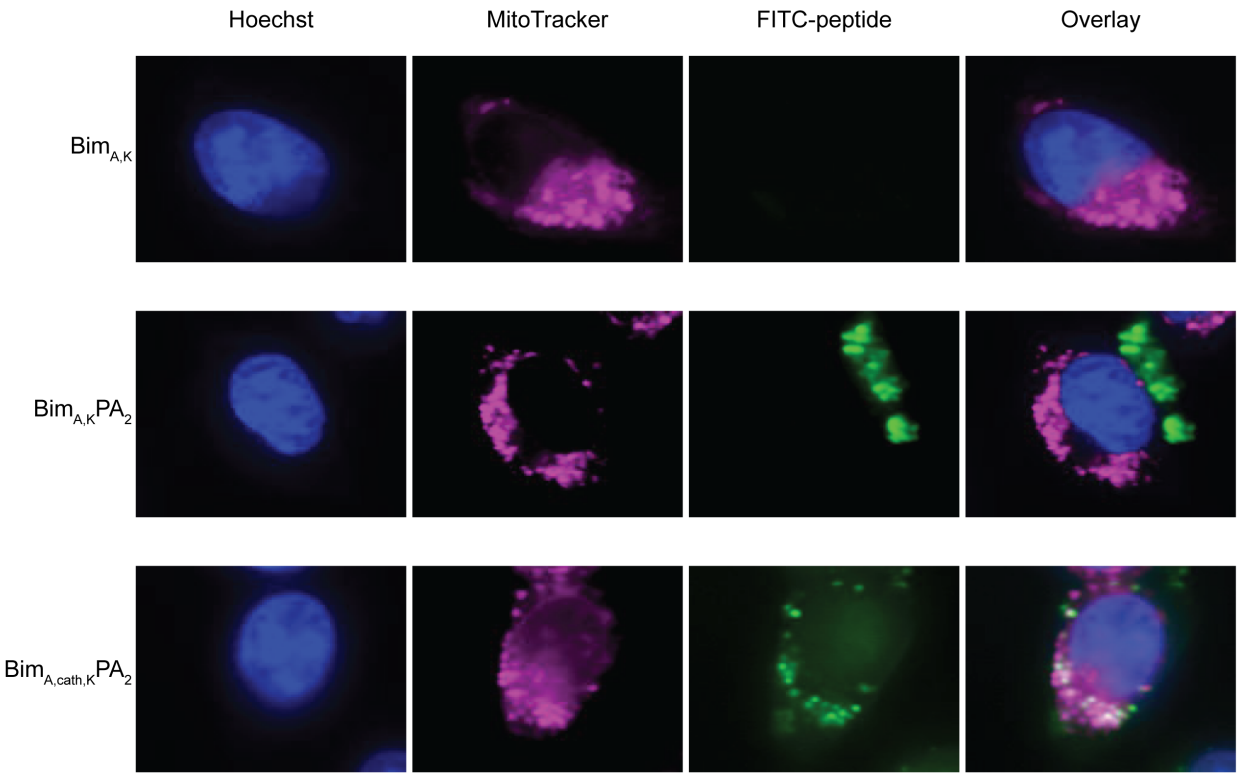

Figure 2.9: Live cell confocal microscopy of HeLa cells treated with FITC-labeled $BIM_{A,K}$ peptide, $BIM_{A,K}PA_2$, or $BIM_{A,cath,K}PA_2$ for 2 h followed by washing. Only $BIM_{A,cath,K}PA_2$ enabled FITC-peptide co-localization with MitoTracker-labeled mitochondria. Original magnification, $\times 100$.

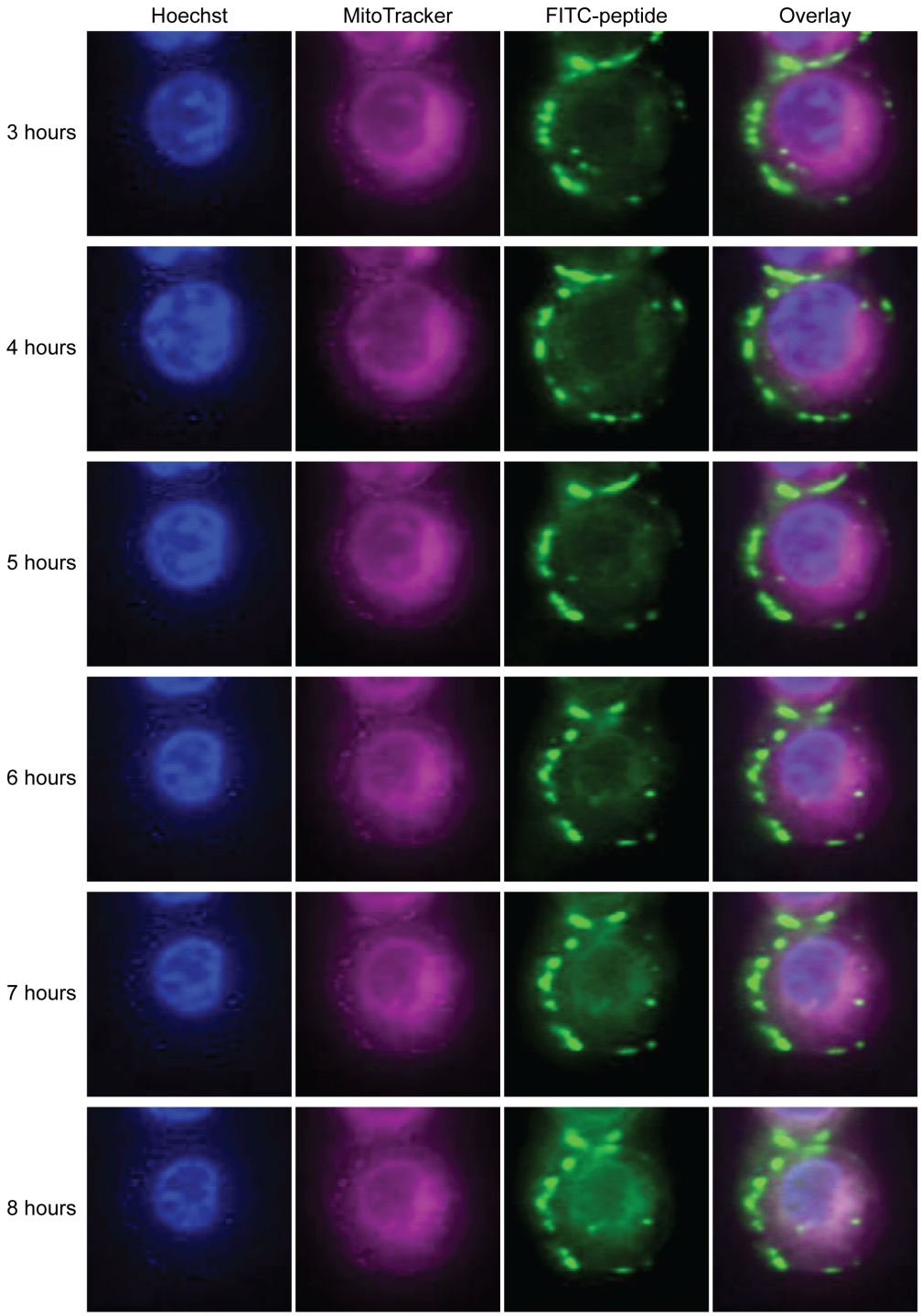

Figure 2.10: Time-lapse, live cell confocal microscopy of HeLa cells treated with FITC-labeled $BIM_{A,cath,K}PA_2$. Cells were treated with 10 μM FITC-$BIM_{A,cath,K}PA_2$ for 2 h before being washed, stained, and imaged. FITC signal was first visible near the edges of the cell, and over 8 h, became diffusely fluorescent and co-localized with MitoTracker-labeled mitochondria. Original magnification, $\times$100.

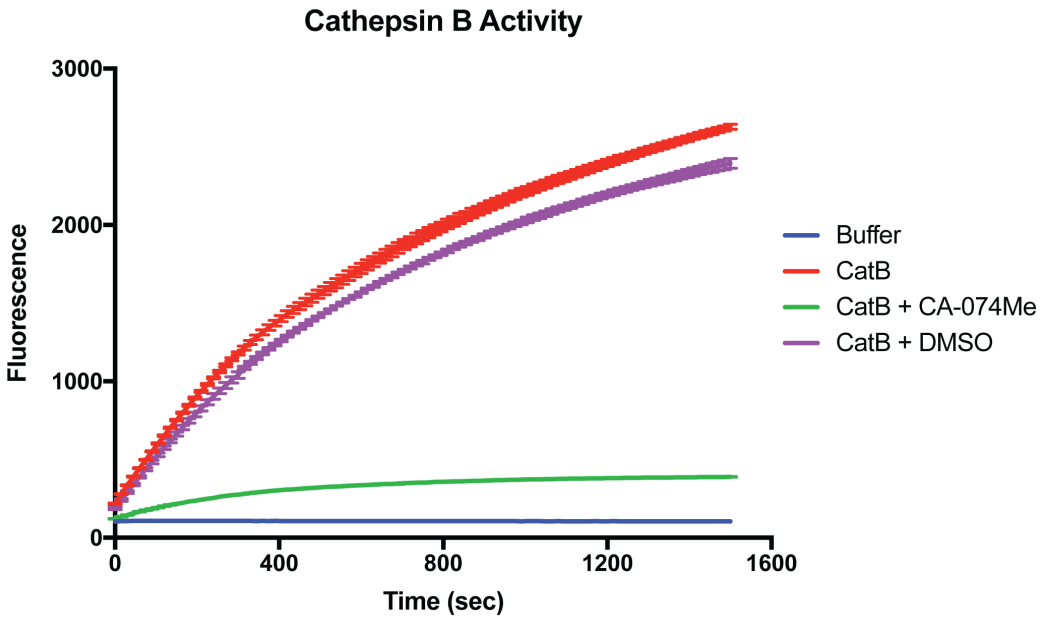

Figure 2.11: The cathepsin B inhibitor CA-074Me efficiently inhibits recombinant cathepsin B activity in vitro. Recombinant cathepsin B was added to a linker substrate that becomes fluorescent following cathepsin cleavage. The reaction was co-incubated with either CA-074Me or DMSO vehicle control.

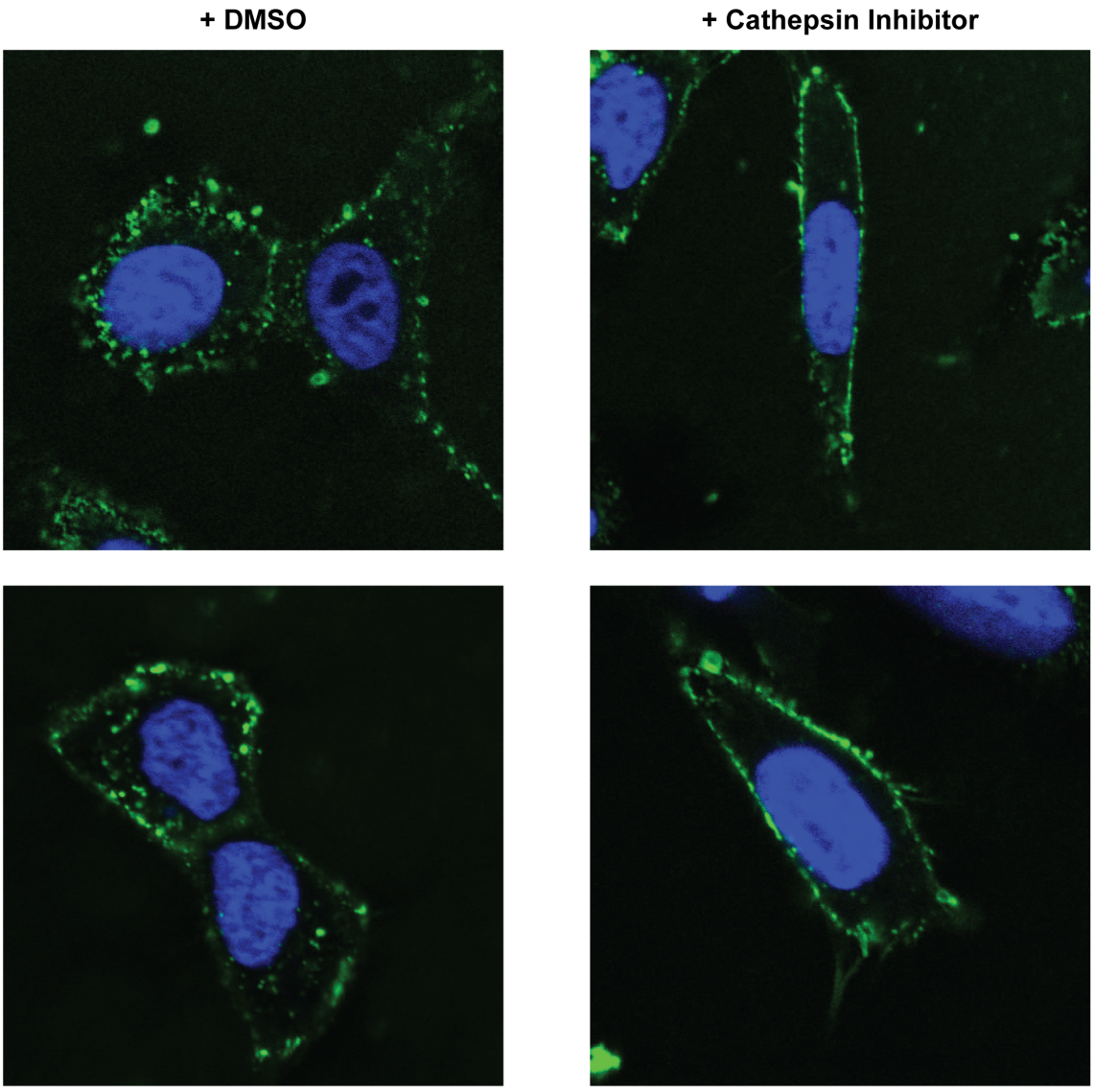

Figure 2.12: The cathepsin inhibitor, CA-074Me, inhibits $BIM_{A,cath,K}PA_2$'s cellular uptake. MEFs were pre-incubated with either 5 μM CA-074Me or 0.1% (v/v) DMSO control in complete media for 1 h. They were then washed and treated with 10 μM FITC-$BIM_{A,cath,K}PA_2$ for 1 h before washing, fixation, staining with Hoechst, and confocal imaging.

CHAPTER 3

SYNTHESIS AND PURIFICATION OF HOMOGENEOUS LIPID-BASED PEPTIDE NANOCARRIERS BY OVERCOMING PHOSPHOLIPID ESTER HYDROLYSIS

This chapter is presented as published [121] in ACS Omega 2018, 3, 10, 14144-14150, with additional, unpublished work in Sections 3.9 and 3.10. While this chapter was published before Chapter 2, the experimental work in this chapter was done after the experimental work in Chapter 2.

3.1 Abstract

Despite the therapeutic promise of phospholipid-based nanocarriers, a major obstacle to their widespread clinical translation is a susceptibility to fatty acid ester hydrolysis, leading to lack of quality control and inconsistencies in self-assembly formulations. Using electrospray ionization mass spectrometry fragmentation in combination with matrix-assisted laser desorption/ionization time-of-flight mass spectrometry, we have demonstrated a method to detect hydrolysis of one or both of the fatty acid esters in a PEGylated phospholipid, DSPE-PEG, in conditions commonly applied during nanocarrier production. Because such carriers are increasingly being used to deliver peptide-based therapeutics, we further investigated the hydrolysis of phospholipid esters in conditions used for solid-phase peptide synthesis and high-performance liquid chromatography of peptides. We ultimately detail a synthetic strategy to reliably produce pure phospholipid–peptide bioconjugates (peptide amphiphiles), while avoiding unintended or unnoticed hydrolyzed byproducts that could lead to polymorphic nanotherapeutics with dampened therapeutic efficacy. We believe that such an approach could help standardize phospholipid–peptide-based therapeutic development, testing, and clinical translation.

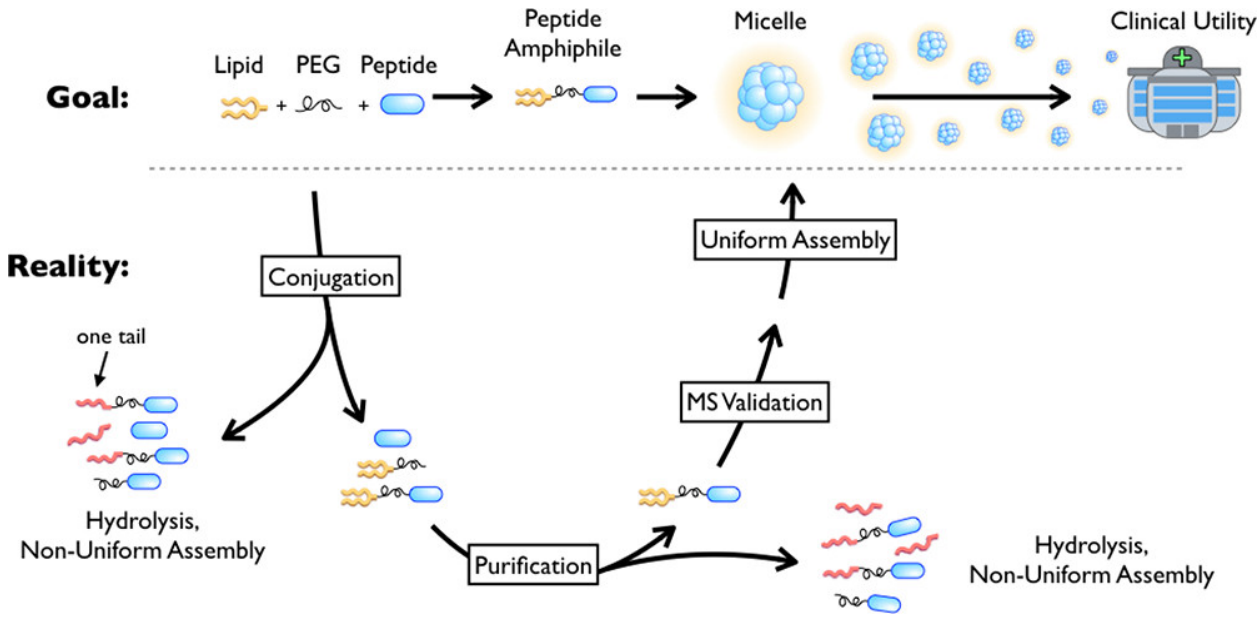

Figure 3.1: The lipid ester hydrolysis problem.

3.2 Introduction

Peptides are increasingly being used to fill a therapeutic gap between small molecules and biologics, particularly for targeting intracellular protein–protein interactions (PPIs) [10]. While only one small molecule drug and zero biologics have been approved by the U.S. Food and Drug Administration (FDA) for targeting intracellular PPIs [4], peptides are entering clinical trials in increasing numbers every year, with more than 100 currently under study [10, 66]. Peptides can harness natural PPI specificity through mimicking a protein's amino acid sequence and secondary structure. Additionally, peptides can possess the biodegradability and low toxicity associated with biologics, while also having the potency and synthetic accessibility typically associated with small molecules [251]. Despite their promise, peptides face a number of obstacles to clinical translation, including rapid clearance, low oral bioavailability, cellular impermeability, and metabolic instability [66, 251]. Phospholipid-based nanocarriers are one approach being used to overcome these obstacles [110, 122].

Phospholipid–peptide conjugation to form peptide amphiphiles (PAs) can improve the pharmacologic potential of peptide drugs that would otherwise be clinically unsuccessful,

as phospholipids are biocompatible, drive nanoparticle self-assembly, can be modified with functional elements (i.e., therapeutic, diagnostic, or targeting), promote cellular internalization, and extend the circulation half-lives of drugs [110, 122, 155, 158, 252–257]. Chemical functionalization and purification of phospholipids with peptides, however, exposes them to conditions that can lead to lipid hydrolysis. Hydrolysis byproducts can significantly affect the structure and properties of these nanostructures [155, 252–255, 257–260]. Consequently, one of the main obstacles to clinical translation of lipid-based nanocarriers, as recently highlighted by the U.S. FDA, is quality assurance and consistency in self-assembly formulations, particularly as it relates to hydrolysis [162, 261–266].

Despite the risks for hydrolysis, there are many examples of lipopeptide synthesis using potentially hydrolytic conditions without documentation of a lack of ester hydrolysis byproducts at the end of synthesis and purification. This can be particularly problematic when a polyethylene glycol (PEG) domain is included in a peptide–lipid conjugate. Here, the molecular weight (MW) becomes polydisperse, and side reactions, including hydrolysis, are more difficult to detect with standard peptide validation techniques such as liquid-chromatography mass spectrometry (LC–MS), matrix-assisted laser desorption/ionization time-of-flight mass spectrometry (MALDI-TOF–MS), and amino acid analysis (AAA), thereby ultimately limiting quality control.

During the synthesis and purification of a PA nanoparticle containing a p53-reactivating therapeutic peptide conjugated to a PEGylated phospholipid, DSPE-PEG, we noticed an uncharacteristic MW signature and investigated its cause and detection. In doing so, we (1) uncovered partial hydrolysis of one or both of DSPE-PEG's fatty acid esters in conditions commonly applied to DSPE-PEG in the literature, (2) validated a detection method using electrospray ionization mass spectrometry (ESI–MS) fragmentation, and (3) demonstrated a synthetic route to reliably produce pure phospholipid–peptide bioconjugates (PAs) without unintended or unnoticed hydrolysis byproducts that can possibly lead to polymorphic nanotherapeutics with dampened efficacy.

3.3 Results and Discussion

We attempted to conjugate a therapeutic peptide ($p53_{14-29}$) to DSPE-PEG in an effort to form $p53_{14-29}$ PA nanoparticles. The $p53_{14-29}$ peptide, in its hydrocarbon stapled form, is known to penetrate cells and reactivate cell death through disruption of the interaction between WTp53 and its endogenous inhibitors, MDM2 and MDM4 [92, 93]. A PA consisting of a ∼2200 Da peptide conjugated to polydisperse DSPE-PEG (∼3000 Da) should have MWs spanning approximately 4700–5700 Da with an average of ∼5200 Da. MALDI-TOF–MS provided little sensitivity to detect small changes in MW because of side reactions for such polydisperse samples. However, during ESI–MS, the dialkylglycerol portion of DSPE-PEG was artifactually cleaved from the rest of the molecule to produce a prominent, monodisperse MW signature at 607 Da (Figure 3.2). When purifying the PA via high-performance liquid chromatography (HPLC)–MS, we discovered a loss of the 607 Da ESI–MS fragmentation peak and a novel 341 Da peak. This new peak corresponded to an alkylglycerol fragment of DSPE-PEG missing one of its C18 fatty acid tails because of ester hydrolysis (Figure 3.2).

To determine which steps of PA manufacturing caused this hydrolysis byproduct, we exposed DSPE-PEG to chemical conditions commonly used for PA synthesis and purification and monitored MW signatures simultaneously using MALDI-TOF–MS and ESI–MS at relevant time points. To avoid misleading artifactual fragmentation, MS techniques were performed in parallel with different ionization modes (Figure 3.2). Our first goal in standardizing the detection of hydrolyzed phospholipids was to establish an inert solvent that could be used to prepare samples for both ESI–MS and MALDI-TOF–MS without affecting DSPE-PEG. Methanol, a polar, protic solvent but poor nucleophile, should not harm DSPE-PEG. To test this, DSPE-PEG was dissolved in methanol and incubated at room temperature (RT) for up to 72 h. MALDI-TOF–MS showed no observable effect of methanol on DSPE-PEG at RT for at least 72 h, and the polydisperse MW distribution remained centered around the expected average MW, 2867 Da (Figure 3.3a). ESI–MS of these samples measured an m/z pattern reflective of intact DSPE-PEG, with polydisperse MW distributions centered around

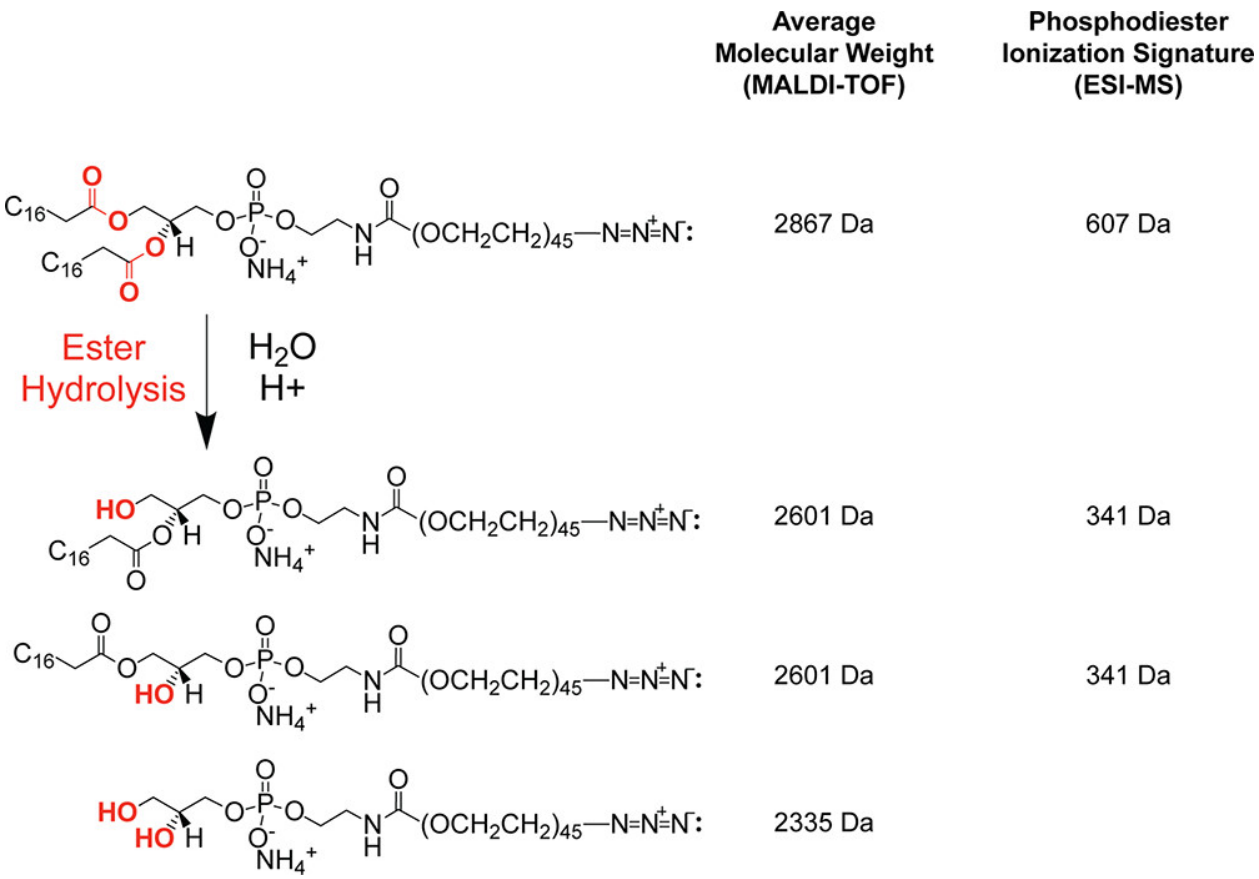

Figure 3.2: Acid-catalyzed ester hydrolysis of DSPE-PEG generates shifts in MW signatures. Hydrolysis of one or both esters in DSPE-PEG generates shifts in absolute MW, observable by MALDI-TOF MS, and in the MW of an alkylglycerol ionization fragment, observable by ESI–MS. Thereby, MALDI-TOF–MS was used to qualitatively measure shifts in the average MW of polydisperse MW distributions, while ESI–MS was used to detect the presence of the hydrolyzed alkylglycerol portion of the molecule at 341 Da.

m/3, m/4, and m/5, and a strong ionization artifact peak at 607 Da corresponding to the existence of double-tailed DSPE-PEG (Figure 3.3b). Therefore, methanol had no effect on DSPE-PEG and was used during MS characterization of all subsequent samples.

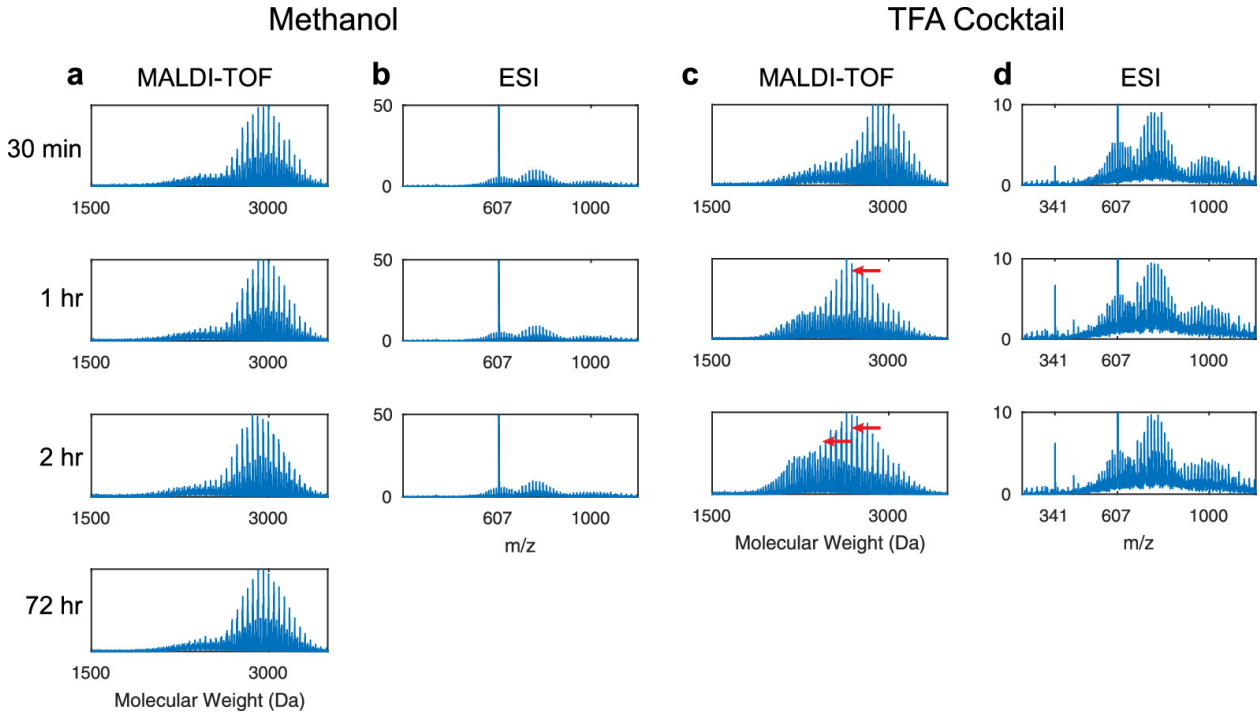

Figure 3.3: MALDI-TOF and ESI–MS reveal phospholipid ester hydrolysis when DSPE-PEG is exposed to a TFA cleavage cocktail used to remove peptides from solid-phase support. (a,b) Esters of DSPE-PEG are stable in methanol at RT. (a) MALDI-TOF shows a time-independent polymeric MW distribution centered at the average MW of 2867 Da. (b) ESI–MS spectra are also time-independent, showing a peak at 607 Da corresponding to an intact dialkylglycerol portion of DSPE-PEG and polymeric distributions centered around the expected values of m/3, m/4, and m/5. (c,d) After incubation with a TFA cocktail commonly used to remove peptides from solid-phase support, MALDI-TOF and ESI–MS both demonstrate leftward shifts in the MW of DSPE-PEG, corresponding to ester hydrolysis. (c) MALDI-TOF shows a leftward shift in the MW distribution of 266 Da per hydrolyzed ester, as indicated by each red arrow. (d) In ESI–MS, the signature ionization fragment at 607 Da shifts to 341 Da, corresponding to phosphodiester fragmentation during ionization of the alkyl-glycerol portion of DSPE-PEG with only one fatty acid tail. In agreement with the MALDI-TOF data, this hydrolyzed fragment appeared as early as 30 min of treatment, with the signal increasing over 2 h.

Because peptides are commonly conjugated to lipids in an increasing variety of biotherapeutic applications, we next tested the compatibility of DSPE-PEG with solid-phase peptide synthesis (SPPS) conditions. Following synthesis, peptides on resin are subjected

to a trifluoroacetic acid (TFA) cleavage cocktail to remove them from solid-phase support and deprotect their amino acid side chains. The removed side-chain protecting groups generate highly reactive carbocations, necessitating the presence of nucleophilic scavengers (e.g., water and triisopropylsilane (TIS)). Because this strong aqueous acid solution could theoretically hydrolyze fatty acid esters within DSPE-PEG, we monitored DSPE-PEG stability in a TFA cleavage cocktail for up to 2 h, the minimum length of time generally used to remove peptides from resin at preparative scales. MALDI-TOF spectra detected a MW distribution shifted to the left by approximately 266 Da after 1 h, corresponding to the hydrolysis of one stearic acid from DSPE-PEG (Figure 3.3c). The MW distribution continued to shift leftward after 2 h of incubation, centering around an average MW corresponding to the loss of two stearic acid molecules from DSPE-PEG. ESI–MS confirmed fatty acid ester hydrolysis with a new peak appearing at 341 Da, corresponding to the hydrolyzed ionization fragment (Figure 3.3d). These results demonstrate that DSPE-PEG is incompatible with solid phase conjugation to peptides using commonly available acid-labile resins and side-chain protecting groups. Fatty acid esters would also not be assumed to be compatible with SPPS conditions.

One strategy to avoid this obstacle to lipid-based peptide nanocarrier synthesis is to exclude water and other nucleophiles from the TFA cleavage cocktail [267]. However, such a strategy would generate a new risk of undesired side reactions between the amino acid side chains and highly reactive carbocations generated during amino acid deprotection. Another potential strategy is to identify nucleophilic scavengers that react readily with carbocations but not esters. However, this brings an increased risk of side reactions that would be buried within the polydispersity of a PEGylated lipid's MW during standard LC–MS, MALDI-TOF–MS, and AAA validation.

Because water is a critical solvent commonly used for phospholipid self-assembly, conjugation, and purification, we next tested the stability of DSPE-PEG in de-ionized water and common buffers used for peptide purification. The rate of phospholipid ester hydrolysis is minimized at pH 6.5 and greatly accelerated at higher or lower pH [258, 268, 269]. MALDI-

TOF analysis of DSPE-PEG dissolved in unbuffered, ultrapure Milli-Q water revealed a distribution of MWs 532 Da smaller than DSPE-PEG after 72 h at RT, corresponding to hydrolysis of both esters (Figure 3.4a). This was accelerated when samples were heated to 60 °C with a leftward shift appearing in the MALDI-TOF spectra after only 2 h (Figure 3.4b). ESI–MS confirmed the presence of hydrolysis byproducts after 2 h with a peak appearing at 341 Da (Figure 3.4c). Unbuffered water, therefore, is not sufficient for preventing hydrolysis of phospholipid esters such as in DSPE-PEG.

Peptides carrying positive charges are most often purified via HPLC using acidic pH 2–3 buffer, imposing another obstacle for purification of PA conjugates, as this acidic pH should accelerate the rate of ester hydrolysis. To test this, we dissolved DSPE-PEG in a commonly used HPLC buffer (water + 0.1% formic acid, pH 2.7) at both RT and 60 °C. There was no detectable MW shift in MALDI-TOF MS at RT for 2 h, but after 72 h the MW shifted to the left, corresponding to hydrolysis of both fatty acid esters (Figures 3.2 and 3.4d). When DSPE-PEG was heated to 60 °C in acidic HPLC buffer, MALDI-TOF revealed a leftward shift starting as early as 30 min (Figure 3.4e). ESI–MS again confirmed the formation of hydrolysis byproducts with the presence of an ionization fragment at 341 Da (Figure 3.4f). In contrast, when DSPE-PEG was dissolved in pH 7.4 phosphate-buffered saline (PBS) buffer, hydrolysis was absent at any time point or temperature, as measured by MALDI-TOF and ESI–MS (Figure 3.5a–c). Therefore, while water and heat are both risks for phospholipid ester hydrolysis, this possibility can be mitigated during HPLC purification by using a neutral pH buffer, lower temperatures, and/or shorter exposure times.

By avoiding the hydrolysis-inducing conditions described above, we generated a pure DSPE-PEG PA nanoparticle with the $p53_{14-29}$ peptide conjugated to DSPE-PEG maleimide via an N-terminal thiol linker. In summary, we cleaved the peptide from the resin before conjugating the phospholipid to avoid exposing the esters to TFA. We then conjugated DSPE-PEG to the peptide in neutral buffered aqueous solution. Lastly, we avoided hydrolysis during HPLC purification by (1) avoiding high temperatures, (2) buffering the fractions

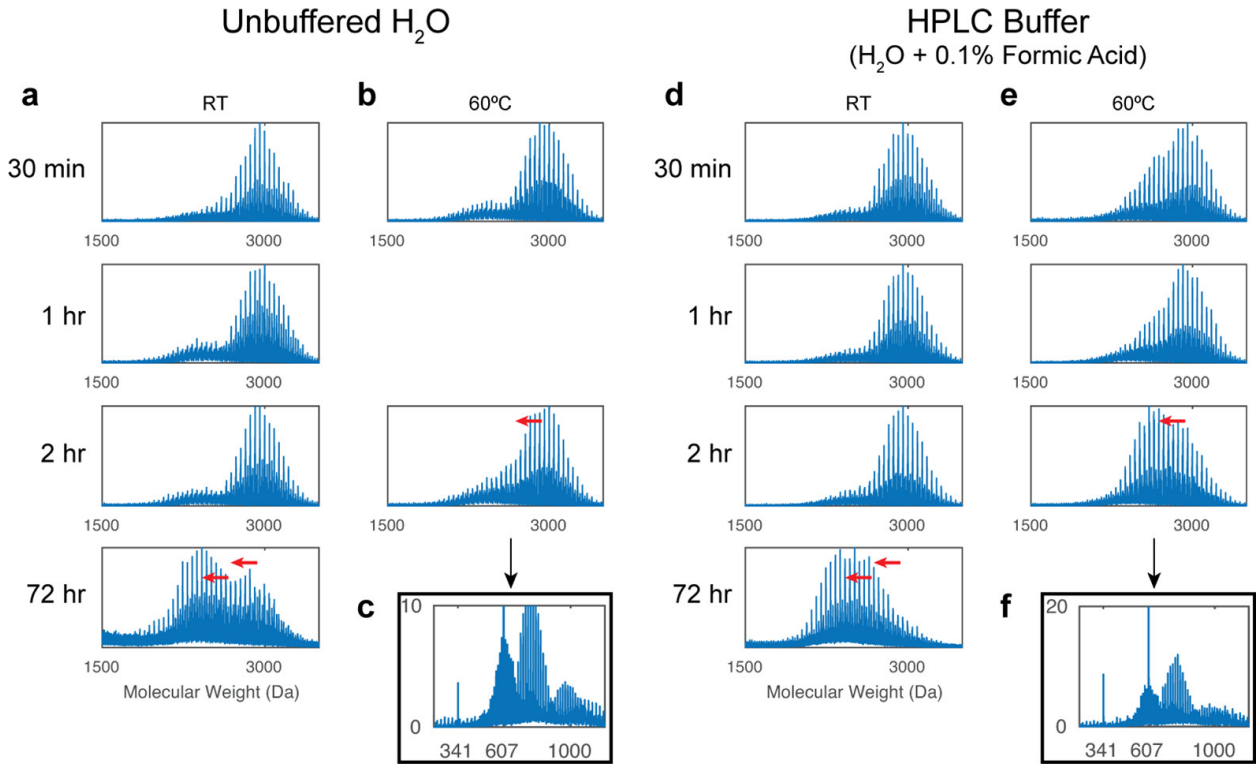

Figure 3.4: Phospholipid esters are hydrolyzed by unbuffered and acidic water, and hydrolysis is accelerated by heat. (a–c) Esters of DSPE-PEG are hydrolyzed in unbuffered water, and hydrolysis is accelerated by heat. (a) DSPE-PEG dissolved in ultrapure Milli-Q water for 72 h at RT results in a leftward shift in MW on MALDI-TOF corresponding to the loss of two stearic acid molecules (-266 Da per hydrolyzed ester, as indicated by each red arrow). (b) Heating to 60 °C accelerates this loss. (c) Analysis of the 2 h, 60 °C sample using ESI–MS confirms hydrolysis with a shift of the signature ionization fragment from 607 to 341 Da. (d–f) Acidic HPLC buffer and heat each increase the rate of hydrolysis of the esters of DSPE-PEG. (d) After DSPE-PEG was incubated in acidic HPLC buffer, MALDI-TOF shows a leftward shift in MW corresponding to the loss of two stearic acid molecules (-266 Da per hydrolyzed ester, as indicated by each red arrow). (e) Identical sample was heated to 60 °C, and hydrolysis was detectable as early as 30 min. (f) As confirmed with ESI–MS, the signature ionization fragment of 607 Da shifts to 341 Da.

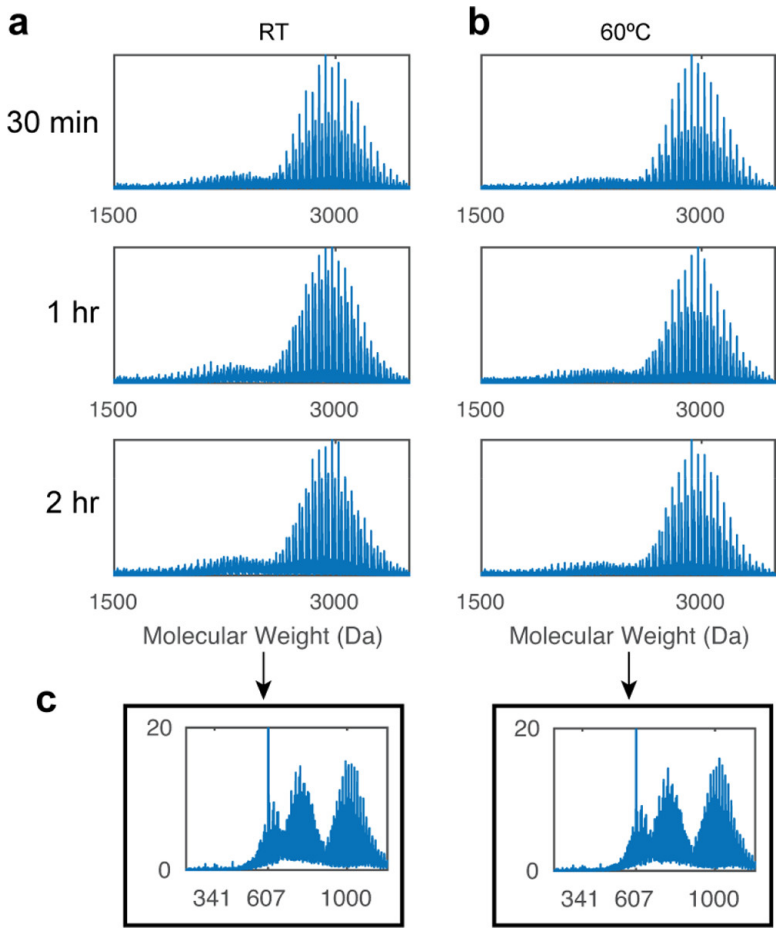

Figure 3.5: Esters of DSPE-PEG are stable in neutral buffered PBS at RT and 60 °C. (a,b) MALDI-TOF MS shows no changes in the absolute MW of DSPE-PEG after incubation in PBS at either (a) RT or (b) 60 °C for at least 2 h (c) ESI–MS shows no detectable peaks at 341 Da, indicating no hydrolysis after 2 h in PBS at RT or 60 °C.

to neutral pH immediately upon elution, and (3) rapidly removing the solvent by rotary evaporation and lyophilization. Following purification, LC–MS showed only one peak with UV absorbance at 280 nm, indicating a solitary pure product. Here, the two intact lipid tails, rather than the polydisperse PEG, was the predominant driver of the hydrophobic interaction between the DSPE-PEG moieties and the LC column, as reflected in the elution of single peak at ∼94% methanol. The corresponding ESI–MS signal had a peak at 607 Da, indicating an intact DSPE-PEG tail with no detectable hydrolysis fragments (Figure 3.6a). MALDI-TOF revealed a polydisperse MW distribution centered around 5205 Da, the expected average MW of the PA (Figure 3.6b). There was also a second distribution of MWs that was smaller by 607 Da, corresponding to the same artifactual fragmentation of DSPE-PEG's phosphodiester bond. Lastly, a closer inspection of the exact MWs within the polydisperse distribution revealed an exact match to the calculated MWs of this PA with 44, 45, or 46 PEG units, with the expected spacing of 44 Da (Figure 3.6c). These PAs formed round, homogenous nanoparticle micelles that were strikingly monodisperse, properties ideal for preclinical testing and clinical translation (Figure 3.6d,e).

3.4 Conclusions

This study highlights the pH- and temperature-dependence of phospholipid ester hydrolysis, raising unique concerns for newly developed phospholipid–peptide conjugates. Unlike SPPS for peptides, there are currently no universal protocols for conjugating, purifying, or otherwise handling phospholipid-based drug delivery systems, and many reports subject phospholipid esters to conditions known to promote their hydrolysis without explicit documentation of final product purity. This is the first report to our knowledge showing the significant limitations that exist when employing widely used peptide synthesis and purification workflows for phospholipids. We believe that techniques such as those presented here should be adapted, especially when a polydisperse polymer, such as PEG, is included in a bioconjugate in advance of preclinical testing.

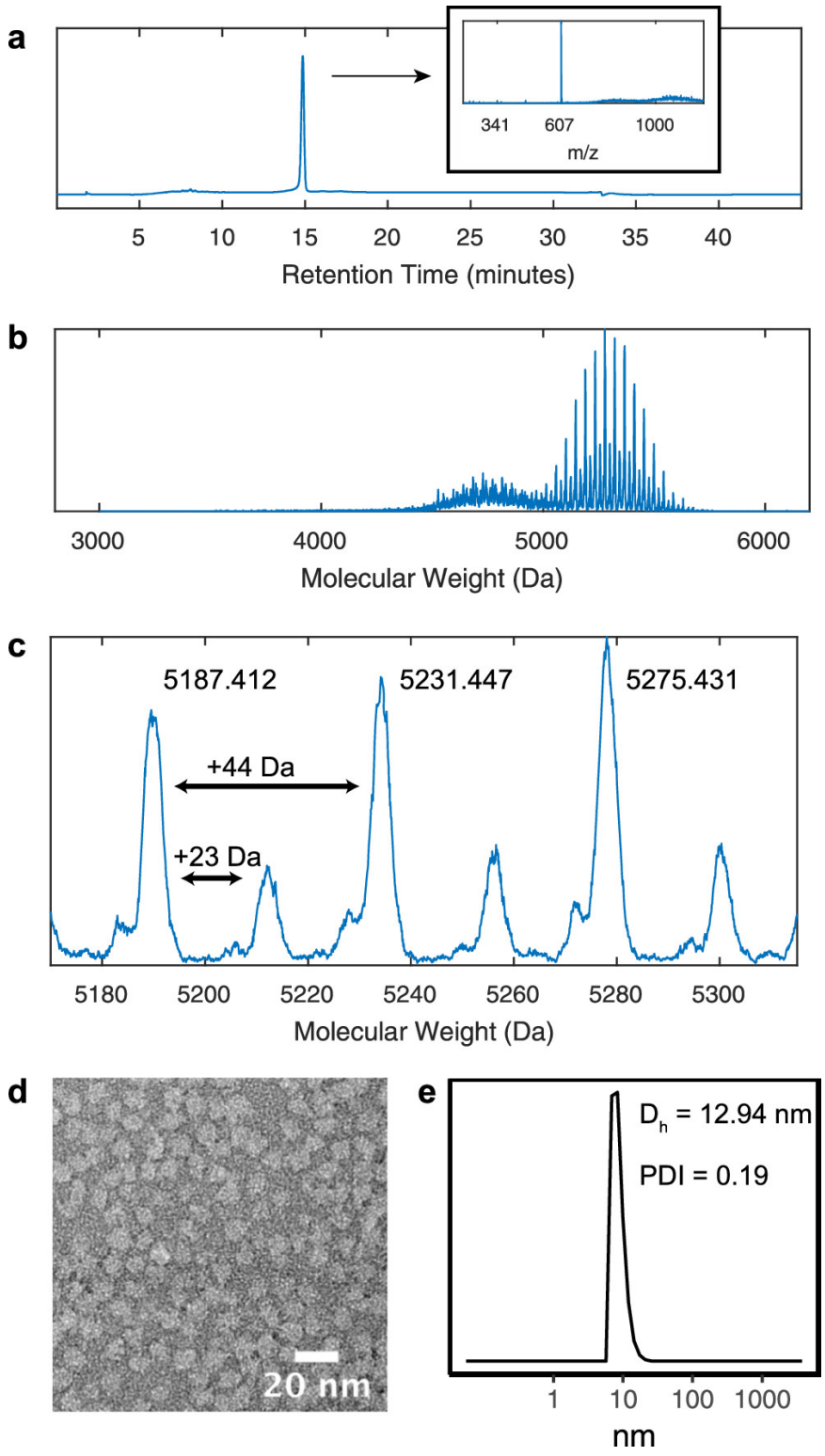

Figure 3.6: Buffered synthesis and purification conditions generate pure DSPE-PEG-PAs with no detectable hydrolysis byproducts. (Continued on the following page.)

Figure 3.6, continued: Buffered synthesis and purification conditions generate pure DSPE-PEG-PAs with no detectable hydrolysis byproducts. Peptide $p53_{14-29}$ was synthesized with an N-terminal thiol linker using SPPS followed by RP-HPLC purification. DSPE-PEG-maleimide was then conjugated using neutral buffer, and the resulting PA was purified using mild RP-HPLC conditions. (a) LCMS of the pure PA fractions shows one peak with 280 nm absorbance, and the corresponding ESI–MS signal at 607 Da confirms that it has an intact DSPE-PEG tail. (b) MALDI-TOF shows a polydisperse MW distribution, centered at approximately 5205 Da, the expected average MW of the PA. A secondary distribution is also visible, approximately 607 Da smaller, corresponding to artifactual fragmentation of the PA's phosphodiester bond. (c) Zooming-in on the MALDI-TOF spectrum reveals peaks matching the expected MWs of PAs with 44, 45, or 46 PEG units. These peaks have the expected PEG spacing of 44 Da, and their corresponding Na+ adducts are also visible at +23 Da. (d) Transmission electron microscopy (TEM) imaging reveals PA self-assembly into spherical micelles (115,000x magnification). (e) Histogram of hydrodynamic radius from DLS measurements shows a monodisperse size distribution with D_h = 12.94 nm and PDI = 0.19.

3.5 Methods

3.5.1 Materials

1,2-Distearoyl-sn-glycero-3-phosphoethanolamine-N-[azido(polyethylene glycol)-2000] (DSPE-PEG(2000)-azide) was purchased from Avanti Polar Lipids, Inc. Methanol, TFA, and PBS were purchased from Fisher Scientific. Milli-Q water was filtered through a 0.2 μm filter. All standard amino acids, N-methylpyrrolidone (NMP), and dichloromethane (DCM) were purchased from Gyros Protein Technologies with standard TFA-labile protecting groups. Fmoc-beta-alanine-OH was purchased from Novabiochem. Formic acid, piperidine, N,N-diisopropylethylamine (DIPEA), acetic anhydride (Ac_2O), ethanedithiol (EDT), TIS, and tris(2-carboxyethyl)phosphine (TCEP) were purchased from Sigma-Aldrich. (7-Azabenzotriazol-1-yloxy)trispyrrolidinophosphonium hexafluorophosphate (PyAOP) was purchased from EMD Millipore. 3-Tritylsulfanyl-propionic acid (Mpa(Trt)-OH) was purchased from Bachem.

3.5.2 DSPE-PEG Hydrolysis Tests

For each solvent to be tested, 10 mg of DSPE-PEG was weighed into a 1.5 mL Eppendorf tube and dissolved in 1 mL of solvent. The solution was then split into two Eppendorf tubes, each 500 μL. One tube was left at RT, and the other was incubated at 60 °C. At each measured time point, 100 μL of each sample was transferred into a new Eppendorf tube for solvent removal. For TFA and methanol samples, the solvent was quickly evaporated under a gentle stream of blowing nitrogen. For other aqueous solvents, the sample was rapidly frozen in liquid nitrogen and lyophilized.

3.5.3 Matrix-Assisted Laser Desorption/Ionization Time-of-Flight Mass Spectrometry

Dried samples were dissolved in 100 μL of methanol, plated with dihydroxybenzoic acid matrix, and analyzed using the Bruker Ultraflextreme MALDI-TOF-TOF in the University of Chicago's Mass Spectrometry Core Facility. To avoid fragmentation artifacts during ionization, the laser power was set using pure DSPE-PEG dissolved in methanol to a level that allowed for sufficient ionization without fragmentation artifacts. The same laser power was then applied to all samples.

3.5.4 Electrospray Ionization Mass Spectrometry

Dried samples were dissolved in 100 μL of methanol for ESI–MS via an Agilent 6130 LCMS. The ionization conditions were set using pure DSPE-PEG dissolved in methanol to a level that allowed for sufficient ionization without fragmentation artifacts. The same ionization conditions were then applied to all samples. The mobile phase was 50% water + 0.1% formic acid, 50% methanol, with a flow rate of 0.4 mL/min. The MS signal was acquired in positive mode, and the settings in the Agilent software were set as follows: fragmentor = 100, gain = 2.00, threshold = 100, step size = 0.10.

3.5.5 Solid-Phase Peptide Synthesis

The $p53_{14-29}$ peptide with N-terminal thiol and flexible linker was synthesized with sequence MPA(bAla)GG(bAla)LSQETFSDLWKLLPEN-NH2. The peptide was synthesized manually in a peptide synthesis vessel from Chemglass using standard Fmoc SPPS protocols on Agilent AmphiSpheres 40 RAM resin. Before and after each reaction, the resin was washed extensively with NMP and DCM. Fmoc deprotection was accomplished with 2 × 10 min reactions with 25% piperidine in NMP, and deprotection was confirmed via the Kaiser Test. Each amino acid (10x with respect to (w.r.t.) resin substitution) and PyAOP (10x w.r.t. resin substitution) were dissolved in NMP immediately before use and activated by DIPEA (20x w.r.t. resin substitution) immediately before addition to the reaction vessel. Coupling was allowed to proceed until the Kaiser Test was clear. After each coupling, a capping solution (4:1:0.1 NMP/Ac_2O/DIPEA) was applied to the resin for 10 min to cap any unreacted amines. As the final coupling, the thiol linker (Mpa(Trt)-OH) was added to the N-terminus of the peptide using the same reaction as the amino acids. After the synthesis, the resin was washed extensively with DCM and dried completely. The peptides were then cleaved from the resin using 94/2.5/2.5/1 TFA/H2O/EDT/TIS for 2.5 h. The TFA solution was removed by precipitating the peptides in ice cold diethyl ether, centrifuging the precipitate, removing the supernatant, and allowing the pellet to dry at RT. The peptides were resuspended in 1:1 (H2O + 0.1% formic acid)/acetonitrile with TCEP for a few hours to ensure complete thiol reduction before HPLC purification.

3.5.6 Reverse-Phase HPLC (RP-HPLC) Purification

HPLC purification was performed on a Shimadzu HPLC–MS system using a Waters column, C8, XBridge BEH OBD Prep Column, 19 mm × 150 mm, 5 μm particle size, and 130 Å pore size. Methanol and acetonitrile were HPLC-grade and purchased from Fisher Scientific. Formic acid was purchased from Sigma-Aldrich. Water was Milli-Q filtered. All peptides were purified using water + 0.1% formic acid and acetonitrile as the mobile phases, with

the column temperature at 60 °C. After elution, the acetonitrile was removed by rotary evaporation, and the samples were immediately lyophilized to minimize disulfide formation. All PAs were purified using water + 0.1% formic acid and methanol as the mobile phases at 25 °C. Immediately after elution, the fractions were buffered with 1 M ammonium bicarbonate buffer, pH 6.8. The methanol was then removed by rotary evaporation with the heat bath set no higher than 30 °C, and the samples were immediately lyophilized.

3.5.7 Conjugation of DSPE-PEG-Maleimide to Thiol-Peptide

DSPE-PEG-maleimide and the thiol-p53_{14-29} peptide (3:1) were each dissolved in dimethylsulfoxide (DMSO) at 37.5 and 50 mM, respectively. The peptide solution was diluted in 0.1 M sodium phosphate buffer, pH 7.4, and DSPE-PEG was then added to the mixture. The final reaction mixture was 1:1 DMF/(sodium phosphate buffer) with 5 mM peptide and 15 mM DSPE-PEG maleimide. The reaction was allowed to proceed for 1 h and then injected into the HPLC for purification.

The DMF allowed for increased concentration of the reaction mixture and increased reaction rate, and the water with pH 7.4 sodium phosphate buffer served to (1) maintain the specificity of the thiol–maleimide reaction, (2) prevent maleimide hydrolysis while thiol conjugation proceeded to completion, and (3) prevent DSPE-PEG ester hydrolysis. After 1 h, the conjugation was complete according to LC–MS evaluation. We then purified the PA from the reaction mixture using RP-HPLC at 25 °C with water + 0.1% formic acid and methanol as the mobile phase solvents. We buffered the collected fractions immediately upon elution using 1 M ammonium bicarbonate buffer, pH 6.8. We then immediately removed the methanol using a rotary evaporator and removed the water by lyophilization.

3.5.8 Analytical Liquid Chromatography and Mass Spectrometry

Analytical LC–MS of the PA was performed on an Agilent 6130 LCMS system in the University of Chicago's Mass Spectrometry Facility, using a Waters column, C8, XBridge, 4.6 mm

× 150 mm, 5 μm particle size, and 130 Å pore size. The ESI–MS conditions were the same as used in part D, except that the fragmentor was increased to 250 to successfully ionize the PA. The mobile phase solvents used were water + 0.1% TFA and methanol at a total flow rate of 1 mL/min. The method used an isocratic phase at 20% methanol from 0 to 2 min, a gradient from 20 to 80% methanol from 2 to 5 min, 80 to 100% methanol from 5 to 15 min, washing at 100% methanol from 15 to 30 min, followed by equilibration at 20% methanol from 30 to 45 min. The dwell volume from the pumps to the UV detector for this machine was measured to be approximately 3 mL.

3.5.9 Micelle Formation and Dynamic Light Scattering

PAs were dissolved in DMSO to form a 10 mM stock solution, followed by dilution to 100 μM in PBS. Following micelle formation, the nanoparticles were filtered through a 0.2 μm filter. A correlation function was measured using a Wyatt Mobius Dynamic Light Scattering (DLS) in the Polymer Size Characterization Suite (sponsored in part by Wyatt Technology Corp.) at the University of Chicago's Institute for Molecular Engineering. The correlation function was used to find the hydrodynamic diameter (D_h) and polydispersity index (PDI) using a cumulant analysis. The average values from 15 measurements were used.

3.5.10 Transmission Electron Microscopy

Samples were prepared and imaged by the Advanced Electron Microscopy Core Facility at the University of Chicago. Grids (continuous carbon on 200-mesh copper grids—EMS CF200-CU) were glow-discharged for 30 s. The sample (100 μM) was applied soon after for 1 min. The excess sample was blotted off. The grids were stained with two washes of 0.75% uranyl formate and 45 s of 0.75% uranyl formate. Each was blotted off. Grids were imaged on a Tecnai G2 F30 (FEI) electron microscope operating at 300 kV.

3.6 Author Contributions

M.R.S., M.V.T., and J.L.L. conceived the work. M.R.S. and S.P.Y. performed the experiments. Data analysis was performed by M.R.S. and J.L.L. The manuscript was written by M.R.S. and J.L.L. with comments and inputs from all authors.

3.7 Conflics of Interest

The authors declare no competing financial interest.

3.8 Acknowledgments

M.R.S. was supported in this research by the National Cancer Institute (NCI) of the National Institutes of Health (NIH) under Award Number F30CA221250 and the University of Chicago MSTP training grant from the NIH under Award Number T32GM007281. The mass spectra presented here were obtained at the University of Chicago's Mass Spectrometry Facility, supported by the National Science Foundation instrumentation grant CHE-1048528. Dynamic light scattering was carried out at the Soft Matter Characterization Facility of the University of Chicago. We would like to thank Tera Lavoie, PhD from the University of Chicago's Advanced Electron Microscopy Core Facility for her assistance with the TEM sample preparation, imaging, and analysis. We would also like to thank Jeffrey M. Ting, PhD for assistance in designing the Table of Contents Graphic.

3.9 Unpublished: Advances in PA (and Stapled PA) Synthesis and Purification

After publishing the strategy for detecting DSPE-PEG hydrolysis by ESI-MS fragmentation [121], I continued working on the synthesis and purification strategy and made these additional improvements.

3.9.1 Peptide-Lipid Conjugation Strategies in Aqueous Buffer at Neutral pH.

After determining the conditions under which DSPE-PEG's lipid esters were stable, I used two different conjugation chemistries to synthesis DSPE-PEG peptide amphiphiles (Figure 3.7).

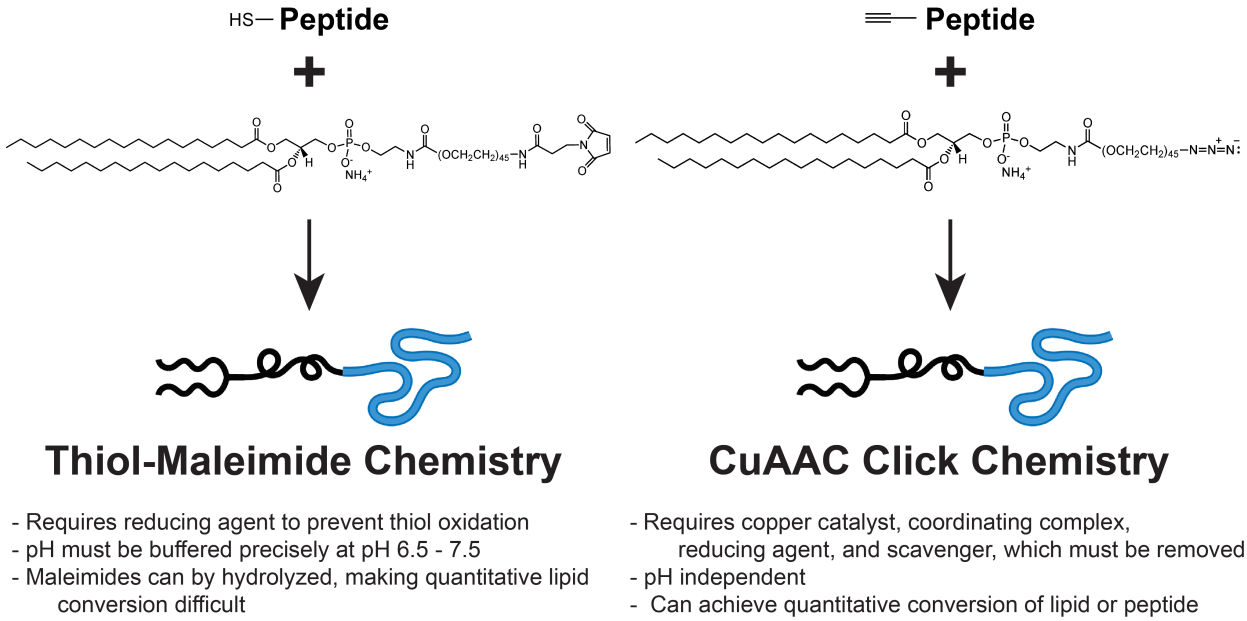

Figure 3.7: Peptide-lipid conjugation examples in aqueous buffer at neutral pH. We have used two conjugation chemistries to form peptide-PEG-lipid conjugates in conditions that do not cause lipid hydrolysis. (a) Thiol-maleimide chemistry: a thiol can be incorporated into a peptide during solid-phase peptide synthesis. After synthesis and peptide purification, the thiol can be reacted with DSPE-PEG maleimide. (b) Copper-catalyzed azide-alkyne cycloaddition (CuAAC) click chemistry: an alkyne can be incorporated into a peptide during solid-phase peptide synthesis. After synthesis and peptide purification, the alkyne can be reacted with DSPE-PEG-azide.

3.9.2 Reverse-Phase Separation Isolates 2-Tailed Molecules.

Reverse-phase (RP) HPLC is the purification strategy most commonly used for peptide purification, but different conditions are needed to purify peptide-lipid conjugates. Because the lipid-portion of the molecule is primarily what drives the reverse-phase retention, anything

with two lipid tails will tend to co-elute (Figure 3.8a). For this reason, it's recommended to purify the peptide before conjugating it to the lipid tail, because after the lipid tail is attached, it will be hard to remove any peptide sequence impurities.

When acetonitrile is used as the "B" mobile phase in RP-HPLC, as is almost always the case, two-tailed peptide amphiphiles and two-tailed lipids fail to elute from the column within reasonable run times (Figure 3.8b). For very late-eluting molecules, methanol is a stronger eluent and can be used to elute two-tailed lipid-based molecules, though they almost always co-elute at very high %B (Figure 3.8c). Isopropanol, an even more non-polar and stronger eluent, can elute two-tailed lipid-based molecules earlier and *sometimes* separate peptide-lipids from free lipid, depending on the peptide sequence (Figure 3.8d). Isopropanol was the lowest polarity solvent I could find that had a low UV-cutoff and was miscible with water.

Of note, isopropanol as the mobile phase greatly increases the system pressure during RP-HPLC. As a compromise, 50% isopropanol with 50% acetonitrile can be used to achieve similar elution strength while minimizing the increase in pressure.

Unlike acetonitrile, these alcohol mobile phases are very difficult to remove by lyophilization. Instead, the majority of organic solvent can be removed by rotary evaporation, the sample diluted extensively with water, and finally lyophilization. Rotary evaporation of lipid-based molecules in mixtures involving water tend to bump and foam a lot and must be monitored closely and carefully.

Ideally, the lipid can be completely consumed in the conjugation reaction, and the peptide lipid conjugate would be pure at this point. For this reason, it would be ideal to use the peptide as the excess reagent in the conjugation reaction to functionalize all of the lipid.

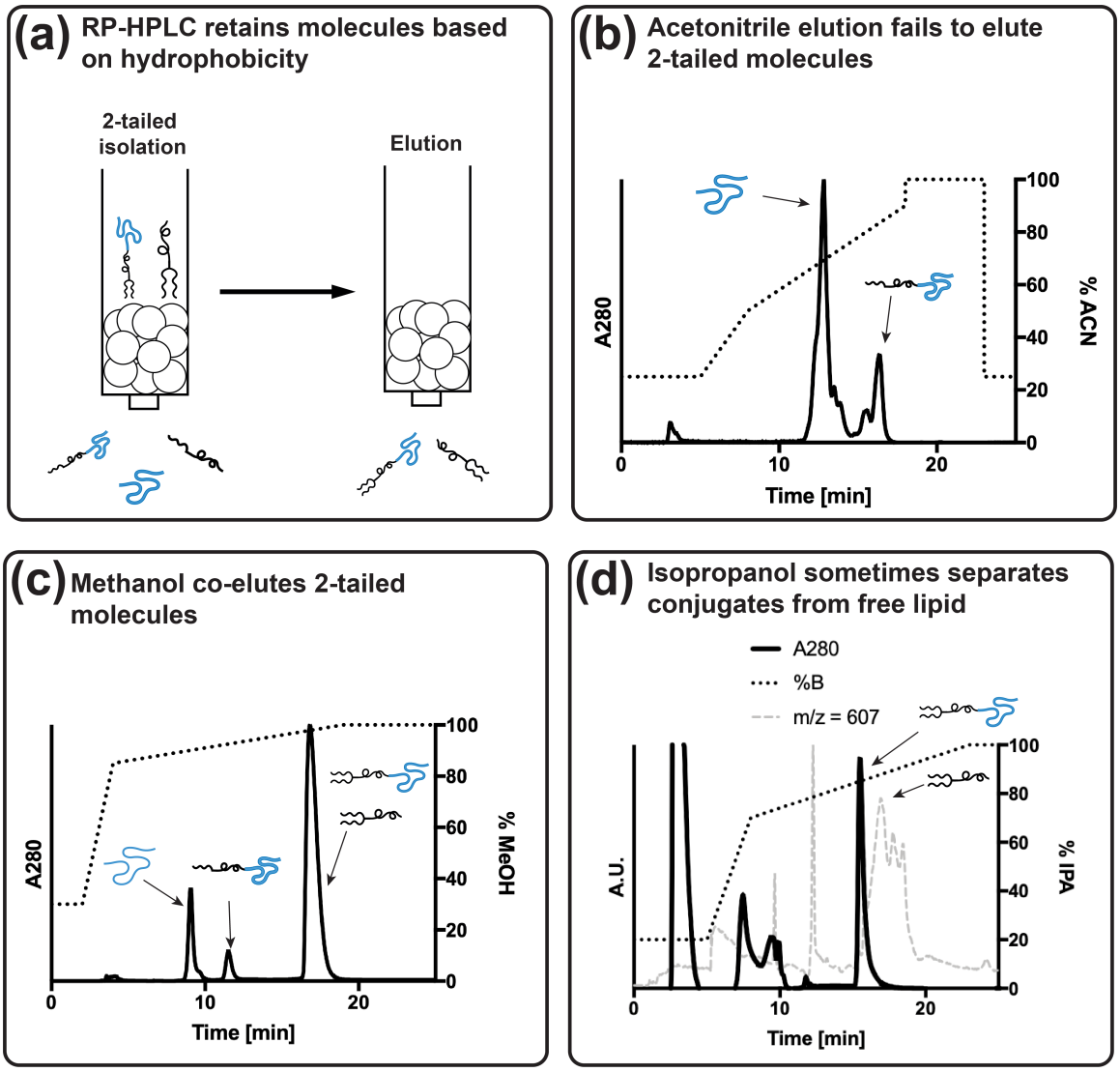

Figure 3.8: Choice of organic mobile-phase in RP-HPLC strongly influences PA elution and purification. After conjugation, the peptide-lipid conjugates need to be isolated. (a) Reverse-phase (RP) chromatography separates molecules based on hydrophobicity. 2-tailed products can be isolated from a reaction mixture, but the peptide-lipid conjugates can rarely be separated from free lipid using this method. (b) Standard RP-HPLC elution with acetonitrile fails to elute 2-tailed molecules. (c) Methanol, a stronger eluent of very hydrophobic molecules, elutes 2-tailed lipids and peptide-lipids, usually as a single peak. (d) Isopropanol, a stronger eluent yet, can sometimes separate free lipid from peptide-lipid.

3.9.3 Addition of Mobile-Phase Additives Improves PA Peak Shapes in RP-HPLC

For peptide amphiphiles with multiple charged groups, I have sometimes seen the intended product elute as multiple peaks during HPLC, and each peak has an identical mass spectrum. I hypothesize this is due to the charged groups either being in different protonation states or different salt forms, due to the lack of mobile-phase additives in the nearly 100% organic mobile phase elution conditions.

First, I tried adding 0.1% acid (formic acid or TFA) to the B mobile phase, but I still saw split peaks. DSPE-PEG has a phosphate group that would still be negatively charged in these conditions, so perhaps the mobile phase needed a modifier that included a salt with a cation.

An ideal mobile phase additive should be volatile, so that it is compatible with HPLC-MS and can be removed by lyophilization, and should be soluble in both water and the organic mobile phase. For this, I chose ammonium acetate, 100 - 200 mM, pH ~4.8. Adding ammonium acetate buffer/salt to the mobile phase improved the peak shape of peptide amphiphiles during RP-HPLC elution, and I stopped seeing split peaks.

Upon elution, I buffered the fractions immediately with ammonium bicarbonate (another volatile buffer, but one that is not very soluble in organic solvents), pH 6.5, to neutralize the pH and prevent DSPE-PEG ester hydrolysis.

3.9.4 Normal-Phase Separation of PAs from Free Lipids

While reverse-phase chromatography will retain peptide amphiphiles based on their hydrophobic domain, normal-phase chromatography will retain peptide amphiphiles based on their polar peptide domain (Figure 3.9a). In theory, this could be used to separate the peptide amphiphile from free lipids, but I have not found a simple and reliable way to elute peptides and peptide amphiphiles from silica. However, this can be used as a quick and sim-

ple test to detect lipid impurities in peptide amphiphiles (Figure 3.9b) after RP-HPLC, in which they may co-elute. MALDI-TOF mass spectrometry can also be used for this purpose.

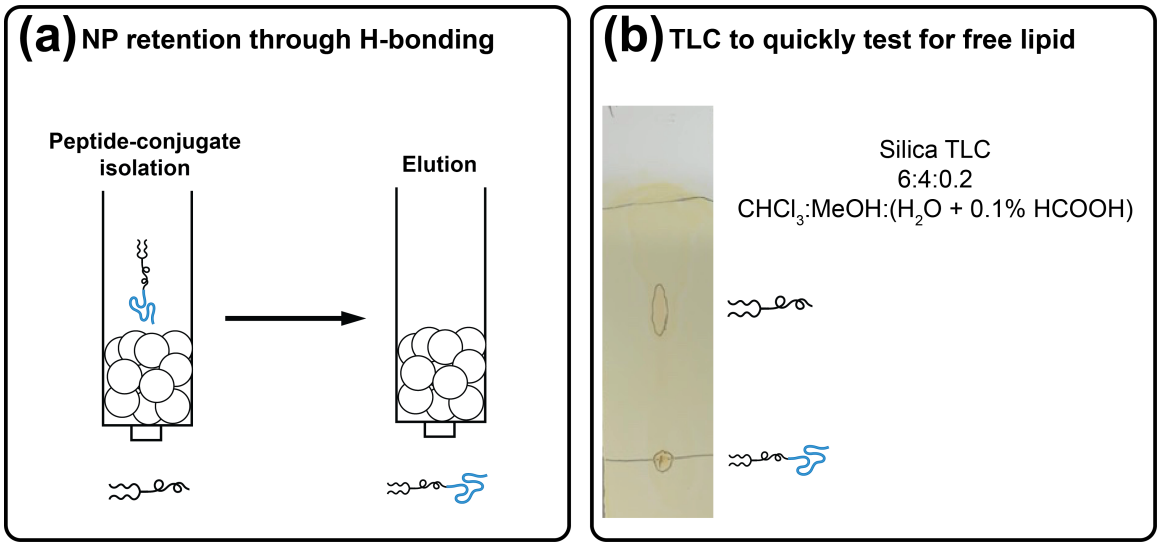

Figure 3.9: Normal-phase retention can be used to separate peptide amphiphiles from free lipid. Normal-phase (NP) TLC retains molecules through hydrogen bonding polar interactions. (a) Peptide-lipid conjugates can be retained on normal-phase silica resin while allowing free lipid to wash away. This can be used either for purification or analysis. (b) TLC on silica can be used to quickly test for the presence of free lipid (representative TLC of a mixture). In a pure peptide-PEG-lipid conjugate, no spots will migrate.

3.10 Unpublished: Intracellular Delivery of Therapeutic Peptides Using Hydrocarbon-Stapling and Peptide Amphiphile Micelles

My goal I proposed in my Qualifying Exam was to combine the ability of stapled-peptides to inhibit cancer-driving PPIs (Section 1.2.2) with the ability of peptide amphiphiles to form supramolcular nanostructures (Section 1.3.2) and facilitate the intracellular accumulation of therapeutic peptides [141, 142]. Using the PA synthesis and purification strategies presented in this chapter, I now had the ability to generate stapled PAs (sPAs) for intracellular delivery of a p53-reactivating stapled peptide, SAH-p53-8 [92, 93], and test its ability to therapeutically reactivate p53 in cancer (Figure 3.10).

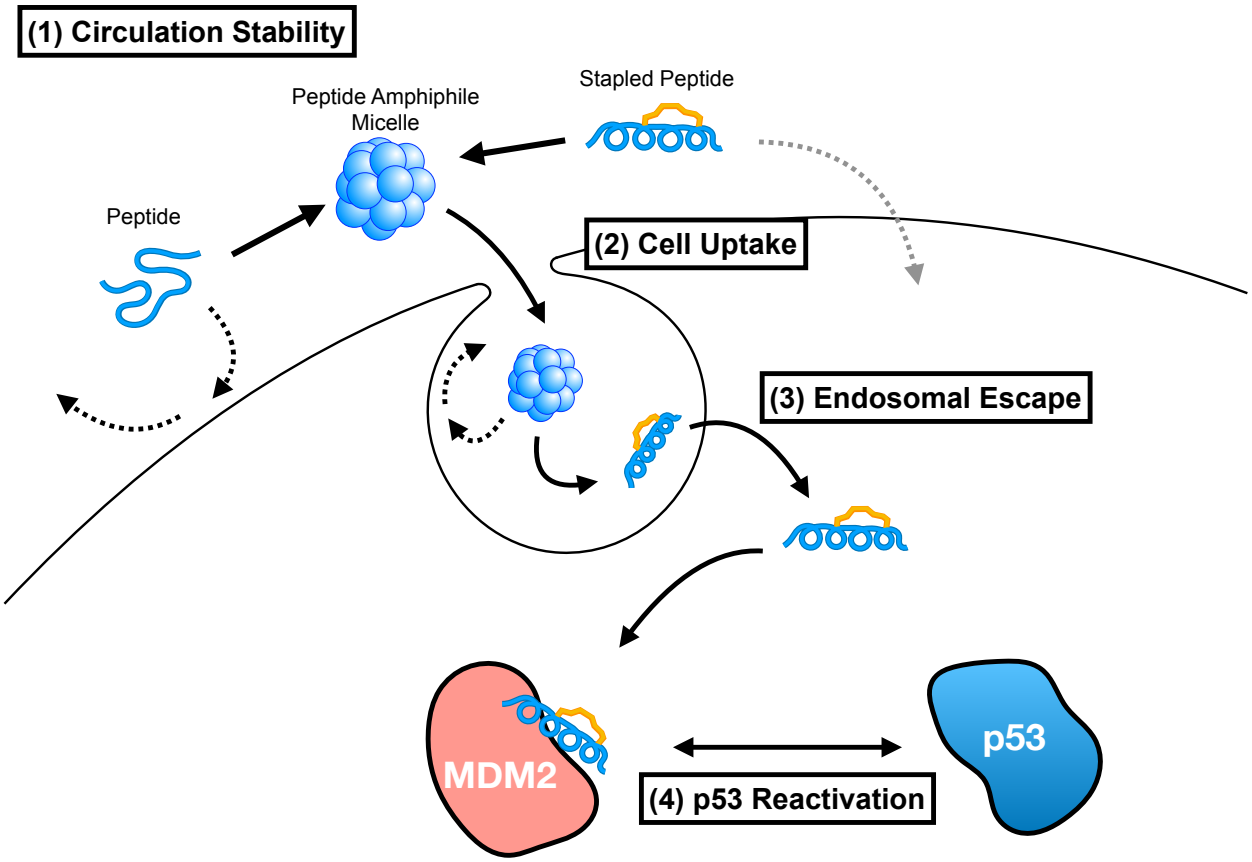

Figure 3.10: A stapled peptide amphiphile (sPA) platform for intracellular delivery of therapeutic peptides. Peptides can be incorporated into spherical, micellar nanoparticles by conjugating them to a PEG-ylated lipid "tail" (e.g. DSPE-PEG), forming petpide amphiphiles (PAs). PA micelles protect peptides in circulation, and they can be targeted to specific tissues and cell types. PAs enhance cellular uptake of peptides. An endosomally cleavable (cathepsin substrate) linker can be used to release the peptide from the tail after internalization to enhance intracellular accumulation. Hydrocarbon-stapled peptides, meanwhile, can escape endosomes and disrupt pathologic protein-protein interactions (PPIs). By combining the therapeutic stapled peptides and PA delivery, we aim to develop a platform for disrupting intracellular PPIs.

3.10.1 Design, Synthesis, and Purification of a Panel of p53-Reactivating Stapled Peptide Amphiphiles

To test this, I used the synthesis and purification strategies outlined in this chapter to make a panel of molecules. I used three different peptides: (1) the unstructured $p53_{14-29}$ binding interface, the stapled SAH-p53-8, and the non-binding point mutant SAH-p53-8-F19A.

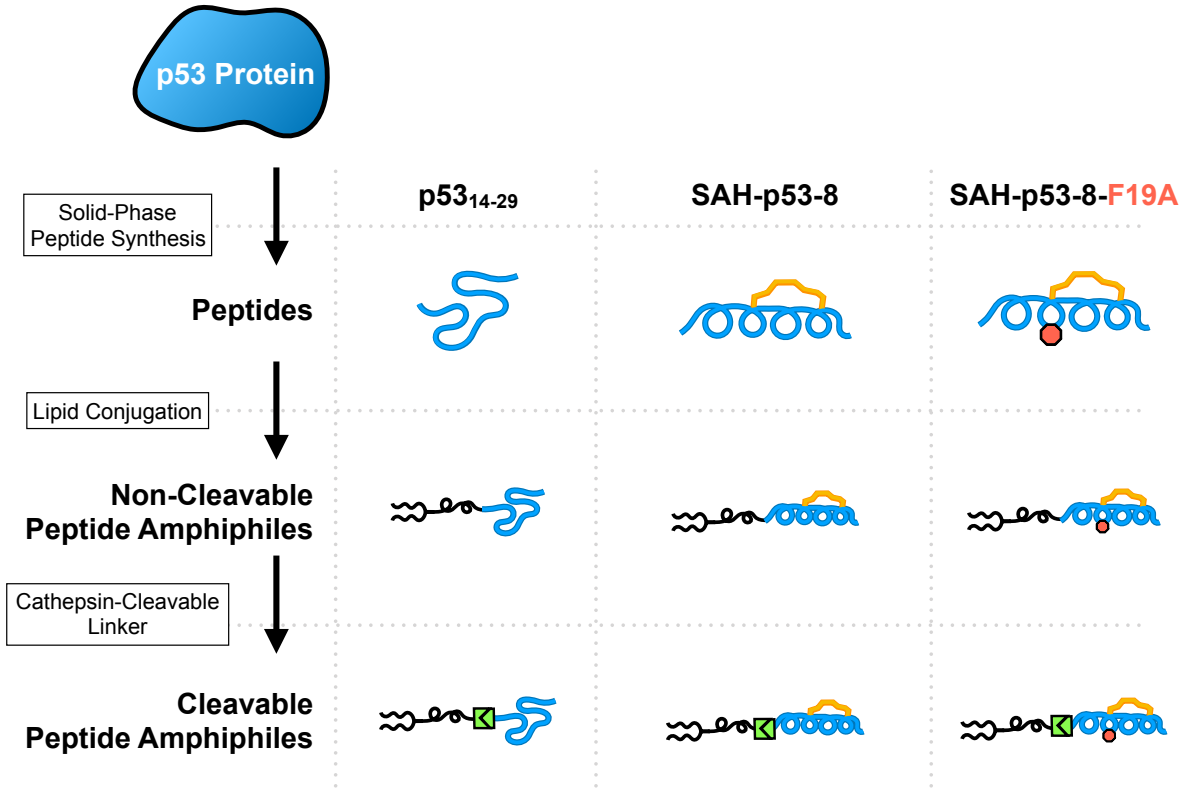

Figure 3.11: Designing and synthesizing a panel of p53-reactivating stapled peptides and stapled PAs. The binding interface of p53 with its inactivating proteins, MDM2 and MDMX, occurs at amino acid positions 14-29. We synthesized three peptides previously published to mimic the p53:MDM2/MDMX binding interface: (1) unstructured $p53_{14-29}$, (2) hydrocarbon-stapled SAH-p53-8, and (3) non-binding point mutant SAH-p53-8-F19A [92, 93]. We covalently linked each peptide to a PEGylated lipid tail (DSPE-PEG) to form non-cleavable PAs. To facilitate endosomal escape after internalization, we also incorporated an endosomally-cleavable, cathepsin-substrate linker between the peptide and the lipid tail.

After synthesis, each molecule was determined to be pure by LCMS, was confirmed not

to contain any contaminating lipid by MALDI-TOF-MS, and was confirmed to have both lipid tails intact by ESI-MS (Figure 3.12).

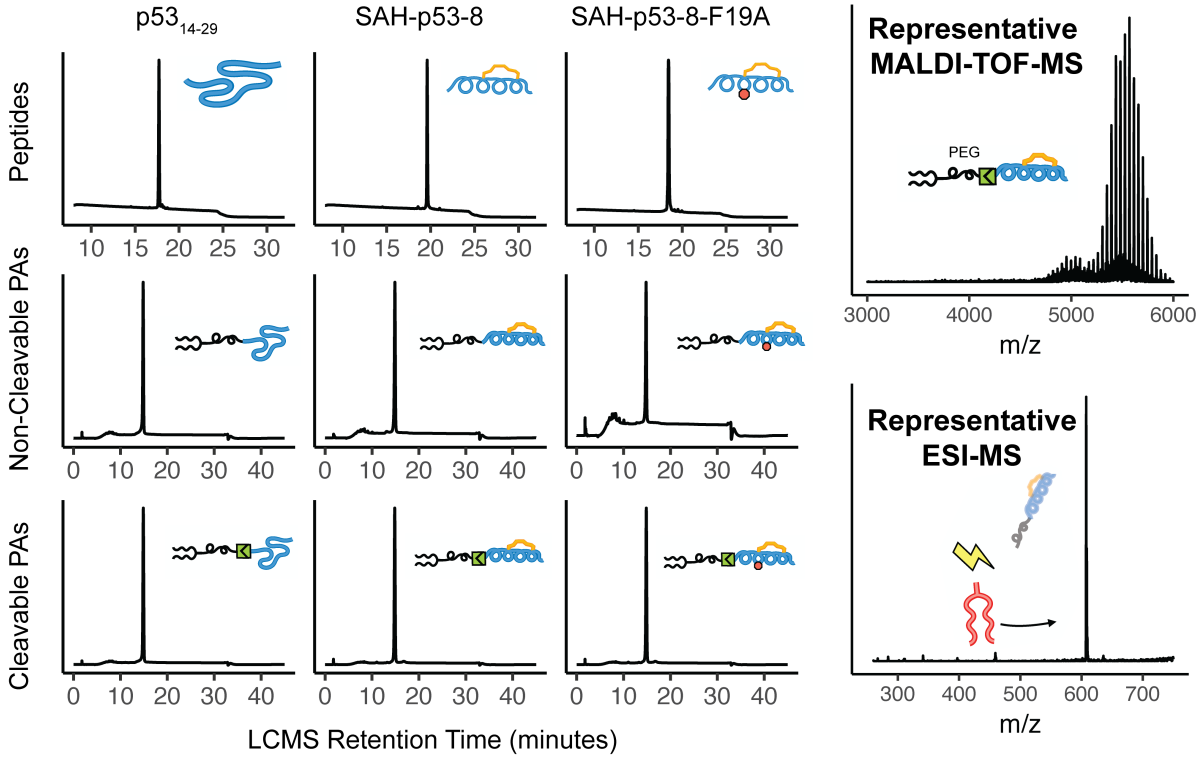

Figure 3.12: Validating purity and molecular identity of sPAs. After synthesis and HPLC purification, we used LCMS to confirm that the molecules were pure and eluted as a single peak (shown is the UV absorbance at 220 nm). By MALDI-TOF-MS, each molecule has a molecular weight distribution that matches the expected molecular weights, with no signal from contaminating free DSPE-PEG lipid. By ESI-MS, the presence of the 607 Da peak and absence of a 341 Da peak indicates an intact phospholipid tail, confirming no lipid hydrolysis side reactions have occurred during synthesis and purification.

3.10.2 Micelle Self-Assembly of Stapled Peptide Amphiphiles.

Next we used the PAs and sPAs to self-assemble micelles. Each of the structures formed spherical micelles as would be expected for DSPE-PEG PAs, and the hydrocarbon staple on the hydrophilic peptide headgroup did not seem to block micelle formation (Figure 3.13).

TEM

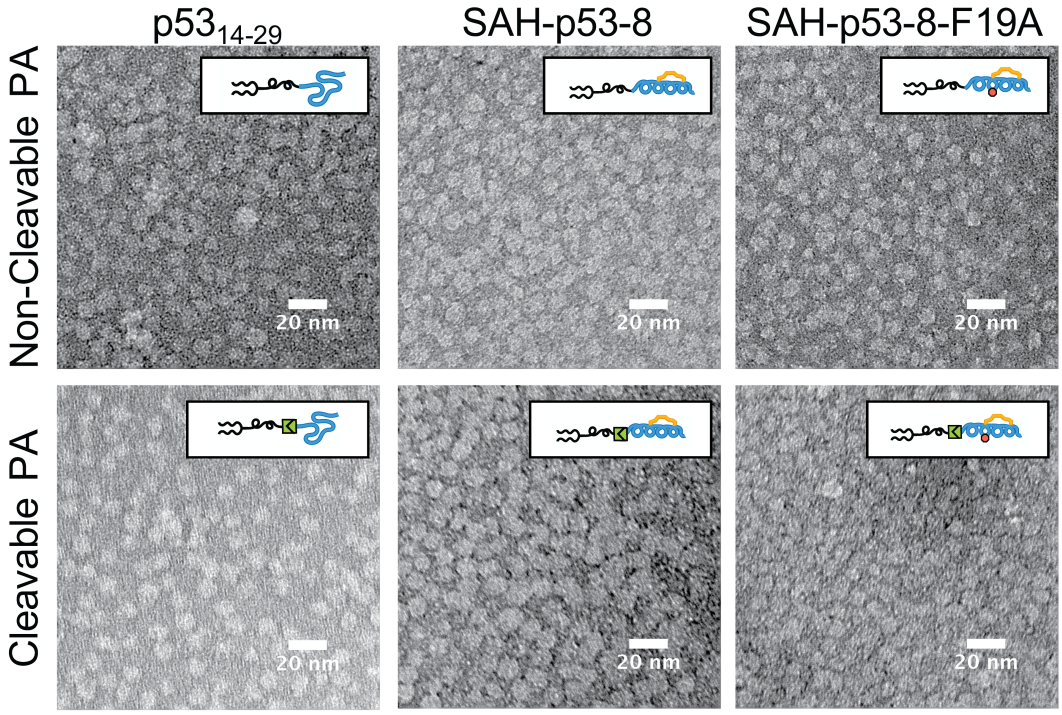

DLS

	Cleavable PA		Non-Cleavable PA	
	R_h (nm)	PDI	R_h (nm)	PDI
$p53_{14-29}$	6.73 ± 0.01	0.11 ± 0.00	6.47 ± 0.07	0.19 ± 0.01
SAH-p53-8	5.95 ± 0.07	0.16 ± 0.02	6.29 ± 0.21	0.19 ± 0.02

Figure 3.13: Hydrocarbon-stapling does not inhibit the formation of PA micelles. PAs were dissolved in a DMSO stock solution (20 mM) and self-assembled into micelles by gradual dilution into PBS. Negative-stain TEM confirms spherical micelle self-assembly of PA micelles, even with a hydrocarbon staple on the hydrophilic peptide headgroup.

3.10.3 SAH-p53-8 Stapled Peptide Amphiphiles Fail to Induce Cell Death in a Wildtype-p53 Cancer Cell Line, SJSA-1.

To test efficacy, we treated a human osteosarcoma cell line (SJSA-1) that is well known to have MDM2 upregulation for p53 inactivation, making it sensitive to p53-reactivating therapeutics. Our compounds were all AAA-quantified to concentration-match the amount of therapeutic peptide in the treatment. When cells were incubated with SAH-p53-8 as a free stapled peptide, it killed SJSA-1 at doses similar to what has been published previously for this peptide in this cell line (Figure 3.14) [28, 92, 93]. However, when the peptide was part of a peptide amphiphile intended to amplify its internalization, it instead completely eliminated its ability to induce cell death.

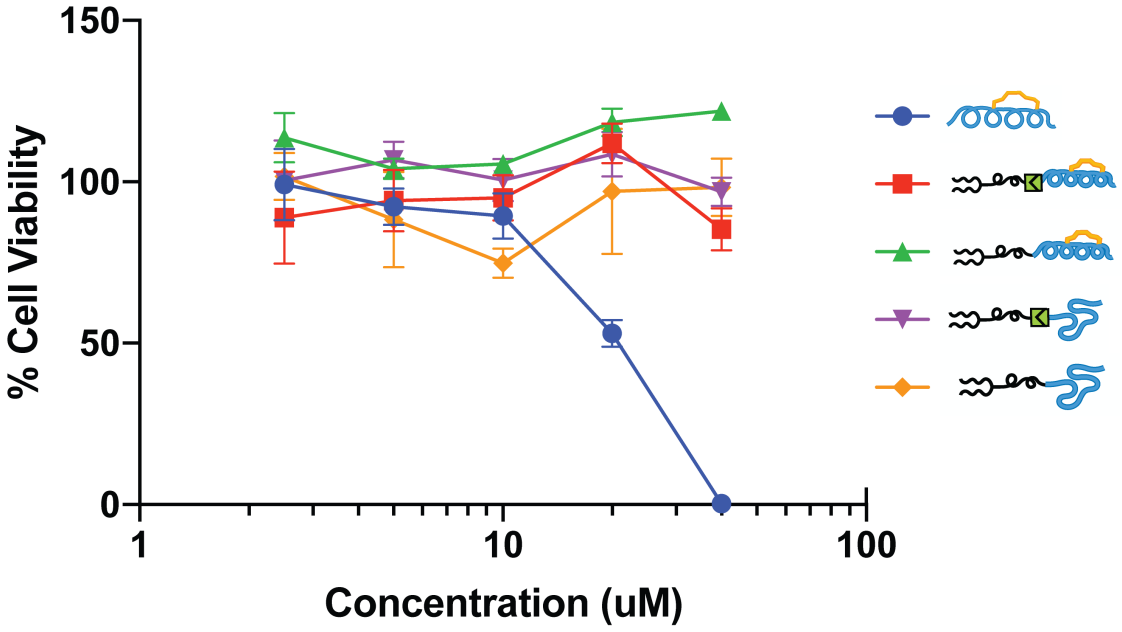

Figure 3.14: SAH-p53-8 PAs fail to induce cell death in SJSA-1, a wildtype-p53 human osteosarcoma cell line. Cells were treated with the indicated compound in the absence of FBS for 4 hours, then 10% FBS was added for 20 hours before analyzing cell viability at 24 hours using CellTiter-Glo 2.0.

This was a very unexpected outcome, because with a non-stapled BIM BH3 peptide amphiphile, in which the peptide alone can not cross cell membranes, a cathepsin-cleavable

PA led to enhanced uptake and somehow allowed the peptide to reach its cytoplasmic and mitochondrial targets (Chapter 2) [142]. Unlike the BIM BH3 peptide, SAH-p53-8 is itself somewhat cell permeable, so if anything, we would expect it to be better at escaping the endosome, not worse.

3.10.4 Cathepsin B Has Only Slight Preferences for Preferred Cleavage Sites, and Linker Cleavage may not be Fast Enough Relative to Therapeutic Peptide Cleavage.

After reading more about Cathepsin B cleavage sites, some sequences are cleaved slightly faster than others (such as valine-citrulline, in our linker), but it is actually a highly promiscuous protease, cleaving almost all amino acid sequences, with only very slight preferences for some sequences relative to others [270]. The antibody-drug conjugates (ADCs) that inspired our cathepsin-cleavable linkers all used small molecule therapeutics, which lacked peptide bonds that could be harmed by proteases. Therefore, even if ADCs take a long time to be degraded in the endo-lysosome pathway, the small molecule will go unharmed. For peptide-based therapeutics, however, early endosomal escape should be crucial to avoid proteolytic degradation of the peptide simultaneously with the linker.

To test this, I tried to measure cleavage of the linker, relative to the rest of a peptide, using cathepsin B in vitro and LCMS monitoring. Due to the difficulties reliably separating PAs during LCMS, and the potential steric hinderance of the cleavage site being burried in a micelle, I instead used a stapled peptide with the same cleavage site as I used for my PAs but before the DSPE-PEG tail was added. The sequence I used was MPA-bAla-Val-Cit-bAla-BIM-SAHB.

Briefly, 10 μM of the peptide with cleavable linker was incubated with cathepsin B (Sigma Aldrich, C8571; 100 nM) at 37 °C, in 100 mM sodium phosphate buffer, pH 6.0, with 1 mM EDTA and 5 mM cysteine. At the indicated timepoint, an aliquot of the reaction was stopped

with E-64 cysteine protease inhibitor (100 μM). LCMS was then used to measure the area-under-the-curve of the chromatogram to measure the relative amounts of the full-length peptide and to look for the cleavage product.

The amount of the peptide in the non-cleaved peak rapidly decreased, but the intended cleavage product (between citrulline and bAla) did not accumulate (Figure 3.15). Instead, a number of non-specific cleavage products were detected throughout the LCMS chromatogram.

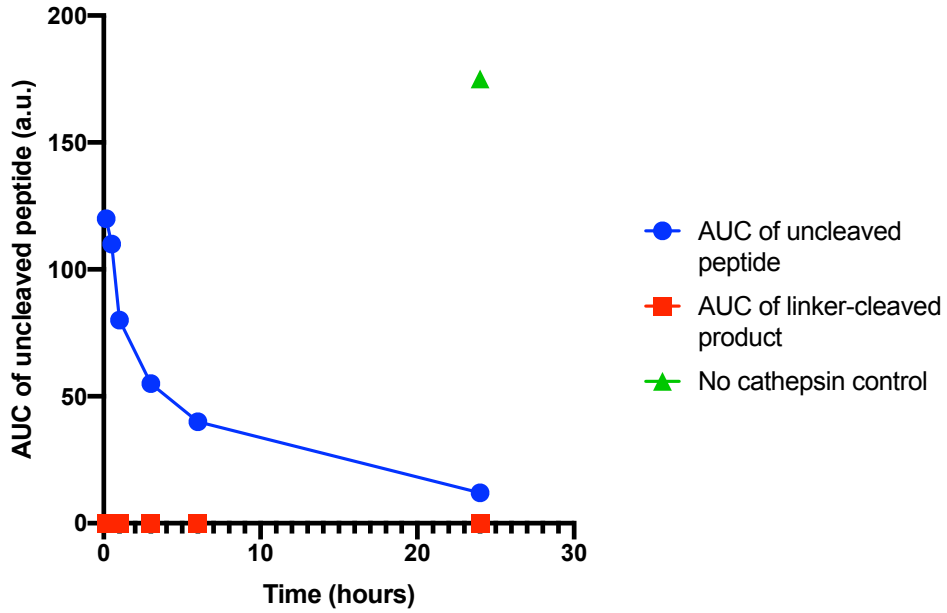

Figure 3.15: Cathepsin B cleaves a stapled peptide in vitro, but not at the intended cleavage site fast enough to detect the intended cleavage product.

These data support the hypothesis that cathepsin cleavage is not remarkably faster for our cleavable linker, relative to proteolytic cleavage elsewhere in the therapeutic peptide, at least for this stapled peptide (BIM SAHB) with this cathepsin-cleavable linker (MPA-bAla-Val-Cit-bAla-...).

3.10.5 Discussion on Cathepsin-Cleavable Stapled Peptide Amphiphiles

After developing a synthesis and purification strategy for hydrocarbon-stapled peptide amphiphiles (sPAs), a SAH-p53-8 sPA was ultimately unable to induce cell death compared to the SAH-p53-8 stapled peptide alone. I hypothesized this was due to an inability to escape the endosome before cathepsin upregulation could harm the therapeutic peptide. I happened to have a different stapled peptide (BIM SAHB) with the same cathepsin-cleavable linker (MPA-bAla-Val-Cit-bAla) before adding the lipid tail, so I tested in vitro cleavage of the linker relative the rest of the peptide using cathepsin B. This peptide was non-specifically cleaved before the linker could be cleaved fast enough to accumulate the desired cleavage product. This finding is supported in the literature on cathepsin B cleavage sequences and the relative rates of cleavage of various amino acid sequences; while cathepsins can cleave some amino acid sequences faster than others, the relative rates are only a few-fold different, not orders of magnitude different [270], which would be required to allow for efficient release of a therapeutic peptide and endosomal escape before being non-specifically cleaved.

There are at least a few potential strategies with which we may be able to mitigate these factors to make sPAs efficacious.

First, it is possible that the beta-alanine spacer, which I used between the citrulline residue of the cleavage sequence and the N-terminus of the therapeutic peptide, is problematic. It is possible that the stapled peptide's alpha-helicity can be propagated through a flexible linker like this, to make the cleavage-site relatively inaccessible. This could potentially be mitigated by using a more rigid spacer, like the self-immolative PABC spacer (e.g. in brentuximab vedotin) or a similar but non-immolative version PABA [141]. I tried synthesizing sPAs by adding a Fmoc-Val-Cit-PABC-PNP spacer to the peptide while still on solid phase, and the PABC spacer turned out to be unstable in the TFA-cleavage step. If this approach is taken, the linker would likely need to be added in solution after the peptide is cleaved from the resin, and then it would be difficult to avoid amino acid side chain groups from interfering with the desired reaction. The rigid PABA spacer could be added more

easily, since it is not self-immolative.

Second, it is possible that the rate of cathepsin cleavage of the linker is too slow, occurring in the late endosome-lysosome when the rest of the therapeutic peptide could also cleaved by proteases. For this reason, another type of linker that allows for earlier release could be beneficial. Endosomes are a relatively reducing environment, and disulfide linkers are commonly used to release cargoes in the endosome. Perhaps a disulfide linker would allow for early endosomal release to give stapled peptides enough time to escape the endosome.

Third, it is possible that stapled peptides are too slow at endosomal escape. This could potentially be improved by making mixed micelles that incorporate both a therapeutic PA and an endosome-lytic PA.

Some of these strategies are being pursued by others in the lab to enhance the efficacy of sPAs. To ultimately harness the therapeutic efficacy of sPA micelles as a nanomedicine, we need a better understanding of their endosomal release and endosomal escape and strategies to enhance those processes. Moreover, for effective targeting and internalization in vivo, their stability will likely need to be greatly improved. Though PA micelles have repeatedly been shown to be capable of active targeting to deliver cargo to specific tissues in the body [128–140], PA micelles dissociate on the timescale of 8 minutes in the presence of serum proteins [271]. Receptor-mediated endocytosis is generally much slower than this timescale on which PA micelles disassemble, so for active targeting and subsequent intracellular delivery in vivo, their stability should need to be greatly improved, through core- or shell-crosslinking or some other means.

CHAPTER 4

TARGETED POLYMERSOMES FOR INTRACELLULAR DELIVERY OF STAPLED PEPTIDES: DRUGGING THE P53:MCL-1 AXIS IN DLBCL

4.1 Abstract

Hydrocarbon-stapled peptides are promising tools for disrupting intracellular protein-protein interactions (PPIs). However, their inability to target and enter cells at therapeutically-relevant concentrations renders most such preclinical drugs clinically untranslatable. To address this, we developed a CD19-targeted nanocarrier to deliver and induce endosomal escape of stapled peptides in human diffuse large B-cell lymphoma (DLBCL). Our nanocarrier platform induced robust CD19-specific uptake and intracellular accumulation in DLBCL. For a marginally cell-permeable therapeutic peptide, nanocarrier delivery improved the peptide's therapeutic potency by orders of magnitude across DLBCL cell lines. We then used this platform to synergistically exploit two major DLBCL chemoresistance mechanisms, namely p53-inactivation and MCL-1 expression. Therapeutic reactivation of p53 sensitized DLBCL to cell death by MCL-1 inhibition and allowed nanocarrier delivery of SAH-MS1-18 to reactivate cell death at 1,000-fold increased potency compared to SAH-MS1-18 peptide alone. In vivo, this targeted nanocarrier was able to deliver a fluorescent model cargo into human DLBCL cells xenografted in mice, and we are now actively testing our nanocarrier's ability to enhance the therapeutic efficacy of the peptide therapeutic SAH-MS1-18 in vivo. This work highlights the potential for using rationally designed nanomaterials to deliver highly-specific yet poorly cell-penetrating peptide-based therapeutics to the cytoplasm of an intended cell type.

4.2 Introduction

Despite their known biomedical importance, intracellular PPIs have long been considered "undruggable" therapeutic targets using traditional, "drug-like" small molecules [3, 11]. Most PPI interfaces are significantly larger (1,500 – 3,000 $Å^2$) than the surface areas bound by small molecules drugs (300 – 1,000 $Å^2$), which prevents small molecule drugs from blocking large PPI interfaces with specificity [5–9]. Meanwhile, hydrocarbon "stapled" peptides have shown great promise for disrupting α-helix-based intracellular PPIs by mimicking a protein's PPI interface through stabilization of a natural α-helical secondary structure while imparting it with drug-like properties including enhanced binding specificity, affinity, protease resistance, and in some cases cellular uptake [74, 76, 78, 81, 82, 98, 272]. The clinical potential of this drug class is reflected in ALRN-6924, a wildtype-p53 (WTp53) reactivating stapled peptide currently in clinical trials [84–88, 273]. However, significant obstacles remain for the clinical translatability of stapled peptides, including achieving cellular uptake at therapeutically-relevant concentrations into the diseased cells of interest.

While the characteristics governing cellular uptake of stapled peptides are beginning to be understood [76, 98], highly-optimized, cell-penetrating stapled peptides still typically require 100-10,000 times higher concentrations for efficacy in assays in which the cell membrane is intact (e.g. in vitro cellular assays) than in assays in which the cell membrane is absent or permeabilized (e.g. ex vitro protein binding assays, mitochondrial depolarization assays) [28, 102, 103]. Moreover, research-grade stapled peptides are often sequestered and completely inhibited by serum proteins [27, 28, 105, 106], and the same modifications that make them cell permeable make them insufficiently water soluble for intravenous injection. For these reasons, few stapled peptides have been successfully applied in in vivo applications, highlighting the potential for dramatically improving their therapeutic translation by improving their delivery to and into diseased cells.

Meanwhile, many PPIs implicated in diseases are also indispensable in normal cells, and on-target toxicities are a major obstacle for PPI inhibitors administered systemically [43–

46, 274, 275]. Antibody-drug conjugates (ADCs) have begun to enable cell-type-specific targeting for small molecule therapeutics, but no such delivery system exists for peptide therapeutics, which would additionally need to undergo endosomal escape to reach intracellular targets. Achieving cell-specific, intracellular delivery of stapled peptides requires a multifunctional delivery vehicle.

Our goal was to develop a targeted nanoparticle delivery system that could deliver stapled peptides to and into diseased cells, regardless of the peptide's intrinsic cellular uptake properties. We chose to test our approach in human diffuse large B-cell lymphoma (DLBCL), the most common form of non-Hodgkin lymphoma, in which 63% of patients are refractory to upfront treatment and 73% of those who relapse will not survive five years [210, 211]. DLBCL subverts cell death through a number of anti-apoptotic mechanisms involving PPIs, including MCL-1 expression and WTp53 sequestration by HDM2 and HDM4 [22, 23, 29, 212–214, 216, 218, 276]. MCL-1 is an anti-apoptotic protein in the BCL-2 family that binds and sequesters the effector proteins of apoptosis and is one of the most commonly upregulated genes in cancers (Figure 4.1a), [29, 216, 217]. A hydrocarbon stapled peptide, SAH-MS1-18, has been developed to precisely bind and inhibit MCL-1 (Figure 4.1b) [102], and this stapled peptide exemplifies both the promise and obstacles related to this drug class. Although qualitatively cell permeable, the doses of SAH-MS1-18 required to induce apoptosis in cells with intact cellular membranes were 10,000-fold greater than those needed for mitochondrial depolarization in membrane-disrupted cells (i.e. EC50 of 5 μM vs. 450 pM) [102], suggesting that the large majority of peptide was unable to reach its intracellular target across an intact cell membrane (Figure 4.1c).

We sought to intracellularly deliver SAH-MS1-18 into DLBCL cells via B-cell surface receptor CD19 in an effort to capitalize on the peptide's potency and PPI specificity without altering the peptide itself. To do this, we used a highly stable polymersome nanoparticle (PSOM) made from the amphiphilic block-copolymer PEG-SS-PPS [181], to encapsulate SAH-MS1-18 ($\text{PSOM}_{\text{SAH-MS1-18}}$) (Figure 4.1d). CD19-binding F(ab) antibody fragments

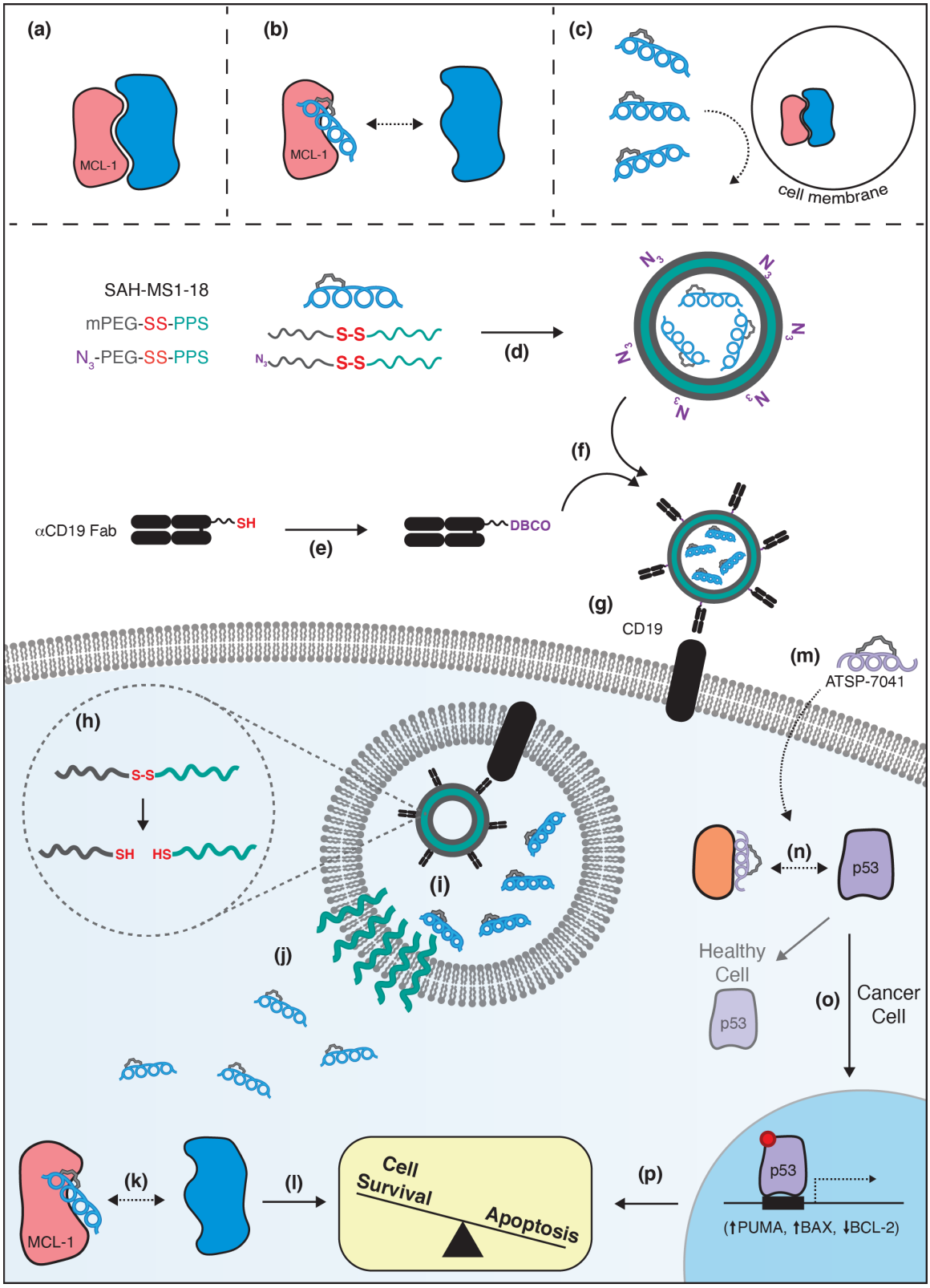

Figure 4.1: CD19-targeted polymersomes deliver SAH-MS1-18 into the cytoplasm of DLBCL cells to reactivate cell death and synergize with p53-reactivation. (Continued on the following page.)

Figure 4.1, continued: CD19-targeted polymersomes deliver SAH-MS1-18 into the cytoplasm of DLBCL cells to reactivate cell death and synergize with p53-reactivation. (a) Cancer cells rely on PPIs for inhibition of apoptosis (e.g. MCL-1 sequesters pro-apoptotic proteins). (b) Therapeutic stapled peptides (e.g. SAH-MS1-18) can potently and specifically block a disease-driving PPI. (c) Cellular uptake is a major obstacle to the clinical translation of therapeutic stapled peptides. (d) Stapled peptides are stably encapsulated in PEG-SS-PPS polymersomes. (e) Recombinant αCD19 Fabs are functionalized with a site-specific click chemistry handle. (f) The polymersomes are decorated with αCD19 Fabs and the targeted polymersomes (αCD19-PSOMs) purified. (g) αCD19-PSOMs bind CD19 on DLBCL cells and initiate endocytosis. (h) In the relatively reducing endosome, the disulfide of PEG-SS-PPS is reduced. (i) Polymersomes are disrupted and release their cargo. (j) The hydrophobic PPS block facilitates endosomal escape. (k) SAH-MS1-18 binds MCL-1 in the cytoplasm to release pro-apoptotic proteins and (l) reactivate apoptosis if the cell is sufficiently primed to die. (m) Treatment with the p53-reactivating stapled peptide ATSP-7041 (n) inhibits p53's inhibitory binding partners. (o) In cancer cells, phosphorylated/activated p53 translocates to the nucleus to upregulate transcription of pro-apoptotic proteins (e.g. PUMA, BAX) and downregulate transcription of anti-apoptotic proteins (e.g. BCL-2). (p) p53 transcriptional changes sensitize DLBCL to cell death by MCL-1 inhibition.

(αCD19 Fabs) were attached to the PSOM outer surface (αCD19-PSOM$_{\text{SAH-MS1-18}}$) to induce antigen-specific endocytosis in DLBCL (Figure 4.1e-g). Endosomal escape of SAH-MS1-18 was amplified through reduction of the disulfide bond within the block copolymer followed by intercalation of the hydrophobic PPS block within the endosomal membrane (Figure 4.1h-j) [181]. Treatment with αCD19-PSOM$_{\text{SAH-MS1-18}}$ greatly enhanced the intracellular accumulation and potency of SAH-MS1-18 compared to stapled peptide alone (Figure 4.1k,l).We further sought to "prime" DLBCL to undergo MCL-1 dependent apoptosis in vitro and in vivo through combination treatment with stapled peptide ATSP-7041, the preclinical precursor to ALRN-6924, to dissociate p53 from its inhibitory PPIs with HDM2/HDM4 and reactivate p53 (Figure 4.1m,n) [28]. Reactivation of p53 increased transcription of pro-apoptotic members of the BCL-2 family (e.g. PUMA, BAX) and decreased transcription of anti-apoptotic members of the BCL-2 family (e.g. BCL-2) (Figure 4.1o). ATSP-7041 treatment strongly synergized with αCD19-PSOM$_{\text{SAH-MS1-18}}$ to potently activate DLBCL killing (Figure 4.1p). Finally, we sought to translate this platform to the in vivo delivery of SAH-MS1-18 to unlock its in vivo therapeutic potential.

4.3 Results

4.3.1 PEG-SS-PPS Polymersomes are Stable in the Presence of Serum and Retain an Encapsulated Stapled Peptide

To assemble our targeted nanocarriers, we first synthesized the individual components. The PPS homopolymer was synthesized through a living, anionic, ring-opening polymerization (Figure 4.2a, Figure 4.3). Though some disulfides were present in the polymerization reactions, disulfide exchange proceeded significantly faster than monomer addition, and both unimeric thiol chains (right peak) and dimeric disulfide chains (left peak) underwent a quantitative, living polymerization (Figure 4.3a). After polymerization, the disulfide chains were reduced to free thiols (Figure 4.3b), capped with a pyridyl disulfide, and purified to generate PPS-PDS (compound 1; Figure 4.3c). Thiol-functionalized PEG polymers (mPEG-SH and N_3-PEG-SH) were then reacted with compound 1 to create mPEG-SS-PPS (compound 2; Figure 4.4) and N_3-PEG-SS-PPS (compound 3; Figure 4.5). Meanwhile, the therapeutic stapled peptide cargoes were synthesized using techniques previously described by others [79, 80], confirmed to be $> 95\%$ pure by LCMS (Figure 4.6), and quantified by amino acid analysis (AAA). These components were then all used to assemble polymersomes.

Two previously reported polymersome assembly methods were compared, and both produced indistinguishable polymersomes (Figure 4.2b-d). In the first method, thin-film assembly, the polymer was deposited on the walls of a glass vial in a thin film via evaporation from an organic solvent (DCM). PBS was added to hydrate the film during mixing for several days to gradually form polymersomes. In the second method, flash nanoprecipitation (FNP), a solvent stream (i.e. polymer in THF) and anti-solvent stream (i.e. PBS) were rapidly impinged against each other and diluted into a PBS reservoir to form polymersomes. FNP assembly has previously been reported for this block copolymer as a rapid and scalable way to produce polymersomes [190, 191]. We made a confined impingement jets with dilution (CIJ-D) device using a design and dimensions published by Han et al. [277], except instead of

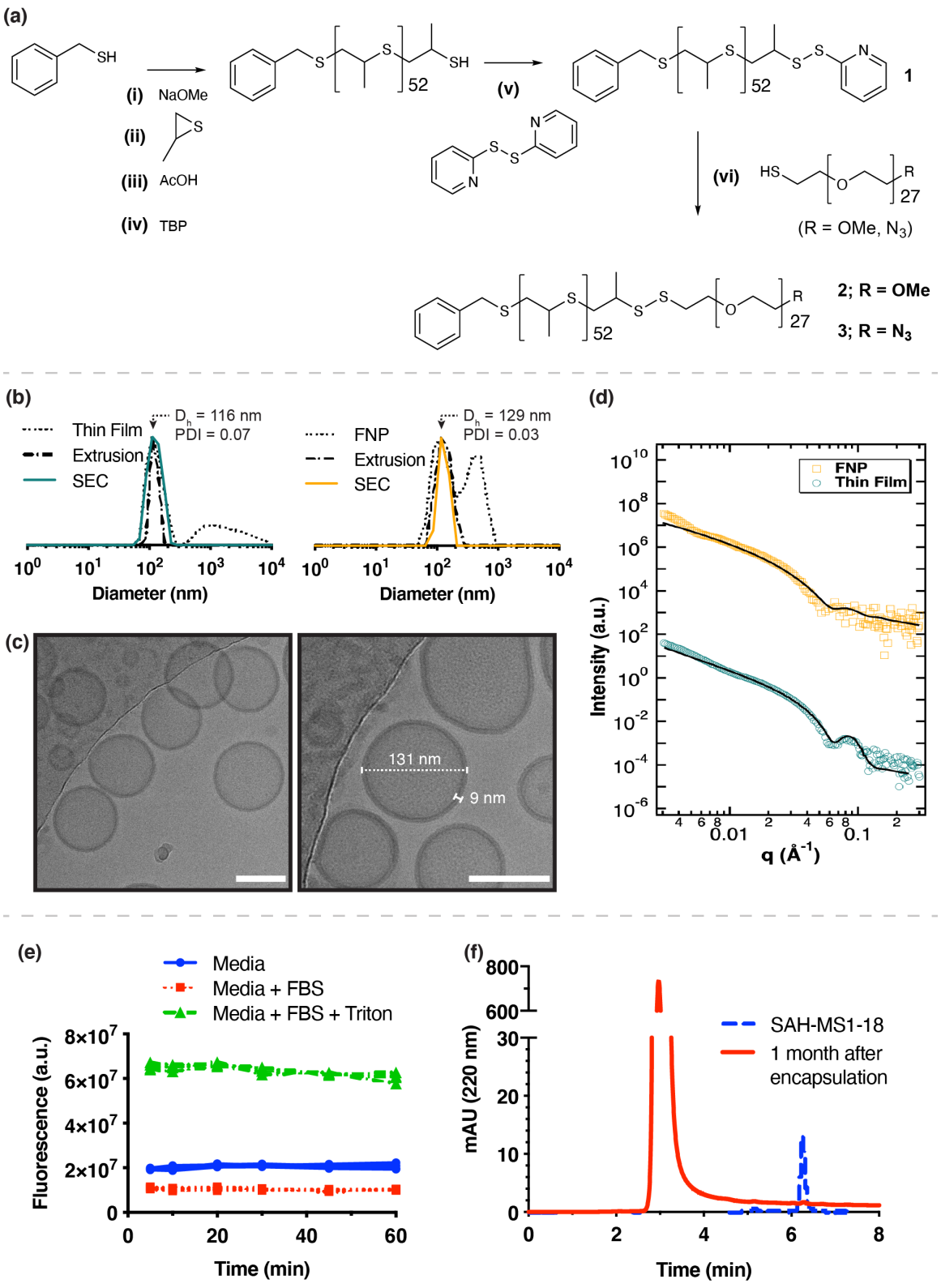

Figure 4.2: PEG-SS-PPS polymersome assembly, characterization, and stability. (Continued on the following page.)

Figure 4.2, continued: PEG-SS-PPS polymersome assembly, characterization, and stability. (a) The PPS polymer block was synthesized by living, anionic, ring-opening polymerization (i – iii) followed by disulfide reduction (iv) and capping with a pyridyl disulfide functional group (v) to generate PPS-PDS (compound 1). PPS-PDS was then reacted with thiolated PEG polymers (vi) to generate PEG-SS-PPS block copolymers with methoxy (OMe; compound 2) or azide (N_3; compound 3) end groups. PEG-SS-PPS block copolymers were then assembled into polymersomes. (b) DLS measurements of empty polymersomes formed by a thin film method ("Thin Film") or by flash nanoprecipitation ("FNP"), followed by extrusion through a 100 nm pore-size membrane ("Extrusion") and desalting into PBS ("SEC"). DLS measurements were repeated until the residuals of the average correlation function fit were negligible (10-120 times). Plotted are the intensity-scaled size distribution from the Regularization fit method. D_h and PDI are given for the SEC-purified samples. (c) Cryo-EM images confirm the polymersomes are uniform, hollow spheres with diameters and bilayer thicknesses that correspond to DLS and SAXS measurements. Scale bars are 100 nm. (d) SAXS data fit well to hollow sphere structures at an ensemble level for both thin-film- and flash-nanoprecipitation-formed polymersomes. Intensity (a.u.) values are shown vertically shifted to prevent overlap of the plots. (e) Polymersomes encapsulating a self-quenching calcein solution were diluted into various solutions, and fluorescence dequenching due to polymersome disruption was monitored for 1 hour at 37 °C. Data plotted are individual quadruplicates, each background subtracted against samples in which an equivalent volume of PBS-blank was added instead of polymersomes. (f) Aqueous SEC HPLC traces of free SAH-MS1-18 peptide (blue, dashed) compared to a polymersome solution encapsulating an equimolar amount of SAH-MS1-18 stored for one month at 4 °C in PBS (red, solid).

drilling channels out of a solid block of material, we used a computer aided design (CAD) file to 3D print the device with patent channels (Figure 4.7). Both thin-film- and FNP-assembly produced a primary population of polymersomes approximately 120 nm in diameter, but larger aggregates were also present in each case (Figure 4.2b). All samples were therefore extruded through a 100 nm pore-size membrane to create monodisperse polymersomes and then purified by either SEC or tangential-flow filtration (TFF) diafiltration. Cryo-EM was used to visually confirm that the assemblies were indeed polymersomes, as opposed to other structures that have been reported from these block copolymers at other block ratios (Figure 4.2c) [190, 278]. To further confirm their vesicular structure at an ensemble level, Small Angle X-ray Scattering (SAXS) data were fitted using a spherical vesicle model, and the nanoparticles from both assembly methods were well-represented as spherical, hollow vesicles with diameter and bilayer thickness corresponding to those seen in cryo-EM (Figure

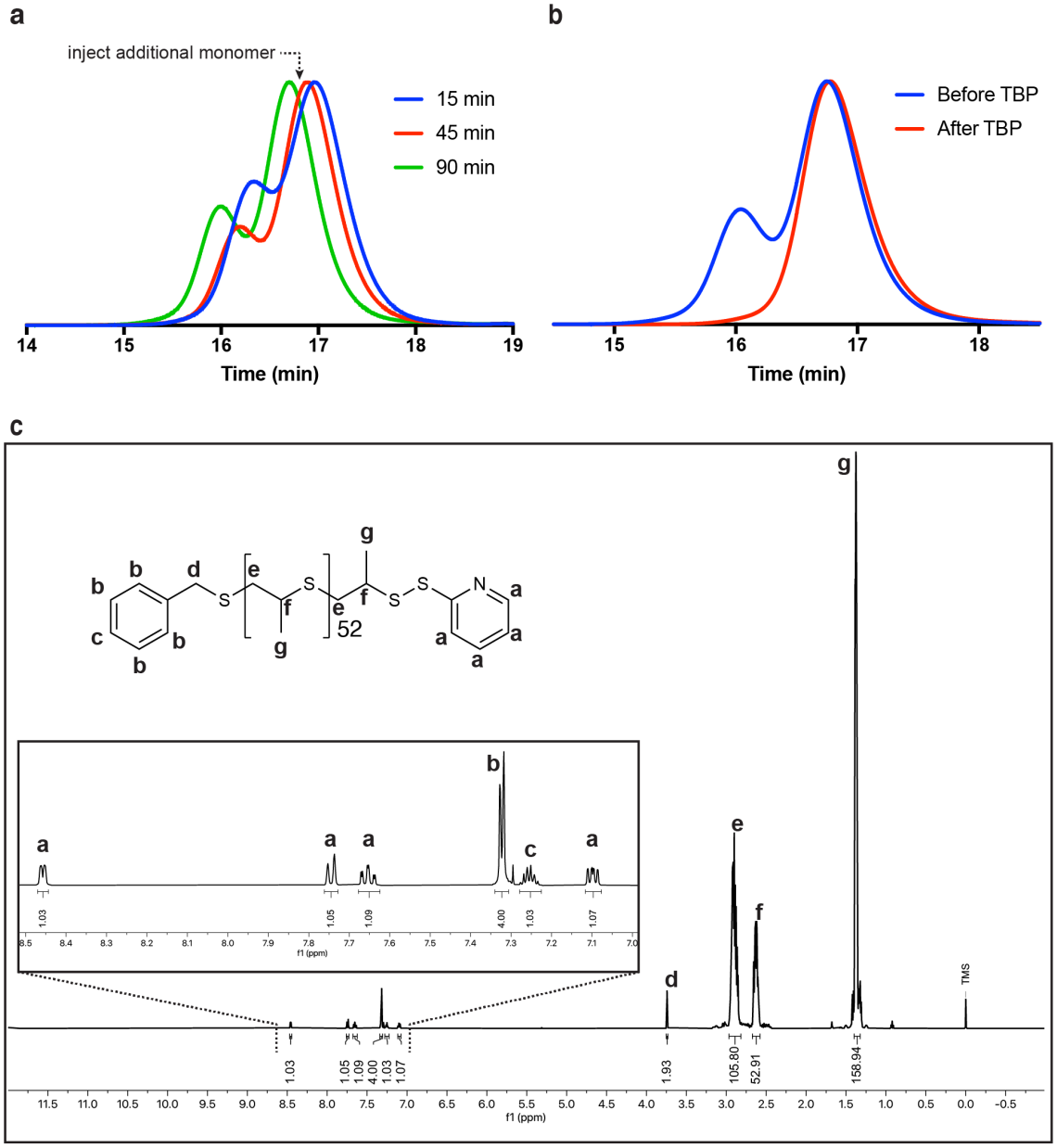

Figure 4.3: Characterization of compound 1 (PPS-PDS). (a) Gel permeation chromatography (GPC) refractive index (RI) traces of PPS polymerization kinetics over time. From right to left, aliquots were taken at 15, 45, and 90 min, quenched with acetic anhydride, precipitated, and analyzed by GPC. Additional monomer was injected immediately after 45 min, and both the unimeric thiol peak (PPS-SH) and dimeric disulfide peak (PPS-SS-PPS) continued growing, suggesting that disulfide exchange in the reaction is fast enough that disulfides did not significantly inhibit the polymerization. (b) SEC RI traces of a completed PPS polymerization reaction with and without using tributylphosphine (TBP) to reduce disulfide chains (PPS-SS-PPS) to free thiol chains (PPS-SH). The dispersity of reduced PPS-SH was 1.17. (c) 1H NMR of PPS-PDS (compound 1) in $CDCl_3$. The density of pure PPS-PDS was measured to be 1.169 g/mL.

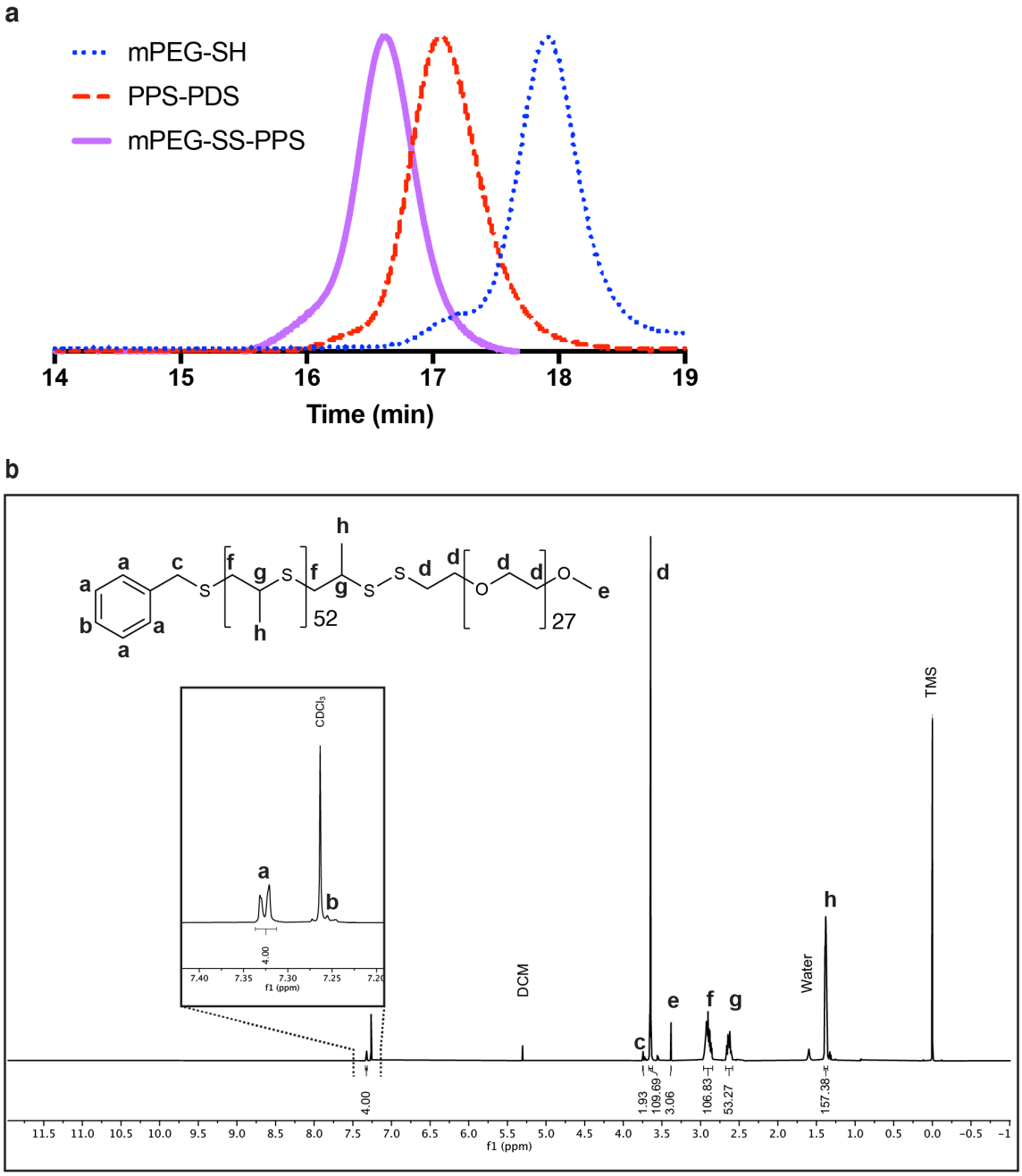

Figure 4.4: Characterization of compound 2 (mPEG-SS-PPS). (a) GPC RI trace of mPEG-SS-PPS (compound 2). Dispersity = 1.08, with no contamination from either polymer block. (b) 1H NMR of mPEG-SS-PPS (compound 2) in $CDCl_3$. One of the benzylic protons overlapped with the $CDCl_3$ peak and could not be integrated.

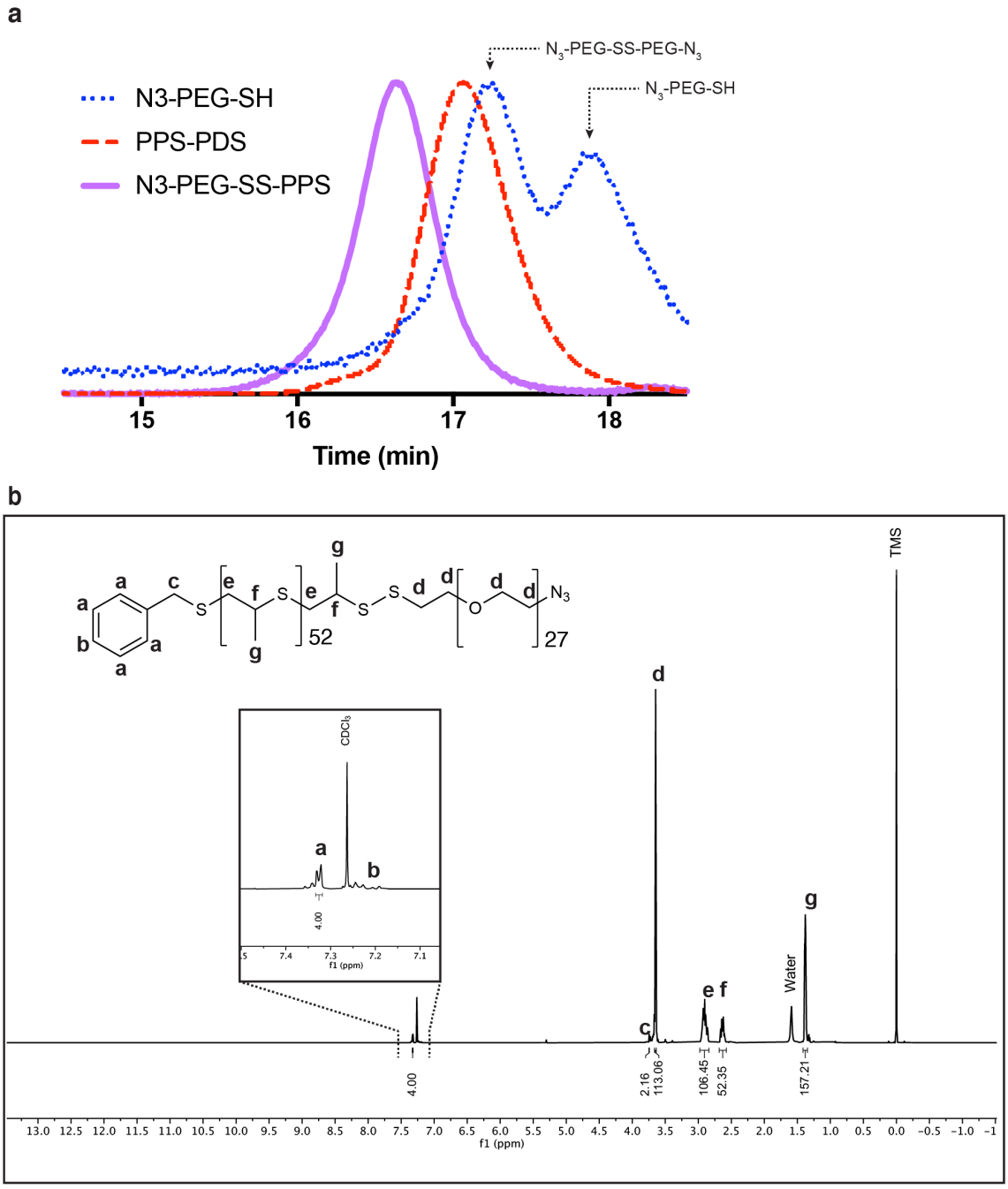

Figure 4.5: Characterization of compound 3 (N_3-PEG-SS-PPS). (a) GPC RI trace of N_3-PEG-SS-PPS (compound 3). Dispersity = 1.06, with no contamination from either polymer block. The commercially-available N_3-PEG-SH had a large percentage of disulfide-dimerized chains (N_3-PEG-SS-PEG-N3). The disulfide chains were considered to be inert bystanders in the reaction and would be removed during later purification steps (namely MeOH extraction). (b) 1H NMR of N_3-PEG-SS-PPS (compound 3) in $CDCl_3$. One of the benzylic protons overlapped with the $CDCl_3$ peak and could not be integrated.

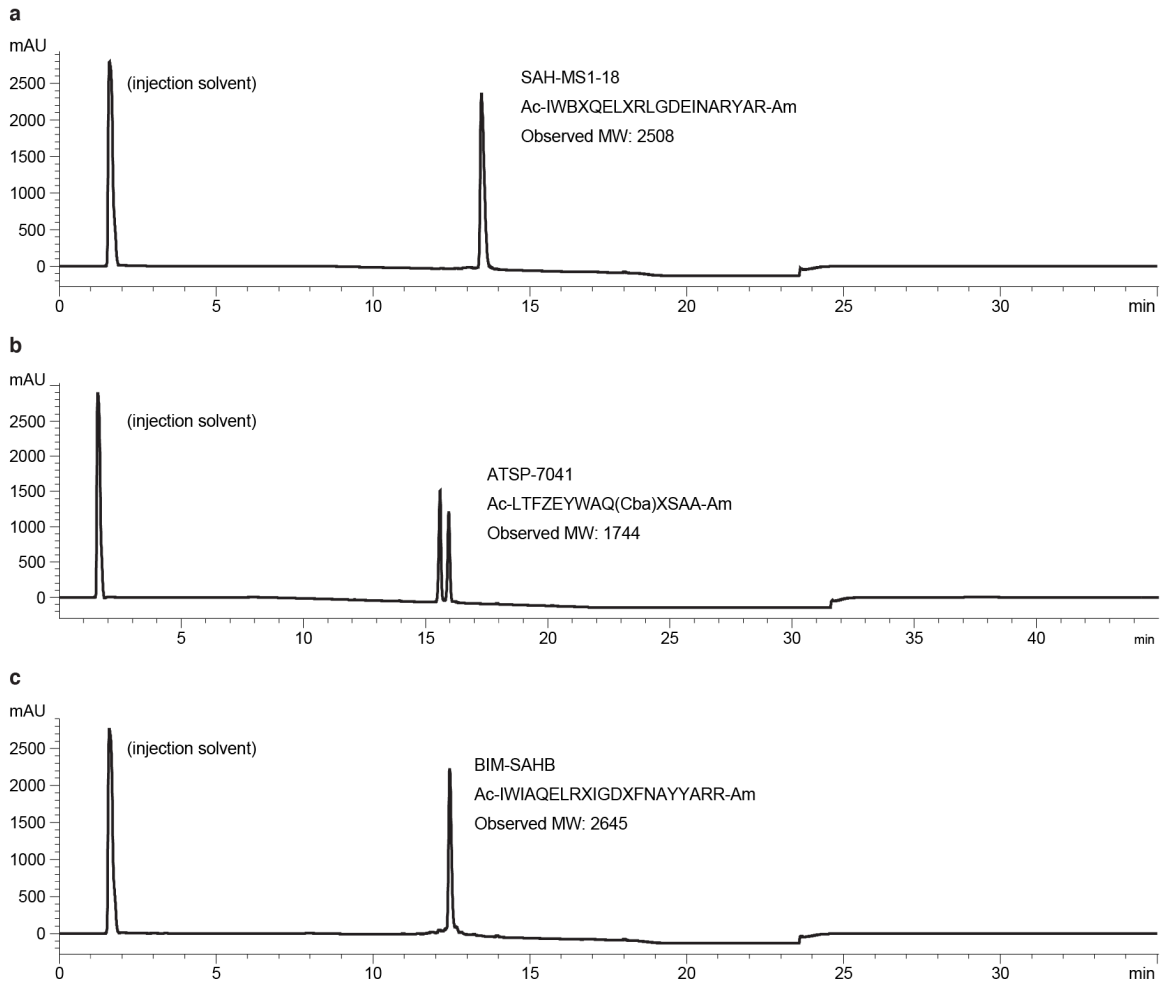

Figure 4.6: LCMS analysis of therapeutic peptides. After purification, the purity and identity of all peptides was confirmed by LCMS analysis. Representative chromatograms of UV absorbance at 220 nm are shown for (a) SAH-MS1-18, (b) ATSP-7041, and (c) BIM-SAHB. Peptides diluted from DMSO stock solutions show a DMSO solvent injection absorbance. Stapled peptides with (i, i+7) staples, such as ATSP-7041, often have two isomers of the staple, as previously described by others, which elute as separate chromatographic peaks after stapling but have identical mass spectra. Ac = acetylated N-terminus. Am = amide C-terminus. B = norleucine. X = S5. Z = R8. Cba = β-cyclobutyl-L-alanine.

4.2d). Of the two assembly methods, the FNP method was more easily scalable and allowed for rapid encapsulation of our therapeutic cargoes, so FNP became our method of choice for assembling polymersomes.

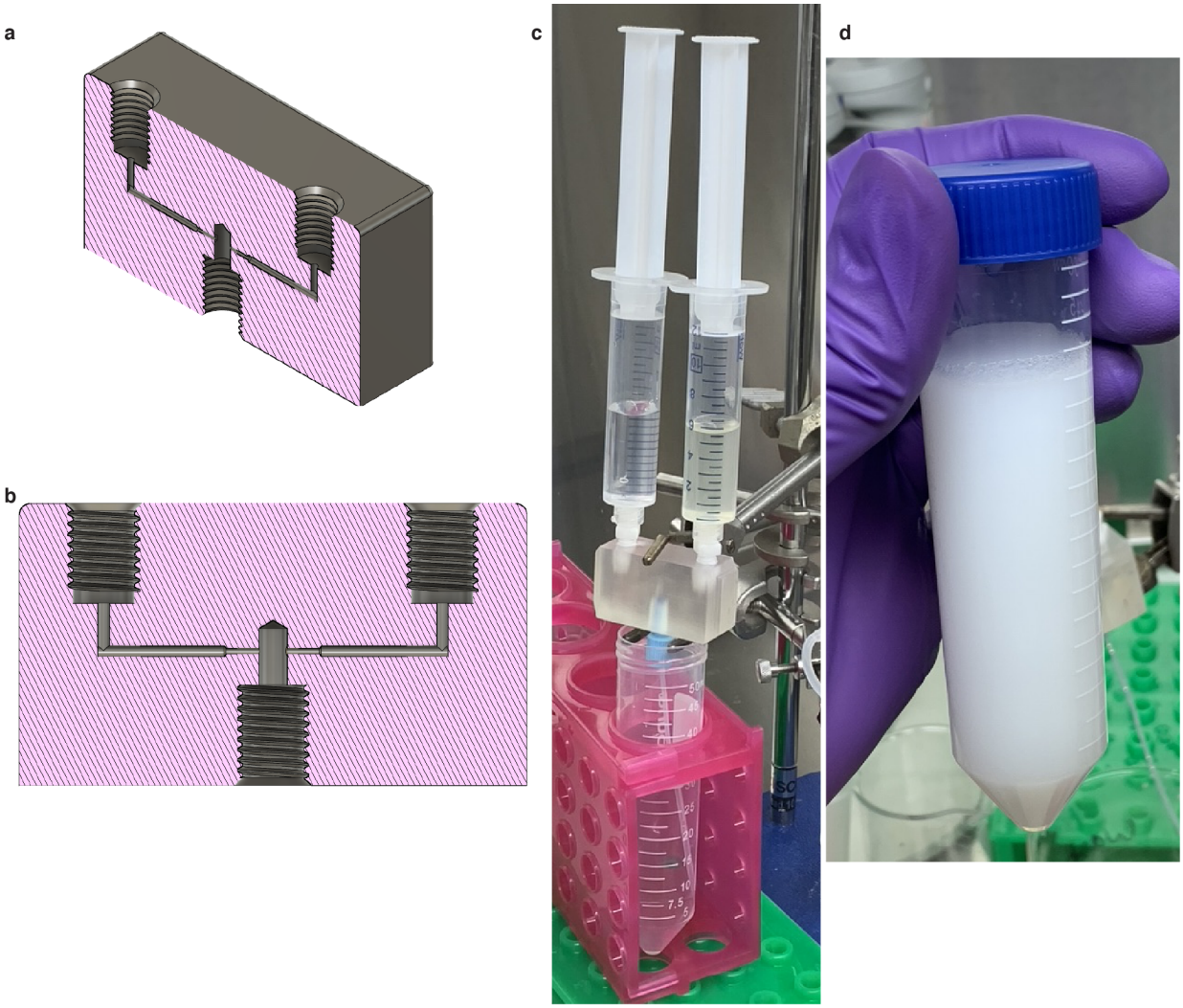

Figure 4.7: Flash nanoprecipitation using a 3D-printed confined impingement jets with dilution (CIJ-D) device. (a,b) Cut-away views of our 3D-printed CAD design using the same dimensions published by Han et al. [277]. (c) Syringes are attached to the CIJ-D device inlets via threaded luer-lock adapters, and an outlet tube is placed into a PBS dilution reservoir. After rapid mixing, an air cushion in the syringes clears the device and mixes the dilution-reservoir with air bubbles. (d) The resulting polymersome solution is opaque, even when the polymersomes are smaller than the wavelength of light, due to their very high concentration.

While most polymersome formulations we have made yielded polymersome formulations

of about the same size (i.e. 120-130 nm), some drug encapsulations have produced other structures (Figure 4.8), presumably micelles in some cases and smaller polymersomes in other cases. SAH-MS1-18, when encapsulated in polymersomes using the FNP method, consistently yielded slightly smaller polymersomes with hydrodynamic diameters of 65-90 nm before extrusion (Figure 4.8a). When S63845 or ATSP-7041 were encapsulated with high drug concentrations, much smaller structures formed (Figure 4.8b,c), and for the S63845 sample, cryo-EM confirmed these were micelles. For both drugs, when the amount of drug relative to polymer was decreased, more typical polymersomes were formed. Of note, using the inverse direct dissolution method previously described by O'Neil et al. in the Hubbell group [189], S63845 and ATSP-7041 were both highly soluble in a pipettable polymer melt made from mixing PEG-SS-PPS and PEG(500)DME, so presumably these drugs have favorable interactions with the PEG-SS-PPS block copolymer during drug encapsulations. In the patent on PEG-PPS block copolymers, the authors mention the occasional formation of metastable micellar aggregates using polymer block length ratios that should normally form polymersomes [279]. Interestingly, they also note that heating of these micelles can help them overcome the kinetic trap to reach a more favorable thermodynamic state as very small polymersomes, similar in size to what we see for SAH-MS1-18 encapsulations (Figure 4.8a) [279]. It seems that drugs that favorably interact with PEG-PPS, including two hydrocarbon stapled peptides, can influence the structure of polymersomes formed in the presence of very high concentrations of drug relative to polymer.

For nanocarriers self-assembled from amphiphilic building blocks, a primary concern is their stability in the presence of serum proteins. Therefore, we first tested the stability of our PEG-SS-PPS polymersomes in the presence of fetal bovine serum (FBS; Figure 4.2e). Polymersomes encapsulating a hydrophilic dye, calcein, at self-quenching concentrations, were used to detect polymersome disruption via fluorescence dequenching. When the polymersome stock solution was diluted into cell culture media and incubated at 37 °C for 1 hour, there was no detectable polymersome disruption (Figure 4.2e, Media). When the polymersomes

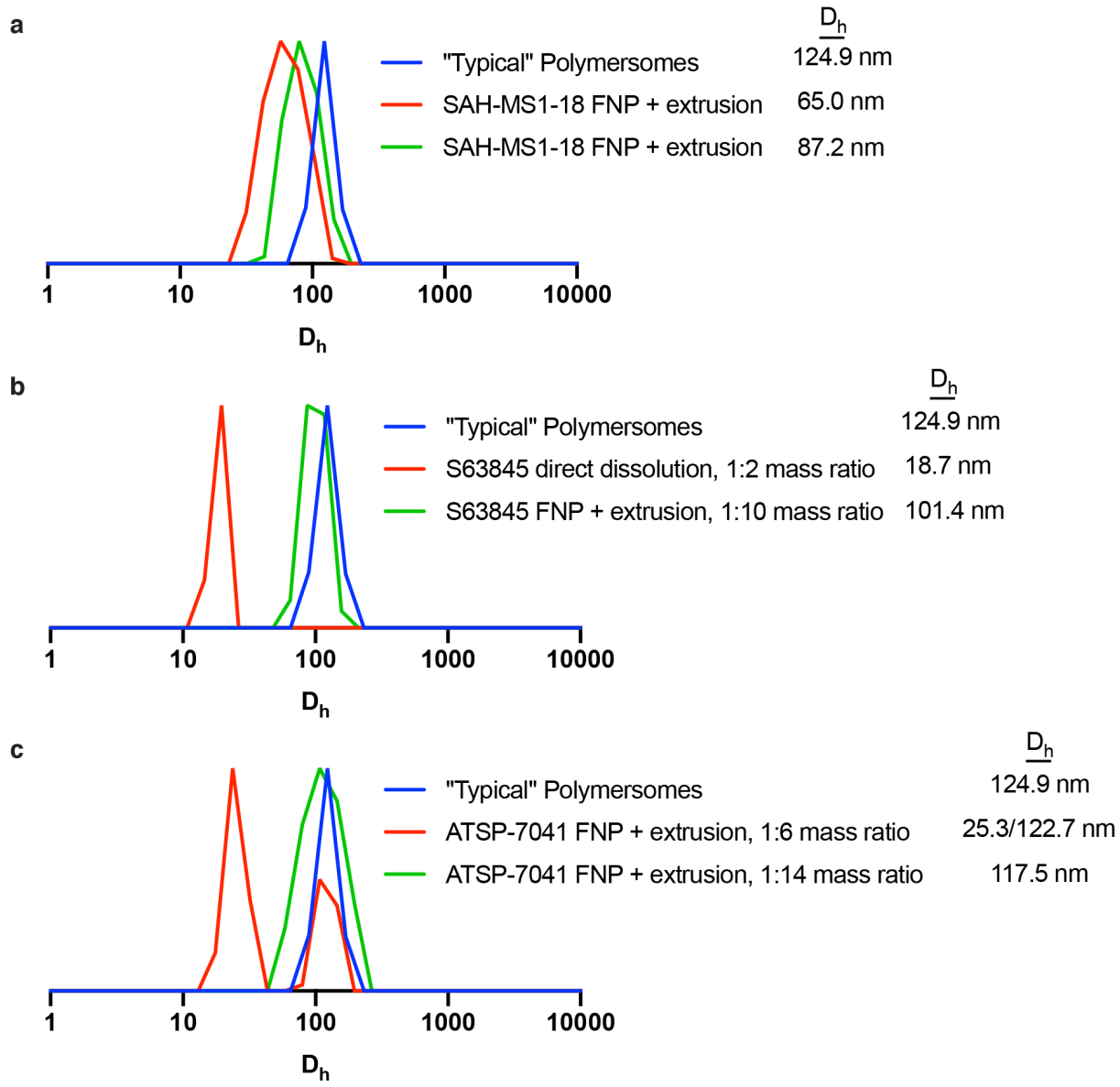

Figure 4.8: Encapsulation of some drugs affects polymersome assembly. Polymersomes made from PEG-SS-PPS block copolymers typically have a primary population with D_h of 120 - 130 nm, and a 100 nm extrusion step breaks up any larger aggregates to that same size. (a) SAH-MS1-18 encapsulation at peptide:polymer mass ratios of 1:4 repeatedly produced polymersomes that are slightly smaller than our typical polymersomes. Two representative encapsulations are shown. (b) S63845 encapsulation at high mass ratios produced micelles (as confirmed by cryo-EM), while a lower mass loading encapsulation via FNP produced typical polymersomes. (c) ATSP-7041 at high mass loading ratios produced a mixed population of (presumably) micelles and polymersomes, with mostly micelles. Decreasing the mass loading ratio allowed the formation of normal polymersomes. All DLS data are intensity-scaled size distributions with D_h calculated from the Regularization fit.

were diluted into media with 10% FBS, the fluorescence still remained constant, indicating no polymersome disruption due to serum proteins (Figure 4.2e, Media + FBS). As a positive control, a detergent (Triton X-100) was added to completely disrupt the polymersomes and release calcein, and this caused a large increase in fluorescence intensity (Figure 4.2e, Media + FBS + Triton). These data indicate that PEG-SS-PPS polymersomes are highly stable in the presence of serum proteins, in agreement with the stability generally associated with polymersomes as a class of nanoparticles.

We next tested whether or not SAH-MS1-18, which is relatively amphiphilic, would diffuse out of the polymersomes during storage. Polymersomes encapsulating SAH-MS1-18 were stored for 1 month at 4 °C in PBS, then the sample was analyzed by aqueous SEC HPLC to detect any peptide released (Figure 4.2f). No detectable amount of free peptide had leaked out of the polymersomes during 1 month of storage, highlighting the stability of stapled peptide encapsulation and compatibility with long-term storage in PBS at 4 °C.

Notably, polymersome encapuslation of SAH-MS1-18 also greatly enhanced the aqueous solubility of the peptide, which is a crucial consideration for intravenous injection of sufficient doses. On larger scales, $PSOM_{SAH\text{-}MS1\text{-}18}$ was concentrated by TFF such that the average SAH-MS1-18 concentration in the solution was in the millimolar (mM) range (e.g. 2.7 mM in the overall solution, but all locally concentrated inside polymersomes), and no aggregation was observed by eye or DLS. This is more than 10 times the solubility limit of the peptide alone in PBS.

4.3.2 αCD19 Polymersomes Deliver Cargo into DLBCL Cells Specifically via CD19

Next, we sought to target these polymersomes to DLBCL cells and optimize their cellular uptake. To do so, we designed a Fab specific for human CD19 (αCD19) and added a cysteine linker (αCD19-cys) for site-specific conjugation to polymersomes. The variable regions of the αCD19-cys Fab were designed from the HD37 mouse-anti-human-CD19 IgG [280, 281],

with constant regions from mouse IgG consensus sequences (Figure 4.9). The cysteine linker was added at the C-terminus of the heavy chain, opposite the antigen-binding face, with a short, flexible, hydrophilic spacer and a terminal cysteine (Figure 4.10a). To generate non-binding control Fabs, the variable regions were grafted from a published sequence targeting the xenoantigen Outer surface protein A (OspA) of *Borrelia burgdorferi* [282, 283], while the constant regions remained unchanged (Figure 4.9). The four Fabs (αCD19, αCD19-cys, αOspA, and αOspA-cys) were cloned in *DH5α*, expressed in HEK293T cells, and purified by Protein G affinity chromatography (Figure 4.10b). We then tested the antigen-specific binding of αCD19-cys to CD19+ DLBCL cells, and it bound specifically, with no apparent influence from the encoded cysteine linker (Figure 4.10c).

We next functionalized the Fabs' cysteine linker with a DBCO handle for click-chemistry attachment to the surface of the polymersomes (Figure 4.11a). When the Fabs were initially purified, the thiol on the cysteine linker was unreactive. Others have shown that solvent-accessible cysteines on recombinant proteins secreted from mammalian cells are initially disulfide-bonded with small molecule thiols, such as cysteine and glutathione [284]. By titrating the amount of reducing agent, TCEP, we were able to specifically reduce the solvent-accessible cysteine linker and convert it to a DBCO handle without disrupting internal disulfides (Figure 4.11b,c).

Interestingly, the amount of TCEP that reduced only the terminal thiol was a range of values, rather than a single point. The range from 0.5 - 1 equivalents of TCEP was a stable range to reduce precisely 1 equivalent of reactive thiol on the Fabs (Figure 4.11b,c). We hypothesize this range may be explained by the relative reducing potentials of the thiols in the system. One TCEP molecule will generate one Fab-thiol and one small molecule thiol, and that liberated small molecule thiol, presumably cysteine or glutathione, appears to favorably reduce the terminal thiol on a second Fab. Therefore, 0.5 equivalents of TCEP generated 1 equivalent of Fab-thiol and, we hypothesize, 0.5 equivalents of a small molecule disulfide. The next 0.5 equivalents of TCEP (0.5 – 1 equivalents total) are then presumably consumed

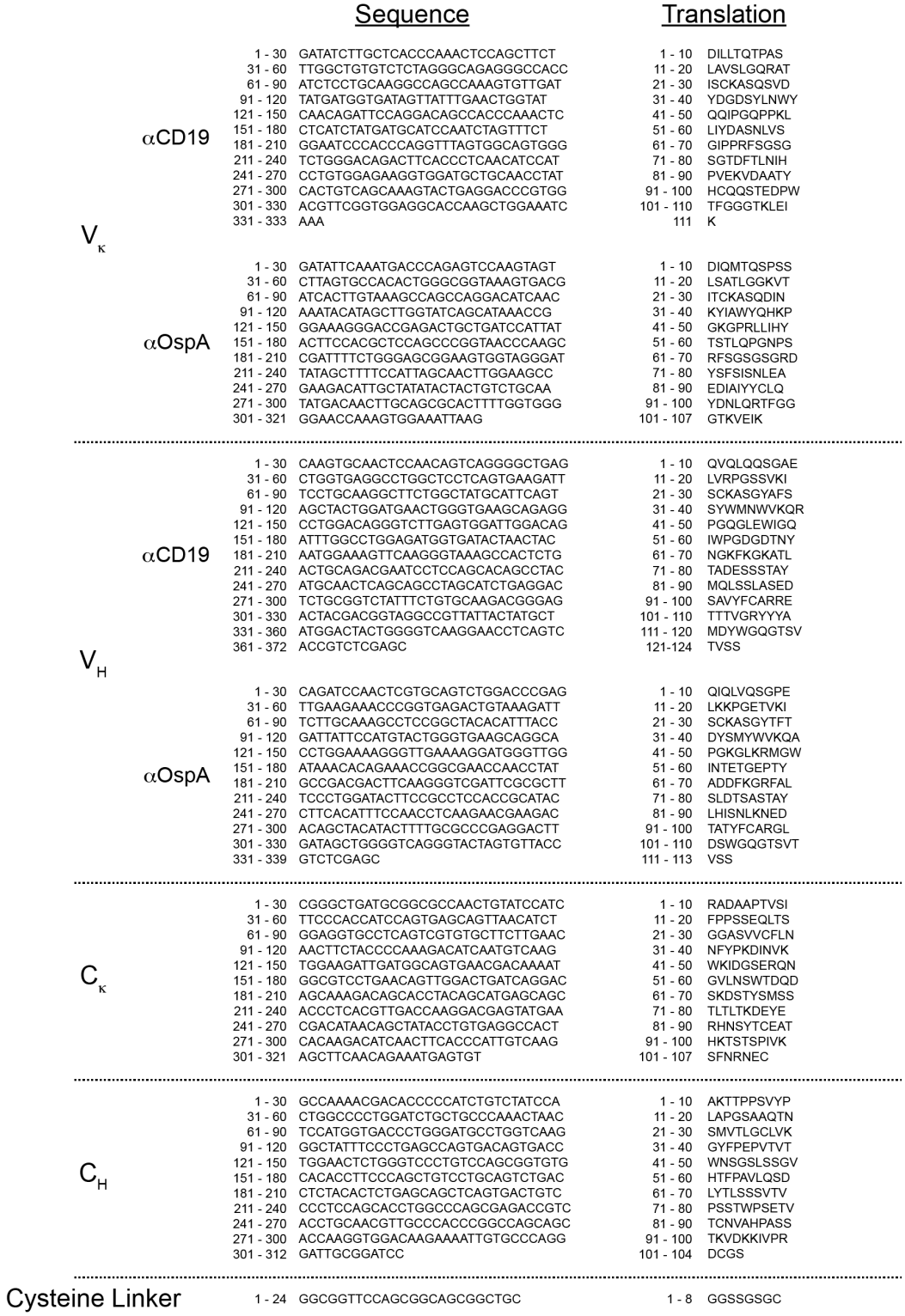

Figure 4.9: DNA coding sequences of engineered Fabs and their protein translations. (Continued on the following page.)

Figure 4.9, continued: DNA coding sequences of engineered Fabs and their protein translations. Fabs were designed with variable domains (V_κ and V_H) for binding to either human CD19 (αCD19) or an irrelevant xenoantigen (αOspA). All Fabs shared the same constant domains ($C\kappa$ and C_H). For αCD19-cys and αOspA-cys, the cysteine linker sequence was added to the C-terminal end of the C_H domain.

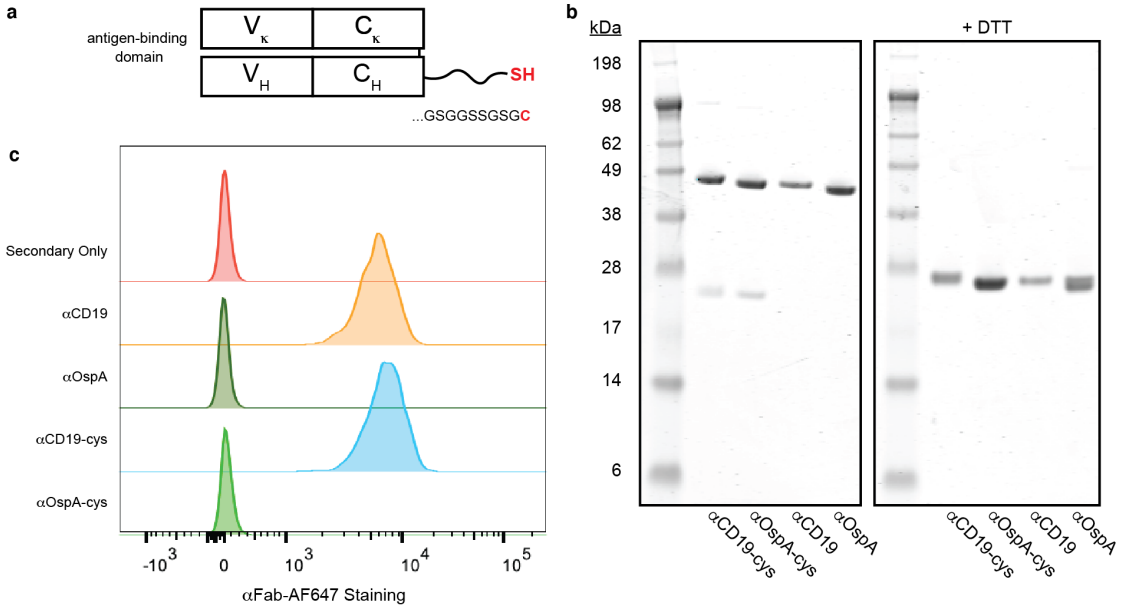

Figure 4.10: Expression and binding validation of Fabs. (a) Fabs were designed using previously published sequences (Figure 4.9) from antibodies that bind either human CD19 (αCD19) or an irrelevant xenoantigen (αOspA). To enable site-specific conjugation to polymersomes, a flexible cysteine linker was encoded at the C-terminus of the heavy chain of each Fab to generate αCD19-cys and αOspA-cys. (b) Coomassie staining of purified Fabs separated on an SDS-PAGE gel. Each Fab appears pure at the expected molecular weights, and addition of DTT in the loading buffer reduces the interchain disulfide to generate polypeptides (heavy chain and light chain) that overlap at their expected molecular weights. (c) Flow cytometry measurement of Fab binding to a CD19+ DLBCL cell line, SU-DHL-5. Cells were stained with the indicated Fab, then with an AF647-labeled αFab secondary antibody. αCD19 Fabs bind CD19+ DLBCL with or without the cysteine linker, and the control (αOspA) Fabs do not.

in reducing the small molecule disulfides and don't further reduce internal disulfides in the Fab. This window, then, from 0.5 – 1 equivalents of TCEP per Fab, was a safe range to precisely functionalize the Fabs with a DBCO click chemistry handle and reliably produced DBCO:Fab ratios of 1. Importantly, these are equivalents with respect to unimeric (not disulfide dimeric) intact (not free heavy or light chain) Fab, as determined by UV absorbance

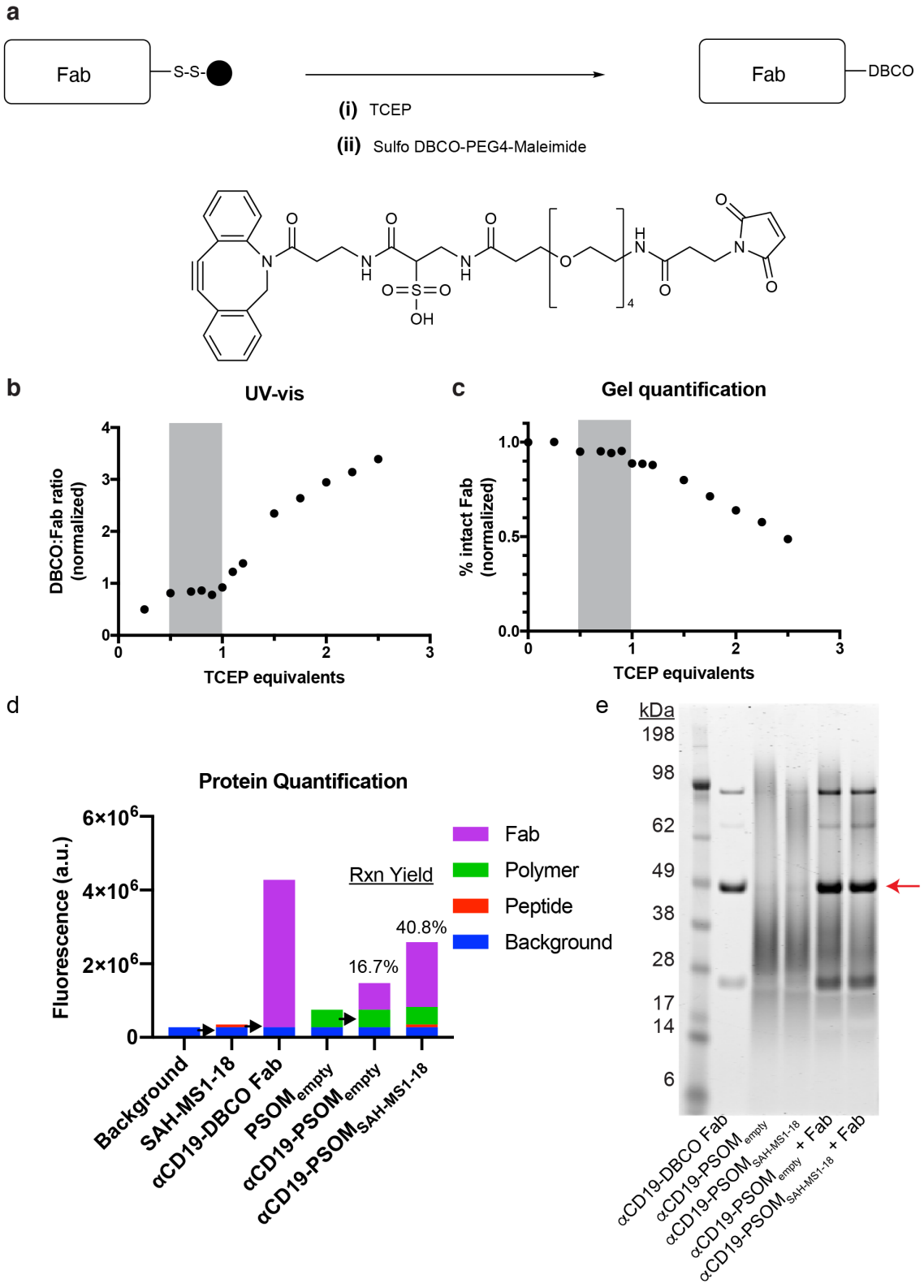

Figure 4.11: Fab functionalization for attachment to polymersomes. (Continued on the following page.)

Figure 4.11, continued: Fab functionalization for attachment to polymersomes. (a) Disulfide-capped Fabs were (i) reduced with TCEP (90 minutes at 37 °C), then (ii) immediately, without workup, reacted with a 100-fold excess of the heterobifunctional linker, Sulfo DBCO-PEG4-Maleimide, for 1 hour at room temperature. Excess linker was then removed by extensive diafiltration (10 kDa MWCO Amicon). (b,c) A range of TCEP stoichiometries was used to determine the optimal amount of TCEP for reducing the cysteine linker without disrupting internal disulfides. (b) The DBCO:Fab ratio was determined by UV-vis absorbance (see Section 4.5.11), and (c) the percent of intact Fab was determined by quantification of a Coomassie-stained SDS-PAGE gel. The y-values were normalized to the ratio of Fab in its intact, unimeric form before the reaction (in this case, 80%), as measured by SDS-PAGE gel quantification. From these data, we determined the reliable range (0.5 - 1 equivalents) of TCEP to reduce only the terminal cysteine linker and functionalize it with DBCO. Using this optimized DBCO-functionalization protocol, we generated αCD19-DBCO and αOspA-DBCO with DBCO:Fab ratios reliably $\sim$1. (d,e) To attach Fabs to the polymersomes, polymersomes were assembled with 5% N_3-PEG-SS-PPS and 95% mPEG-SS-PPS. Fab-DBCO was added to react overnight, and then any non-conjugated Fab was removed by size (SEC or TFF diafiltration). In this example, enough DBCO was added to theoretically functionalize 0.1% of the polymer chains on the external polymersome surface (or 0.05% of the total polymer chains in the sample). (d) After purification, the CBQCA protein quantification assay was used to detect Fab retained in the final samples, accounting for background signal contributions from blank, peptide-only, and empty polymersome samples. The polymer and peptide concentrations of every sample were known from GPC and LCMS measurements, respectively, to calculate their relative background contributions. From this, the fluorescence contribution from Fab was calculated (purple bars), and the unknown Fab concentrations were calculated by comparing to the Fab-only control sample. (e) To confirm the Fab remaining in the samples (detected in (d)) was attached to the polymersomes and not just contaminating, non-conjugated Fab, a Coomassie-stained SDS-PAGE gel was used to confirm the disappearance of the Fab-DBCO band. Importantly, this band disappearance is due to covalent, rather than non-covalent, Fab:polymer interaction, because spiking more Fab (the same amount as the Fab-only lane) into the polymersome samples restored the Fab band. Gel samples were loaded such that, assuming 100% Fab conjugation, the Fab bands would be identical. All gel samples were prepared in the presence of sodium azide (to quench DBCO:azide reactions) and NEM (to quench thiols and disulfide shuffling). The broad polymer smearing is due to the presence of sodium azide.

at 280 nm for total protein concentration combined with Coomassie-stained SDS-PAGE gel quantification for the relative percentage of each species. TCEP was chosen as the reducing agent due to its powerful reducing potential nearly independent of pH and its relative non-reactivity with maleimides, which allows the reduced-Fab TCEP mixture to be directly reacted with the maleimide-DBCO linker without any workup and chance for re-oxidation.

The DBCO-functionalized Fabs were then "clicked" onto the polymersomes. We gen-

erated polymersome treatments with a range of Fab densities on the surface by using the N_3 on the polymersome surface as the excess functional group (5% N_3-PEG-SS-PPS, 95% mPEG-SS-PPS) and adding different molar amounts of Fab-DBCO into aliquots from a common polymersome stock solution (Figure 4.11c). Using reaction stoichiometries targeting 0.1%, 0.5%, and 1% polymer functionalization, we generated low (+), medium (++), and high (+++) Fab densities. The resulting Fab-polymersomes were purified by size to remove any non-conjugated Fab. The amount of Fab attached to the polymersome surface could be quantified using the CBQCA protein quantification assay according to the manufacturer's instructions (representative example in Figure 4.11d), and the successful removal of non-conjugated Fab could be verified using a Coomassie-stained SDS-PAGE gel (Figure 4.11e).

At this point, knowing the aggregation number of these polymersomes would be useful to have an understanding of roughly how many Fabs are attached to each particle and how they are spaced. The aggregation number could be precisely measured using light scattering experiments, but we already had enough relevant data to make a rough estimation from two different techniques.

First, using the density of PPS and volume of the the PPS layer of the polymersome, we can roughly estimate how many chains there are per particle if we assume the PPS layer has a density equivalent to bulk PPS. This is likely an upper-limit estimation of the number of chains per particle. From our large scale synthesis of PPS-PDS, we measured the density of the pure bulk homopolymer as 1.169 g/mL. For a polymersome with roughly 130 nm diameter and a 9 nm PPS layer thickness from cryo-EM, the volume of the PPS layer can be roughly estimated as Volume $= \frac{4}{3}\pi(r \text{ nm})^3 - \frac{4}{3}\pi(r - \frac{9}{2} \text{ nm})^3$ with $r = \frac{130}{2} = 65$ nm, or Volume $= 222,759 \text{ nm}^3$. Then with the volume of the PPS layer (222,759 nm^3), the density of bulk PPS (1.169 g/mL), and the average molar mass of PPS_{53} (3181 g/mol), we can estimate the number of chains per particle as Volume $\times$ Density $\div$ Molar Mass $= 49,281$ polymers per particle.

Meanwhile, we had done a simple Nanoparticle Tracking Analysis (NTA) measurement to measure the concentration of nanoparticles (nanoparticles/mL) for a sample with a known concentration of polymer (mg/mL) with a known molar mass (5,324 g/mol for $mPEG_{28}$-SS-PPS_{53}). From this, we can estimate $15,632$ polymers per particle.

While neither of these methods are as accurate as measuring aggregation number by light scattering, they both give us a rough estimation that there are on the order of magnitude of 15,632 - 49,281 polymers per polymersome for a 130 nm D_h polymersome made of PEG_{28}-SS-PPS_{53}. Functionalizing 1% of the polymers in the outer bilayer (assuming half, and no flipping of the N_3 groups across the bilayer) means adding roughly 78 - 246 Fabs per particle, and functionalizing 0.1% would mean roughly 8 - 25 Fabs per particle, assuming 100% reaction efficiency. Our reaction efficiencies were typically 10 - 40% and seemed to vary based on the concentration of the samples during the reaction.

Theoretically, the density of αCD19 Fab on the polymersome surface could greatly influence cellular uptake [285], so we measured uptake by DLBCL cells at multiple Fab densities. To measure uptake, we encapsulated a self-quenching solution of the hydrophilic fluorophore calcein into polymersomes and attached either αCD19 Fab (αCD19-$PSOM_{calcein}$) or an irrelevant Fab (αOspA-$PSOM_{calcein}$) to the surface at varying densities (high (+++), medium (++), and low (+)). We treated four DLBCL cell lines (SU-DHL-5, OCI-Ly1, OCI-Ly3, and OCI-Ly8) with the fluorescence-quenched polymersomes and measured uptake by flow cytometry. In each cell line, we observed antigen-specific, dose-dependent, and time-dependent accumulation of calcein fluorescence (Figure 4.12a). Even OCI-Ly3, which expresses low but non-zero levels of CD19 (Figure 4.12), exhibited low levels of antigen-specific uptake (Figure 4.13a,b). Regardless of cell line, the αCD19-$PSOM_{calcein}$ with the lowest Fab densities (+) were endocytosed to the greatest degree. As further evidence of active targeting, if the same treatments were performed without the final purification step to remove non-conjugated Fabs from the samples, antigen-specific uptake was almost completely blocked by the contaminating free Fabs (Figure 4.13c,d).

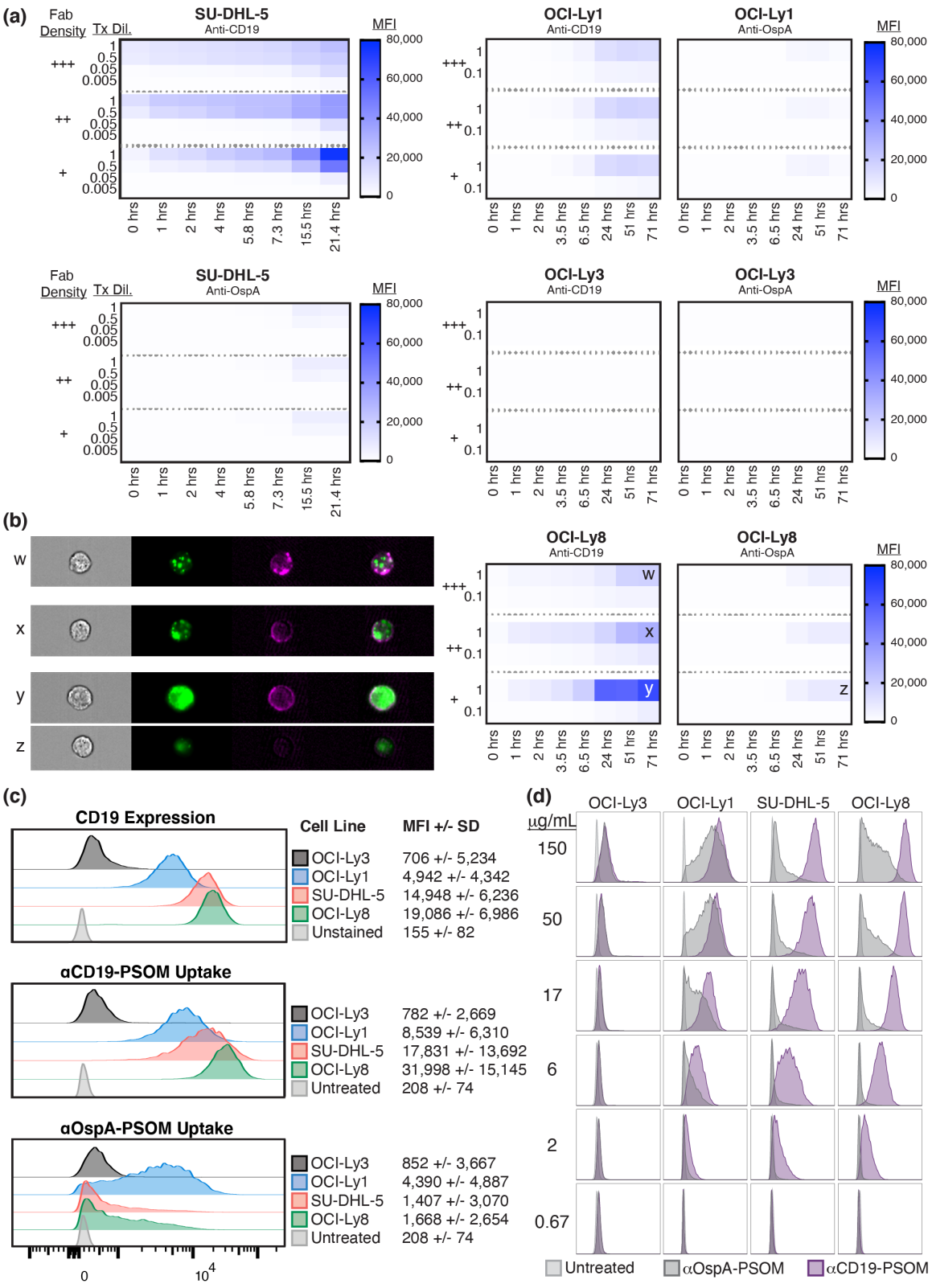

Figure 4.12: CD19 targeting enhances polymersome delivery into DLBCL cells. (Continued on the following page.)

Figure 4.12, continued: CD19 targeting enhances polymersome delivery into DLBCL cells. A self-quenching calcein solution was encapsulated in PEG-SS-PPS polymersomes with 5% N_3 functionalization. Aliquots of this stock solution were then functionalized with either αCD19 or irrelevant (αOspA) Fabs at various Fab:polymer densities (+++, ++, +). DLBCL cell lines were treated as indicated and analyzed by flow cytometry and imaging cytometry. Treatment concentrations were normalized by calcein absorbance after Triton X-100 disruption and calcein dequenching. (a) Uptake of fluorescent polymersomes into four DLBCL cell lines was measured by flow cytometry to evaluate time-, concentration-, Fab-, and Fab-density-dependence. αCD19 Fab functionalization greatly improved cellular uptake, and lower Fab densities caused more uptake. (b) The same samples from (a) were subsequently analyzed by ImageStream imaging cytometry for single-cell fluorescence images. Representative images are shown with the following channels: brightfield, calcein (green), anti-Fab extracellular staining (magenta), and an overlay. (c) CD19-specific polymer uptake correlates with CD19 expression. Cells were either stained with fluorescent αCD19 IgG or treated with αCD19-PSOM$_{\text{calcein}}$ or αOspA-PSOM$_{\text{calcein}}$ for 24 hours. An unstained, untreated sample of SU-DHL-5 is shown for comparison. (d) Polymersome-uptake after 24 hours is dose-dependent for both specific uptake (αCD19) and non-specific uptake (αOspA). The total polymer concentration in the treatment is indicated in μg/mL.

To confirm that the polymersomes were enhancing intracellular calcein accumulation and dequenching rather than simply binding more to the cell surface, we imaged the same samples using ImageStream imaging cytometry (Figure 4.12b). Indeed, the lower Fab densities enhanced antigen-specific uptake and diffuse, intracellular calcein (green) accumulation. We also stained extracellular polymersomes on the cell surface using a fluorescent anti-Fab antibody, and the extracellular anti-Fab staining (magenta) did not overlap with the intracellular calcein staining (green), confirming that the diffuse calcein signal was a result of enhanced intracellular accumulation and fluorescence dequenching rather than simply increased extracellular binding.

The uptake of αCD19-PSOM$_{\text{calcein}}$ was also highly antigen specific. Uptake of αCD19-PSOM$_{\text{calcein}}$ in each cell line correlated with expression levels of CD19, while uptake of αOspA-PSOM$_{\text{calcein}}$ was less, more heterogeneous, and uncorrelated with CD19 expression (Figure 4.12c). This trend was consistent across a range of doses (Figure 4.12d).

Together, these data show that αCD19-PSOMs are endocytosed antigen-specifically with lower Fab densities causing the greatest intracellular accumulation. We therefore used this

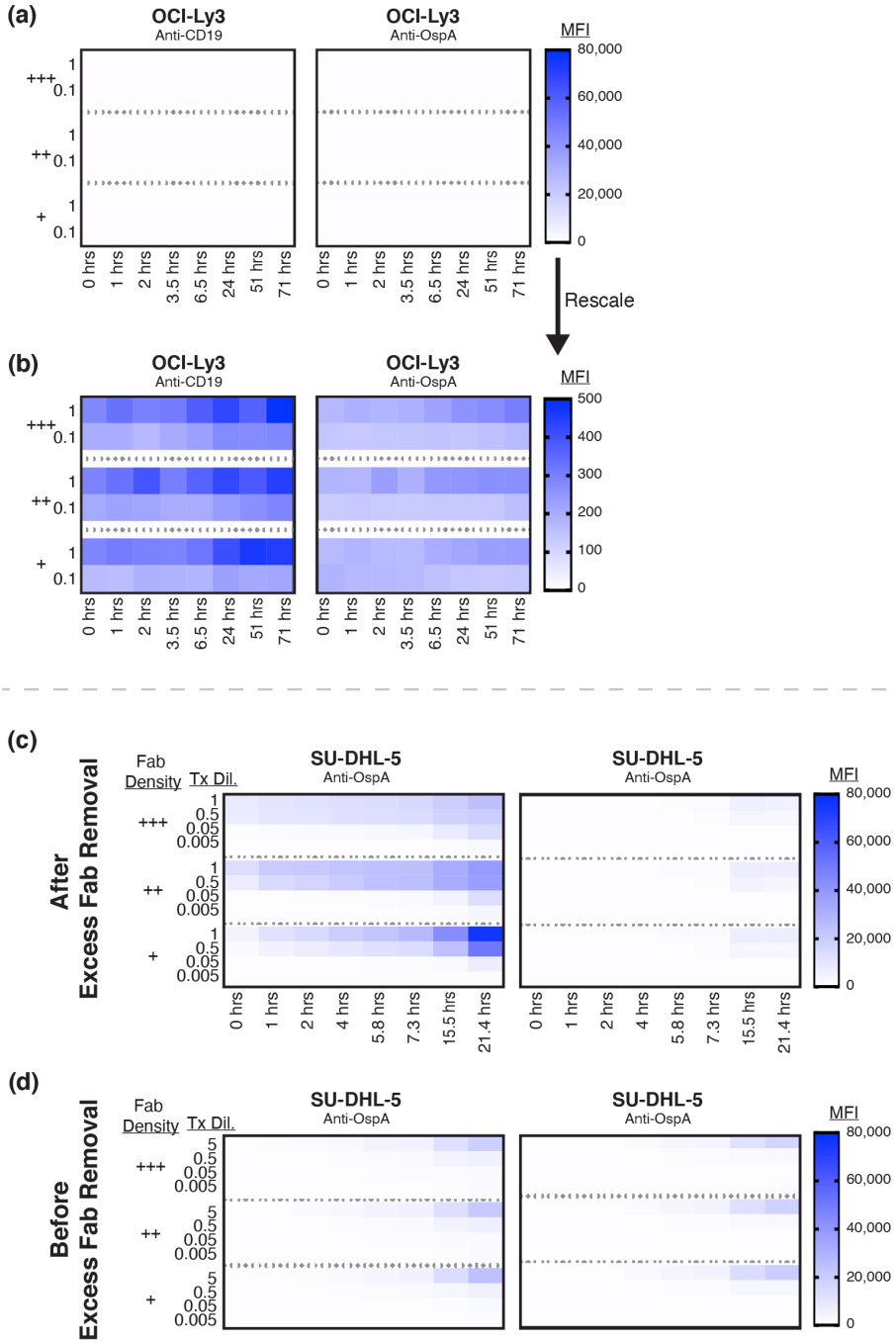

Figure 4.13: Calcein uptake heatmaps (supplementary). (a) Data as shown in Figure 4.12a measuring uptake of calcein-loaded polymersomes in OCI-Ly3. (b) Data from (a) re-scaled to visualize CD19-specific uptake in OCI-Ly3. (c) Data as shown in Figure 4.12a measuring uptake of calcein-loaded polymersomes in SU-DHL-5. (d) A similar experiment to (c) was conducted without the final purification step in which excess Fab was removed from the treatments. Excess Fab blocked nearly all antigen-specific uptake. Of note, the highest concentration treatments in (d) are 5-times higher than in (c) in terms of calcein concentration.

lowest Fab density formulation (+) for all further experiments with therapeutic cargoes.

4.3.3 Polymersome-Mediated Intracellular Delivery Enhances the Therapeutic Efficacy of BH3-Mimetic Stapled Peptides

Calcein was a useful model cargo to optimize polymersome uptake into DLBCL cells, and next we made polymersomes encapsulating our therapeutic cargo, SAH-MS1-18 [102], to ultimately test the polymersomes' ability to improve the intracellular delivery and efficacy of stapled peptides.

After encapsulating SAH-MS1-18 in polymersomes ($PSOM_{SAH\text{-}MS1\text{-}18}$) and functionalizing them with Fabs (αCD19-$PSOM_{SAH\text{-}MS1\text{-}18}$ and αOspA-$PSOM_{SAH\text{-}MS1\text{-}18}$), we tested the ability of SAH-MS1-18 to induce apoptosis in DLBCL when it was either used as a free peptide or when its intracellular delivery was facilitated by PEG-SS-PPS polymersomes.

First, SU-DHL-5 was treated with equivalent doses of SAH-MS1-18 either as a free drug, inside of αCD19- or αOspA-PSOMs, or on the outside of empty αCD19- or αOspA-PSOMs (Figure 4.14a). Delivery of SAH-MS1-18 inside of polymersomes enhanced its potency by ~100-fold. Importantly, when the same doses of peptide were used but on the outside of empty polymersomes, cell death was completely eliminated. This confirms that the greatly enhanced potency is due to the facilitated delivery, rather than any non-specific toxicity due to the combination of materials. We then treated other DLBCL cell lines, including OCI-Ly1, OCI-Ly3, and OCI-Ly8 (Figure 4.14b). Delivery inside of polymersomes enhanced the potency of SAH-MS1-18 by ~10-fold in OCI-Ly1 and OCI-Ly8. OCI-Ly3, which endocytosed very low levels of αCD19- or αOspA-PSOMs (Figure 4.12, Figure 4.13a,b) exhibited little cell death. Even for this qualitatively cell permeable staple peptide [102], intracellular delivery using PEG-SS-PPS polymersomes greatly enhanced its efficacy.

To confirm this delivery benefit was not unique to SAH-MS1-18, we delivered another apoptosis-inducing stapled peptide, BIM SAHB [103, 104, 244], into DLBCL cells using polymersomes (Figure 4.15). The potency of BIM SAHB was improved 10x by polymersome

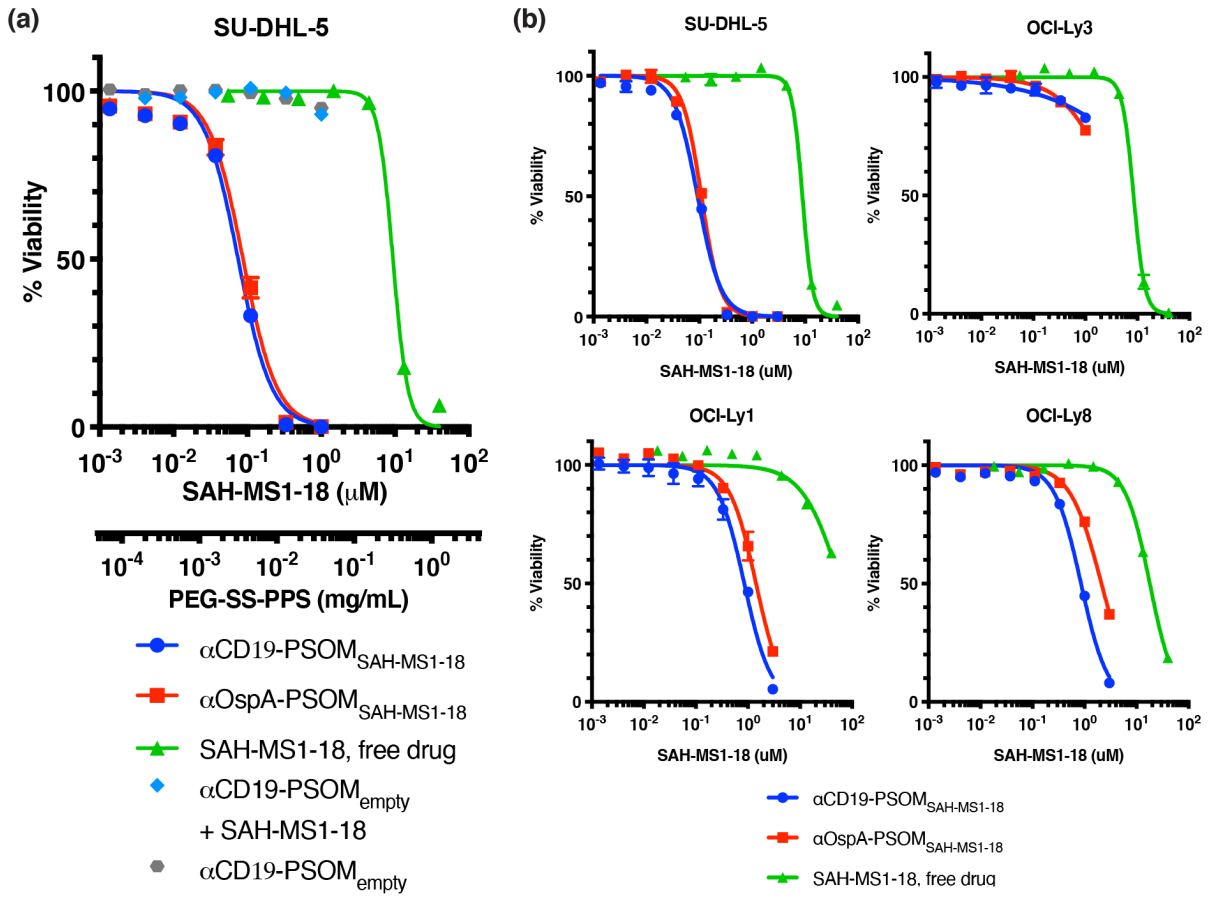

Figure 4.14: Polymersome delivery enhances the therapeutic potency of SAH-MS1-18 in DLBCL. (a) When SAH-MS1-18 was delivered into SU-DHL-5 DLBCL cells using polymersomes, its potency was amplified by orders of magnitude. When the cells were treated with the same materials but formulated with free peptide on the outside of empty polymersomes, the therapeutic effect was completely eliminated. (b) Across four different DLBCL cell lines, polymersome delivery enhances the therapeutic efficacy of SAH-MS1-18. Plotted points are the means of duplicates +/- S.E.M. fitted to a normalized non-linear regression with variable slope.

delivery into OCI-Ly1 and OCI-Ly8. Importantly, SU-DHL-5 was not sensitive to BIM SAHB delivered in polymersomes, even though it was extremely sensitive to SAH-MS1-18 delivered in the same way. This highlights the mechanistic specificity of these peptides' induction of apoptosis and the benefit this system provides specifically by enhancing cellular uptake.

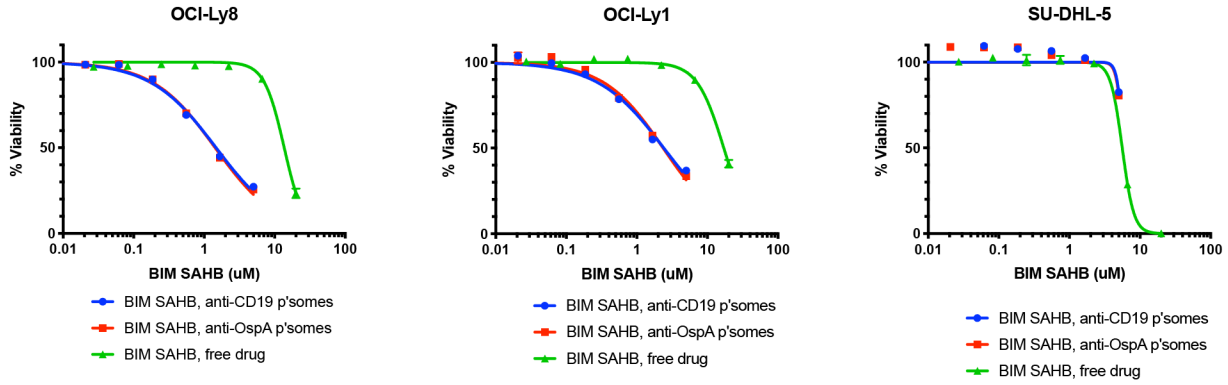

Figure 4.15: αCD19-PSOM delivery enhances the potency of BCL-2 family pan-activator, BIM-SAHB. BIM-SAHB was delivered to DLBCL cells either as free peptide, in CD19-targeted polymersomes, or in irrelevantly-targeted polymersomes, and viability was measured by CellTiter-Glo 2.0. Plotted points are the mean of duplicates +/- S.E.M. and fitted by normalized non-linear regression with variable slope (GraphPad Prism).

Unexpectedly, αOspA-PSOMs loaded with therapeutic cargoes were almost as potent as αCD19-PSOMs (Figures 4.14, 4.15), even though αCD19-PSOMs facilitated greater uptake of a calcein model cargo (Figure 4.12). One possible explanation for this could be the threshold character of apoptosis as opposed to the continuous scale of calcein fluorescence. If a small amount of peptide is delivered non-specifically into the cell by αOspA-PSOMs, and if it is enough to induce apoptosis, then no further accumulation could be facilitated by CD19 targeting and appreciated in a cell death assay. These data suggest that the majority of improved potency in vitro is likely due to facilitated endosomal escape and/or protecting the peptide cargo from serum protein sequestration. For targeted nanocarriers, the benefits of targeting are usually more pronounced in vivo than in vitro.

4.3.4 p53-Reactivation Primes DLBCL for Cell Death by MCL-1 Inhibition and Sensitizes DLBCL to αCD19-PSOM$_{SAH\text{-}MS1\text{-}18}$

With PEG-SS-PPS polymersomes able to enhance the intracellular delivery and therapeutic potency of PPI-inhibiting stapled peptides, we sought to target a synergistic combination of PPIs that are commonly deregulated in clinical DLBCL, namely MCL-1 over-expression and WTp53-inactivation. Tumor suppressor protein p53 is known to modulate transcription of a number of BCL-2 family members in a pro-apoptotic way. There is a p53-reactivating stapled peptide, ALRN-6924, currently in clinical trials. While the sequence of ALRN-6924 is proprietary and unpublished, its pre-clinical predecessor, ATSP-7041, has a published sequence and has used by multiple groups for p53 reactivation. ATSP-7041 has been highly optimized to be cell-permeable and drug-like, and its therapeutic efficacy is not negated by serum proteins [28]. ATSP-7041 is also one of the few stapled peptides that has been successfully applied in vivo. We therefore used ATSP-7041 as our p53-reactivating stapled peptide to prime DLBCL for apoptosis.

Interestingly and surprisingly, we found that p53 primes DLBCL cell lines for cell death specifically with increased sensitivity to MCL-1 inhibition rather than to other anti-apoptotic proteins such as BCL-2 or BCL-XL. We sought to characterize this p53:MCL-1 axis and therapeutically exploit it in DLBCL using stapled peptides (ATSP-7041 to reactivate p53, and αCD19-PSOM$_{\text{SAH-MS1-18}}$ to inhibit MCL-1).

To determine therapeutically-relevant treatment concentrations, we first tested the cell death sensitivity of DLBCL cell lines to ATSP-7041 at 24 and 72 hours (Figure 4.16). For three cell lines with wildtype p53 (SU-DHL-5, OCI-Ly19, and DOHH2), 1 μM ATSP-7041 was an amount that induced some apoptosis at 24 hours and a lot more apoptosis by 72 hours. A fourth DLBCL cell line with wildtype p53, OCI-Ly3, was less sensitive to ATSP-7041 treatment, and this cell line was included as a more resistant WTp53 control. Two DLBCL cell lines with mutant p53 (OCI-Ly1 and OCI-Ly8) had no cell death in response to ATSP-7041, except a small amount at the highest dose, 30 μM, for 72 hours of treatment.

This 30 μM dose is higher than the highest dose I have found in the literature in in vitro treatments (10 μM; [28]), and this cell death is likely non-specific due to the high dose. After 24 hours of treatment, ATSP-7041 has previously been shown to induce p53 transcriptional activation [28], and with these data, I chose 1 μM as the 24-hour treatment dose to evaluate BCL-2 family changes in response to p53 re-activation.

When DLBCL cell lines were treated with the p53-reactivating stapled peptide ATSP-7041 for 24 hours, DLBCL with WTp53 exhibited transcriptional changes within the BCL-2 family consistent with known p53 transcriptional targets (Figure 4.17). First, CDKN1A (p21) transcription was highly upregulated, indicating robust p53-reactivation. Within the BCL-2 family, the mRNA of p53 upregulated modulator of apoptosis (PUMA) was strongly upregulated across each of the cell lines with WTp53. BAX, an effector of apoptosis and another known p53-transcriptional target, was also upregulated across each of the WTp53 cell lines. Interestingly, NOXA mRNA appeared unchanged after p53-reactivation. NOXA is a canonical transcriptional target of p53, though it is also regulated by multiple other transcription factors [286]. In general, the WTp53 cell lines responded to p53 reactivation by increasing expression of PUMA and BAX, transcriptional changes consistent with priming the cells for apoptosis.

We then evaluated how these transcriptional changes after p53-reactivation affected protein levels of PUMA (Figure 4.17b). Consistent with the changes in PUMA mRNA, PUMA protein was also upregulated after p53-reactivation in DLBCL lines with wildtype p53 (i.e. SU-DHL-5, OCI-Ly3) but not in lines with mutant p53 (i.e. OCI-Ly1, OCI-Ly8).

Next, we measured how p53-induced changes in the BCL-2 family affected the cells' functional sensitivity to apoptosis. Mitochondrial outer membrane permeabilization (MOMP) by BAX and BAK, and the resulting mitochondrial depolarization, is the point-of-no-return when a cell initiates the feed-forward process of apoptosis. Cells' sensitivities to mitochondrial depolarization and apoptosis can be measured by permeabilizing the cell membrane and treating with varying concentrations of a BIM BH3 peptide, the BH3 binding domain of

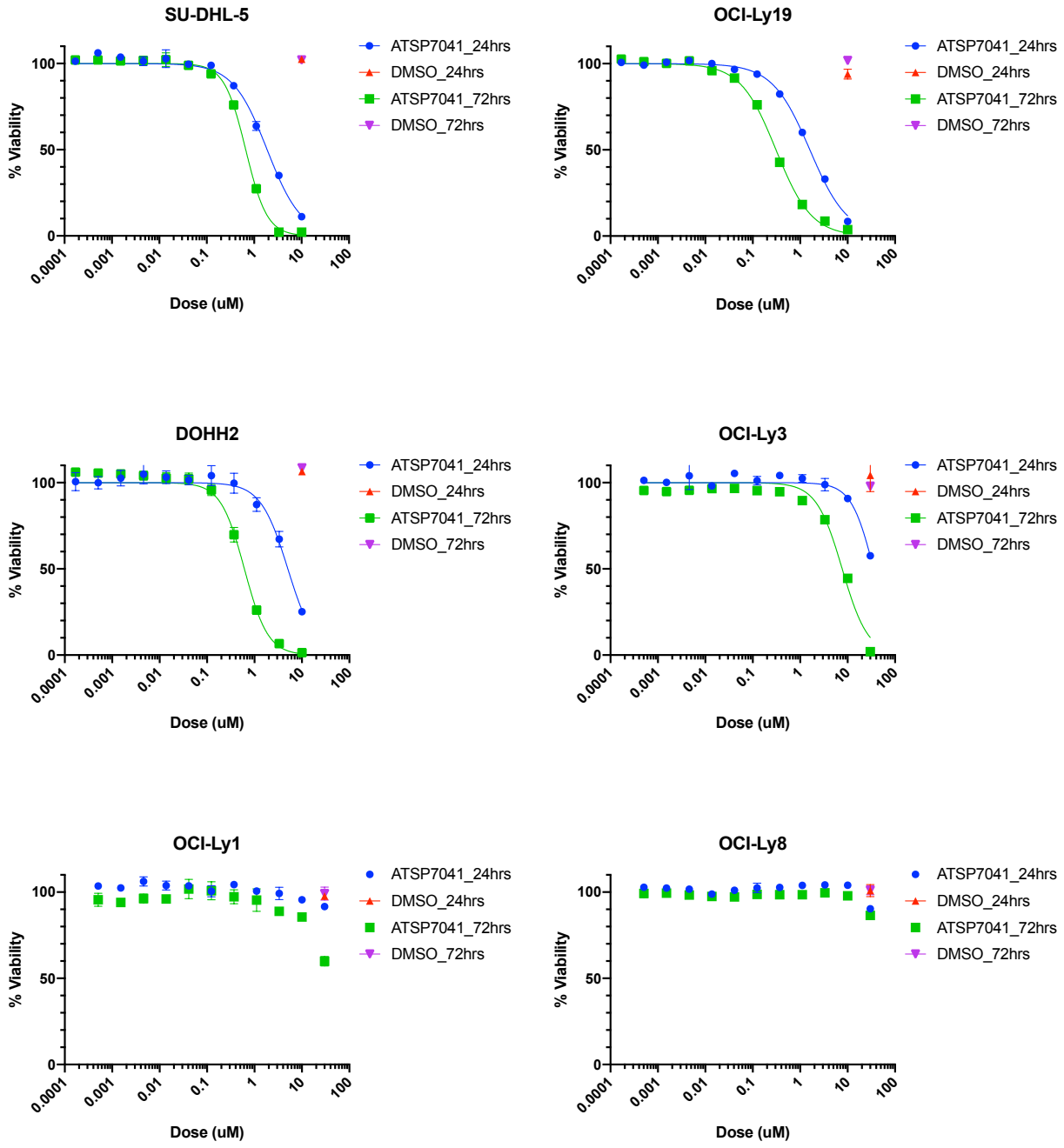

Figure 4.16: Cell death sensitivities of DLBCL cell lines to ATSP-7041. Four DLBCL cell lines with WTp53 and two with mutant p53 (OCI-Ly1 and OCI-Ly8) were treated with ATSP-7041 at a range of doses for 24 or 72 hours when viability was measured using CellTiter Glo 2.0 relative to an untreated control. DMSO controls were included with a volume of DMSO equal to the highest peptide treatments. Data plotted are the mean of duplicates +/- S.E.M. fitted to a normalized non-linear regression with variable slope (GraphPad Prism 8).

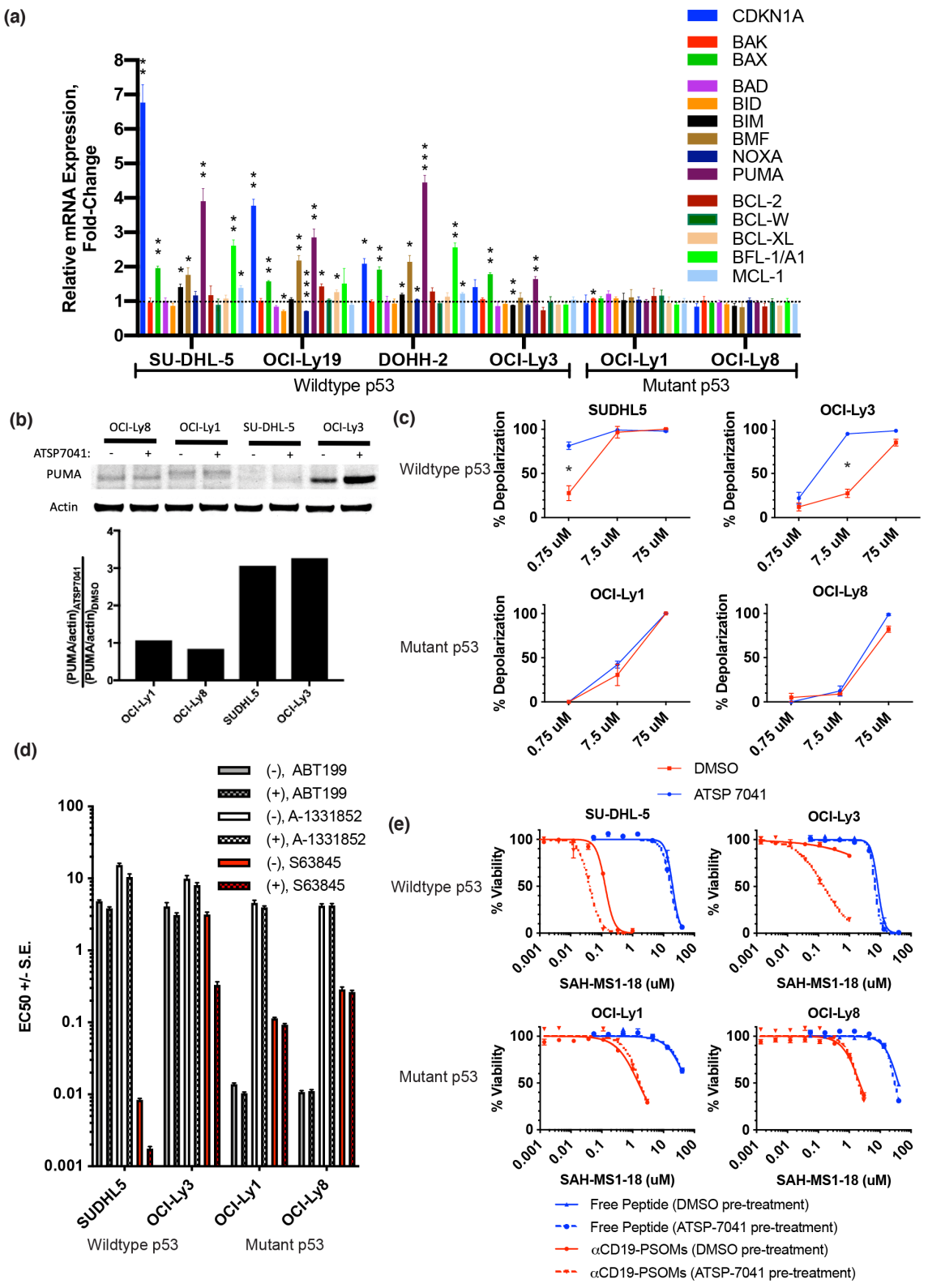

Figure 4.17: p53-reactivation with ATSP-7041 primes DLBCL for apoptosis, particularly through MCL-1 inhibition. (Continued on the following page.)

Figure 4.17, continued: p53-reactivation with ATSP-7041 primes DLBCL for apoptosis, particularly through MCL-1 inhibition. DLBCL cell lines were treated for 24 hours with either ATSP-7041 or vehicle control (DMSO) to assess the effects of p53-reactivation on the BCL-2 family of proteins. (a) The relative mRNA expression levels of DLBCL cell lines with and without p53-reactivation were quantified for the BCL-2 family members and for p53's classic transcriptional target, *CDKN1A*/p21. Plotted values are the mean of biological triplicates (each in technical triplicate) +/- S.E.M. (b) Western blot of PUMA protein in DLBCL cell lines with or without p53-reactivation. Bands were quantified in ImageJ, normalized to actin, and quantified as the ratio of PUMA in the ATSP-7041 treatment to the vehicle control. (c) Apoptotic priming with or without p53-reactivation. After pre-treatment with ATSP-7041, mitochondrial depolarization was measured in response to varying doses of BIM BH3 peptide. A t-test was used to compare each pair of points. * p ¡ 0.005. (d) Sensitivities to a BCL-2 inhibitor (ABT-199), BCL-XL inhibitor (A-1331852), and MCL-1 inhibitor (S63845) were measured with (+) or without (-) prior p53-reactivation by ATSP-7041. Dilution curves were made in duplicate, normalized to an untreated control receiving the same pre-treatment, and analyzed by non-linear regression to calculate the IC50 +/- S.E. Individual dose curves are presented in Figure 4.18. (e) Cell death sensitivities to SAH-MS1-18 delivered in polymersomes with or without p53-reactivation. Plotted values are the mean of duplicates +/- S.E.M., normalized to untreated control and fitted using non-linear regression.

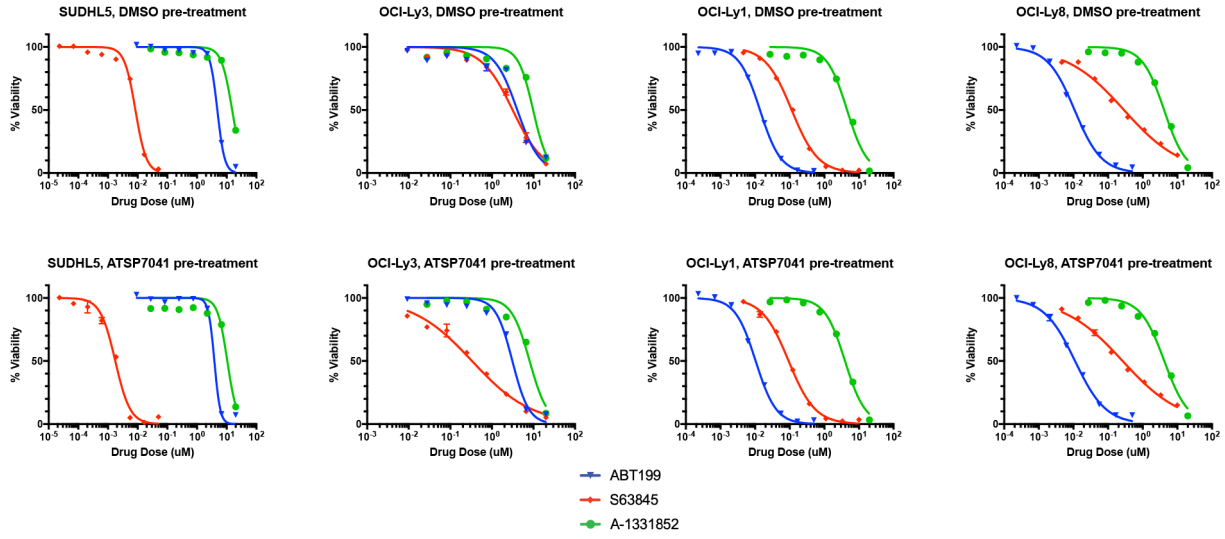

Figure 4.18: DLBCL sensitivities to BH3-mimetics with and without p53 priming. Each cell line was treated for 24 hours with either ATSP-7041 or vehicle control (DMSO), washed, then treated for 24 hours with the indicated BH3 mimetic. Plotted points are means of duplicates +/- S.E.M., normalized to an untreated control that received the same pre-treatment, and fitted using nonlinear regression.

pan-activating protein BIM. The more "primed to die" the cells are, the less BIM BH3 peptide is required to induce mitochondrial depolarization. After treatment with p53-reactivator

ATSP-7041, cell lines with wildtype *TP53* (i.e. SU-DHL-5, OCI-Ly3) were significantly more "primed to die" than vehicle-treated controls (Figure 4.17c). In agreement with the mRNA and protein changes in the BCL-2 family, p53-reactivation functionally sensitized DLBCL to MOMP.

While DLBCL was primed for apoptosis after p53-reactivation, it was not yet clear which anti-apoptotic proteins the surviving cells were relying on for survival, because increased levels of PUMA and BAX could theoretically be sequestered by any of the anti-apoptotic proteins in the BCL-2 family. Three of the anti-apoptotic proteins, BCL-2, BCL-XL, and MCL-1, are the most commonly implicated in chemoresistant and chemorefractory cancers, and each of these three proteins has recently been successfully inhibited using specific small molecule therapeutics. We tested whether or not p53-reactivation changed the sensitivity of these DLBCL cell lines to therapeutic inhibition of BCL-2 by ABT-199 (a.k.a. venetoclax), BCL-XL by A-1331852, or MCL-1 by S63845 (Figures 4.17d, 4.18). Cells were pre-treated with ATSP-7041 (+) or a vehicle control (-) for 24 hours, washed, and then treated with varying doses of each therapeutic, and dose-death curves were fitted to calculate EC50 sensitivities. After p53-reactivation, the cell lines with WTp53 were much more sensitive to the MCL-1 inhibitor (S63845). Both an MCL-1-sensitive cell line (SU-DHL-5) and a relatively resistant cell line (OCI-Ly3) were made much more sensitive to MCL-1 inhibition by first reactivating p53 with ATSP-7041. Surprisingly, there was no notable change in sensitivity to the BCL-2 inhibitor (ABT-199) or BCL-XL inhibitor (A-1331852), even though each of these anti-apoptotic proteins is capable of sequestering PUMA and BAX. This highlights MCL-1 as a synergistic therapeutic target with p53-reactivation, such as by ATSP-7041.

We then tested the sensitivity of DLBCL to the stapled peptide MCL-1 inhibitor, SAH-MS1-18, delivered either in polymersomes or as free drug, with and without p53-reactivation (Figure 4.17e). After priming cells for 24 hours with ATSP-7041 and washing off the drug, each cell line was then treated for 72 hours with equivalent doses of SAH-MS1-18, either in polymersomes or as free peptide. DLBCL with WTp53 was made more sensitive to SAH-

MS1-18 delivered as αCD19-PSOM$_{\text{SAH-MS1-18}}$ after p53-reactivation. As with the small molecule inhibitor of MCL-1 (S63845), a sensitive cell line (SU-DHL-5) was made even more sensitive by p53-reactivation. Notably, a resistant cell line, OCI-Ly3, became a sensitive cell line simply by reactivating p53. OCI-Ly3 also endocytosed very small amounts of αCD19-PSOM$_{\text{calcein}}$ (Figure 4.12, Figure 4.13a,b), so this dramatic sensitization by p53-reactivation is noteworthy. While SAH-MS1-18 with polymersome delivery was made much more potent, SAH-MS1-18 as a free drug showed no change. This peptide is reportedly highly MCL-1 specific and is reported to cause no non-specific cell membrane disruption [102]. Somehow SAH-MS1-18, without assisted cellular uptake, is unable to exploit the apoptotic priming induced by p53-reactivation. In DLBCL with WTp53, αCD19-PSOM$_{\text{SAH-MS1-18}}$ paired with p53-reactivator ATSP-7041 is a potent therapeutic combination in vitro, rivaling cell death sensitivities commonly seen for potent small molecule therapeutics.

4.3.5 αCD19-PSOM$_{calcein}$ Delivers Calcein to DLBCL In Vivo

While αCD19-PSOMs were taken up by DLBCL cells in vitro (Figure 4.12), we ultimately sought to apply this stapled peptide delivery platform in vivo. We next tested the ability of αCD19-PSOM$_{\text{calcein}}$ to deliver calcein into DLBCL cells in vivo. We engrafted OCI-Ly8 DLBCL cells in NSG mice in both a disseminated (i.v.) model and an orthotopic (subcutaneous tumor) model. We treated with one dose of αCD19-PSOMs or vehicle (PBS) six days later, and 24 hours after treatment sacrificed the mice to analyze the DLBCL cells by flow cytometry. The disseminated OCI-Ly8 cells (CD19+ CD20+) were found in the bone marrow but not in the liver and spleen. Both disseminated (bone marrow) and orthotopic (subcutaneous tumor) DLBCL cells had measureable calcein fluorescence compared to vehicle-treated controls (Figure 4.19). Though this pilot experiment only had two mice per group, this proof of concept motivated scale-up and testing of SAH-MS1-18-loaded polymersomes in DLBCL xenograft models in vivo.

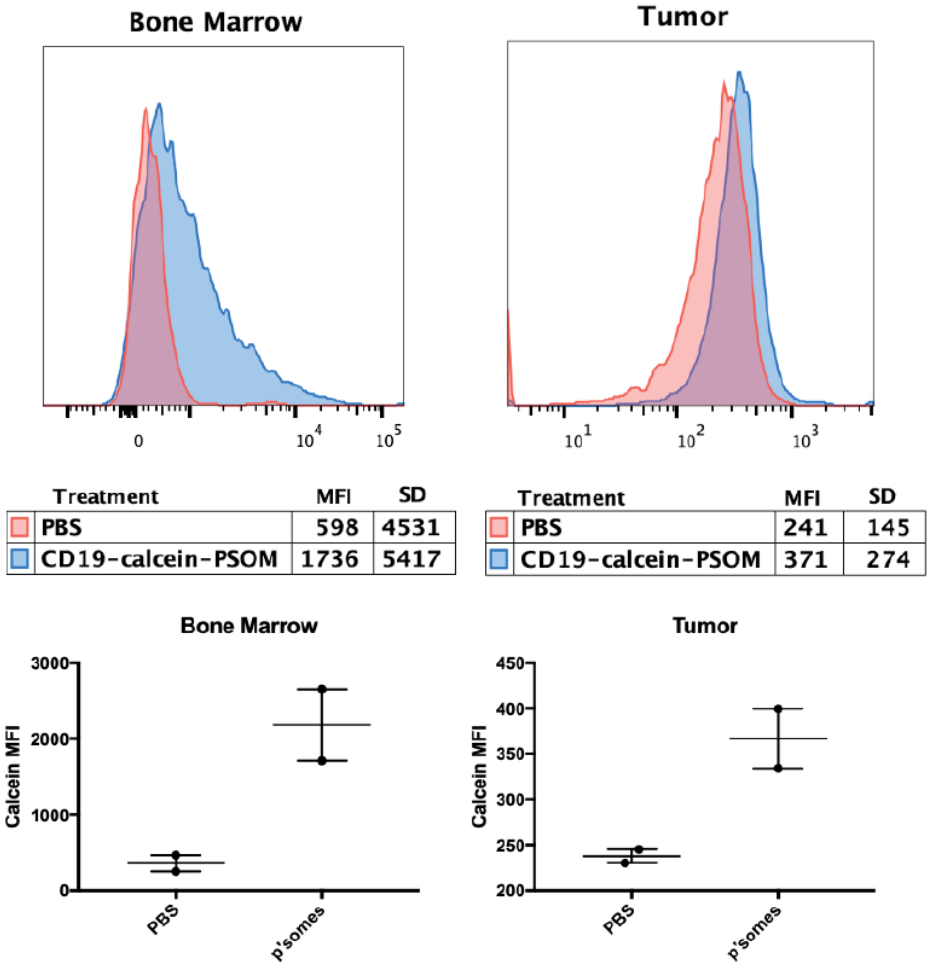

Figure 4.19: Polymersome delivery to DLBCL cells in vivo: pilot experiment. αCD19-PSOM$_{\text{calcein}}$ delivers calcein to OCI-Ly8 DLBCL cells in both disseminated (bone marrow) and orthotopic (subcutaneous tumor) xenograft models in NSG mice. Mice were engrafted with OCI-Ly8 on day 0, treated once with αCD19-PSOM$_{\text{calcein}}$ on day 6, and the DLBCL cells analyzed by flow cytometry on day 7. OCI-Ly8 cells were gated by size and CD19+ CD20+ staining. N = 2 mice per group. Plotted are the mean and range of the MFI.

4.4 Conclusions, Discussion, and Future Directions

Stapled peptides are promising tools for mimicking α-helices at PPI-interfaces and disrupting disease-driving PPIs with high affinity and specificity. Their primary weaknesses towards clinical translation are (1) their minimal cellular uptake, (2) their lack of cellular targeting, and (3) their solubility. In this work, we found that these weaknesses, and thereby the efficacy, of a pre-clinical stapled peptide, SAH-MS1-18, could be dramatically improved by using PEG-SS-PPS polymersomes for cytoplasmic delivery. For delivery into DLBCL cells, we functionalized the outer surface of PEG-SS-PPS polymersomes with CD19-binding Fab antibody fragments, and this facilitated robust uptake and cytoplasmic dissemination into DLBCL cells. While stapled peptides are often only minimally water soluble, encapsulation in PEG-SS-PPS polymersomes allowed for stable solubilization of stapled peptides at concentrations orders of magnitude higher than for the peptides alone (i.e. low mM overall concentrations in polymersome stock solutions). With SAH-MS1-18 as a therapeutic cargo, polymersome delivery improved its therapeutic efficacy by multiple orders of magnitude. We then used this new system for drugging PPIs to exploit a synergistic therapeutic weakness in DLBCL, namely p53-reactivation and MCL-1 inhibition. By therapeutically reactivating p53 in DLBCL using the stapled peptide ATSP-7041, DLBCL cell lines were primed for apoptosis with a specific sensitivity to therapeutic inhibition of MCL-1. While the polymersomes improved the efficacy of the MCL-1 inhibiting stapled peptide by orders of magnitude, priming DLBCL with p53-reactivation made resistant cell lines sensitive and sensitive cell lines more sensitive to MCL-1 inhibition. Together, these data highlight the utility of using rationally designed nanocarriers to facilitate the targeted, cytoplasmic delivery of therapeutic peptides to fully harness their affinity, specificity, and therapeutic potential.

We now aim to use this platform for robust in vivo delivery of stapled peptides. Few stapled peptides in the literature have been successfully applied in in vivo experiments, and this platform could facilitate their in vivo delivery. A pilot experiment using a fluorescent model cargo showed that αCD19 polymersomes could facilitate delivery to both disseminated

and subcutaneous xenograft models of DLBCL. Meanwhile, we are in the process of scaling up the synthesis of our peptides, polymers, and Fabs by multiple orders of magnitude to produce enough polymersomes for in vivo drug treatment experiments, and we have now established methods for assembling and purifying these polymersomes at these much larger scales. We have also been testing xenograft models of wildtype *TP53* DLBCL, and we are about to begin our in vivo treatments.

While these polymersomes greatly enhanced the efficacy of two stapled peptides, SAH-MS1-18 and BIM SAHB, their encapsulation and retention mechanisms in PEG-SS-PPS polymersomes are not completely understood. I hypothesize both the hydrocarbon staple and their charged side chains are indispensable factors for their high degrees of encapsulation and stable retention. When I attempted to encapsulate non-stapled versions similar to these stapled peptides, very little encapsulation was measureable (data not shown). On the other end of the spectrum, a less polar, less charged stapled peptide, ATSP-7041 (-1 charge), was also encapsulated in PEG-SS-PPS polymersomes in large amounts, but upon dilution, it readily diffused out of polymersomes to equilibrate with the extra-vesicular space (data not shown). Hydrophobic small molecules, such as S63845, were likewise able to be encapsulated to a high degree but ultimately leak out of the polymersomes upon dilution. It seems that the hydrophobic, all-hydrocarbon staple of these peptides is critical for the high degrees of encapsulation we routinely see for hydrocarbon-stapled peptides, while polar side chains and charged groups are critical for keeping the peptides in the interior of the polymersomes and preventing them from diffusing across the PPS layer to leak out. While no polymeric carrier will be ideal for all types of therapeutic cargoes, PEG-SS-PPS polymersomes seems particularly ideal for encapsulation and retention of pre-clinical stapled peptides that have not been extensively optimized for cellular uptake by removing most of their native polar/charged groups (e.g. ATSP-7041).

We were able to achieve robust uptake into DLBCL cells by decorating these polymersomes with CD19-binding Fab antibody fragments. This block co-polymer, PEG-PPS, has

previously been shown in many applications to be useful for delivering both hydrophilic and hydrophobic cargoes into immune cells via non-specific phagocytosis. The disulfide version in particular, PEG-SS-PPS, has been shown in macrophages to rapidly facilitate endosomal escape and diffuse intracellular dissemination of a fluorescent cargo after phagocytosis [181]. In this work, we were able to functionalize the surface of the polymersomes with a targeting moiety for antigen-specific cellular uptake into DLBCL cells via CD19. However, B cells are also a phagocytic cell type, and we saw some uptake of fluorescent cargo and improved therapeutic efficacy for non-targeted polymersomes too, suggesting that in vitro, a large portion of the improved therapeutic efficacy of SAH-MS1-18 was due to enhanced cellular uptake, endosomal escape, or minimized serum sequestration, rather than solely enhanced receptor-mediated endocytosis. While we only tested three Fab functionalization densities, we saw a large effect on the amount of uptake for different densities. The targeted uptake of these polymersomes can likely be optimized much more than we have done here, and the optimal density should be different for each receptor:ligand pair.

Reactivation of p53 has long been known to cause pro-apoptotic transcriptional changes within the BCL-2 family. In DLBCL, a cancer in which wildtype *TP53* is far more common than mutated *TP53*, we showed that p53 reactivation was particularly pro-apoptotic in a way that sensitized DLBCL to therapeutic inhibition of MCL-1 specifically. Tong et al. recently showed that MCL-1 is particularly important for cancer cell survival in the context of PUMA upregulation [287], and our data support their findings. The applicability of this therapeutic p53:MCL-1 synergy should be fruitful to explore in other types of cancers with wildtype *TP53*. Both of these are classically considered "undruggable" PPI targets in cancer for which therapeutics are now being tested in clinical trials.

Ultimately, this work demonstrates the therapeutic utility of using supramolecular nanomaterials for targeted, intracellular delivery of therapeutic peptides. More specifically, we present here a PEG-SS-PPS polymersome delivery platform that seems to be ideal for targeted delivery of all-hydrocarbon stapled peptides. These polymersomes meet all the criteria

of a robust in vivo nanomedicine platform (stability, targetability, active uptake, endosomal escape, biocompatibility, and scalability). While this work enhances the efficacy of stapled peptides that are already somewhat cell permeable (i.e. SAH-MS1-18, BIM-SAHB), the greater utility of this platform could come from enhancing the delivery of peptides that are potent and specific binders to their target proteins but therapeutically inert due to a lack of cellular uptake. By bypassing the requirements for cellular uptake, rationally-designed, peptide-based PPI inhibitors could potentially be more rapidly developed without requiring extensive empirical screening to simultaneously optimize target binding, serum sequestration, and cellular uptake. This modular nanomedicine platform can likely be adapted for the targeted intracellular delivery of many different hydrocarbon-stapled peptides to and into a variety of cell types of interest.

4.5 Materials and Methods

4.5.1 Synthesis of PPS-PDS: Poly(Propylene Sulfide) (PPS) with Pyridyl Disulfide (PDS) End-Group (Compound 1)

Thiol-functionalized PEGs were purchased from Laysan Bio Inc. (mPEG-SH) and Nanosoft Polymers (N_3-PEG-SH) and used as delivered. Both PEGs were advertised with MW 1,000 Da, though by our NMR and MALDI measurements were approximately 1,200 Da, and our PPS degree of polymerization (DP) was scaled accordingly to maintain previously reported block ratios.

Benzyl mercaptan (1 eq.) in degassed, anhydrous THF (20 mM) was deprotonated with sodium methoxide (NaOMe; 1.1 eq.) under nitrogen protection for 30 minutes. Propylene sulfide (53.3 eq.) was rapidly added by syringe under vigorous stirring and nitrogen protection. The reaction was carried out under a constant flow of vented nitrogen protection to prevent pressure accumulation. The reaction proceeded to completion within 1 hour, according to 1H NMR, at which point the thiolates were quenched with acetic acid (AcOH;

2 eq.). Disulfide-dimerized PPS chains were then reduced by adding triethylamine (TEA; 3 eq.), water (H_2O; 8 eq.), and tributylphosphine (TBP; 8 eq.) under nitrogen protection for four hours. Aldrithiol-2 (25 eq.) was dissolved in a minimal amount of THF and degassed, and the PPS reaction mixture was cannulated dropwise into the capping solution under nitrogen protection and vigorous stirring and stirred overnight. THF was then removed, and the crude yellow oil was extracted with methanol repeatedly until clear. The removal of aldrithiol-2 and the mercaptopyridine byproduct were confirmed by silica TLC with a mobile phase of 2% methanol in DCM. The fluorescence indicator under UV light was used to detect aldrithiol-2 and mercaptopyridine. CAM staining was used to detect PPS-PDS. Dragendorff staining was used to detect mercaptopyridine. The pure PPS-PDS was dried under high vacuum, and the final product was a clear oil with a slight yellow tint. Purity was confirmed by DMF GPC, NMR (Figure 4.3), and TLC. Compound 1 was stored under argon protection at -80 °C.

4.5.2 Synthesis of Methoxy- and Azide-Poly(Ethylene Glycol)-block-Poly(Propylene Sulfide) (mPEG-SS-PPS (Compound 2) and N_3-PEG-SS-PPS (Compound 3))

PPS-PDS (1.2 eq. PDS) and R-PEG-SH (R = OMe or N_3; 1 eq. free thiol (as determined by polymer mass and dimerization degree by GPC) were each dissolved in DCM (1 g/mL and 0.01 g/mL respectively) and degassed under nitrogen bubbling. The PEG solution was cannulated dropwise into the PPS solution under vigorous stirring and allowed to react overnight, and the reaction mixture gradually turned yellow. The crude product was concentrated and purified over a gradient silica flash column. 30 grams of dry silica per gram of crude mixture (assuming no solvent) was loaded into a flash column as a slurry in DCM. The concentrated sample was loaded onto the column in DCM, in which there was very little migration. The column was then washed with 2% methanol in DCM, in which PPS-PDS and

PPS-PPS disulfides washed off the column. Due to the refractive index matching of the silica and solvent, this migration was visible by eye as an opaque band. The yellow mercaptopyridine byproduct also visibly eluted in this washing step. The PEG-SS-PPS band, still visible at the top of the column, was then eluted with 10% methanol in DCM. Behind the eluting band, the silica visibly turned opaque as the methanol saturated the silica. The solvent from the eluted product was then removed by rotary evaporation. A minimal amount of DMF was used to transfer the polymer to 50 mL centrifuge tubes. The polymer was precipitated with -20 °C MeOH at a ratio of 1:10 or greater and centrifuged at 4,700 g at -10 °C until the supernatant was visibly clear. The deceleration rate was minimized to avoid disturbing the oil when the centrifuge stopped. The clear supernatant was decanted, and the oil was then extracted two more times with -20 °C MeOH, centrifugation, and decanting. After the MeOH extractions, removal of DMF and co-eluting PEG was confirmed by NMR and by TLC with CAM staining and a mobile phase of 8% methanol in DCM. The polymer was then redissolved in DCM, filtered through a 0.2 μm filter into pre-weighed scintillation vials, and immediately dried by rotary evaporation followed by high vacuum. The final product was a clear, slightly yellow oil, confirmed pure by DMF GPC, NMR (Figures 4.4,4.5), and TLC. All polymers were stored under argon protection at -80 °C.

In our first syntheses, the heterodisulfides were synthesized in the opposite direction, by first making PEG-PDS and reacting it with PPS-SH. However, the method elaborated upon above allowed for a simpler, more effective workup and a stable, capped PPS intermediate. Therefore, our scaled-up syntheses were done as presented above, though both synthesis routes produced indistinguishable final products.

4.5.3 Synthesis and Purification of Hydrocarbon-Stapled Peptides

For peptide synthesis, rink amide AM low loading resin was purchased from Sigma Aldrich (8.55120). Solvents and natural amino acids were purchased from Gyros Protein Technologies, while stapling amino acids were purchased from Sigma Aldrich or Advanced ChemTech.

All-hydrocarbon stapled peptides were synthesized on a PreludeX peptide synthesizer from Gyros Protein Technologies, primarily using chemistries described by Bird et al. [79]. First, the resin was swelled in DCM for 15 min followed by DMF for 15 min. Deprotection reactions were done with 20% piperidine in NMP for 2 x 10 min, with the exception of stapling amino acids, which were deprotected for 4 x 10 min. Of note, because the α-carbon of the stapling amino acids is di-substituted, their N-termini fail to generate a purple Kaiser test, even when they are successfully deprotected. Unless otherwise specified, coupling reactions used 10 eq. of amino acid (300 mM solution in NMP), 9.5 eq of HATU (285 mM solution in NMP), and 20 eq of DIPEA (600 mM solution in NMP) for 30 min. Stapling amino acids were coupled using half the amount of each solution for 1 hr. To couple the amino acid directly following a stapling amino acid, the coupling reaction was repeated for 4 x 1 hr, except Cba, which was repeated for 2 x 4 hr. For very large scale synthesis of SAH-MS1-18, double coupling with 5 eq. amino acid was used for regular amino acids, and longer reaction times with 5 eq. amino acid were used for the positions after S5 and R8. After each coupling reaction, the resin was exposed to capping solution (4/1/0.1 NMP/Ac_2O/DIPEA) for 10 min to cap any unreacted amines, generate truncation impurities instead of deletion impurities, and simplify HPLC purification. After every reaction step, the resin was washed with alternating washes of DMF and DCM.

After completing the linear synthesis, peptides to be acetylated were deprotected and capped with capping solution. For FITC-labeled peptides, the N-terminal beta-alanine remained FMOC-protected during the RCM reaction. For RCM stapling, the resin was washed thoroughly with DCM, then suspended in a 4 mg/mL solution of Grubbs 1st generation catalyst in anhydrous 1,2-dichloroethane with 20 mol% catalyst with respect to resin substitution. The catalyst solution was prepared fresh immediately before stapling. The stapling reaction was carried out under nitrogen bubbling for cycles of 3 x 2 hr followed by 3 x 4 hr, with DCM washing between cycles. Stapling was confirmed by LCMS through the loss of ethylene (28 Da). For FITC-labeled peptides, the resin was then deprotected and reacted

with 300 mM FITC, isomer I (Sigma Aldrich, F7250) and 600 mM DIPEA for overnight or longer. FITC-conjugation was confirmed with LCMS.

Completed peptides were then cleaved from the resin. The resin was washed thoroughly with DCM and dried, followed by TFA cleavage using a fresh solution of 95/2.5/2.5 TFA/H_2O/TIS for 2 hours. After the TFA solution was collected, the resin was washed once with TFA solution, the TFA solutions pooled, and the peptide immediately precipitated using 50/50 hexane/diethyl ether in 50 mL centrifuge tubes at a volume ratio of 10:1 or greater. The solution was chilled at -80 °C for 1 hour, then the peptide was pelleted by centrifugation at 1,500 g for 20 min at -10 °C. The crude pellet was dried, resuspended in an H_2O/ACN mixture, and lyophilized. The peptide was then resuspended in a minimum volume 50/50 H_2O/ACN with ammonium bicarbonate buffer at roughly neutral pH and allowed to sit at room temperature at least overnight. This facilitated the complete deprotection of the carbamic acid on tryptophan side chains, as identified by MW + 44 impurities in LCMS [79]. Complete deprotection of ATSP-7041 proceeded slowly, and the peptide began to precipitate after a few hours. A large quantity or urea was dissolved into the solution and sonicated, which redissolved the peptide.

The peptide solutions were then filtered and purified via reverse-phase HPLC-MS using a C18 column from Waters (XBridge Peptide BEH C18, 130 Å, 5μm, 19 mm x 150 mm) with mobile phases A (water + 0.1% formic acid) and B (ACN) unless otherwise noted. The pure fractions were pooled, concentrated by rotary evaporation, and lyophilized. The peptides were redissolved in 30% ACN in H_2O, filtered, aliquoted, lyophilized, confirmed pure by LCMS, and quantified by amino acid analysis (AAA; UC Davis Molecular Structure Facility).

SAH-MS1-18 had poor chromatographic shape and inconsistent retention times with formic acid as the mobile phase modifier. Instead, 0.1% TFA was added to both A and B mobile phases for this peptide, which improved the chromatography significantly. After the purified peptide was lyophilized, it was dissolved in a minimal amount of glacial acetic acid

with a small amount of water and acetonitrile for complete dissolution. After a few minutes, the solution was diluted with Milli-Q water, re-lyophilized, then aliquoted and analyzed as described above.

4.5.4 Reverse-Phase Liquid-Chromatography Mass-Spectrometry (LCMS) Analysis of Peptides

LCMS was used to confirm the completion of synthesis reactions, measure peptide purity, and measure peptide concentrations in polymersome formulations.

An analytical column was used to match the purification column and facilitate method transfer (XBridge Peptide BEH C18, 130 Å, 5μm, 4 mm x 150 mm) with mobile phases A (water + 0.1% TFA) and B (ACN). An example of a general method includes a 5 minute isocratic loading phase at 10% B, a 3-5%/minute separation gradient, then a column wash at 100% B for 5-10 minutes, followed by re-equilibration at 10% B. Columns were always stored in 100% acetonitrile. All samples were filtered through a 0.2 μm filter, except polymersomes that had been extruded, which should also remove dust and debris.

Peptide purity was calculated by the Agilent software integrating the 220 nm absorbance chromatogram.

Peptide concentration in polymersomes was measured by running a AAA-quantified standard sample and using the area under the curve of the peptide peak's UV absorbance to calculate the amount of peptide injected from an unknown sample. The area under the curve is directly proportional to the amount of peptide injected. The polymer seemed to interact strongly with the column, so after a set of polymersome samples, the column was washed with acetonitrile, DCM, then acetonitrile again, being careful to never have water and DCM in the column at the same time.

4.5.5 Polymersome Assembly

For thin film assembly, the polymers were dissolved in DCM, and 10 mg of polymer was transferred to a 2 mL glass vial that had first been piranha-etched. The DCM was evaporated under high vacuum to form a thin layer of polymer film on the glass walls. 250 μL of sterile PBS was added to the vial, and the vial was slowly rotated at room temperature for 2-3 days, until no polymer was visible on the vial walls.

For flash nanoprecipitation (FNP), we 3D-printed a CIJ-D device (Figure 4.7) using the same design parameters originally reported by Han et al. [277] and previously used by others for assembly of PEG-PPS polymersomes [190, 191]. 3D-printing allowed for rapid, reproducible assembly of these devices. Syringe adapters (IDEX P604) and outlet adapters (IDEX P202X, IDEX P200X) were purchased from Fisher Scientific. The outlet tubing used was 1/16" O.D. and 0.04" I.D. Before each use, the device was sterilized and cleaned with 0.5 M NaOH and rinsed repeatedly with Milli-Q water. All assemblies were done in a sterile hood, following the protocols and ratios previously described by Allen et al. [190, 191].

For calcein encapsulations, a 100 mM calcein solution was prepared at physiological osmolarity ($\sim$313 mOsm). Calcein in its protonated form (Calcein High Purity, Thermo Fisher Scientific) was first dissolved in 2 molar equivalents of NaOH from a 1 M solution, then 13 mOsm worth of 1X PBS, pH 7.4 (Gibco, Thermo Fisher Scientific), was added. The solution was then diluted to a final calcein concentration of 100 mM using Milli-Q water for a final osmolarity of 313 mOsm. This solution was used both as the anti-solvent stream in the syringe and as the dilution reservoir during FNP encapsulation.

For stapled peptide encapsulations, polymer was dissolved in THF at 40 - 100 mg/mL. SAH-MS1-18 or BIM-SAHB was added from a DMSO stock solution (20 - 100 mM) at peptide:polymer mass ratios of $\sim$1:4, then this THF solution was diluted 1:1 with PBS in an attempt to solubilize as much peptide as possible. This solution was then impinged against PBS into a PBS reservoir. For our largest-scale assemblies, the PBS-dilution step was omitted, and THF was removed from the FNP-mixed solution by rotary evaporation to

make a highly concentrated polymersome solution.

All polymersome samples were then extruded 11 - 21 times through a 100 nm pore-size membrane (Whatman Nucleopore Track-Etched Membrane, 19 mm, 100 nm) using a syringe-driven Mini Extruder (Avanti Polar Lipids) in a sterile hood. Size and dispersity were monitored by DLS. The polymersomes were then immediately purified from any residual organic solvents using gravity-driven disposable PD-10 desalting columns containing Sephadex G-25 resin (GE Healthcare) into 1x PBS, pH 7.4 (Gibco, Thermo Fisher Scientific). If non-encapsulated cargoes needed to be fully removed and no further workup would be performed, then the polymersomes were instead purified into PBS over Sepharose CL-4B or using a 300 kDa MWCO MicroKros device to fully remove non-encapsulated cargoes.

4.5.6 Measuring Polymersome Stability in Serum via Calcein Fluorescence Dequenching

Polymersomes encapsulating a self-quenching calcein solution were assembled as described above. The resulting stock solution was diluted 1:100 into either RPMI 1640 ("media"), media + 10% fetal bovine serum (FBS), or media + 10% FBS + 5 mM Triton X-100 in a black, flat-bottom 96-well plate. Samples were incubated at 37 °C, and the calcein fluorescence was monitored for 1 hour via plate reader (SpectraMax iD5, Molecular Devices). Each sample was prepared in quadruplicate, and each value was background-subtracted using corresponding samples prepared by diluting pure PBS instead of polymersomes into the indicated solution (though all background solutions had negligible fluorescence values).

4.5.7 Aqueous Size-Exclusion High-Performance Liquid Chromatography (SEC HPLC)

The same PBS solution was used as the mobile phase as for polymersome assembly and for dissolving lyophilized peptides before SEC HPLC. The column used was AdvanceBio SEC,

130 Å, 2.7 μm, 4.6 mm diameter with a 50 mm length guard column in series with a 150 mm column (Agilent). The polymersome solution was stored at 4 °C for one month before analysis. Peptide concentrations in the polymersome solution were measured by LCMS using the area under the curve of the UV absorbance chromatogram, and SEC HPLC samples injected were equimolar in peptide as measured by reverse-phase LCMS.

4.5.8 Fab Design

The αCD19 Fab was designed using published variable region sequences (V_κ and V_H) from HD37 mouse-anti-human-CD19 IgG [280, 281], for both light chain (GenBank CAA67620, amino acids 1-111) and heavy chain (GenBank CAA67618, amino acids 1-124), combined with constant regions (C_κ and C_H) from mouse IgG consensus sequences for light chain (UniProt P01837, amino acids 1-107) and heavy chain (UniProt P01868, amino acids 1-104). To create an irrelevant control Fab, the variable regions were substituted for those from an antibody specific for xenoantigen OspA without changing the constant regions [282, 283]. A cysteine linker (...GSGGSSGSGC) was encoded on the C-terminus of the heavy chain to create αCD19-cys and αOspA-cys for site-specific conjugation to polymersomes.

4.5.9 Fab Cloning

Fab sequences were acquired as gBlocks Gene Fragments (Integrated DNA Technologies) and cloned into an AbVec2.0 plasmid under a cytomegalovirus (CMV) promoter for constitutive mammalian expression [288]. A signal peptide sequence derived from osteonectin was added to the N-terminus of both light and heavy chains to induce protein secretion. The plasmid also contained an ampicillin resistance gene under a constitutive *E. coli* promoter. After cloning and transformation into competent *DH5α*, the plasmid was selected for using ampicillin, and propagated by bacterial growth in lysogeny broth (LB) with 100 μg/mL ampicillin in shaker flasks at 37 °C. The plasmid was isolated using NuelcoBond Xtra Maxi kits (Machery Nagel). Purified plasmids were sequenced at the University of Chicago Comprehensive

Cancer Center DNA Sequencing and Genotyping Facility (UCCCC-DSF), and all sequences were confirmed to align with the designed sequences (Benchling).

4.5.10 Fab Expression and Purification

Fabs were expressed in HEK293T suspension cells in FreeStyle 293 Expression Medium (Thermo Fisher Scientific). At 1 million cells/mL in log-phase growth, cells were transfected with 1 μg of plasmid and 2 μg of polyethylenamine in 40 μL OptiPRO SFM (Gibco) per million cells. Transfected cells were cultured for 6 days in shake flasks at 37 °C and 5% CO2. The cells were then pelleted by centrifugation, and the supernatant was filtered through a 0.22 μm filter and pH-adjusted to 7.0 using 1 M Tris buffer, pH 9.0. The Fabs were then purified by affinity chromatography using 5 mL HiTrap Protein G HP columns (GE Life Sciences) via fast protein liquid chromatography (AKTA FPLC, GE Healthcare). A dedicated column was used for each Fab to prevent cross-contamination. For large scale purification, up to 3 x 5 mL columns were connected in series. The column was first equilibrated with 5 column volumes (CVs) of PBS at 5 mL/min. The crude Fab solution was then flowed over the column at 5 mL/min and the column washed with 10 CVs of PBS. Pure Fab was eluted with 0.1 M glycine-HCl, pH 2.7, into 3 mL fractions pre-buffered with 125 μL of 1 M Tris buffer, pH 9.0, and 1 mL of 1x PBS, pH 7.4, to achieve a neutral pH in each fraction upon elution. The crude flow-through was collected and the purification repeated multiple times until the UV-absorbance of the elution peak was minimal. Elution peaks were pooled, dialyzed extensively (Slide-A-Lyzer, G2 Dialysis Cassettes, 10 kDa MWCO, Thermo Fisher Scientific) against 1x PBS, pH 7.4, concentrated (Amicon Ultra-15, 10 kDa MWCO, Millipore Sigma) to no more than 10 mg/mL, sterile filtered, and either stored at 4 °C or aliquoted and frozen for later use.

Fab concentrations were calculated using UV absorbance based on their calculated extinction coefficients at 280 nm (48,923 $M^{-1}cm^{-1}$ for αCD19-cys and 47,432 $M^{-1}cm^{-1}$ for αOspA-cys).

4.5.11 Fab Functionalization with DBCO

Coomassie-stained SDS-PAGE was used to determine the fraction of each sample that was unimeric, intact Fab, as opposed to Fab-Fab disulfides or free heavy/light chain, which were the two other minor bands in some samples (Figure 4.10). The fraction of intact, unimeric Fab was always > 80%. The concentration of unimeric, intact Fab, was then calculated as the product of the concentration determined by UV absorbance at 280 nm and the fraction determined by SDS-PAGE.

Before the reduction reaction, EDTA (UltraPure, 0.5 M EDTA, pH 8.0; Invitrogen) was added to a final concentration of 10 mM to the Fabs in PBS, pH 7.4. TCEP, aliquoted in Milli-Q water and frozen at 1 M, was diluted immediately before use to 1 mM in PBS + 10 mM EDTA, pH 7.4. TCEP (0.85 equivalents with respect to the concentration of intact, unimeric Fab) was added to the Fab, and the reaction was immediately vortexed. The reaction was incubated at 37 °C for 90 minutes. The heterobifunctional linker, Sulfo-DBCO-PEG4-Maleimide (Click Chemistry Tools), was dissolved immediately before use at 20 mM in PBS with 10 mM EDTA, pH 7.4. 100 equivalents of the linker were added to the reduced Fab without workup, and the reaction was immediately vortexed and incubated at room temperature for 1 hour. After 1 hour, the Fab was immediately purified by 8 rounds of diafiltration into 1x PBS, pH 7.4, at 4 °C, using Amicon ultrafiltration devices with a 10 kDa MWCO and a volume appropriate to the scale of the reaction to avoid concentrating the Fabs to greater than 10 mg/mL. Functionalized Fabs were then sterile filtered.

After purification of Fab-DBCO, the Fab concentration was calculated using equation 4.1:

$$\text{Concentration of Fab (M)} = \frac{A_{280} - (A_{309} \times \text{CF})}{\epsilon_{\text{Fab},280}} \tag{4.1}$$

with A_{280} and A_{309} the sample absorbance at 280 nm and 309 nm respectively, the correction factor $\text{CF} = \frac{\epsilon_{\text{DBCO},280}}{\epsilon_{\text{DBCO},309}} = 1.089$, and $\epsilon_{\text{Fab},280}$, the extinction coefficient of the Fab at 280 nm

(48,923 $M^{-1}cm^{-1}$ for αCD19-cys and 47,432 $M^{-1}cm^{-1}$ for αOspA-cys).

DBCO concentration was calculated using equation 4.2:

$$\text{Concentration of DBCO (M)} = \frac{A_{309}}{\epsilon_{\text{DBCO},309}} \tag{4.2}$$

with $\epsilon_{\text{DBCO},309} = 12,000 M^{-1}cm^{-1}$.

The number of DBCO groups per Fab was then calculated as the ratio of their concentrations as measured by UV absorbance.

DBCO-functionalized Fabs were stored at 4 °C if they would be used within a few weeks, and the rest were aliquoted and frozen at -20 °C.

4.5.12 Fab Conjugation to Polymersomes

Polymersomes were assembled as described above, with 5% N_3-PEG-SS-PPS and 95% mPEG-SS-PPS. DBCO-functionalized Fabs were then reacted with the N_3-functionalized polymersomes with Fab-DBCO as the limiting functional group. The smaller volume, the DBCO-functionalized Fab, was added to the tube first, and the larger volume, the N_3-functionalized polymersomes, was then added rapidly and immediately mixed by pipetting or vortexing to ensure uniform distribution within the reaction. The click reaction was allowed to proceed overnight at room temperature. The samples were then either purified or transferred to 4 °C until purification.

Fab-functionalized polymersomes were purified by size into PBS either by gravity-driven SEC using Sepharose CL-4B resin or by diafiltration using TFF (MicroKros, 300 kDa MWCO, mPES, 0.5 mm; Repligen) driven either by syringe or, at larger scales, by peristaltic pump (Figure 4.20; Fisher Scientific, 13-876-2). The gravity column or TFF flow path was first sterilized using 0.5 M NaOH, then equilibrated with PBS prior to purification, all in a sterile hood.

For purified, Fab-functionalized polymersomes, SAH-MS1-18:polymer mass ratios were

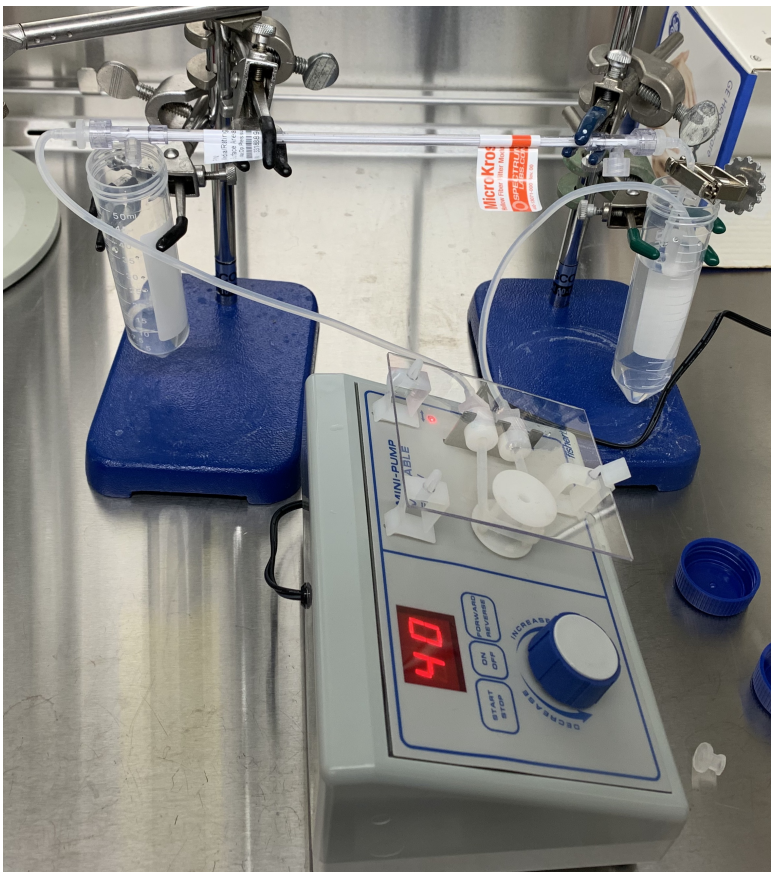

Figure 4.20: Peristaltic-pump tangential flow filtration (TFF). A peristaltic pump (Fisher Scientific, 13-876-2) was set up with tubing on the pump spindle (3/32") such that a medium-speed (40 - 50) corresponds to no more than 12 mL/min. Using 1/16" tubing, the sample was drawn clockwise through the setup shown: from the bottom of the sample reservoir (right side, 50 mL tube), through the pump, to the MicroKros module inlet, and from the MicroKros module outlet back to the sample reservoir. The filtrate was collected in a separate 50 mL tube (left side). To increase the rate of filtration, a slight amount of backpressure (not enough to slow the flow rate much) was generated using a screw compressor clamp on the outlet tubing from the MicroKros outlet to the sample reservoir (Humboldt H-8665). Using this setup, the dead volume was minimal, approximately 2 mL, and polymersome concentration and diafiltration were semi-automated.

typically ∼1:10 - 1:20, with encapsulation efficiency ∼10 - 20%. For every formulation, peptide concentrations were measured by LCMS against a AAA-quantified sample, polymer concentrations measured by GPC using refractive index AUC, and Fab concentrations measured using CBQCA against a UV-vis quantified Fab-DBCO control.

4.5.13 Flow Cytometry Staining

Purchased from BioLegend were mouse Fc block (TruStain FcX (anti-mouse CD16/32) antibody, 101320), PE anti-human CD45 (304039, clone HI30), APC anti-human CD19 (363006, clone SJ25C1), and APC-Cy7 anti-human CD20 (302314, clone 2H7). Human Fc block (BD Biosciences 564220, clone 3070) was purchased from Fisher Scientific. Depending on the available lasers on the cytometer used, live/dead (L/D) stain was either a UV-excitation dye (Invitrogen Fixable Blue Dead Cell Stain, L23105) or a violet excitation dye (BioLegend, Zombie Violet Fixable Viability Kit, 423113). To detect our mouse-backbone Fabs by flow cytometry, a secondary anti-Fab $F(ab')_2$ was purchased from Jackson ImmunoResearch (Alexa Fluor 647 AffiniPure $F(ab')_2$ Fragment Donkey Anti-Mouse IgG (H+L), 715-606-151).

For a general staining protocol, cells were washed with PBS and stained with L/D stain 1:500 in PBS for 15 minutes on ice. Fc block was then added directly to the mixture (1:200 for human Fc block, 1:50 for mouse Fc block) for 15 minutes on ice. Antibodies were then added (final dilution 1:100) for 30 minutes on ice. Cells were centrifuged, resuspend in FACS buffer (5% FBS in PBS), and analyzed by flow cytometry.

4.5.14 Cell Culture

Human DLBCL cell lines were cultured in RPMI 1640 (Gibco, Thermo Fisher Scientific) supplemented with 10% FBS, 10 mM HEPES (Gibco, 1 M), 2 mM L-glutamine (Gibco, 200 mM), MEM non-essential amino acids (Gibco, from 100x solution), and 100 U/mL penicillin-streptomycin (Gibco, 10,000 U/mL) at 37 °C and 5% CO_2. Cells were split every 2-3 days. Most cell lines were split to 0.5 million cells per mL, but SU-DHL-5 and OCI-Ly3 were split

to 0.1 million cells per mL or lower and not allowed to reach densities higher than 1 million cells per mL.

SU-DHL-5 was acquired from ATCC, and OCI-Ly3 and OCI-Ly19 were acquired from DSMZ. The Kline lab kindly shared with us OCI-Ly1, OCI-Ly8, DOHH-2, VAL, and RCK-8.

4.5.15 Cell Death Assays

Treatments were prepared in 96-well plates in 50 μL at 2x concentration. Cells were suspended at 0.2 million cells per mL, and 50 μL (10,000 cells) were added to each well and pipette-mixed. The plates were incubated for 24 - 72 hours, depending on the experiment, then 100 μL of CellTiter-Glo 2.0 (Promega) was added and pipette-mixed, followed by luminescence reading (SpectraMax iD5, Molecular Devices).

4.5.16 Quantitative Real-Time PCR (qRT-PCR)

Following relevant drug treatments as indicated, cells were lysed with Trizol (Life Technologies) and total RNA was isolated from each sample using the Direct-zol RNA MiniPrep kit (Zymo Research) per the manufacturer's instructions and quantified (DeNovix DS-11 Spectrophotometer). RNA from each biological replicate (500 ng) was converted to double-stranded cDNA using the Superscript III first strand synthesis reverse transcription kit (Invitrogen) per the manufacturer's directions.

qRT-PCR was performed using TaqMan Master Mix and Gene Expression Probes (Applied Biosystems) for each of the following genes: A1: Hs00187845, B2M: Hs00984230, BAD: Hs00188930, BAK: Hs00832876, BAX: Hs00180269, BCL2: Hs00608023, BCLW: Hs00187848, BCLXL: Hs00236329, BID: Hs00609632, BIM: Hs00708019, BMF: Hs00372937, CDKN1A: Hs00355782, GAPDH: Hs02758991, MCL1: H01050896, NOXA: Hs00560402, PUMA: Hs00248075. Samples were run on the 7500 Fast Real-Time PCR System (Applied Biosciences). Data was analyzed with the ExpressionSuite software utilizing the $\Delta\Delta$CT method with GAPDH and B2M as two housekeeping genes and DMSO-treated cells as ref-

erence samples.

4.5.17 Xenografts

Cells were resuspended in either PBS or 50% matrigel in PBS for subcutaneous engraftments using no more than 200 μL. Typically 5 million cells were engrafted per tumor. For disseminated engraftments, no more than 200 μL of cells in PBS were injected through either retro-orbital or tail vein injection.

4.6 Author Contributions

Many co-authors have contributed to the work in this chapter. Katrina Maxcy conducted qPCR experiments, mouse injections, mouse dissections, tumor measurements, and helped maintain the mouse colony. Elyse Watkins designed, cloned, and expressed the Fabs and advised on their purification, storage, and handling. Logan Leak did qPCR, cell death assays, western blotting, BH3 profiling/priming, and cell culture. Dr. Jeffrey Ting contributed to the synthesis and analysis of the PEG-SS-PPS polymers, as well as SAXS data analysis of the polymersomes. Isadora Kucera contributed to peptide synthesis, purification, and analysis, in addition to Fab plasmid production and purification. Rosy Liao contributed to western blotting. Dr. Lindsey Ludwig contributed to BH3 priming and profiling. Michal Raczy contributed to polymer synthesis, polymersome formation and purification, and polymersome characterizations. Yu Tian did electron microscopy imaging and contributed to the peptide synthesis and purification processes. Sicheng Jiang contributed to peptide purification. Professors James LaBelle, Matthew Tirrell, and Jeffrey Hubbell guided, advised, and supported the many various aspects of this project, contributing to data analysis, experiment conception, and the general directions of the project along the way.

4.7 Acknowledgements

Parts of this work were carried out at the Soft Matter Characterization Facility at the University of Chicago. We thank Tera Lavoie, Ph.D., in the Advanced Electron Microscopy Facility at the University of Chicago for her expertise and contributions to the cryo-EM imaging experiments. We acknowledge the MRSEC Shared User Facilities (NSF DMR-1420709) and Jeffrey Gustafson for assistance in 3D-printing our CIJ-D devices. Some flow cytometry experiments were carried in the Cytometry and Antibody Technology (CAT) core facility with support of the NCI Cancer Center Support Grant (P30CA014599).

I would like to thank Professor Evan Scott and Molly Frey in the Scott Lab at Northwestern University for helpful conversations and for sharing their expertise working with PEG-PPS block copolymers and polymersomes. I would also like to thank Dr. Edoardo Scarpa, from the Battaglia Lab, for his advice on tangential flow filtration purification and concentration of polymersomes. Dr. Kline's lab at the University of Chicago shared with us a number of DLBCL cell lines, and Dr. James Godfrey and Sravya Tumuluru shared with us their expertise in using them for xenografts.

CHAPTER 5

DISCUSSION, FUTURE DIRECTIONS, AND CONCLUSIONS

5.1 Molecular Medicines vs. Supramolecular Nanomedicines

Almost all of the most widely used medicines today rely on one molecule to be able to have reasonable pharmacokinetics in the blood stream, reach its target in a specific place in the body, and once there exert its therapeutic effect. The properties that one molecule must have to be able to do that – to be a "drug-like" molecule – are fairly well understood. However, when developing drugs, there are trade-offs between properties such as molecular size, binding specificity, potency, toxicity, cellular uptake, and solubility, among other considerations. Optimizing one of these important parameters is typically detrimental to others, and these trade-offs present the dilemma of "undruggable" targets that cannot be drugged by a single molecule, including intracellular PPIs (see Section 1.1).

Supramolecular nanomaterials have started to overcome some of these trade-offs. By encapsulating drugs in nanomaterials, a drug molecule can be used that meets only some of the "drug-like" requirements (e.g. binding potency and specificity with its target), while a nanocarrier can bolster the drug's other drug-like properties (e.g. pharmacokinetics, tumor accumulation, cellular uptake, endosomal escape). There are now numerous examples of supramolecular nanomedicines that are being used clinically (as thoroughly reviewed recently by Anselmo and Mitragotri [114, 115]). The most successful class of nanomedicines for cancers are liposomes encapsulating cytotoxic small molecule drugs (see Section 1.3.3). By encapsulating the drugs in nanocarriers, the pharmacokinetics can be improved, the toxicity lessened, and the intratumoral accumulation increased. An exciting recent breakthrough example is patisiran, a now clinically approved supramolecular nanomedicine that delivers an siRNA into hepatocytes to knock down a disease-driving protein. In this case, an siRNA could never be a therapeutic on its own due to a complete lack of drug-like properties (rapid clearance, immunogenicity, lack of cellular uptake), but a carefully designed nanocar-

rier can address the drug-like weaknesses to unlock a new set of druggable disease targets. Supramolecular nanomedicines represent an important paradigm shift that expands the pool of druggable targets beyond the classic one-molecule-drug paradigm.

Our work, as shown throughout this thesis, seeks to develop supramolecular nanocarriers to use peptide-based therapeutics to drug intracellular PPIs. While peptides can be designed to specifically and tightly bind to a target protein, they lack drug-like properties necessary to be able to reach their target proteins inside diseased cells within the body (see Section 1.2.2). With a supramolecular delivery system, a PPI inhibitor could ideally be developed focusing solely on binding specificity at the molecular level, while letting a supramolecular nanocarrier address the pharmacokinetics, cellular uptake, and endosomal escape.

Here, I first discuss the supramolecular nanocarriers used in this thesis for intracellular delivery of therapeutic peptides and their relative strengths, weaknesses, and future outlooks. Then I discuss ways in which the pool of druggable PPIs might be further expanded, either by delivery of even more complex drug cargoes or by conceptualizing new ways to think about drugging PPIs other than simple orthosteric inhibition. I then discuss targeted nanomedicines, how our work conceptually advances the field, and exciting new directions in which targeted nanomedicines have room for improvement toward clinical efficacy.

5.2 Intracellular Delivery of Therapeutic Peptides Using Supramolecular Nanomaterials

Our goal was to develop a nanoparticle delivery system that could deliver stapled peptides to and into cancer cells in large doses, regardless of the peptide's intrinsic cellular uptake properties. To that end, we developed a peptide amphiphile micelle delivery system (Chapters 2 and 3) then a targeted polymersome delivery system (Chapter 4).

5.2.1 Peptide Amphiphiles

Our group's first iterations on this goal of intracellular peptide delivery involved attaching a lipid tail to a peptide to generate a peptide amphiphile (PA) [120, 121], which incorporated peptides into micellar nanostructures and allowed non-cell-permeable peptides to interact with a cell membrane and be internalized [125–127]. When we incorporated an endosome-labile linker between the peptide and the lipid tail, the peptide accumulated more within cells and had more potent therapeutic efficacy [141, 142].

This platform has numerous strengths for the intracellular delivery of therapeutic peptides, as discussed in Section 1.3.2. In summary, PA micelles protect the peptides from premature degradation and clearance, are amenable to targeting, facilitate cellular uptake, are biocompatible with unimers cleared through the kidneys upon disassembly, and the majority of a PA micelle's mass is comprised of the therapeutic peptide itself, which participates in the self-assembly as the hydrophilic headgroup.

For in vivo, intracellular delivery of peptide therapeutics, PA micelles face three remaining primary obstacles.

First, the dynamic nature of lipid-based micelles causes them to dissociate in the presence of serum proteins within 8 minutes [271]. While this is often enough time to actively target PA nanoparticles to accumulate in a specific tissue [128–140], complete stability would allow for RME of an intact, supramolecular nanostructure with its entire therapeutic payload. Attaching targeting elements (e.g. Fabs) to the surface of a highly dynamic, lipid based micelle should also prove quite difficult. As some of the targeting elements dissociate from the rest of the structure, they would become competitive inhibitors of the other targeting elements still associated with the therapeutic cargoes.

Some potential strategies come to mind for stabilizing PA micelles and thereby enabling intact targeting and RME. One possibility, as has been done by Liu et al. [236], is to incorporate four or more guanine repeats between the hydrophobic tail domain and the hydrophilic head group. This allowed for the formation of G-quadruplex entanglements be-

tween unimers, thereby stabilizing the micelles in the presence of serum proteins. In fact, these G-quadruplexes accomplished precisely what we seek to do, which is completely inhibiting the interactions of the PAs with albumin [236]. Some other form of crosslinking or entanglement in the corona could also be used to make the micelles more stable. Alternatively, it might be possible to cross-link the lipid cores of the micelles. This would require new lipid tails to be synthesized, with chemical functionalities suitable for crosslinking. The saturated hydrocarbons we typically use are not chemically reactive in any ways conducive to crosslinking. In fact, many crosslinking chemistries require at least some polarity in their functional groups, so one would need to be careful not to disrupt the propensity of the PAs to form micelles while trying to cross-link lipid tails. If some sort of stabilizing interactions were added to PA micelles, they could be made more conducive to targeting and RME of an intact micelle.

Second, after endocytosis, non-membrane-permeable therapeutic peptides require some intentional mechanism for endosomal escape. In Chapter 2 [142], a BIM BH3 peptide was endocytosed as a PA, after which endo-lysosomal cathepsins cleaved a linker to remove the peptide from the tail, and by some unknown means the peptide escaped the endosome to act as a therapeutic and activate apoptosis. However, this approach was not universally generalizable to other peptides, which failed to exert a therapeutic effect using a very similar molecular design (e.g. Acar et al. 2017 with an unstructured p53 peptide [141], Section 3.10 with p53 stapled peptide amphiphiles). To overcome this, a mechanism for endosomal escape should be incorporated into the PA micelle design. For example, mixed micelles could be made with endosome-escape peptides as PAs mixed with the therapeutic PAs. Ideally, these should be peptide sequences that are activated only in the endosome (e.g. at acidifying pH, such as TAT, Penetratin, or HA2) and not always active (e.g. Arginine-repeat sequences, such as R8), in order to avoid non-specific uptake by cells before reaching the targeted cell type.

Third, there is potential to improve the PA linker for intracellular peptide release. In our

current work, we have used a cathepsin-cleavable linker [141, 142], but it is possible that this waits until too late in endo-lysosomal maturation to cleave the linker when cathepsins could also start cleaving the therapeutic peptide. Moreover, if an endosome escape element is incorporated into PA micelles, the cleavable linker would need to be cleaved before endosomal escape. Using a linker that is cleaved late in endosome maturation could lead to non-cleaved PAs being released from the endosome, instead of the released therapeutic peptide. One possible alternative could be a disulfide-based linker, which could allow for earlier release in endosomes [175–181], before acidification and protease activation. The cytoplasmic environment is also relatively reducing compared to the extracellular space, and if the PA is released to the cytoplasm without tail removal, the linker could still be cleaved there. The cathepsin-cleavable linker has proven quite promising for releasing the therapeutic peptide in the endosome, but when endosome escape functionalities are incorporated, the timing and mechanism of linker release will need to be coordinated with the timing of endosomal escape.

Finally, while this delivery platform is amenable to peptides, which participate in the self-assembly process, it would be difficult to extrapolate this strategy to whole proteins. It should be possible to use this platform to drug PPIs that rely primarily on primary structure or α-helical secondary structure, but expanding to more complicated tertiary structures could prove difficult without correspondingly larger therapeutics, such as proteins.

5.2.2 Polymersomes

The second platform we used for intracellular delivery of peptide therapeutics was PEG-SS-PPS polymersomes with αCD19 Fab targeting moieties (Chapter 4). The Hubbell lab had previously developed the PEG-PPS polymersome system (discussed in Section 1.3.5 and Chapter 4) for vaccine applications, including delivering protein antigens to phagocytic immune cells. With a few modifications, this system seemed to have ideal characteristics of a targeted nanocarrier for intracellular delivery of hydrocarbon-stapled peptide therapeutics.

These polymersomes are highly stable, polymeric vesicles, somewhat analogous to li-

posomes [169, 174, 188]. As our polymer building block, we chose an amphiphilic block copolymer composed of a hydrophilic poly(ethylene glycol) (PEG) block and a hydrophobic poly(propylene sulfide) (PPS) block with a disulfide bond between the two blocks (PEG-SS-PPS) [181]. This block copolymer and its similar counterparts have previously been shown to have characteristics of an ideal nano-excipient for intracellular delivery of stapled peptides. First, the excellent stability of polymersomes should allow for attachment of targeting ligands to the surface and RME of the intact nanocarrier. In collaboration with the Hubbell lab, we designed a CD19-binding Fab with a site-specific conjugation handle to make polymersomes that bind to DLBCL cells and facilitate endocytosis. Second, while liposomes can only achieve 5-10% PEGylation before their structure is disrupted [163–166], the 100% PEG functionalization on a polymersome surface produces a dense PEG brush, which resists protein-adsorption that would otherwise lead to non-specific uptake and clearance from the body. Third, PPS-based polymersomes have been shown to successfully encapsulate both hydrophilic cargoes in the aqueous core and hydrophobic cargoes in the PPS phase [181, 189, 196–198]. We hypothesized this dual hydrophobic/hydrophilic loading character would allow for successful encapsulation of hydrocarbon-stapled peptides, which have both a hydrophilic peptide domain and a hydrophobic all-hydrocarbon staple. Fourth, Cerritelli et al. showed that when a disulfide bond is used to link the PEG and PPS blocks together (i.e. PEG-SS-PPS), the block copolymer can be rapidly cleaved in the reducing endosome, which disrupts the polymersomes and allows the PPS block to rapidly facilitate endosomal escape and intracellular accumulation [181]. Fifth, the PPS backbone can be oxidized to become hydrophilic, which should allow the polymer to be cleared by glomerular filtration through the kidneys [192]. And sixth, this polymer's non-reducible counterpart (PEG-PPS) has recently been shown to be non-toxic in high doses in both mice and non-human primates [191]. Together, these characteristics describe a theoretically ideal nanocarrier for cytoplasmic delivery of a hydrocarbon stapled peptide to and into a targeted cell type.

Future work is needed to understand the role of the all-hydrocarbon staple in facilitating

encapsulation into these polymersomes and the utility targeted polymersomes for other cargoes. Anecdotally, multiple all-hydrocarbon-stapled peptides have been successfully loaded into these polymersomes, all with high degrees of encapsulation, while very similar peptides lacking only the staple had much lower degrees of encapsulation (data not shown). We hypothesize that the hydrocarbon staple has some beneficial interactions with the PPS bilayer, while the polar/charged peptide prefers the aqueous core and prevents the peptide from being able to diffuse out through the PPS bilayer.

Hydrophobic cargoes that might be more miscible with PPS, such as some small molecule drugs, might also benefit from solubilization and targeting in similar polymersomes, though their ability to diffuse out of the polymersomes would be an important question to evaluate. Anecdotally (data not shown here), certain small molecule BH3 mimetics seemed to rapidly leak out of PEG-SS-PPS polymersomes, while some were better retained. To adapt these targeted polymersomes to other types of cargoes, slight design changes may be beneficial, such as finding ways to retain cargoes in the core (e.g. Doxil pH entrapment in liposomes) or using a polymer with higher glass transition temperature. Whereas PPS has a glass transition temperature well below physiological temperature, modifying the polymersomes such that they are more solid-like could make them more resistant to hydrophobic cargo leakage.

Another benefit of this delivery platform for targeted, intracellular peptide delivery is its modularity. For example, click chemistry functionalization on the polymersome surface is easily amenable to any variety of surface ligands as well as ligand densities. The cargoes, meanwhile, can be hydrophilic, hydrophobic, or amphiphilic, thanks to the presence of both the hydrophobic PPS layer and the hollow, aqueous lumen. Importantly, the cargo encapsulation is a physical process, which allows for unmodified cargoes to be rapidly encapsulated. Chemically modifying peptides to incorporate them into a nanocarrier, for example as peptide amphiphiles, is relatively synthetically challenging and low throughput. Moreover, appending a lipid to a peptide can interfere with the peptide's binding to its target

protein and requires a cleavable linker to release the tail from the peptide after internalization. With a physical encapsulation process, such as with these polymersomes, unmodified peptide cargoes can be rapidly encapsulated without chemical modifications or labile linkers. The flexibility and modularity of targeted PEG-SS-PPS polymersomes, in both its cargo encapsulation and targeting ligands, allows for rapid screening of therapeutic formulations and targeting ligands.

5.3 Increasing the Pool of Druggable PPIs

Currently, the majority of known, disease-driving PPIs are considered undruggable, and the main reason is the large size of PPIs relative to the small size of "drug-like" molecules (see Section 1.1). Very few PPIs are mediated by small "hotpot" domains that can be drugged with small molecules, but for those that are, small molecules have proven effective (e.g. venetoclax inhibiting BCL-2's PPI interface). Stapled peptides have begun to expand the druggable set of PPIs to include those that are primarily mediated by an α-helix (e.g. ALRN-6924 to competitively release and reactivate p53). However, the majority of PPIs have much more complicated interaction interfaces mediated by residues spanning tertiary structures that are larger than even stapled peptides can inhibit. For this majority of PPIs, larger biologics may need to be used as PPI inhibitors, and as the therapeutics get larger and more polar, their intracellular delivery gets more difficult.

5.3.1 Intracellular Delivery of Proteins

Nanomaterials such as PEG-SS-PPS could prove to be useful for cell-specific, cytoplasmic delivery of whole proteins. PEG-PPS polymersomes have repeatedly been used for protein encapsulation for immune-modulation applications, and with the reducible PEG-SS-PPS to facilitate rapid endosomal escape, this platform could be amenable to cell-specific, cytoplasmic delivery of entire proteins. If this works, one could imagine numerous applications that

would be enabled.

First, recombinant proteins with precise tertiary structures could be used as inhibitors of very large PPIs that could otherwise not be blocked with other, smaller tools. As one exciting example, antibodies and antibody fragments could be used as intracellular PPI inhibitors. Antibodies have been remarkably effective and successful at targeting extracellular proteins as biologic therapeutics, and enabling their intracellular access would unlock an entire domain of druggable targets.

In another interesting application, an intracellular immunity function exists involving TRIM21, which recognizes intracellular, antibody-bound ligands and facilitates their degradation [289]. With intracellular delivery of entire antibodies, this would unlock a more rapid development platform for intracellular PPI inhibitors in a way that not only inhibits the protein but degrades it.

With intracellular protein delivery at sufficient doses, one could also imagine replacing lost or mutated proteins in a transient way. Tools such as CRISPR have proven promising for addressing genetic diseases, but the ethical concerns and implications of genetic editing, especially inheritable edits, are still being established. Delivering copies of the protein would be a transient therapeutic to accomplish the same goal. As one example, in cancers with mutated p53, perhaps a recombinant wildtype p53 could be delivered into cancer cells. Since the cancer cells were not pressured to develop p53-inactivating mechanisms, these cancer cells should theoretically be quite sensitive to p53-induced cell death. Because p53 is a transcription factor, its therapeutic effect would be greatly amplified, and less protein might be required to be delivered into the cell.

5.3.2 Intracellular Delivery of Nucleic Acids

In addition to proteins, nucleic acids could unlock countless druggable targets with sufficient intracellular delivery. Rather than blocking or degrading a disease-driving PPI partner, one could deliver an siRNA to knock down the protein in diseased cells. This is precisely the

mechanism used by patisiran, the first FDA-approved nanomedicine for intracellular delivery of a nucleic acid, namely siRNA (see Section 1.3.1). Currently, this strategy is clinically applied to a genetic disease to knock down a mutant protein. With active-targeting functionalities, one could imagine extending this platform to countless disease-driving PPIs, in which the proteins are not mutated but their relative levels and interactions are deregulated.

As with protein delivery, mRNA delivery could be used to replace lost proteins in a transient manner, without permanent DNA modifications. Using the same example as above, mRNA encoding the wildtype p53 protein could be delivered into cancer cells that have mutated or deleted p53. This sudden introduction of a tumor suppressor might rapidly induce apoptosis in cancers with mutated p53.

5.3.3 Modulating PPIs without Orthosteric Inhibitors

In addition to the *supramolecular* medicine approaches presented above, there are currently many active lines of research into *molecular* medicine modalities that can also be used for drugging "undruggable" targets such as intracellular PPIs.

For example, proteolysis targeting chimeras (PROTACs) are two-headed therapeutics in which one head binds to the target protein and the other head binds to an E3 ubiquitin ligase. This creates a ternary complex to catalyze the ubiquitination and degradation of the target protein. With this approach, a small molecule would not need to orthosterically inhibit a PPI interface, which is nearly impossible for small molecules to do (see Section 1.1). Instead, a small molecule could be used that binds anywhere on the target protein, then by turning it into a PROTAC, it could inhibit that protein by proteolytic knockdown. This is a relatively new therapeutic paradigm that could allow more traditionally "drug-like" molecules to expand the pool of druggable PPIs.

Alternatively, some "undruggable" proteins are mediated by more druggable targets upstream. By drugging these more druggable upstream targets, one can indirectly affect the protein of interest. For an example relevant to our work with apoptosis and the BCL-2

family, simultaneous inhibition of BCL-2, MCL-1, and BCL-XL, three of the primary anti-apoptotic members of the BCL-2 family responsible for cancer cell survival (see Section 1.1.1), is potently synergistic to reactivate apoptosis in many cancers. While a BCL-2 inhibitor is clinically approved (i.e. venetoclax), a specific and effective inhibitor of MCL-1 or BCL-XL has been difficult to develop via the classic PPI inhibition paradigm of orthosteric binding. Meanwhile, kinases can readily be drugged using classic, drug-like inhibitors. Ibrutinib is a drug that inhibits Bruton's tyrosine kinase (BTK), a critical kinase in B-cell signaling, and this inhibition leads to downstream downregulation of MCL-1 and BCL-XL in malignant B cells [290]. Therefore, ibrutinib treatment can be used to indirectly downregulate MCL-1 and BCL-XL and thereby synergize with direct BCL-2 inhibition by venetoclax [290, 291]. This is one example of drugging more druggable upstream targets of an undruggable protein, and in this case it even does so in a specific cell type (i.e. B cells). This is a less direct strategy than simply inhibiting the problematic protein, and a lot of other cell signaling changes occur downstream in addition to the intended change. However, thinking about and discovering upstream regulators such as BTK could unlock new ways to drug known but undruggable disease-driving PPIs.

5.4 Targeted Nanoparticle Drug Delivery

Targeted nanoparticles are an exciting improvement over the non-targeted nanoparticles that are currently approved for clinical use (introduced in Section 1.3.6). In addition to the potential benefits simply from encapsulation (e.g. improving the pharmacokinetics of a drug, minimizing toxicity, facilitating intratumoral accumulation via the enhanced permeability and retention (EPR) effect), such as for clinically-approved liposomes, nanoparticles can be functionalized with active targeting ligands to cause accumulation in specific tissues or cell types and even promote endocytosis into targeted cells [158]. While no actively targeted nanoparticles have yet been translated into clinical use, there are countless pre-clinical examples of the benefits of active targeting, including our work in Chapter 4.

5.4.1 Fabs as Engineered Targeting Moieties

In our first attempt to develop a recombinant, CD19-binding antibody fragment for targeting nanocarriers to DLBCL, we cloned an scFv antibody fragment for expression in *E. coli*. This αCD19 scFv had a 6x His tag and a site-specific cysteine conjugation handle. The scFv domain was designed using the sequences from the scFv portion of the chimeric antigen receptor (CAR) of αCD19 CAR T cells. Despite trying to optimize the expression in *E. coli*, either from whole-cell lysates, periplasmic extracts, or secreted protein, the majority of the scFv was trapped in insoluble inclusion bodies.

At this point, we stepped back and found a wealth of literature on nanoparticles with antibody targeting fragments, particularly work with liposomes from the lab of Theresa Allen (as introduced in Section 1.3.6). From that literature, we learned that scFv fragments often have problems with soluble expression or, if successfully expressed, instability during storage. Full IgG molecules however, while being very stable, have Fc domains that can be recognized by immune cells' Fc receptors to cause rapid clearance of the nanocarriers from the bloodstream (discussed in Section 1.3.6).

Meanwhile, Fab fragments were shown to be an ideal intermediate between an scFv and an IgG. In addition to the variable regions of the antibody "arm," a Fab also contains the constant portion of the antibody arm, and adding this domain seems to greatly contribute to the solubility and stability of Fabs relative to scFvs. While Fabs are about twice as large as scFvs, they are still about 1/3 the size of an IgG. And most importantly, Fabs completely lack the Fc domain that causes recognition and clearance of IgGs. For these reasons, they found that Fabs had ideal properties for nanoparticle targeting.

However, at the time of their work, Fabs were produced through proteolytic digestion of IgG into F(ab')2 fragments and subsequent disulfide reduction into F(ab') fragments. This production process greatly limited the economic scalability of Fab production for antibody-nanoparticle targeting, and thus they concluded that scFvs were more promising and scalable due to their potential ability to be recombinantly expressed at large scale. They then devised

strategies to enhance the stability of scFvs in solution to try to overcome their primary weakness: stability.

The production process presented in Chapter 4, using recombinant, engineered Fabs with a site-specific conjugation handle, represents an important advancement for ligand-targeted nanoparticles. Recombinant expression in mammalian cells overcomes the primary obstacle (i.e. scalability) of Fabs as targeting ligands. Moreover, it allows for the introduction of engineered modifications to the C-terminus of the heavy chain fragment, opposite the antigen binding face, such as a site-specific cysteine linker in our case. With this system, the antibody fragments are highly stable (unlike scFv fragments), scalable (unlike F(ab') fragments), have no Fc domain to facilitate clearance (unlike IgG), and require no recombinant tags for affinity purification as many common antibody affinity ligands can be used to bind Fabs (in our case, Protein G for Fabs with a mouse backbone). This system is also highly amenable to both rational design (e.g. from a known IgG sequence, as in Chapter 4) or screening development (e.g. phage display, yeast display). In our case, we designed the Fab from literature sequences, and it was soluble, highly expressed, correctly folded, and functional on the first try.

Much theoretical and experimental work has been done by others on understanding the receptor-mediated binding and uptake of targeted nanoparticles into cells. For example, the density of targeting ligands on the nanoparticle surface can greatly influence cellular uptake of the nanoparticles [285]. In our work, the density of targeting Fabs on the surface of the polymersomes did impact their uptake into DLBCL cells, but our optimization of that uptake was a crude approximation with only a few densities tested. Further fine-tuning the density of Fabs on the polymersome surface could potentially further improve their uptake into DLBCL cells.

5.4.2 "Super Selectivity" Using Cooperative Targeting Ligands

Targeting CD19+ malignant B cells is a good place to start with ligand targeted nanoparticles, because CD19 is an endocytic receptor, is expressed only on B cells, and is expressed on the vast majority of malignant B cells. However, there are many types of cancers, and indeed many other therapeutic applications, in which there is no known, obvious, and selective endocytic surface receptor to target. In these cases, which are the majority of applications, how can ligand-targeted nanoparticles be of any use?

Within the last 9 - 10 years, a new idea for ligand targeted nanoparticles has begun to emerge called "super selectivity" [292], which allows for designing nanoparticles that bind cells not only based on the presence of a surface receptor, but based on levels of expression, or even combinations of levels of expression of multiple receptors. Nanoparticles targeted to a single cell surface receptor, such as CD19, with a high affinity ligand, such as a Fab, fail to discriminate against high and low receptor expressing cells. They bind both. However, targeted nanoparticles benefit from the combined avidity of the many targeting ligands on the surface. Thanks to avidity, the ligand:receptor affinity can be decreased while still leaving the nanoparticle with excellent avidity to the target. Perhaps unexpectedly, this decrease in ligand affinity and reliance instead on avidity can generate a sharp on/off binding characteristic for nanoparticles that can be finely tuned based on the cell surface receptor expression levels. This concept, decreasing ligand affinity and fine-tuning avidity to achieve highly selective binding, has been called "super selectivity" [292]. In addition to theoretical and simulation work on this idea [292], numerous groups have successfully applied it to targeting nanoparticle to specific cell types. For example, this idea can be used to target nanoparticles to cells based on combinations of levels of surface receptors, tightly binding cells that express both of two receptors while failing to bind cells that only express one or the other [293, 294]. Theoretically, this concept can be extrapolated to a combination of any number of cell surface receptors [294], such that nanoparticles might be designed to bind to specific cell types based on very slight changes in cell surface expression patterns.

The idea of "super selectivity," or even more powerfully, cooperative super selectivity with multiple surface receptors, is an exciting new avenue for ligand targeted nanoparticles. This idea is especially powerful for applications in which no single, high affinity receptor:ligand pair seems like an obvious choice. For example, one could imagine delivering cargoes to specific subsets of immune cells that would otherwise be impossible to therapeutically manipulate separately. Or in cancer, many cancers have no one unique receptor to target, unlike B cell malignancies, but perhaps they can be distinguished (and drugged) using subtle differences in surface receptor patterns instead. Now that the theoretical frameworks and simulations on nanoparticle super selectivity have been established, the first proof-of-concept applications have begun to emerge, and this is likely to be an emerging branch of research in the coming years due to its potential for broad clinical applications.

5.4.3 Beyond Passive versus Active Targeting

We showed that active targeting facilitated uptake into DLBCL cells, and others have similarly demonstrated the cell-specific delivery benefits of active targeting. However, no actively-targeted nanoparticles have yet succeeded in clinical translation. There are numerous obstacles facing actively-targeted nanoparticles in vivo that rapidly clear them from the bloodstream before they can even encounter and bind to their targeted cells. For the clinical translation of actively targeted nanomedicines, it will be equally important to understand how to prevent their clearance from circulation as it will be to understand how to cause the targeted cells to internalize them. There are many parameters beginning to be understood that influence the pharmacokinetics of nanoparticles, and these upstream parameters will be important to understand to control the fate of a dose of nanoparticles.

A common obstacle for nanoparticle therapeutics is phagocytosis by immune cells. Sosale et al. recently summarized this problem and presented some potential ways to mitigate it [295]. Phagocytosis of nanoparticles is largely promoted by non-specific adsorption of serum proteins, including IgG, and then immune cell recognition of those proteins, such as

by Fc receptors. While protein adsorption and phagocytosis can be lessened, for example by PEGylation, even densely PEGylated polymersomes do not completely inhibit protein adsorption and phagocytosis.

In addition to preventing protein adsorption, nanoparticles can be functionalized with signals that actively inhibit phagocytosis. Phagocytes use a surface receptor, SIRPα, to recognize "self" cells by their expression of CD47, and this SIRPα-CD47 interaction serves as a "don't eat me" signal to prevent phagocytosis. Work from the lab of Dennis Discher has harnessed this mechanism to label nanoparticles with CD47 epitopes to prevent their phagocytosis and enhance their delivery [296]. Mechanisms such as these, which inhibit phagocytosis, should greatly enhance the ability of nanoparticles to deliver cargo to their intended cell types and thereby enhance their efficacy and minimize their side-effects.

Very recently, another exciting strategy was published for overcoming nanoparticle phagocytosis, particularly by Kupffer cells in the liver [297]. Ouyang et al. in the Chan lab showed that a critical dose threshold exists, which for mice is $\sim$1 trillion nanoparticles. For doses below this threshold, Kupffer cells are able to phagocytose a majority of the nanoparticles, proportional to the administered dose. For doses above this threshold, the Kupffer cells' rate of uptake is saturated, and a much larger proportion of nanoparticles above this threshold dose accumulate in tumors instead of being cleared by Kupffer cells. By simply co-administering a large bolus of empty liposomes as "delivery enhancers," they saturated Kupffer cell uptake such that a much larger percentage of therapeutic liposomes accumulated in tumors, thereby boosting the therapeutic effect for an equivalent dose. The authors then show that across the literature, this same dose threshold exists, with much greater accumulation in tumors for doses above 1 trillion nanoparticles in mice. This threshold existed regardless of the type of nanoparticle (i.e. organic, inorganic), targeting (i.e. passive targeting, active targeting), or size (i.e. small (10 - 50 nm) or large (i.e. $>$ 50 nm)). This is an exciting new concept for nanomedicines, as it highlights the potential for inhibiting off-target uptake, such as by Kupffer cells, to maximize on-target uptake, such as in tumors.

Another recent finding from Sindhwani et al. in the Chan lab showed that transcytosis plays an important role in extravasation of nanoparticles into many solid tumors [298]. Nanoparticle uptake into solid tumors has typically been conceptualized as a passive process, occurring primarily through leaky vasculature due to the enhanced permeability and retention (EPR) effect. This recent publication shows that active transcytosis plays a key role, if not a larger role than the EPR effect. As we develop a greater understanding of how nanoparticle transcytosis works, and how to harness it, we should be able to greatly improve the targeted, intentional delivery of nanoparticles to specific tissues and cell types, especially if they are compartmentalized away from the circulatory system by an intact endothelium.

Relevant to our work in Chapter 4, the PEG-SS-PPS polymersomes we assembled have excess N_3 functional groups on the surface that could easily be functionalized with CD47 peptide epitopes to minimize phagocytosis [296]. PEG-PPS polymersomes are also highly non-toxic [191], and empty polymersomes should be safe "delivery enhancers" to saturate Kupffer cell clearance in the liver [297]. Finally, the high degree of stability of polymersomes makes them a promising candidate class of nanoparticles to be able to withstand transcytosis into tumors, once we understand how to harness it. Using these simple strategies, among others, the pharmacokinetics of targeted nanoparticles such as ours can likely be greatly improved, before a nanoparticle even encounters its target.

5.5 Conclusions

The work in this thesis seeks to contribute to the areas of PPI therapeutics, stapled peptides, cancer cell death biology, and nanoparticle drug delivery. We have developed a targeted nanocarrier that facilitates the delivery of therapeutic stapled peptides to and into DLBCL cells to unlock the druggability of otherwise "undruggable" PPIs. This is an exciting avenue of research with the potential for adaptation in a wide variety of clinical applications. While the work presented here may move these fields forward ever so slightly, there remain countless known but undruggable disease targets due to our lack of chemical tools, and an even greater

number of disease targets yet to be discovered. Through collaboration across the boundaries of biology, chemistry, and physics, we can continue to engineer tools to understand and manipulate human disease with precision at the molecular level.

REFERENCES

[1] Mathew R. Schnorenberg. A potent and specific approach to targeting B-cell lymphoma: Disrupting malignant protein-protein interactions using CD19-targeted stapled peptide amphiphile nanoparticles. *National Cancer Institute, National Institutes of Health*, 5F30CA221250, July 2017.

[2] Michael P. H. Stumpf, Thomas Thorne, Eric de Silva, Ronald Stewart, Hyeong Jun An, Michael Lappe, and Carsten Wiuf. Estimating the size of the human interactome. *Proceedings of the National Academy of Sciences of the United States of America*, 105(19):6959–6964, May 2008.

[3] Andrei A. Ivanov, Fadlo R. Khuri, and Haian Fu. Targeting protein–protein interactions as an anticancer strategy. *Trends in Pharmacological Sciences*, 34(7):393–400, July 2013.

[4] Douglas R. Green. A BH3 Mimetic for Killing Cancer Cells. *Cell*, 165(7):1560, June 2016.

[5] James A. Wells and Christopher L. McClendon. Reaching for high-hanging fruit in drug discovery at protein–protein interfaces. *Nature*, 450(7172):1001–1009, December 2007. Number: 7172 Publisher: Nature Publishing Group.

[6] S. Jones and J. M. Thornton. Principles of protein-protein interactions. *Proceedings of the National Academy of Sciences*, 93(1):13–20, January 1996. Publisher: National Academy of Sciences Section: Research Article.

[7] Loredana Lo Conte, Cyrus Chothia, and Joël Janin. The atomic structure of protein-protein recognition sites11Edited by A. R. Fersht. *Journal of Molecular Biology*, 285(5):2177–2198, February 1999.

[8] Alan C. Cheng, Ryan G. Coleman, Kathleen T. Smyth, Qing Cao, Patricia Soulard, Daniel R. Caffrey, Anna C. Salzberg, and Enoch S. Huang. Structure-based maximal affinity model predicts small-molecule druggability. *Nature Biotechnology*, 25(1):71–75, January 2007. Number: 1 Publisher: Nature Publishing Group.

[9] Richard D. Smith, Liegi Hu, Jayson A. Falkner, Mark L. Benson, Jason P. Nerothin, and Heather A. Carlson. Exploring protein–ligand recognition with Binding MOAD. *Journal of Molecular Graphics and Modelling*, 24(6):414–425, May 2006.

[10] Natia Tsomaia. Peptide therapeutics: Targeting the undruggable space. *European Journal of Medicinal Chemistry*, 94:459–470, April 2015.

[11] Duncan E. Scott, Andrew R. Bayly, Chris Abell, and John Skidmore. Small molecules, big targets: drug discovery faces the protein–protein interaction challenge. *Nature Reviews Drug Discovery*, 15(8):533–550, August 2016. Number: 8 Publisher: Nature Publishing Group.

[12] Douglas Hanahan and Robert A. Weinberg. The Hallmarks of Cancer. *Cell*, 100(1):57–70, January 2000. Publisher: Elsevier.

[13] Douglas Hanahan and Robert A Weinberg. Hallmarks of cancer: the next generation. *Cell*, 144(5):646–674, March 2011.

[14] Jerry E. Chipuk, Tudor Moldoveanu, Fabien Llambi, Melissa J. Parsons, and Douglas R. Green. The BCL-2 Family Reunion. *Molecular Cell*, 37(3):299–310, February 2010.

[15] Min H. Kang and C. Patrick Reynolds. Bcl-2 inhibitors: targeting mitochondrial apoptotic pathways in cancer therapy. *Clinical Cancer Research: An Official Journal of the American Association for Cancer Research*, 15(4):1126–1132, February 2009.

[16] Triona Ni Chonghaile, Kristopher A. Sarosiek, Thanh Trang Vo, Jeremy A. Ryan, Anupama Tammareddi, Victoria Del Gaizo Moore, Jing Deng, Kenneth C. Anderson, Paul Richardson, Yu Tzu Tai, Constantine S. Mitsiades, Ursula A. Matulonis, Ronny Drapkin, Richard Stone, Daniel J. DeAngelo, David J. McConkey, Stephen E. Sallan, Lewis Silverman, Michelle S. Hirsch, Daniel Ruben Carrasco, and Anthony Letai. Pretreatment mitochondrial priming correlates with clinical response to cytotoxic chemotherapy. *Science*, 334(6059):1129–1133, November 2011. Publisher: American Association for the Advancement of Science.

[17] Patrick D. Bhola and Anthony Letai. Mitochondria-Judges and Executioners of Cell Death Sentences. *Molecular Cell*, 61(5):695–704, March 2016.

[18] Alex R. D. Delbridge, Stephanie Grabow, Andreas Strasser, and David L. Vaux. Thirty years of BCL-2: translating cell death discoveries into novel cancer therapies. *Nature Reviews Cancer*, 16(2):99–109, February 2016.

[19] A. R. D. Delbridge and A. Strasser. The BCL-2 protein family, BH3-mimetics and cancer therapy. *Cell Death and Differentiation*, 22(7):1071, July 2015.

[20] Tom Strachan and Andrew P. Read. Chapter 18: Cancer Genetics. In *Human Molecular Genetics 2*. New York: Wiley, 1999.

[21] Christopher J. Brown, Sonia Lain, Chandra S. Verma, Alan R. Fersht, and David P. Lane. Awakening guardian angels: drugging the p53 pathway. *Nature Reviews. Cancer*, 9(12):862–873, December 2009.

[22] Georg Lenz and Louis M. Staudt. Aggressive Lymphomas. *New England Journal of Medicine*, 362(15):1417–1429, April 2010. Publisher: Massachusetts Medical Society _eprint: https://doi.org/10.1056/NEJMra0807082.

[23] Stefano Monti, Bjoern Chapuy, Kunihiko Takeyama, Scott J. Rodig, Yansheng Hao, Kelly T. Yeda, Haig Inguilizian, Craig Mermel, Treeve Currie, Ahmet Dogan, Jeffery L. Kutok, Rameen Beroukhim, Donna Neuberg, Thomas M. Habermann, Gad Getz, Andrew L. Kung, Todd R. Golub, and Margaret A. Shipp. Integrative Analysis Reveals

an Outcome-Associated and Targetable Pattern of p53 and Cell Cycle Deregulation in Diffuse Large B Cell Lymphoma. *Cancer Cell*, 22(3):359–372, September 2012.

[24] Lenka Stefancikova, Mojmir Moulis, Pavel Fabian, Ingrid Vasova, Frantisek Zedek, Barbora Ravcukova, Jan Muzik, Petr Kuglik, Vladimira Vranova, Iva Falkova, Renata Hrabalkova, and Jana Smardova. Prognostic impact of p53 aberrations for R-CHOP-treated patients with diffuse large B-cell lymphoma. *International Journal of Oncology*, 39(6):1413–1420, December 2011.

[25] Yi Xie, Mohmad Ajaz Bulbul, Lingyun Ji, Casey M. Inouye, Susan G. Groshen, Anil Tulpule, Dennis P. O'Malley, Endi Wang, and Imran N. Siddiqi. p53 expression is a strong marker of inferior survival in de novo diffuse large B-cell lymphoma and may have enhanced negative effect with MYC coexpression: a single institutional clinicopathologic study. *American Journal of Clinical Pathology*, 141(4):593–604, April 2014.

[26] Ryan D. Morin, Maria Mendez-Lago, Andrew J. Mungall, Rodrigo Goya, Karen L. Mungall, Richard D. Corbett, Nathalie A. Johnson, Tesa M. Severson, Readman Chiu, Matthew Field, Shaun Jackman, Martin Krzywinski, David W. Scott, Diane L. Trinh, Jessica Tamura-Wells, Sa Li, Marlo R. Firme, Sanja Rogic, Malachi Griffith, Susanna Chan, Oleksandr Yakovenko, Irmtraud M. Meyer, Eric Y. Zhao, Duane Smailus, Michelle Moksa, Suganthi Chittaranjan, Lisa Rimsza, Angela Brooks-Wilson, John J. Spinelli, Susana Ben-Neriah, Barbara Meissner, Bruce Woolcock, Merrill Boyle, Helen McDonald, Angela Tam, Yongjun Zhao, Allen Delaney, Thomas Zeng, Kane Tse, Yaron Butterfield, Inanç Birol, Rob Holt, Jacqueline Schein, Douglas E. Horsman, Richard Moore, Steven J. M. Jones, Joseph M. Connors, Martin Hirst, Randy D. Gascoyne, and Marco A. Marra. Frequent mutation of histone-modifying genes in non-Hodgkin lymphoma. *Nature*, 476(7360):298–303, July 2011.

[27] Christopher J. Brown, Soo T. Quah, Janice Jong, Amanda M. Goh, Poh C. Chiam, Kian H. Khoo, Meng L. Choong, May A. Lee, Larisa Yurlova, Kourosh Zolghadr, Thomas L. Joseph, Chandra S. Verma, and David P. Lane. Stapled peptides with improved potency and specificity that activate p53. *ACS chemical biology*, 8(3):506–512, March 2013.

[28] Yong S. Chang, Bradford Graves, Vincent Guerlavais, Christian Tovar, Kathryn Packman, Kwong-Him To, Karen A. Olson, Kamala Kesavan, Pranoti Gangurde, Aditi Mukherjee, Theresa Baker, Krzysztof Darlak, Carl Elkin, Zoran Filipovic, Farooq Z. Qureshi, Hongliang Cai, Pamela Berry, Eric Feyfant, Xiangguo E. Shi, James Horstick, D. Allen Annis, Anthony M. Manning, Nader Fotouhi, Huw Nash, Lyubomir T. Vassilev, and Tomi K. Sawyer. Stapled α-helical peptide drug development: A potent dual inhibitor of MDM2 and MDMX for p53-dependent cancer therapy. *Proceedings of the National Academy of Sciences*, 110(36):E3445–E3454, September 2013. Publisher: National Academy of Sciences Section: PNAS Plus.

[29] Rameen Beroukhim, Craig H. Mermel, Dale Porter, Guo Wei, Soumya Raychaudhuri, Jerry Donovan, Jordi Barretina, Jesse S. Boehm, Jennifer Dobson, Mitsuyoshi Urashima, Kevin T. Mc Henry, Reid M. Pinchback, Azra H. Ligon, Yoon-Jae Cho, Leila

Haery, Heidi Greulich, Michael Reich, Wendy Winckler, Michael S. Lawrence, Barbara A. Weir, Kumiko E. Tanaka, Derek Y. Chiang, Adam J. Bass, Alice Loo, Carter Hoffman, John Prensner, Ted Liefeld, Qing Gao, Derek Yecies, Sabina Signoretti, Elizabeth Maher, Frederic J. Kaye, Hidefumi Sasaki, Joel E. Tepper, Jonathan A. Fletcher, Josep Tabernero, José Baselga, Ming-Sound Tsao, Francesca Demichelis, Mark A. Rubin, Pasi A. Janne, Mark J. Daly, Carmelo Nucera, Ross L. Levine, Benjamin L. Ebert, Stacey Gabriel, Anil K. Rustgi, Cristina R. Antonescu, Marc Ladanyi, Anthony Letai, Levi A. Garraway, Massimo Loda, David G. Beer, Lawrence D. True, Aikou Okamoto, Scott L. Pomeroy, Samuel Singer, Todd R. Golub, Eric S. Lander, Gad Getz, William R. Sellers, and Matthew Meyerson. The landscape of somatic copy-number alteration across human cancers. *Nature*, 463(7283):899–905, February 2010. Number: 7283 Publisher: Nature Publishing Group.

[30] Y. Tsujimoto, L. R. Finger, J. Yunis, P. C. Nowell, and C. M. Croce. Cloning of the chromosome breakpoint of neoplastic B cells with the t(14;18) chromosome translocation. *Science (New York, N.Y.)*, 226(4678):1097–1099, November 1984.

[31] D. L. Vaux, S. Cory, and J. M. Adams. Bcl-2 gene promotes haemopoietic cell survival and cooperates with c-myc to immortalize pre-B cells. *Nature*, 335(6189):440–442, September 1988.

[32] Francesca Pentimalli. BCL2: a 30-year tale of life, death and much more to come. *Cell Death and Differentiation*, 25(1):7–9, January 2018.

[33] Lindsey M. Ludwig, Michele L. Nassin, Abbas Hadji, and James L. LaBelle. Killing Two Cells with One Stone: Pharmacologic BCL-2 Family Targeting for Cancer Cell Death and Immune Modulation. *Frontiers in Pediatrics*, 4, 2016. Publisher: Frontiers.

[34] J. C. Reed, M. Cuddy, S. Haldar, C. Croce, P. Nowell, D. Makover, and K. Bradley. BCL2-mediated tumorigenicity of a human T-lymphoid cell line: synergy with MYC and inhibition by BCL2 antisense. *Proceedings of the National Academy of Sciences*, 87(10):3660–3664, May 1990. Publisher: National Academy of Sciences Section: Research Article.

[35] Asher A. Chanan-Khan, Ruben Niesvizky, Raymond J. Hohl, Todd M. Zimmerman, Neal P. Christiansen, Gary J. Schiller, Natalie Callander, John Lister, Martin Oken, and Sundar Jagannath. Phase III randomised study of dexamethasone with or without oblimersen sodium for patients with advanced multiple myeloma. *Leukemia & Lymphoma*, 50(4):559–565, January 2009. Publisher: Taylor & Francis _eprint: https://doi.org/10.1080/10428190902748971.

[36] Agop Y. Bedikian, Michael Millward, Hubert Pehamberger, Robert Conry, Martin Gore, Uwe Trefzer, Anna C. Pavlick, Ronald DeConti, Evan M. Hersh, Peter Hersey, John M. Kirkwood, and Frank G. Haluska. Bcl-2 Antisense (oblimersen sodium) Plus Dacarbazine in Patients With Advanced Melanoma: The Oblimersen Melanoma Study Group. *Journal of Clinical Oncology*, 24(29):4738–4745, October 2006. Publisher: American Society of Clinical Oncology.

[37] Manchao Zhang, Hongpeng Liu, Ribo Guo, Yan Ling, Xiaojin Wu, Bihua Li, Peter P. Roller, Shaomeng Wang, and Dajun Yang. Molecular mechanism of gossypol-induced cell growth inhibition and cell death of HT-29 human colon carcinoma cells. *Biochemical Pharmacology*, 66(1):93–103, July 2003.

[38] Aitor Etxebarria, Olatz Landeta, Bruno Antonsson, and Gorka Basañez. Regulation of antiapoptotic MCL-1 function by gossypol: Mechanistic insights from in vitro reconstituted systems. *Biochemical Pharmacology*, 76(11):1563–1576, December 2008.

[39] Maria Q. Baggstrom, Yingwei Qi, Marianna Koczywas, Athanassios Argiris, Elizabeth A. Johnson, Michael J. Millward, Sara C. Murphy, Charles Erlichman, Charles M. Rudin, and Ramaswamy Govindan. A Phase II Study of AT-101 (Gossypol) in Chemotherapy-Sensitive Recurrent Extensive-Stage Small Cell Lung Cancer. *Journal of Thoracic Oncology*, 6(10):1757–1760, October 2011. Publisher: Elsevier.

[40] Tilman Oltersdorf, Steven W. Elmore, Alexander R. Shoemaker, Robert C. Armstrong, David J. Augeri, Barbara A. Belli, Milan Bruncko, Thomas L. Deckwerth, Jurgen Dinges, Philip J. Hajduk, Mary K. Joseph, Shinichi Kitada, Stanley J. Korsmeyer, Aaron R. Kunzer, Anthony Letai, Chi Li, Michael J. Mitten, David G. Nettesheim, ShiChung Ng, Paul M. Nimmer, Jacqueline M. O'Connor, Anatol Oleksijew, Andrew M. Petros, John C. Reed, Wang Shen, Stephen K. Tahir, Craig B. Thompson, Kevin J. Tomaselli, Baole Wang, Michael D. Wendt, Haichao Zhang, Stephen W. Fesik, and Saul H. Rosenberg. An inhibitor of Bcl-2 family proteins induces regression of solid tumours. *Nature*, 435(7042):677–681, June 2005.

[41] Suzanne B. Shuker, Philip J. Hajduk, Robert P. Meadows, and Stephen W. Fesik. Discovering High-Affinity Ligands for Proteins: SAR by NMR. *Science*, 274(5292):1531–1534, November 1996. Publisher: American Association for the Advancement of Science Section: Reports.

[42] Christin Tse, Alexander R. Shoemaker, Jessica Adickes, Mark G. Anderson, Jun Chen, Sha Jin, Eric F. Johnson, Kennan C. Marsh, Michael J. Mitten, Paul Nimmer, Lisa Roberts, Stephen K. Tahir, Yu Xiao, Xiufen Yang, Haichao Zhang, Stephen Fesik, Saul H. Rosenberg, and Steven W. Elmore. ABT-263: a potent and orally bioavailable Bcl-2 family inhibitor. *Cancer Research*, 68(9):3421–3428, May 2008.

[43] Kylie D. Mason, Marina R. Carpinelli, Jamie I. Fletcher, Janelle E. Collinge, Adrienne A. Hilton, Sarah Ellis, Priscilla N. Kelly, Paul G. Ekert, Donald Metcalf, Andrew W. Roberts, David C. S. Huang, and Benjamin T. Kile. Programmed Anuclear Cell Death Delimits Platelet Life Span. *Cell*, 128(6):1173–1186, March 2007.

[44] Wyndham H Wilson, Owen A O'Connor, Myron S Czuczman, Ann S LaCasce, John F Gerecitano, John P Leonard, Anil Tulpule, Kieron Dunleavy, Hao Xiong, Yi-Lin Chiu, Yue Cui, Todd Busman, Steven W Elmore, Saul H Rosenberg, Andrew P Krivoshik, Sari H Enschede, and Rod A Humerickhouse. Navitoclax, a targeted high-affinity inhibitor of BCL-2, in lymphoid malignancies: a phase 1 dose-escalation study of safety, pharmacokinetics, pharmacodynamics, and antitumour activity. *The Lancet Oncology*, 11(12):1149–1159, December 2010.

[45] A.W. Roberts, J.F. Seymour, J.R. Brown, W.G. Wierda, T.J. Kipps, S.L. Khaw, D.A. Carney, S.Z. He, D.C.S. Huang, H. Xiong, Y. Cui, T.A. Busman, E.M. McKeegan, A.P. Krivoshik, S.H. Enschede, and R. Humerickhouse. Substantial susceptibility of chronic lymphocytic leukemia to BCL2 inhibition: Results of a phase I study of navitoclax in patients with relapsed or refractory disease. *Journal of Clinical Oncology*, 30(5):488–496, 2012.

[46] L. Gandhi, D.R. Camidge, M.R. De Oliveira, P. Bonomi, D. Gandara, D. Khaira, C.L. Hann, E.M. McKeegan, E. Litvinovich, P.M. Hemken, C. Dive, S.H. Enschede, C. Nolan, Y.-L. Chiu, T. Busman, H. Xiong, A.P. Krivoshik, R. Humerickhouse, G.I. Shapiro, and C.M. Rudin. Phase I study of navitoclax (ABT-263), a novel bcl-2 family inhibitor, in patients with small-cell lung cancer and other solid tumors. *Journal of Clinical Oncology*, 29(7):909–916, 2011.

[47] Andrew J. Souers, Joel D. Leverson, Erwin R. Boghaert, Scott L. Ackler, Nathaniel D. Catron, Jun Chen, Brian D. Dayton, Hong Ding, Sari H. Enschede, Wayne J. Fairbrother, David C. S. Huang, Sarah G. Hymowitz, Sha Jin, Seong Lin Khaw, Peter J. Kovar, Lloyd T. Lam, Jackie Lee, Heather L. Maecker, Kennan C. Marsh, Kylie D. Mason, Michael J. Mitten, Paul M. Nimmer, Anatol Oleksijew, Chang H. Park, Cheol-Min Park, Darren C. Phillips, Andrew W. Roberts, Deepak Sampath, John F. Seymour, Morey L. Smith, Gerard M. Sullivan, Stephen K. Tahir, Chris Tse, Michael D. Wendt, Yu Xiao, John C. Xue, Haichao Zhang, Rod A. Humerickhouse, Saul H. Rosenberg, and Steven W. Elmore. ABT-199, a potent and selective BCL-2 inhibitor, achieves antitumor activity while sparing platelets. *Nature Medicine*, 19(2):202–208, February 2013.

[48] Guilherme Fleury Perini, Glaciano Nogueira Ribeiro, Jorge Vaz Pinto Neto, Laura Tojeiro Campos, and Nelson Hamerschlak. BCL-2 as therapeutic target for hematological malignancies. *Journal of Hematology & Oncology*, 11(1):65, May 2018.

[49] Luis Miguel Juárez-Salcedo, Viraj Desai, and Samir Dalia. Venetoclax: evidence to date and clinical potential. *Drugs in Context*, 8, October 2019.

[50] Alexander W. Hird and Adriana E. Tron. Recent advances in the development of Mcl-1 inhibitors for cancer therapy. *Pharmacology & Therapeutics*, 198:59–67, June 2019.

[51] András Kotschy, Zoltán Szlavik, James Murray, James Davidson, Ana Leticia Maragno, Gaëtane Le Toumelin-Braizat, Maïa Chanrion, Gemma L. Kelly, Jia-Nan Gong, Donia M. Moujalled, Alain Bruno, Márton Csekei, Attila Paczal, Zoltán B. Szabo, Szabolcs Sipos, Gábor Radics, Agnes Proszenyak, Balázs Balint, Levente Ondi, Gábor Blasko, Alan Robertson, Allan Surgenor, Pawel Dokurno, Ijen Chen, Natalia Matassova, Julia Smith, Christopher Pedder, Christopher Graham, Aurélie Studeny, Gaëlle Lysiak-Auvity, Anne-Marie Girard, Fabienne Gravé, David Segal, Chris D. Riffkin, Giovanna Pomilio, Laura C. A. Galbraith, Brandon J. Aubrey, Margs S. Brennan, Marco J. Herold, Catherine Chang, Ghislaine Guasconi, Nicolas Cauquil, Fabien Melchiore, Nolwen Guigal-Stephan, Brian Lockhart, Frédéric Colland, John A. Hickman, Andrew W. Roberts, David C. S. Huang, Andrew H. Wei, Andreas Strasser, Guillaume

Lessene, and Olivier Geneste. The MCL1 inhibitor S63845 is tolerable and effective in diverse cancer models. *Nature*, 538(7626):477–482, October 2016. Number: 7626 Publisher: Nature Publishing Group.

[52] Novartis Pharmaceuticals. Phase I Open Label, Multi-center Study to Characterize the Safety, Tolerability and Pharmacokinetics of Intravenously Administered MIK665, a Mcl-1 Inhibitor, in Patients With Refractory or Relapsed Lymphoma or Multiple Myeloma. Clinical trial registration NCT02992483, clinicaltrials.gov, April 2020. submitted: December 12, 2016.

[53] Institut de Reserches Internationales Servier. Phase I Study of S64315 Administred Intravenously in Patients With Acute Myeloid Leukaemia or Myelodysplastic Syndrome - Full Text View - ClinicalTrials.gov. Technical Report NCT02979366, December 2016.

[54] Institut de Reserches Internationales Servier. Phase I Dose Escalation Study of Intravenously Administered S64315 in Combination With Orally Administered Venetoclax in Patients With Acute Myeloid Leukaemia. - Full Text View - ClinicalTrials.gov. Technical Report NCT03672695, September 2018.

[55] Adriana E. Tron, Matthew A. Belmonte, Ammar Adam, Brian M. Aquila, Lawrence H. Boise, Elisabetta Chiarparin, Justin Cidado, Kevin J. Embrey, Eric Gangl, Francis D. Gibbons, Gareth P. Gregory, David Hargreaves, J. Adam Hendricks, Jeffrey W. Johannes, Ricky W. Johnstone, Steven L. Kazmirski, Jason G. Kettle, Michelle L. Lamb, Shannon M. Matulis, Ajay K. Nooka, Martin J. Packer, Bo Peng, Philip B. Rawlins, Daniel W. Robbins, Alwin G. Schuller, Nancy Su, Wenzhan Yang, Qing Ye, Xiaolan Zheng, J. Paul Secrist, Edwin A. Clark, David M. Wilson, Stephen E. Fawell, and Alexander W. Hird. Discovery of Mcl-1-specific inhibitor AZD5991 and preclinical activity in multiple myeloma and acute myeloid leukemia. *Nature Communications*, 9(1):5341, December 2018. Number: 1 Publisher: Nature Publishing Group.

[56] AstraZeneca. A Phase 1/1b/2a, 3-Part, Open-Label, Multicentre Study to Assess the Safety, Tolerability, Pharmacokinetics and Preliminary Antitumor Activity of Ascending Doses of AZD5991 in Subjects With Relapsed or Refractory Haematologic Malignancies. Clinical trial registration NCT03218683, clinicaltrials.gov, May 2020. submitted: July 6, 2017.

[57] Sean Caenepeel, Sean P. Brown, Brian Belmontes, Gordon Moody, Kathleen S. Keegan, Danny Chui, Douglas A. Whittington, Xin Huang, Leszek Poppe, Alan C. Cheng, Mario Cardozo, Jonathan Houze, Yunxiao Li, Brian Lucas, Nick A. Paras, Xianghong Wang, Joshua P. Taygerly, Marc Vimolratana, Manuel Zancanella, Liusheng Zhu, Elaina Cajulis, Tao Osgood, Jan Sun, Leah Damon, Regina K. Egan, Patricia Greninger, Joseph D. McClanaghan, Jianan Gong, Donia Moujalled, Giovanna Pomilio, Pedro Beltran, Cyril H. Benes, Andrew W. Roberts, David C. Huang, Andrew Wei, Jude Canon, Angela Coxon, and Paul E. Hughes. AMG 176, a Selective MCL1 Inhibitor, Is Effective in Hematologic Cancer Models Alone and in Combination with Established Therapies. *Cancer Discovery*, 8(12):1582–1597, December 2018. Publisher: American Association for Cancer Research Section: Research Articles.

[58] Amgen. A Phase 1 Open-label Study Evaluating the Safety, Tolerability, Pharmacokinetics and Efficacy of AMG 397 in Subjects With Selected Relapsed or Refractory Hematological Malignancies. Clinical trial registration NCT03465540, clinicaltrials.gov, March 2020. submitted: March 8, 2018.

[59] J. D. Leverson, H. Zhang, J. Chen, S. K. Tahir, D. C. Phillips, J. Xue, P. Nimmer, S. Jin, M. Smith, Y. Xiao, P. Kovar, A. Tanaka, M. Bruncko, G. S. Sheppard, L. Wang, S. Gierke, L. Kategaya, D. J. Anderson, C. Wong, J. Eastham-Anderson, M. J. C. Ludlam, D. Sampath, W. J. Fairbrother, I. Wertz, S. H. Rosenberg, C. Tse, S. W. Elmore, and A. J. Souers. Potent and selective small-molecule MCL-1 inhibitors demonstrate on-target cancer cell killing activity as single agents and in combination with ABT-263 (navitoclax). *Cell Death & Disease*, 6(1):e1590–e1590, January 2015. Number: 1 Publisher: Nature Publishing Group.

[60] Zhi-Fu Tao, Lisa Hasvold, Le Wang, Xilu Wang, Andrew M. Petros, Chang H. Park, Erwin R. Boghaert, Nathaniel D. Catron, Jun Chen, Peter M. Colman, Peter E. Czabotar, Kurt Deshayes, Wayne J. Fairbrother, John A. Flygare, Sarah G. Hymowitz, Sha Jin, Russell A. Judge, Michael F. T. Koehler, Peter J. Kovar, Guillaume Lessene, Michael J. Mitten, Chudi O. Ndubaku, Paul Nimmer, Hans E. Purkey, Anatol Oleksijew, Darren C. Phillips, Brad E. Sleebs, Brian J. Smith, Morey L. Smith, Stephen K. Tahir, Keith G. Watson, Yu Xiao, John Xue, Haichao Zhang, Kerry Zobel, Saul H. Rosenberg, Chris Tse, Joel D. Leverson, Steven W. Elmore, and Andrew J. Souers. Discovery of a Potent and Selective BCL-XL Inhibitor with in Vivo Activity. *ACS Medicinal Chemistry Letters*, 5(10):1088–1093, October 2014. Publisher: American Chemical Society.

[61] Joel D. Leverson, Darren C. Phillips, Michael J. Mitten, Erwin R. Boghaert, Dolores Diaz, Stephen K. Tahir, Lisa D. Belmont, Paul Nimmer, Yu Xiao, Xiaoju Max Ma, Kym N. Lowes, Peter Kovar, Jun Chen, Sha Jin, Morey Smith, John Xue, Haichao Zhang, Anatol Oleksijew, Terrance J. Magoc, Kedar S. Vaidya, Daniel H. Albert, Jacqueline M. Tarrant, Nghi La, Le Wang, Zhi-Fu Tao, Michael D. Wendt, Deepak Sampath, Saul H. Rosenberg, Chris Tse, David C. S. Huang, Wayne J. Fairbrother, Steven W. Elmore, and Andrew J. Souers. Exploiting selective BCL-2 family inhibitors to dissect cell survival dependencies and define improved strategies for cancer therapy. *Science Translational Medicine*, 7(279):279ra40–279ra40, March 2015. Publisher: American Association for the Advancement of Science Section: Research Article.

[62] Guillaume Lessene, Peter E. Czabotar, Brad E. Sleebs, Kerry Zobel, Kym N. Lowes, Jerry M. Adams, Jonathan B. Baell, Peter M. Colman, Kurt Deshayes, Wayne J. Fairbrother, John A. Flygare, Paul Gibbons, Wilhelmus J. A. Kersten, Sanji Kulasegaram, Rebecca M. Moss, John P. Parisot, Brian J. Smith, Ian P. Street, Hong Yang, David C. S. Huang, and Keith G. Watson. Structure-guided design of a selective BCL-X L inhibitor. *Nature Chemical Biology*, 9(6):390–397, June 2013. Number: 6 Publisher: Nature Publishing Group.

[63] Lyubomir T. Vassilev, Binh T. Vu, Bradford Graves, Daisy Carvajal, Frank Podlaski, Zoran Filipovic, Norman Kong, Ursula Kammlott, Christine Lukacs, Christian

Klein, Nader Fotouhi, and Emily A. Liu. In vivo activation of the p53 pathway by small-molecule antagonists of MDM2. *Science (New York, N.Y.)*, 303(5659):844–848, February 2004.

[64] Andrew Burgess, Kee Ming Chia, Sue Haupt, David Thomas, Ygal Haupt, and Elgene Lim. Clinical Overview of MDM2/X-Targeted Therapies. *Frontiers in Oncology*, 6, January 2016.

[65] Anna K. Mapp, Rachel Pricer, and Steven Sturlis. Targeting transcription is no longer a quixotic quest. *Nature Chemical Biology*, 11(12):891–894, December 2015.

[66] Keld Fosgerau and Torsten Hoffmann. Peptide therapeutics: current status and future directions. *Drug Discovery Today*, 20(1):122–128, January 2015.

[67] Valeria Azzarito, Kérya Long, Natasha S. Murphy, and Andrew J. Wilson. Inhibition of α-helix-mediated protein-protein interactions using designed molecules. *Nature Chemistry*, 5(3):161–173, March 2013.

[68] Paulina Wójcik and Łukasz Berlicki. Peptide-based inhibitors of protein–protein interactions. *Bioorganic & Medicinal Chemistry Letters*, 26(3):707–713, February 2016.

[69] Anthony Letai, Michael C. Bassik, Loren D. Walensky, Mia D. Sorcinelli, Solly Weiler, and Stanley J. Korsmeyer. Distinct BH3 domains either sensitize or activate mitochondrial apoptosis, serving as prototype cancer therapeutics. *Cancer Cell*, 2(3):183–192, September 2002.

[70] Glenna Wink Foight, Jeremy A. Ryan, Stefano V. Gullá, Anthony Letai, and Amy E. Keating. Designed BH3 peptides with high affinity and specificity for targeting Mcl-1 in cells. *ACS chemical biology*, 9(9):1962–1968, September 2014.

[71] Naomi S. Robertson and Andrew G. Jamieson. Regulation of protein-protein interactions using stapled peptides. *Reports in Organic Chemistry*, 5:65–74, August 2015. Publisher: Dove Press Volume: 5.

[72] Ameena M. Ali, Jack Atmaj, Niels Van Oosterwijk, Matthew R. Groves, and Alexander Dömling. Stapled Peptides Inhibitors: A New Window for Target Drug Discovery. *Computational and Structural Biotechnology Journal*, 17:263–281, January 2019.

[73] Loren D. Walensky, Andrew L. Kung, Iris Escher, Thomas J. Malia, Scott Barbuto, Renee D. Wright, Gerhard Wagner, Gregory L. Verdine, and Stanley J. Korsmeyer. Activation of Apoptosis in Vivo by a Hydrocarbon-Stapled BH3 Helix. *Science*, 305(5689):1466–1470, September 2004. Publisher: American Association for the Advancement of Science Section: Report.

[74] Christian E. Schafmeister, Julia Po, and Gregory L. Verdine. An All-Hydrocarbon Cross-Linking System for Enhancing the Helicity and Metabolic Stability of Peptides. *Journal of the American Chemical Society*, 122(24):5891–5892, June 2000. Publisher: American Chemical Society.

[75] Gregory H. Bird, Navid Madani, Alisa F. Perry, Amy M. Princiotto, Jeffrey G. Supko, Xiaoying He, Evripidis Gavathiotis, Joseph G. Sodroski, and Loren D. Walensky. Hydrocarbon double-stapling remedies the proteolytic instability of a lengthy peptide therapeutic. *Proceedings of the National Academy of Sciences of the United States of America*, 107(32):14093–14098, August 2010.

[76] Gregory H. Bird, Emanuele Mazzola, Kwadwo Opoku-Nsiah, Margaret A. Lammert, Marina Godes, Donna S. Neuberg, and Loren D. Walensky. Biophysical determinants for cellular uptake of hydrocarbon-stapled peptide helices. *Nature Chemical Biology*, 12(10):845–852, October 2016.

[77] Loren D. Walensky and Gregory H. Bird. Hydrocarbon-Stapled Peptides: Principles, Practice, and Progress. *Journal of Medicinal Chemistry*, 57(15):6275–6288, August 2014.

[78] Helen E. Blackwell and Robert H. Grubbs. Highly Efficient Synthesis of Covalently Cross-Linked Peptide Helices by Ring-Closing Metathesis. *Angewandte Chemie International Edition*, 37(23):3281–3284, 1998. _eprint: https://onlinelibrary.wiley.com/doi/pdf/10.1002/%28SICI%291521-3773%2819981217%2937%3A23%3C3281%3A%3AAID-ANIE3281%3E3.0.CO%3B2-V.

[79] Gregory H. Bird, W. Christian Crannell, and Loren D. Walensky. Chemical Synthesis of Hydrocarbon-Stapled Peptides for Protein Interaction Research and Therapeutic Targeting. *Current Protocols in Chemical Biology*, 3(3):99–117, 2011.

[80] Young-Woo Kim, Tom N. Grossmann, and Gregory L. Verdine. Synthesis of all-hydrocarbon stapled α-helical peptides by ring-closing olefin metathesis. *Nature Protocols*, 6(6):761–771, June 2011. Number: 6 Publisher: Nature Publishing Group.

[81] Gregory H. Bird, Federico Bernal, Kenneth Pitter, and Loren D. Walensky. Chapter 22 Synthesis and Biophysical Characterization of Stabilized α-Helices of BCL-2 Domains. In *Methods in Enzymology*, volume 446 of *Programmed Cell Death, The Biology and Therapeutic Implications of Cell Death, Part B*, pages 369–386. Academic Press, January 2008.

[82] Gregory L. Verdine and Gerard J. Hilinski. Chapter one - Stapled Peptides for Intracellular Drug Targets. In K. Dane Wittrup and Gregory L. Verdine, editors, *Methods in Enzymology*, volume 503 of *Protein Engineering for Therapeutics, Part B*, pages 3–33. Academic Press, January 2012.

[83] Aileron Therapeutics. Phase 1 Safety Study of ALRN-5281 in Healthy Subjects - Tabular View - ClinicalTrials.gov. Technical Report NCT01775358, January 2013.

[84] M.D. Anderson Cancer Center. ALRN-6924 and Paclitaxel in Treating Patients With Advanced, Metastatic, or Unresectable Solid Tumors - Full Text View - ClinicalTrials.gov. Technical Report NCT03725436, clinicaltrials.gov, February 2020.

[85] Aileron Therapeutics. A Phase 1/1b Open-Label Study to Determine the Safety and Tolerability of ALRN-6924 Alone and in Combination With Cytarabine (Ara-C) in Patients With Relapsed/Refractory Acute Myeloid Leukemia or Advanced Myelodysplastic Syndrome With Wild-Type TP53. Clinical trial registration NCT02909972, clinicaltrials.gov, November 2019. submitted: September 9, 2016.

[86] Aileron Therapeutics. A Phase 1b/2 Study of the Dual MDMX/MDM2 Inhibitor, ALRN-6924, for the Prevention of Topotecan-induced Myelosuppression During Treatment for Small Cell Lung Cancer. Clinical trial registration NCT04022876, clinicaltrials.gov, January 2020. submitted: July 12, 2019.

[87] Aileron Therapeutics. A Phase 1/2a Open-Label Study to Determine the Safety and Tolerability of ALRN-6924 Alone or in Combination in Patients With Advanced Solid Tumors or Lymphomas Expressing Wild-Type p53 Protein. Clinical trial registration NCT02264613, clinicaltrials.gov, January 2020. submitted: October 7, 2014.

[88] Dana-Farber Cancer Institute. Phase 1 Study of the Dual MDM2/MDMX Inhibitor ALRN-6924 in Pediatric Cancer - Full Text View - ClinicalTrials.gov. Technical Report NCT03654716, clinicaltrials.gov, November 2019.

[89] David A. Sallman, Uma Borate, Elizabeth H. Cull, William B. Donnellan, Rami S. Komrokji, Ulrich G. Steidl, Maria M. Corvez, Marie Payton, D. Allen Annis, Dawn Pinchasik, Manuel Aivado, and Amit Verma. Phase 1/1b Study of the Stapled Peptide ALRN-6924, a Dual Inhibitor of MDMX and MDM2, As Monotherapy or in Combination with Cytarabine for the Treatment of Relapsed/Refractory AML and Advanced MDS with TP53 Wild-Type. *Blood*, 132, November 2018. WOS:000454842803102.

[90] Funda Meric-Bernstam, Mansoor N. Saleh, Jeffrey R. Infante, Sanjay Goel, Gerald Steven Falchook, Geoffrey Shapiro, Ki Y. Chung, Robert Martin Conry, David S. Hong, Judy Sing-Zan Wang, Ulrich Steidl, Loren D. Walensky, Vincent Guerlavais, Marie Payton, D. Allen Annis, Manuel Aivado, and Manish R. Patel. Phase I trial of a novel stapled peptide ALRN-6924 disrupting MDMX- and MDM2-mediated inhibition of WT p53 in patients with solid tumors and lymphomas. *Journal of Clinical Oncology*, 35, May 2017. WOS:000411895704108.

[91] M. Payton, D. Pinchasik, A. Mehta, S. Goel, J. M. Zain, L. Sokol, E. Jacobsen, M. R. Patel, S. M. Horwitz, F. Meric-Bernstam, A. Shustov, D. Weinstock, M. Aivado, and D. A. Annis. Phase 2a study of a novel stapled peptide ALRN-6924 disrupting MDMX- and MDM2-mediated inhibition of wild-type TP53 in patients with peripheral t-cell lymphoma. *Annals of Oncology*, 28, September 2017. WOS:000411324002227.

[92] Federico Bernal, Andrew F. Tyler, Stanley J. Korsmeyer, Loren D. Walensky, and Gregory L. Verdine. Reactivation of the p53 Tumor Suppressor Pathway by a Stapled p53 Peptide. *Journal of the American Chemical Society*, 129(9):2456–2457, March 2007. Publisher: American Chemical Society.

[93] Federico Bernal, Mark Wade, Marina Godes, Tina N. Davis, David G. Whitehead, Andrew L. Kung, Geoffrey M. Wahl, and Loren D. Walensky. A Stapled p53 Helix

Overcomes HDMX-Mediated Suppression of p53. *Cancer Cell*, 18(5):411–422, November 2010.

[94] Björn Stolte, Amanda Balboni Iniguez, Neekesh V. Dharia, Amanda L. Robichaud, Amy Saur Conway, Ann M. Morgan, Gabriela Alexe, Nathan J. Schauer, Xiaoxi Liu, Gregory H. Bird, Aviad Tsherniak, Francisca Vazquez, Sara J. Buhrlage, Loren D. Walensky, and Kimberly Stegmaier. Genome-scale CRISPR-Cas9 screen identifies druggable dependencies in TP53 wild-type Ewing sarcoma. *Journal of Experimental Medicine*, 215(8):2137–2155, August 2018. Publisher: The Rockefeller University Press.

[95] Thomas P. Howard, Taylor E. Arnoff, Melinda R. Song, Andrew O. Giacomelli, Xiaofeng Wang, Andrew L. Hong, Neekesh V. Dharia, Su Wang, Francisca Vazquez, Minh-Tam Pham, Ann M. Morgan, Franziska Wachter, Gregory H. Bird, Guillaume Kugener, Elaine M. Oberlick, Matthew G. Rees, Hong L. Tiv, Justin H. Hwang, Katherine H. Walsh, April Cook, John M. Krill-Burger, Aviad Tsherniak, Prafulla C. Gokhale, Peter J. Park, Kimberly Stegmaier, Loren D. Walensky, William C. Hahn, and Charles W. M. Roberts. MDM2 and MDM4 Are Therapeutic Vulnerabilities in Malignant Rhabdoid Tumors. *Cancer Research*, 79(9):2404–2414, May 2019. Publisher: American Association for Cancer Research Section: Translational Science.

[96] Luis A Carvajal, David Sutton, Mariam Mounir, Joseph McClanaghan, Vincent Guerlavais, Manuel Aivado, Vojislav Vukovic, and Allen Annis. The Investigational Peptide Drug ALRN-6924, a Dual Inhibitor of MDMX and MDM2, is an Effective Myelopreservation Agent. Technical Report Abstract #C064, AACR-NCI-EORTC International Conference on Molecular Targets and Cancer Therapeutics, Aileron Therapeutics, Inc., October 2019.

[97] Mattia Moiola, Misal G. Memeo, and Paolo Quadrelli. Stapled Peptides—A Useful Improvement for Peptide-Based Drugs. *Molecules*, 24(20), October 2019.

[98] Qian Chu, Raymond E. Moellering, Gerard J. Hilinski, Young-Woo Kim, Tom N. Grossmann, Johannes T.-H. Yeh, and Gregory L. Verdine. Towards understanding cell penetration by stapled peptides. *MedChemComm*, 6(1):111–119, 2015. Publisher: Royal Society of Chemistry.

[99] Yuan Tian, Yanhong Jiang, Jingxu Li, Dongyuan Wang, Hui Zhao, and Zigang Li. Effect of Stapling Architecture on Physiochemical Properties and Cell Permeability of Stapled α-Helical Peptides: A Comparative Study. *ChemBioChem*, 18(21):2087–2093, November 2017. Publisher: John Wiley & Sons, Ltd.

[100] Gregory L. Verdine and Gerard J. Hilinski. Stapled peptides for intracellular drug targets. *Methods in Enzymology*, 503:3–33, 2012.

[101] Xiayang Xie, Lixia Gao, Austin Y Shull, and Yong Teng. Stapled peptides: providing the best of both worlds in drug development. *Future Medicinal Chemistry*, 8(16):1969–1980, September 2016. Publisher: Future Science.

[102] Raheleh Rezaei Araghi, Gregory H. Bird, Jeremy A. Ryan, Justin M. Jenson, Marina Godes, Jonathan R. Pritz, Robert A. Grant, Anthony Letai, Loren D. Walensky, and Amy E. Keating. Iterative optimization yields Mcl-1–targeting stapled peptides with selective cytotoxicity to Mcl-1–dependent cancer cells. *Proceedings of the National Academy of Sciences*, 115(5):E886–E895, January 2018.

[103] James L. LaBelle, Samuel G. Katz, Gregory H. Bird, Evripidis Gavathiotis, Michelle L. Stewart, Chelsea Lawrence, Jill K. Fisher, Marina Godes, Kenneth Pitter, Andrew L. Kung, and Loren D. Walensky. A stapled BIM peptide overcomes apoptotic resistance in hematologic cancers. *The Journal of Clinical Investigation*, 122(6):2018–2031, June 2012.

[104] Abbas Hadji, Greta K. Schmitt, Mathew R. Schnorenberg, Lauren Roach, Connie M. Hickey, Logan B. Leak, Matthew V. Tirrell, and James L. LaBelle. Preferential targeting of MCL-1 by a hydrocarbon-stapled BIM BH3 peptide. *Oncotarget*, 10(58):6219–6233, October 2019.

[105] Yao-Cheng Li, Luo Wei Rodewald, Christian Hoppmann, Ee Tsin Wong, Sylvain Lebreton, Pavel Safar, Marcel Patek, Lei Wang, Kenneth F. Wertman, and Geoffrey M. Wahl. A Versatile Platform to Analyze Low-Affinity and Transient Protein-Protein Interactions in Living Cells in Real Time. *Cell Reports*, 9(5):1946–1958, December 2014.

[106] Amanda L. Edwards, Evripidis Gavathiotis, James L. LaBelle, Craig R. Braun, Kwadwo A. Opoku-Nsiah, Gregory H. Bird, and Loren D. Walensky. Multimodal Interaction with BCL-2 Family Proteins Underlies the Proapoptotic Activity of PUMA BH3. *Chemistry & Biology*, 20(7):888–902, July 2013.

[107] Vladimir Torchilin. Intracellular delivery of protein and peptide therapeutics. *Drug Discovery Today: Technologies*, 5(2):e95–e103, September 2008.

[108] Dan Peer, Jeffrey M. Karp, Seungpyo Hong, Omid C. Farokhzad, Rimona Margalit, and Robert Langer. Nanocarriers as an emerging platform for cancer therapy. *Nature Nanotechnology*, 2(12):751–760, December 2007. Number: 12 Publisher: Nature Publishing Group.

[109] Andrew Z. Wang, Robert Langer, and Omid C. Farokhzad. Nanoparticle Delivery of Cancer Drugs. *Annual Review of Medicine*, 63(1):185–198, 2012. _eprint: https://doi.org/10.1146/annurev-med-040210-162544.

[110] Handan Acar, Jeffrey M. Ting, Samanvaya Srivastava, James L. LaBelle, and Matthew V. Tirrell. Molecular engineering solutions for therapeutic peptide delivery. *Chemical Society Reviews*, 46(21):6553–6569, October 2017.

[111] Harshad K. Shete, Rashmi H. Prabhu, and Vandana B. Patravale. Endosomal Escape: A Bottleneck in Intracellular Delivery. *Journal of Nanoscience and Nanotechnology*, 14(1):460–474, January 2014.

[112] Gaurav Sahay, Daria Y. Alakhova, and Alexander V. Kabanov. Endocytosis of nanomedicines. *Journal of Controlled Release*, 145(3):182–195, August 2010.

[113] Gary J. Doherty and Harvey T. McMahon. Mechanisms of Endocytosis. *Annual Review of Biochemistry*, 78(1):857–902, 2009. _eprint: https://doi.org/10.1146/annurev.biochem.78.081307.110540.

[114] Aaron C. Anselmo and Samir Mitragotri. Nanoparticles in the clinic. *Bioengineering & Translational Medicine*, 1(1):10–29, 2016. _eprint: https://aiche.onlinelibrary.wiley.com/doi/pdf/10.1002/btm2.10003.

[115] Aaron C. Anselmo and Samir Mitragotri. Nanoparticles in the clinic: An update. *Bioengineering & Translational Medicine*, 4(3):e10143, 2019. _eprint: https://aiche.onlinelibrary.wiley.com/doi/pdf/10.1002/btm2.10143.

[116] Akin Akinc, Martin A. Maier, Muthiah Manoharan, Kevin Fitzgerald, Muthusamy Jayaraman, Scott Barros, Steven Ansell, Xinyao Du, Michael J. Hope, Thomas D. Madden, Barbara L. Mui, Sean C. Semple, Ying K. Tam, Marco Ciufolini, Dominik Witzigmann, Jayesh A. Kulkarni, Roy van der Meel, and Pieter R. Cullis. The Onpattro story and the clinical translation of nanomedicines containing nucleic acid-based drugs. *Nature Nanotechnology*, 14(12):1084–1087, December 2019.

[117] David Adams, Alejandra Gonzalez-Duarte, William D. O'Riordan, Chih-Chao Yang, Mitsuharu Ueda, Arnt V. Kristen, Ivailo Tournev, Hartmut H. Schmidt, Teresa Coelho, John L. Berk, Kon-Ping Lin, Giuseppe Vita, Shahram Attarian, Violaine Planté-Bordeneuve, Michelle M. Mezei, Josep M. Campistol, Juan Buades, Thomas H. Brannagan, Byoung J. Kim, Jeeyoung Oh, Yesim Parman, Yoshiki Sekijima, Philip N. Hawkins, Scott D. Solomon, Michael Polydefkis, Peter J. Dyck, Pritesh J. Gandhi, Sunita Goyal, Jihong Chen, Andrew L. Strahs, Saraswathy V. Nochur, Marianne T. Sweetser, Pushkal P. Garg, Akshay K. Vaishnaw, Jared A. Gollob, and Ole B. Suhr. Patisiran, an RNAi Therapeutic, for Hereditary Transthyretin Amyloidosis. *New England Journal of Medicine*, 379(1):11–21, July 2018. Publisher: Massachusetts Medical Society _eprint: https://doi.org/10.1056/NEJMoa1716153.

[118] Elvin Blanco, Haifa Shen, and Mauro Ferrari. Principles of nanoparticle design for overcoming biological barriers to drug delivery. *Nature Biotechnology*, 33(9):941–951, September 2015.

[119] Sheva Naahidi, Mousa Jafari, Faramarz Edalat, Kevin Raymond, Ali Khademhosseini, and P. Chen. Biocompatibility of engineered nanoparticles for drug delivery. *Journal of Controlled Release*, 166(2):182–194, March 2013.

[120] Peter Berndt, Gregg B. Fields, and Matthew Tirrell. Synthetic lipidation of peptides and amino acids: monolayer structure and properties. *Journal of the American Chemical Society*, 117(37):9515–9522, September 1995.

[121] Mathew R. Schnorenberg, Sang Pil Yoo, Matthew V. Tirrell, and James L. LaBelle. Synthesis and Purification of Homogeneous Lipid-Based Peptide Nanocarriers by Overcoming Phospholipid Ester Hydrolysis. *ACS Omega*, 3(10):14144–14150, October 2018.

[122] Handan Acar, Samanvaya Srivastava, Eun Ji Chung, Mathew R. Schnorenberg, John C. Barrett, James L. LaBelle, and Matthew Tirrell. Self-assembling peptide-based building blocks in medical applications. *Advanced Drug Delivery Reviews*, 110-111:65–79, February 2017.

[123] Eun Ji Chung, Laurie B. Mlinar, Matthew J. Sugimoto, Kathryn Nord, Brian B. Roman, and Matthew Tirrell. In vivo biodistribution and clearance of peptide amphiphile micelles. *Nanomedicine: Nanotechnology, Biology and Medicine*, 11(2):479–487, February 2015.

[124] P. Dasgupta and R. Mukherjee. Lipophilization of somatostatin analog RC-160 with long chain fatty acid improves its antiproliferative and antiangiogenic activity in vitro. *British Journal of Pharmacology*, 129(1):101–109, 2000. _eprint: https://bpspubs.onlinelibrary.wiley.com/doi/pdf/10.1038/sj.bjp.0702990.

[125] Dimitris Missirlis, Daniel V. Krogstad, and Matthew Tirrell. Internalization of p5314-29 Peptide Amphiphiles and Subsequent Endosomal Disruption Results in SJSA-1 Cell Death. *Molecular Pharmaceutics*, 7(6):2173–2184, December 2010.

[126] Dimitris Missirlis, Htet Khant, and Matthew Tirrell. Mechanisms of Peptide Amphiphile Internalization by SJSA-1 Cells in Vitro. *Biochemistry*, 48(15):3304–3314, April 2009.

[127] Dimitris Missirlis, Tambet Teesalu, Matthew Black, and Matthew Tirrell. The Non-Peptidic Part Determines the Internalization Mechanism and Intracellular Trafficking of Peptide Amphiphiles. *PLOS ONE*, 8(1):e54611, January 2013.

[128] David Peters, Mark Kastantin, Venkata Ramana Kotamraju, Priya P. Karmali, Kunal Gujraty, Matthew Tirrell, and Erkki Ruoslahti. Targeting atherosclerosis by using modular, multifunctional micelles. *Proceedings of the National Academy of Sciences*, 106(24):9815–9819, June 2009.

[129] Priya Prakash Karmali, Venkata Ramana Kotamraju, Mark Kastantin, Matthew Black, Dimitris Missirlis, Matthew Tirrell, and Erkki Ruoslahti. Targeting of albumin-embedded paclitaxel nanoparticles to tumors. *Nanomedicine: Nanotechnology, Biology and Medicine*, 5(1):73–82, March 2009.

[130] Eun Ji Chung, Yu Cheng, Ramin Morshed, Kathryn Nord, Yu Han, Michelle L. Wegscheid, Brenda Auffinger, Derek A. Wainwright, Maciej S. Lesniak, and Matthew V. Tirrell. Fibrin-binding, peptide amphiphile micelles for targeting glioblastoma. *Biomaterials*, 35(4):1249–1256, January 2014.

[131] Laurie B. Mlinar, Eun Ji Chung, Emily A. Wonder, and Matthew Tirrell. Active targeting of early and mid-stage atherosclerotic plaques using self-assembled

peptide amphiphile micelles. *Biomaterials*, 35(30):8678–8686, October 2014. WOS:000340849600021.

[132] Eun Ji Chung Federico Pineda. Fibrin-Targeting, Peptide Amphiphile Micelles as Contrast Agents for Molecular MRI. *Journal of Cell Science & Therapy*, 05(05), 2014.

[133] Eun Ji Chung, Laurie B. Mlinar, Kathryn Nord, Matthew J. Sugimoto, Emily Wonder, Francis J. Alenghat, Yun Fang, and Matthew Tirrell. Monocyte-Targeting Supramolecular Micellar Assemblies: A Molecular Diagnostic Tool for Atherosclerosis. *Advanced Healthcare Materials*, 4(3):367–376, 2015. _eprint: https://onlinelibrary.wiley.com/doi/pdf/10.1002/adhm.201400336.

[134] Sang Pil Yoo, Federico Pineda, John C. Barrett, Christopher Poon, Matthew Tirrell, and Eun Ji Chung. Gadolinium-Functionalized Peptide Amphiphile Micelles for Multimodal Imaging of Atherosclerotic Lesions. *ACS Omega*, 1(5):996–1003, November 2016. Publisher: American Chemical Society.

[135] Christopher Poon, Sampreeti Chowdhuri, Cheng-Hsiang Kuo, Yun Fang, Francis J. Alenghat, Danielle Hyatt, Kian Kani, Mitchell E. Gross, and Eun Ji Chung. Protein Mimetic and Anticancer Properties of Monocyte-Targeting Peptide Amphiphile Micelles. *ACS Biomaterials Science & Engineering*, 3(12):3273–3282, December 2017. Publisher: American Chemical Society.

[136] Jonathan Wang, Christopher Poon, Deborah Chin, Sarah Milkowski, Vivian Lu, Kenneth R. Hallows, and Eun Ji Chung. Design and in vivo characterization of kidney-targeting multimodal micelles for renal drug delivery. *Nano Research*, 11(10):5584–5595, October 2018.

[137] Johan Joo, Christopher Poon, Sang Pil Yoo, and Eun Ji Chung. Shape Effects of Peptide Amphiphile Micelles for Targeting Monocytes. *Molecules*, 23(11):2786, November 2018. Number: 11 Publisher: Multidisciplinary Digital Publishing Institute.

[138] Christopher Poon, Juan Gallo, Johan Joo, Timothy Chang, Manuel Bañobre-López, and Eun Ji Chung. Hybrid, metal oxide-peptide amphiphile micelles for molecular magnetic resonance imaging of atherosclerosis. *Journal of Nanobiotechnology*, 16(1):92, November 2018.

[139] Deborah D. Chin, Jonathan Wang, Margot Mel de Fontenay, Anastasia Plotkin, Gregory A. Magee, and Eun Ji Chung. Hydroxyapatite-binding micelles for the detection of vascular calcification in atherosclerosis. *Journal of Materials Chemistry B*, 7(41):6449–6457, October 2019. Publisher: The Royal Society of Chemistry.

[140] Deborah D. Chin, Christopher Poon, Noah Trac, Jonathan Wang, Jackson Cook, Johan Joo, Zhangjingyi Jiang, Naomi Sulit Sta Maria, Russell E. Jacobs, and Eun Ji Chung. Collagenase-Cleavable Peptide Amphiphile Micelles as a Novel Theranostic Strategy in Atherosclerosis. *Advanced Therapeutics*, 3(3):1900196, 2020. _eprint: https://onlinelibrary.wiley.com/doi/pdf/10.1002/adtp.201900196.

[141] Handan Acar, Ravand Samaeekia, Mathew R. Schnorenberg, Dibyendu K. Sasmal, Jun Huang, Matthew V. Tirrell, and James L. LaBelle. Cathepsin-Mediated Cleavage of Peptides from Peptide Amphiphiles Leads to Enhanced Intracellular Peptide Accumulation. *Bioconjugate Chemistry*, 28(9):2316–2326, September 2017.

[142] Mathew R. Schnorenberg, Joseph A. Bellairs, Ravand Samaeekia, Handan Acar, Matthew V. Tirrell, and James L. LaBelle. Activating the Intrinsic Pathway of Apoptosis Using BIM BH3 Peptides Delivered by Peptide Amphiphiles with Endosomal Release. *Materials*, 12(16):2567, January 2019.

[143] Jacob N. Israelachvili, D. John Mitchell, and Barry W. Ninham. Theory of self-assembly of hydrocarbon amphiphiles into micelles and bilayers. *Journal of the Chemical Society, Faraday Transactions 2: Molecular and Chemical Physics*, 72(0):1525–1568, January 1976. Publisher: The Royal Society of Chemistry.

[144] Gerald J. Mizejewski. Role of Integrins in Cancer: Survey of Expression Patterns. *Proceedings of the Society for Experimental Biology and Medicine*, 222(2):124–138, 1999. _eprint: https://onlinelibrary.wiley.com/doi/pdf/10.1046/j.1525-1373.1999.d01-122.x.

[145] Poonam Saraf, Xiaoling Li, Lisa Wrischnik, and Bhaskara Jasti. In Vitro and In Vivo Efficacy of Self-Assembling RGD Peptide Amphiphiles for Targeted Delivery of Paclitaxel. *Pharmaceutical Research*, 32(9):3087–3101, September 2015.

[146] R. Helen Zha, Shantanu Sur, Job Boekhoven, Heidi Y. Shi, Ming Zhang, and Samuel I. Stupp. Supramolecular assembly of multifunctional maspin-mimetic nanostructures as a potent peptide-based angiogenesis inhibitor. *Acta Biomaterialia*, 12:1–10, January 2015.

[147] Li Qin and Ming Zhang. Maspin Regulates Endothelial Cell Adhesion and Migration through an Integrin Signaling Pathway. *Journal of Biological Chemistry*, 285(42):32360–32369, October 2010. Publisher: American Society for Biochemistry and Molecular Biology.

[148] Michael P. Endsley, Yanqiu Hu, Yong Deng, Xiaolin He, Debra J. Warejcka, Sally S. Twining, Steven L. Gonias, and Ming Zhang. Maspin, the Molecular Bridge between the Plasminogen Activator System and $\beta 1$ Integrin That Facilitates Cell Adhesion. *Journal of Biological Chemistry*, 286(28):24599–24607, July 2011. Publisher: American Society for Biochemistry and Molecular Biology.

[149] Ming Zhang, Olga Volpert, Yihui H. Shi, and Noël Bouck. Maspin is an angiogenesis inhibitor. *Nature Medicine*, 6(2):196–199, February 2000. Number: 2 Publisher: Nature Publishing Group.

[150] Courtney E. Morgan, Amanda W. Dombrowski, Charles M. Rubert Pérez, Edward S.M. Bahnson, Nick D. Tsihlis, Wulin Jiang, Qun Jiang, Janet M. Vercammen, Vivek S. Prakash, Timothy A. Pritts, Samuel I. Stupp, and Melina R. Kibbe. Tissue-Factor Targeted Peptide Amphiphile Nanofibers as an Injectable Therapy To Control

Hemorrhage. *ACS Nano*, 10(1):899–909, January 2016. Publisher: American Chemical Society.

[151] He Dong, Nikhil Dube, Jessica Y. Shu, Jai W. Seo, Lisa M. Mahakian, Katherine W. Ferrara, and Ting Xu. Long-Circulating 15 nm Micelles Based on Amphiphilic 3-Helix Peptide–PEG Conjugates. *ACS Nano*, 6(6):5320–5329, June 2012. Publisher: American Chemical Society.

[152] Upendra Bulbake, Sindhu Doppalapudi, Nagavendra Kommineni, and Wahid Khan. Liposomal Formulations in Clinical Use: An Updated Review. *Pharmaceutics*, 9(2), March 2017.

[153] Esteban Beltrán-Gracia, Adolfo López-Camacho, Inocencio Higuera-Ciapara, Jesús B. Velázquez-Fernández, and Alba A. Vallejo-Cardona. Nanomedicine review: clinical developments in liposomal applications. *Cancer Nanotechnology*, 10(1):11, December 2019.

[154] Giuseppina Bozzuto and Agnese Molinari. Liposomes as nanomedical devices. *International Journal of Nanomedicine*, 10:975–999, February 2015.

[155] Theresa M. Allen and Pieter R. Cullis. Liposomal drug delivery systems: From concept to clinical applications. *Advanced Drug Delivery Reviews*, 65(1):36–48, January 2013.

[156] María Rocío Villegas, Alejandro Baeza, and María Vallet-Regí. Nanotechnological Strategies for Protein Delivery. *Molecules*, 23(5):1008, May 2018. Number: 5 Publisher: Multidisciplinary Digital Publishing Institute.

[157] Moumita Ray, Yi-Wei Lee, Federica Scaletti, Ruijin Yu, and Vincent M Rotello. Intracellular delivery of proteins by nanocarriers. *Nanomedicine*, 12(8):941–952, March 2017. Publisher: Future Medicine.

[158] Gavin T. Noble, Jared F. Stefanick, Jonathan D. Ashley, Tanyel Kiziltepe, and Basar Bilgicer. Ligand-targeted liposome design: challenges and fundamental considerations. *Trends in Biotechnology*, 32(1):32–45, January 2014.

[159] Yi-Wei Lee, David C. Luther, Jessica A. Kretzmann, Andrew Burden, Taewon Jeon, Shumei Zhai, and Vincent M. Rotello. Protein Delivery into the Cell Cytosol using Non-Viral Nanocarriers. *Theranostics*, 9(11):3280–3292, May 2019.

[160] Tatiana A. Slastnikova, A. V. Ulasov, A. A. Rosenkranz, and A. S. Sobolev. Targeted Intracellular Delivery of Antibodies: The State of the Art. *Frontiers in Pharmacology*, 9, 2018. Publisher: Frontiers.

[161] Twan Lammers, Fabian Kiessling, Wim E. Hennink, and Gert Storm. Drug targeting to tumors: Principles, pitfalls and (pre-) clinical progress. *Journal of Controlled Release*, 161(2):175–187, July 2012.

[162] Lisa Sercombe, Tejaswi Veerati, Fatemeh Moheimani, Sherry Y. Wu, Anil K. Sood, and Susan Hua. Advances and Challenges of Liposome Assisted Drug Delivery. *Frontiers in Pharmacology*, 6, 2015. Publisher: Frontiers.

[163] Jung Soo Suk, Qingguo Xu, Namho Kim, Justin Hanes, and Laura M. Ensign. PEGylation as a strategy for improving nanoparticle-based drug and gene delivery. *Advanced Drug Delivery Reviews*, 99:28–51, April 2016.

[164] S Belsito, R Bartucci, and L Sportelli. Lipid chain length effect on the phase behaviour of PCs/PEG:2000-PEs mixtures. A spin label electron spin resonance and spectrophotometric study. *Biophysical Chemistry*, 93(1):11–22, October 2001.

[165] Olga Garbuzenko, Yechezkel Barenholz, and Aba Priev. Effect of grafted PEG on liposome size and on compressibility and packing of lipid bilayer. *Chemistry and Physics of Lipids*, 135(2):117–129, June 2005.

[166] Yechezkel Barenholz. Liposome application: problems and prospects. *Current Opinion in Colloid & Interface Science*, 6(1):66–77, February 2001.

[167] Nancy Dos Santos, Christine Allen, Anne-Marie Doppen, Malathi Anantha, Kelly A. K. Cox, Ryan C. Gallagher, Goran Karlsson, Katarina Edwards, Gail Kenner, Lacey Samuels, Murray S. Webb, and Marcel B. Bally. Influence of poly(ethylene glycol) grafting density and polymer length on liposomes: Relating plasma circulation lifetimes to protein binding. *Biochimica et Biophysica Acta (BBA) - Biomembranes*, 1768(6):1367–1377, June 2007.

[168] Hwankyu Lee and Ronald G. Larson. Adsorption of Plasma Proteins onto PEGylated Lipid Bilayers: The Effect of PEG Size and Grafting Density. *Biomacromolecules*, 17(5):1757–1765, May 2016. Publisher: American Chemical Society.

[169] Bohdana M. Discher, You-Yeon Won, David S. Ege, James C.-M. Lee, Frank S. Bates, Dennis E. Discher, and Daniel A. Hammer. Polymersomes: Tough Vesicles Made from Diblock Copolymers. *Science*, 284(5417):1143–1146, May 1999. Publisher: American Association for the Advancement of Science Section: Report.

[170] Peter J. Photos, Lucie Bacakova, Bohdana Discher, Frank S. Bates, and Dennis E. Discher. Polymer vesicles in vivo: correlations with PEG molecular weight. *Journal of Controlled Release*, 90(3):323–334, July 2003.

[171] Birgit Romberg, Wim E. Hennink, and Gert Storm. Sheddable Coatings for Long-Circulating Nanoparticles. *Pharmaceutical Research*, 25(1):55–71, January 2008.

[172] Susana Martins, Bruno Sarmento, Domingos C Ferreira, and Eliana B Souto. Lipid-based colloidal carriers for peptide and protein delivery – liposomes versus lipid nanoparticles. *International Journal of Nanomedicine*, 2(4):595–607, December 2007.

[173] Roberta Caruso, Neil Warner, Naohiro Inohara, and Gabriel Núñez. NOD1 and NOD2: Signaling, Host Defense, and Inflammatory Disease. *Immunity*, 41(6):898–908, December 2014.

[174] Léa Messager, Jens Gaitzsch, Luca Chierico, and Giuseppe Battaglia. Novel aspects of encapsulation and delivery using polymersomes. *Current Opinion in Pharmacology*, 18:104–111, October 2014.

[175] W. C. Shen, H. J. Ryser, and L. LaManna. Disulfide spacer between methotrexate and poly(D-lysine). A probe for exploring the reductive process in endocytosis. *Journal of Biological Chemistry*, 260(20):10905–10908, September 1985. Publisher: American Society for Biochemistry and Molecular Biology.

[176] E. Papini, R. Rappuoli, M. Murgia, and C. Montecucco. Cell penetration of diphtheria toxin. Reduction of the interchain disulfide bridge is the rate-limiting step of translocation in the cytosol. *The Journal of Biological Chemistry*, 268(3):1567–1574, January 1993.

[177] D. S. Collins, E. R. Unanue, and C. V. Harding. Reduction of disulfide bonds within lysosomes is a key step in antigen processing. *Journal of Immunology (Baltimore, Md.: 1950)*, 147(12):4054–4059, December 1991.

[178] Marc Fivaz, Francis Vilbois, Sarah Thurnheer, Christian Pasquali, Laurence Abrami, Perry E. Bickel, Robert G. Parton, and F. Gisou van der Goot. Differential sorting and fate of endocytosed GPI-anchored proteins. *The EMBO journal*, 21(15):3989–4000, August 2002.

[179] Chensu Wang, Tian Zhao, Yang Li, Gang Huang, Michael A. White, and Jinming Gao. Investigation of endosome and lysosome biology by ultra pH-sensitive nanoprobes. *Advanced Drug Delivery Reviews*, 113:87–96, 2017.

[180] Balasubramanian Arunachalam, Uyen T. Phan, Hans J. Geuze, and Peter Cresswell. Enzymatic reduction of disulfide bonds in lysosomes: Characterization of a Gamma-interferon-inducible lysosomal thiol reductase (GILT). *Proceedings of the National Academy of Sciences*, 97(2):745–750, January 2000. Publisher: National Academy of Sciences Section: Biological Sciences.

[181] Simona Cerritelli, Diana Velluto, and Jeffrey A. Hubbell. PEG-SS-PPS: Reduction-Sensitive Disulfide Block Copolymer Vesicles for Intracellular Drug Delivery. *Biomacromolecules*, 8(6):1966–1972, June 2007. Publisher: American Chemical Society.

[182] Ira Mellman, Renate Fuchs, and Ari Helenius. Acidification of the Endocytic and Exocytic Pathways. *Annual Review of Biochemistry*, 55(1):663–700, 1986. _eprint: https://doi.org/10.1146/annurev.bi.55.070186.003311.

[183] Jatta Huotari and Ari Helenius. Endosome maturation. *The EMBO Journal*, 30(17):3481–3500, August 2011.

[184] Cary D. Austin, Xiaohui Wen, Lewis Gazzard, Christopher Nelson, Richard H. Scheller, and Suzie J. Scales. Oxidizing potential of endosomes and lysosomes limits intracellular cleavage of disulfide-based antibody–drug conjugates. *Proceedings of the National Academy of Sciences*, 102(50):17987–17992, December 2005. Publisher: National Academy of Sciences Section: Biological Sciences.

[185] Ariel Savina and Sebastian Amigorena. Phagocytosis and antigen presentation in dendritic cells. *Immunological Reviews*, 219(1):143–156, 2007. _eprint: https://onlinelibrary.wiley.com/doi/pdf/10.1111/j.1600-065X.2007.00552.x.

[186] Fanfan Du, Yu-Gang Liu, and Evan Alexander Scott. Immunotheranostic Polymersomes Modularly Assembled from Tetrablock and Diblock Copolymers with Oxidation-Responsive Fluorescence. *Cellular and Molecular Bioengineering*, 10(5):357–370, April 2017.

[187] Lélia Delamarre, Margit Pack, Henry Chang, Ira Mellman, and E. Sergio Trombetta. Differential lysosomal proteolysis in antigen-presenting cells determines antigen fate. *Science (New York, N.Y.)*, 307(5715):1630–1634, March 2005.

[188] Alessandro Napoli, Nicola Tirelli, Ernst Wehrli, and Jeffrey A. Hubbell. Lyotropic Behavior in Water of Amphiphilic ABA Triblock Copolymers Based on Poly(propylene sulfide) and Poly(ethylene glycol). *Langmuir*, 18(22):8324–8329, October 2002. Publisher: American Chemical Society.

[189] Conlin P. O'Neil, Tomoake Suzuki, Davide Demurtas, Andrija Finka, and Jeffrey A. Hubbell. A Novel Method for the Encapsulation of Biomolecules into Polymersomes via Direct Hydration. *Langmuir*, 25(16):9025–9029, August 2009. Publisher: American Chemical Society.

[190] Sean Allen, Omar Osorio, Yu-Gang Liu, and Evan Scott. Facile assembly and loading of theranostic polymersomes via multi-impingement flash nanoprecipitation. *Journal of Controlled Release*, 262:91–103, September 2017.

[191] Sean D. Allen, Yu-Gang Liu, Sharan Bobbala, Lei Cai, Peter I. Hecker, Ryan Temel, and Evan A. Scott. Polymersomes scalably fabricated via flash nanoprecipitation are non-toxic in non-human primates and associate with leukocytes in the spleen and kidney following intravenous administration. *Nano Research*, 11(10):5689–5703, October 2018.

[192] Alessandro Napoli, Massimiliano Valentini, Nicola Tirelli, Martin Müller, and Jeffrey A. Hubbell. Oxidation-responsive polymeric vesicles. *Nature Materials*, 3(3):183–189, March 2004. Number: 3 Publisher: Nature Publishing Group.

[193] Alessandro Napoli, Mark J. Boerakker, Nicola Tirelli, Roeland J. M. Nolte, Nico A. J. M. Sommerdijk, and Jeffrey A. Hubbell. Glucose-oxidase Based Self-Destructing Polymeric Vesicles. *Langmuir*, 20(9):3487–3491, April 2004. Publisher: American Chemical Society.

[194] Sai T. Reddy, Annemie Rehor, Hugo G. Schmoekel, Jeffrey A. Hubbell, and Melody A. Swartz. In vivo targeting of dendritic cells in lymph nodes with poly(propylene sulfide) nanoparticles. *Journal of Controlled Release*, 112(1):26–34, May 2006.

[195] Sachiko Hirosue, Iraklis C. Kourtis, André J. van der Vlies, Jeffrey A. Hubbell, and Melody A. Swartz. Antigen delivery to dendritic cells by poly(propylene sulfide)

nanoparticles with disulfide conjugated peptides: Cross-presentation and T cell activation. *Vaccine*, 28(50):7897–7906, November 2010.

[196] Evan A. Scott, Armando Stano, Morgane Gillard, Alexandra C. Maio-Liu, Melody A. Swartz, and Jeffrey A. Hubbell. Dendritic cell activation and T cell priming with adjuvant- and antigen-loaded oxidation-sensitive polymersomes. *Biomaterials*, 33(26):6211–6219, September 2012.

[197] Diana Velluto, Davide Demurtas, and Jeffrey A. Hubbell. PEG-b-PPS Diblock Copolymer Aggregates for Hydrophobic Drug Solubilization and Release: Cyclosporin A as an Example. *Molecular Pharmaceutics*, 5(4):632–642, August 2008. Publisher: American Chemical Society.

[198] Karen Y. Dane, Chiara Nembrini, Alice A. Tomei, Jackson K. Eby, Conlin P. O'Neil, Diana Velluto, Melody A. Swartz, Luca Inverardi, and Jeffrey A. Hubbell. Nano-sized drug-loaded micelles deliver payload to lymph node immune cells and prolong allograft survival. *Journal of Controlled Release*, 156(2):154–160, December 2011.

[199] Theresa M. Allen, Davis R. Mumbengegwi, and Gregory J. R. Charrois. Anti-CD19-Targeted Liposomal Doxorubicin Improves the Therapeutic Efficacy in Murine B-Cell Lymphoma and Ameliorates the Toxicity of Liposomes with Varying Drug Release Rates. *Clinical Cancer Research*, 11(9):3567–3573, May 2005. Publisher: American Association for Cancer Research Section: Cancer Therapy: Preclinical.

[200] Daniel E. Lopes de Menezes, Marc J. Kirchmeier, Jean-Francois Gagne, Linda M. Pilarski, and Theresa M. Allen. Cellular Trafficking and Cytotoxicity of Anti-Cd19-Targeted Liposomal Doxorubicin in B Lymphoma Cells. *Journal of Liposome Research*, 9(2):199–228, January 1999. Publisher: Taylor & Francis _eprint: https://doi.org/10.3109/08982109909024786.

[201] Puja Sapra and Theresa M. Allen. Internalizing Antibodies Are Necessary for Improved Therapeutic Efficacy of Antibody-targeted Liposomal Drugs. *Cancer Research*, 62(24):7190–7194, December 2002. Publisher: American Association for Cancer Research Section: Advances in Brief.

[202] Puja Sapra and Theresa M. Allen. Improved Outcome When B-Cell Lymphoma Is Treated with Combinations of Immunoliposomal Anticancer Drugs Targeted to Both the CD19 and CD20 Epitopes. *Clinical Cancer Research*, 10(7):2530–2537, April 2004. Publisher: American Association for Cancer Research Section: Regular Articles.

[203] Wilson W. K. Cheng and Theresa M. Allen. Targeted delivery of anti-CD19 liposomal doxorubicin in B-cell lymphoma: A comparison of whole monoclonal antibody, Fab' fragments and single chain Fv. *Journal of Controlled Release*, 126(1):50–58, February 2008.

[204] WW Cheng and TM Allen. The use of single chain Fv as targeting agents for immunoliposomes: an update on immunoliposomal drugs for cancer treatment. *Expert opinion on drug delivery*, 7(4):461–478, April 2010.

[205] Jörg Willuda, Annemarie Honegger, Robert Waibel, P. August Schubiger, Rolf Stahel, Uwe Zangemeister-Wittke, and Andreas Plückthun. High Thermal Stability Is Essential for Tumor Targeting of Antibody Fragments: Engineering of a Humanized Anti-epithelial Glycoprotein-2 (Epithelial Cell Adhesion Molecule) Single-Chain Fv Fragment. *Cancer Research*, 59(22):5758–5767, November 1999. Publisher: American Association for Cancer Research Section: Experimental Therapeutics.

[206] Arne Wörn, Adrian Auf der Maur, Dominik Escher, Annemarie Honegger, Alcide Barberis, and Andreas Plückthun. Correlation between in Vitro Stability and in Vivo Performance of Anti-GCN4 Intrabodies as Cytoplasmic Inhibitors. *Journal of Biological Chemistry*, 275(4):2795–2803, January 2000. Publisher: American Society for Biochemistry and Molecular Biology.

[207] Veronica Quintero-Hernández, Victor R. Juárez-González, Mauricio Ortíz-León, Rosalba Sánchez, Lourival D. Possani, and Baltazar Becerril. The change of the scFv into the Fab format improves the stability and in vivo toxin neutralization capacity of recombinant antibodies. *Molecular Immunology*, 44(6):1307–1315, February 2007.

[208] Camille Laurent, Catherine Do, Randy D. Gascoyne, Laurence Lamant, Loïc Ysebaert, Guy Laurent, Georges Delsol, and Pierre Brousset. Anaplastic Lymphoma Kinase–Positive Diffuse Large B-Cell Lymphoma: A Rare Clinicopathologic Entity With Poor Prognosis. *Journal of Clinical Oncology*, 27(25):4211–4216, September 2009.

[209] Zenggang Pan, Shimin Hu, Min Li, Yi Zhou, Young S. Kim, Vishnu Reddy, Jennifer N. Sanmann, Lynette M. Smith, Mingyi Chen, Zifen Gao, Huan-You Wang, and Ji Yuan. ALK-positive Large B-cell Lymphoma: A Clinicopathologic Study of 26 Cases With Review of Additional 108 Cases in the Literature. *The American Journal of Surgical Pathology*, 41(1):25–38, January 2017.

[210] Bertrand Coiffier, Catherine Thieblemont, Eric Van Den Neste, Gérard Lepeu, Isabelle Plantier, Sylvie Castaigne, Sophie Lefort, Gérald Marit, Margaret Macro, Catherine Sebban, Karim Belhadj, Dominique Bordessoule, Christophe Fermé, and Hervé Tilly. Long-term outcome of patients in the LNH-98.5 trial, the first randomized study comparing rituximab-CHOP to standard CHOP chemotherapy in DLBCL patients: a study by the Groupe d'Etudes des Lymphomes de l'Adulte. *Blood*, 116(12):2040–2045, September 2010. Publisher: American Society of Hematology.

[211] Jean-François Larouche, Françoise Berger, Catherine Chassagne-Clément, Martine Ffrench, Evelyne Callet-Bauchu, Catherine Sebban, Hervé Ghesquières, Florence Broussais-Guillaumot, Gilles Salles, and Bertrand Coiffier. Lymphoma Recurrence 5 Years or Later Following Diffuse Large B-Cell Lymphoma: Clinical Characteristics and Outcome. *Journal of Clinical Oncology*, 28(12):2094–2100, March 2010. Publisher: American Society of Clinical Oncology.

[212] Zijun Y. Xu-Monette, Lin Wu, Carlo Visco, Yu Chuan Tai, Alexander Tzankov, Weimin Liu, Santiago Montes-Moreno, Karen Dybkær, April Chiu, Attilio Orazi, Youli Zu, Govind Bhagat, Kristy L. Richards, Eric D. Hsi, X. Frank Zhao, William W. L. Choi,

Xiaoying Zhao, J. Han van Krieken, Qin Huang, Jooryung Huh, Weiyun Ai, Maurilio Ponzoni, Andrés J. M. Ferreri, Fan Zhou, Brad S. Kahl, Jane N. Winter, Wei Xu, Jianyong Li, Ronald S. Go, Yong Li, Miguel A. Piris, Michael B. Møller, Roberto N. Miranda, Lynne V. Abruzzo, L. Jeffrey Medeiros, and Ken H. Young. Mutational profile and prognostic significance of TP53 in diffuse large B-cell lymphoma patients treated with R-CHOP: report from an International DLBCL Rituximab-CHOP Consortium Program Study. *Blood*, 120(19):3986–3996, November 2012. Publisher: American Society of Hematology.

[213] Jenny Zhang, Vladimir Grubor, Cassandra L. Love, Anjishnu Banerjee, Kristy L. Richards, Piotr A. Mieczkowski, Cherie Dunphy, William Choi, Wing Yan Au, Gopesh Srivastava, Patricia L. Lugar, David A. Rizzieri, Anand S. Lagoo, Leon Bernal-Mizrachi, Karen P. Mann, Christopher Flowers, Kikkeri Naresh, Andrew Evens, Leo I. Gordon, Magdalena Czader, Javed I. Gill, Eric D. Hsi, Qingquan Liu, Alice Fan, Katherine Walsh, Dereje Jima, Lisa L. Smith, Amy J. Johnson, John C. Byrd, Micah A. Luftig, Ting Ni, Jun Zhu, Amy Chadburn, Shawn Levy, David Dunson, and Sandeep S. Dave. Genetic heterogeneity of diffuse large B-cell lymphoma. *Proceedings of the National Academy of Sciences*, 110(4):1398–1403, January 2013. Publisher: National Academy of Sciences Section: Biological Sciences.

[214] Clare M. Adams, Sean Clark-Garvey, Pierluigi Porcu, and Christine M. Eischen. Targeting the Bcl-2 Family in B Cell Lymphoma. *Frontiers in Oncology*, 8, January 2019.

[215] Matthew S. Davids, Andrew W. Roberts, John F. Seymour, John M. Pagel, Brad S. Kahl, William G. Wierda, Soham Puvvada, Thomas J. Kipps, Mary Ann Anderson, Ahmed Hamed Salem, Martin Dunbar, Ming Zhu, Franklin Peale, Jeremy A. Ross, Lori Gressick, Monali Desai, Su Young Kim, Maria Verdugo, Rod A. Humerickhouse, Gary B. Gordon, and John F. Gerecitano. Phase I First-in-Human Study of Venetoclax in Patients With Relapsed or Refractory Non-Hodgkin Lymphoma. *Journal of Clinical Oncology*, 35(8):826–833, January 2017. Publisher: American Society of Clinical Oncology.

[216] S.-S. Wenzel, M. Grau, C. Mavis, S. Hailfinger, A. Wolf, H. Madle, G. Deeb, B. Dörken, M. Thome, P. Lenz, S. Dirnhofer, F. J. Hernandez-Ilizaliturri, A. Tzankov, and G. Lenz. MCL1 is deregulated in subgroups of diffuse large B-cell lymphoma. *Leukemia*, 27(6):1381–1390, June 2013. Number: 6 Publisher: Nature Publishing Group.

[217] Ping Zhou, Norman B. Levy, Haiyi Xie, Liping Qian, Chi-Yu Gregory Lee, Randy D. Gascoyne, and Ruth W. Craig. MCL1 transgenic mice exhibit a high incidence of B-cell lymphoma manifested as a spectrum of histologic subtypes. *Blood*, 97(12):3902–3909, June 2001. Publisher: American Society of Hematology.

[218] Ken Kuramoto, Akira Sakai, Kazushi Shigemasa, Yasuo Takimoto, Hideki Asaoku, TakAko Tsujimoto, Kenji Oda, Akiro Kimura, Toshihiro Uesaka, Hiromitsu Watanabe, and Osamu Katoh. High expression of MCL1 gene related to vascular endothelial growth factor is associated with poor outcome in non-Hodgkin's

lymphoma. *British Journal of Haematology*, 116(1):158–161, 2002. _eprint: https://onlinelibrary.wiley.com/doi/pdf/10.1046/j.1365-2141.2002.03253.x.

[219] Claudia Stolz, Georg Hess, Patricia S. Hähnel, Florian Grabellus, Sandra Hoffarth, Kurt W. Schmid, and Martin Schuler. Targeting Bcl-2 family proteins modulates the sensitivity of B-cell lymphoma to rituximab-induced apoptosis. *Blood*, 112(8):3312–3321, October 2008. Publisher: American Society of Hematology.

[220] G. S. Choudhary, S. Al-harbi, S. Mazumder, B. T. Hill, M. R. Smith, J. Bodo, E. D. Hsi, and A. Almasan. MCL-1 and BCL-xL-dependent resistance to the BCL-2 inhibitor ABT-199 can be overcome by preventing PI3K/AKT/mTOR activation in lymphoid malignancies. *Cell Death & Disease*, 6(1):e1593–e1593, January 2015. Number: 1 Publisher: Nature Publishing Group.

[221] Melisa A. Martínez-Paniagua, Stavroula Baritaki, Sara Huerta-Yepez, Vianney F. Ortiz-Navarrete, Cesar González-Bonilla, Benjamin Bonavida, and Mario I. Vega. Mcl-1 and YY1 inhibition and induction of DR5 by the BH3-mimetic Obatoclax (GX15-070) contribute in the sensitization of B-NHL cells to TRAIL apoptosis. *Cell Cycle*, 10(16):2792–2805, August 2011. Publisher: Taylor & Francis _eprint: https://doi.org/10.4161/cc.10.16.16952.

[222] Guillaume Jacquemin, Virginie Granci, Anne Sophie Gallouet, Najoua Lalaoui, Aymeric Morlé, Elisabetta Iessi, Alexandre Morizot, Carmen Garrido, Thierry Guillaudeux, and Olivier Micheau. Quercetin-mediated Mcl-1 and survivin downregulation restores TRAIL-induced apoptosis in non-Hodgkin's lymphoma B cells. *Haematologica*, 97(1):38–46, January 2012. Publisher: Haematologica.

[223] D. C. Phillips, Y. Xiao, L. T. Lam, E. Litvinovich, L. Roberts-Rapp, A. J. Souers, and J. D. Leverson. Loss in MCL-1 function sensitizes non-Hodgkin's lymphoma cell lines to the BCL-2-selective inhibitor venetoclax (ABT-199). *Blood Cancer Journal*, 5(11):e368–e368, November 2015. Number: 11 Publisher: Nature Publishing Group.

[224] Joseph T. Opferman, Anthony Letai, Caroline Beard, Mia D. Sorcinelli, Christy C. Ong, and Stanley J. Korsmeyer. Development and maintenance of B and T lymphocytes requires antiapoptotic MCL-1. *Nature*, 426(6967):671–676, December 2003. Number: 6967 Publisher: Nature Publishing Group.

[225] Joseph T. Opferman, Hiromi Iwasaki, Christy C. Ong, Heikyung Suh, Shin-ichi Mizuno, Koichi Akashi, and Stanley J. Korsmeyer. Obligate Role of Anti-Apoptotic MCL-1 in the Survival of Hematopoietic Stem Cells. *Science*, 307(5712):1101–1104, February 2005. Publisher: American Association for the Advancement of Science Section: Report.

[226] Ivan Dzhagalov, Ashley St. John, and You-Wen He. The antiapoptotic protein Mcl-1 is essential for the survival of neutrophils but not macrophages. *Blood*, 109(4):1620–1626, February 2007. Publisher: American Society of Hematology.

[227] Hayato Hikita, Tetsuo Takehara, Satoshi Shimizu, Takahiro Kodama, Wei Li, Takuya Miyagi, Atsushi Hosui, Hisashi Ishida, Kazuyoshi Ohkawa, Tatsuya Kanto, Naoki Hiramatsu, Xiao-Ming Yin, Lothar Hennighausen, Tomohide Tatsumi, and Norio Hayashi. Mcl-1 and Bcl-xL cooperatively maintain integrity of hepatocytes in developing and adult murine liver. *Hepatology*, 50(4):1217–1226, 2009. _eprint: https://aasldpubs.onlinelibrary.wiley.com/doi/pdf/10.1002/hep.23126.

[228] Binje Vick, Achim Weber, Toni Urbanik, Thorsten Maass, Andreas Teufel, Peter H. Krammer, Joseph T. Opferman, Marcus Schuchmann, Peter R. Galle, and Henning Schulze-Bergkamen. Knockout of myeloid cell leukemia-1 induces liver damage and increases apoptosis susceptibility of murine hepatocytes. *Hepatology*, 49(2):627–636, 2009. _eprint: https://aasldpubs.onlinelibrary.wiley.com/doi/pdf/10.1002/hep.22664.

[229] Robert L. Thomas, David J. Roberts, Dieter A. Kubli, Youngil Lee, Melissa N. Quinsay, Jarvis B. Owens, Kimberlee M. Fischer, Mark A. Sussman, Shigeki Miyamoto, and Åsa B. Gustafsson. Loss of MCL-1 leads to impaired autophagy and rapid development of heart failure. *Genes & Development*, 27(12):1365–1377, June 2013. Company: Cold Spring Harbor Laboratory Press Distributor: Cold Spring Harbor Laboratory Press Institution: Cold Spring Harbor Laboratory Press Label: Cold Spring Harbor Laboratory Press Publisher: Cold Spring Harbor Lab.

[230] Xi Wang, Madhavi Bathina, John Lynch, Brian Koss, Christopher Calabrese, Sharon Frase, John D. Schuetz, Jerold E. Rehg, and Joseph T. Opferman. Deletion of MCL-1 causes lethal cardiac failure and mitochondrial dysfunction. *Genes & Development*, 27(12):1351–1364, June 2013. Company: Cold Spring Harbor Laboratory Press Distributor: Cold Spring Harbor Laboratory Press Institution: Cold Spring Harbor Laboratory Press Label: Cold Spring Harbor Laboratory Press Publisher: Cold Spring Harbor Lab.

[231] Nika N Danial and Stanley J Korsmeyer. Cell Death: Critical Control Points. *Cell*, 116(2):205–219, January 2004.

[232] Pascal Meier, Andrew Finch, and Gerard Evan. Apoptosis in development. *Nature*, 407(6805):796, October 2000.

[233] Andreas Strasser. The role of BH3-only proteins in the immune system. *Nature Reviews Immunology*, 5(3):189, March 2005.

[234] Michael Certo, Victoria Del Gaizo Moore, Mari Nishino, Guo Wei, Stanley Korsmeyer, Scott A. Armstrong, and Anthony Letai. Mitochondria primed by death signals determine cellular addiction to antiapoptotic BCL-2 family members. *Cancer Cell*, 9(5):351–365, May 2006.

[235] Philipp M. Cromm, Jochen Spiegel, and Tom N. Grossmann. Hydrocarbon Stapled Peptides as Modulators of Biological Function. *ACS Chemical Biology*, 10(6):1362–1375, June 2015.

[236] Haipeng Liu, Kelly D. Moynihan, Yiran Zheng, Gregory L. Szeto, Adrienne V. Li, Bonnie Huang, Debra S. Van Egeren, Clara Park, and Darrell J. Irvine. Structure-based programming of lymph-node targeting in molecular vaccines. *Nature*, 507(7493):519–522, March 2014.

[237] Samuel G. Katz, James L. LaBelle, Hailong Meng, Regina P. Valeriano, Jill K. Fisher, Heather Sun, Scott J. Rodig, Steven H. Kleinstein, and Loren D. Walensky. Mantle cell lymphoma in cyclin D1 transgenic mice with Bim-deficient B cells. *Blood*, 123(6):884–893, February 2014.

[238] Amanda L. Edwards, Franziska Wachter, Margaret Lammert, Annissa J. Huhn, James Luccarelli, Gregory H. Bird, and Loren D. Walensky. Cellular Uptake and Ultrastructural Localization Underlie the Pro-apoptotic Activity of a Hydrocarbon-stapled BIM BH3 Peptide. *ACS Chemical Biology*, 10(9):2149–2157, September 2015.

[239] Greg H. Bird, Evripidis Gavathiotis, James L. LaBelle, Samuel G. Katz, and Loren D. Walensky. Distinct BimBH3 (BimSAHB) Stapled Peptides for Structural and Cellular Studies. *ACS Chemical Biology*, 9(3):831–837, March 2014.

[240] Ying-Ching Yu, Peter Berndt, Matthew Tirrell, and Gregg B. Fields. Self-Assembling Amphiphiles for Construction of Protein Molecular Architecture. *Journal of the American Chemical Society*, 118(50):12515–12520, January 1996.

[241] Ilona Laczkó, Miklós Hollósi, Elemér Vass, and Gábor K. Tóth. Liposome-Induced Conformational Changes of an Epitopic Peptide and its Palmitoylated Derivative of Influenza Virus Hemagglutinin. *Biochemical and Biophysical Research Communications*, 249(1):213–217, August 1998.

[242] Pilar Forns, Janelle L. Lauer-Fields, Su Gao, and Gregg B. Fields. Induction of protein-like molecular architecture by monoalkyl hydrocarbon chains. *Biopolymers*, 54(7):531–546, 2000.

[243] Evripidis Gavathiotis, Motoshi Suzuki, Marguerite L. Davis, Kenneth Pitter, Gregory H. Bird, Samuel G. Katz, Ho-Chou Tu, Hyungjin Kim, Emily H.-Y. Cheng, Nico Tjandra, and Loren D. Walensky. BAX activation is initiated at a novel interaction site. *Nature*, 455(7216):1076–1081, October 2008.

[244] Loren D. Walensky, Kenneth Pitter, Joel Morash, Kyoung Joon Oh, Scott Barbuto, Jill Fisher, Eric Smith, Gregory L. Verdine, and Stanley J. Korsmeyer. A Stapled BID BH3 Helix Directly Binds and Activates BAX. *Molecular Cell*, 24(2):199–210, October 2006.

[245] Lingyan Jin, Weiru Wang, and Guowei Fang. Targeting Protein-Protein Interaction by Small Molecules. *Annual Review of Pharmacology and Toxicology*, 54(1):435–456, 2014.

[246] Jeremy Ryan and Anthony Letai. BH3 profiling in whole cells by fluorimeter or FACS. *Methods*, 61(2):156–164, June 2013.

[247] Amir K. Varkouhi, Marije Scholte, Gert Storm, and Hidde J. Haisma. Endosomal escape pathways for delivery of biologicals. *Journal of Controlled Release*, 151(3):220–228, May 2011.

[248] J. Martin Scholtz, Hong Qian, Eunice J. York, John M. Stewart, and Robert L. Baldwin. Parameters of helix-coil transition theory for alanine-based peptides of varying chain lengths in water. *Biopolymers*, 31(13):1463–1470, November 1991.

[249] Kenneth Pitter, Federico Bernal, James LaBelle, and Loren D. Walensky. Chapter 23 Dissection of the BCL-2 Family Signaling Network with Stabilized α-Helices of BCL-2 Domains. In *Methods in Enzymology*, volume 446 of *Programmed Cell Death, The Biology and Therapeutic Implications of Cell Death, Part B*, pages 387–408. Academic Press, January 2008.

[250] Jozefa Wesierska-Gadek, Marieta Gueorguieva, Carmen Ranftler, and Gerlinde Zerza-Schnitzhofer. A new multiplex assay allowing simultaneous detection of the inhibition of cell proliferation and induction of cell death. *Journal of Cellular Biochemistry*, 96(1):1–7, 2005.

[251] David J. Craik, David P. Fairlie, Spiros Liras, and David Price. The Future of Peptide-based Drugs. *Chemical Biology & Drug Design*, 81(1):136–147, 2013. _eprint: https://onlinelibrary.wiley.com/doi/pdf/10.1111/cbdd.12055.

[252] Amrita Banerjee and Hayat Onyuksel. Peptide delivery using phospholipid micelles. *WIREs Nanomedicine and Nanobiotechnology*, 4(5):562–574, 2012. _eprint: https://onlinelibrary.wiley.com/doi/pdf/10.1002/wnan.1185.

[253] Anu Puri, Kristin Loomis, Brandon Smith, Jae-Ho Lee, Amichai Yavlovich, Eliahu Heldman, and Robert Blumenthal. Lipid-Based Nanoparticles as Pharmaceutical Drug Carriers: From Concepts to Clinic. *Critical Reviews™ in Therapeutic Drug Carrier Systems*, 26(6), 2009. Publisher: Begel House Inc.

[254] Erkki Ruoslahti. Peptides as Targeting Elements and Tissue Penetration Devices for Nanoparticles. *Advanced Materials*, 24(28):3747–3756, 2012. _eprint: https://onlinelibrary.wiley.com/doi/pdf/10.1002/adma.201200454.

[255] Rupa R. Sawant and Vladimir P. Torchilin. Multifunctionality of lipid-core micelles for drug delivery and tumour targeting. *Molecular Membrane Biology*, 27(7):232–246, October 2010. Publisher: Taylor & Francis _eprint: https://doi.org/10.3109/09687688.2010.516276.

[256] Marije Slingerland, Henk-Jan Guchelaar, and Hans Gelderblom. Liposomal drug formulations in cancer therapy: 15 years along the road. *Drug Discovery Today*, 17(3):160–166, February 2012.

[257] Vladimir P. Torchilin. Lipid-Core Micelles for Targeted Drug Delivery, 2005. Library Catalog: www.ingentaconnect.com Publisher: Bentham Science Publishers.

[258] Ludger M. Ickenstein, Maria C. Sandström, Lawrence D. Mayer, and Katarina Edwards. Effects of phospholipid hydrolysis on the aggregate structure in DPPC/DSPE-PEG2000 liposome preparations after gel to liquid crystalline phase transition. *Biochimica et Biophysica Acta (BBA) - Biomembranes*, 1758(2):171–180, February 2006.

[259] N. J. Zuidam and D. J. A. Crommelin. Chemical hydrolysis of phospholipids. *Journal of Pharmaceutical Sciences*, 84(9):1113–1119, 1995. _eprint: https://onlinelibrary.wiley.com/doi/pdf/10.1002/jps.2600840915.

[260] Nicolaas J. Zuidam, H. K. Martin E. Gouw, Yechezkel Barenholz, and Daan J. A. Crommelin. Physical (in) stability of liposomes upon chemical hydrolysis: the role of lysophospholipids and fatty acids. *Biochimica et Biophysica Acta (BBA) - Biomembranes*, 1240(1):101–110, November 1995.

[261] Sheetal R. D'Mello, Celia N. Cruz, Mei-Ling Chen, Mamta Kapoor, Sau L. Lee, and Katherine M. Tyner. The evolving landscape of drug products containing nanomaterials in the United States. *Nature Nanotechnology*, 12(6):523–529, June 2017. Number: 6 Publisher: Nature Publishing Group.

[262] Chiraz Jaafar-Maalej, Abdelhamid Elaissari, and Hatem Fessi. Lipid-based carriers: manufacturing and applications for pulmonary route. *Expert Opinion on Drug Delivery*, 9(9):1111–1127, September 2012. Publisher: Taylor & Francis _eprint: https://doi.org/10.1517/17425247.2012.702751.

[263] John C. Kraft, Jennifer P. Freeling, Ziyao. Wang, and Rodney J. Y. Ho. Emerging Research and Clinical Development Trends of Liposome and Lipid Nanoparticle Drug Delivery Systems. *Journal of Pharmaceutical Sciences*, 103(1):29–52, January 2014.

[264] Ajits. Narang, Rong-Kun Chang, and Munir A. Hussain. Pharmaceutical Development and Regulatory Considerations for Nanoparticles and Nanoparticulate Drug Delivery Systems. *Journal of Pharmaceutical Sciences*, 102(11):3867–3882, November 2013.

[265] Rupa R. Sawant and Vladimir P. Torchilin. Challenges in Development of Targeted Liposomal Therapeutics. *The AAPS Journal*, 14(2):303–315, June 2012.

[266] U.S. F.D.A. Liposome Drug Products: Chemistry, Manufacturing, and Controls; Human Pharmacokinetics and Bioavailability; and Labeling Documentation. Guidance for Industry.

[267] Jian-Chiou Su, Chin-Lu Tseng, Ting-Gung Chang, Wen-Jen Yu, and Shih-Kwang Wu. A synthetic method for peptide-PEG-lipid conjugates: Application of Octreotide-PEG-DSPE synthesis. *Bioorganic & Medicinal Chemistry Letters*, 18(16):4593–4596, August 2008.

[268] Mustafa Grit, Willy J. M. Underberg, and Daan J. A. Crommelin. Hydrolysis of saturated soybean phosphatidylcholine in aqueous liposome dispersions. *Journal of Pharmaceutical Sciences*, 82(4):362–366, 1993. _eprint: https://onlinelibrary.wiley.com/doi/pdf/10.1002/jps.2600820405.

[269] Jia-ai Allen Zhang and John Pawelchak. Effect of pH, ionic strength and oxygen burden on the chemical stability of EPC/cholesterol liposomes under accelerated conditions: Part 1: Lipid hydrolysis. *European Journal of Pharmaceutics and Biopharmaceutics*, 50(3):357–364, November 2000.

[270] Martin L. Biniossek, Dorit K. Nägler, Christoph Becker-Pauly, and Oliver Schilling. Proteomic Identification of Protease Cleavage Sites Characterizes Prime and Non-prime Specificity of Cysteine Cathepsins B, L, and S. *Journal of Proteome Research*, 10(12):5363–5373, December 2011. Publisher: American Chemical Society.

[271] Mark Kastantin, Dimitris Missirlis, Matthew Black, Badriprasad Ananthanarayanan, David Peters, and Matthew Tirrell. Thermodynamic and Kinetic Stability of DSPE-PEG(2000) Micelles in the Presence of Bovine Serum Albumin. *The Journal of Physical Chemistry B*, 114(39):12632–12640, October 2010. Publisher: American Chemical Society.

[272] Naomi S. Robertson and David R. Spring. Using Peptidomimetics and Constrained Peptides as Valuable Tools for Inhibiting Protein–Protein Interactions. *Molecules*, 23(4):959, April 2018. Number: 4 Publisher: Multidisciplinary Digital Publishing Institute.

[273] Clinical Programs. Library Catalog: www.aileronrx.com.

[274] Edward J. Hennessy. Selective inhibitors of Bcl-2 and Bcl-xL: Balancing antitumor activity with on-target toxicity. *Bioorganic & Medicinal Chemistry Letters*, 26(9):2105–2114, May 2016.

[275] H. Zhang, P. M. Nimmer, S. K. Tahir, J. Chen, R. M. Fryer, K. R. Hahn, L. A. Iciek, S. J. Morgan, M. C. Nasarre, R. Nelson, L. C. Preusser, G. A. Reinhart, M. L. Smith, S. H. Rosenberg, S. W. Elmore, and C. Tse. Bcl-2 family proteins are essential for platelet survival. *Cell Death & Differentiation*, 14(5):943–951, May 2007. Number: 5 Publisher: Nature Publishing Group.

[276] Georg Lenz, George W. Wright, N. C. Tolga Emre, Holger Kohlhammer, Sandeep S. Dave, R. Eric Davis, Shannon Carty, Lloyd T. Lam, A. L. Shaffer, Wenming Xiao, John Powell, Andreas Rosenwald, German Ott, Hans Konrad Muller-Hermelink, Randy D. Gascoyne, Joseph M. Connors, Elias Campo, Elaine S. Jaffe, Jan Delabie, Erlend B. Smeland, Lisa M. Rimsza, Richard I. Fisher, Dennis D. Weisenburger, Wing C. Chan, and Louis M. Staudt. Molecular subtypes of diffuse large B-cell lymphoma arise by distinct genetic pathways. *Proceedings of the National Academy of Sciences*, 105(36):13520–13525, September 2008. Publisher: National Academy of Sciences Section: Biological Sciences.

[277] Jing Han, Zhengxi Zhu, Haitao Qian, Adam R. Wohl, Charles J. Beaman, Thomas R. Hoye, and Christopher W. Macosko. A simple confined impingement jets mixer for flash nanoprecipitation. *Journal of Pharmaceutical Sciences*, 101(10):4018–4023, 2012. _eprint: https://onlinelibrary.wiley.com/doi/pdf/10.1002/jps.23259.

[278] Sharan Bobbala, Sean David Allen, and Evan Alexander Scott. Flash nanoprecipitation permits versatile assembly and loading of polymeric bicontinuous cubic nanospheres. *Nanoscale*, 10(11):5078–5088, 2018. Publisher: Royal Society of Chemistry.

[279] James Brandon Dixon, Jeffrey A. Hubbell, Conlin P. O'Neil, Melody Swartz, and Diana Velluto. Block copolymers and uses thereof, March 2016. Library Catalog: Google Patents.

[280] A. Pezzutto, B. Dörken, P. S. Rabinovitch, J. A. Ledbetter, G. Moldenhauer, and E. A. Clark. CD19 monoclonal antibody HD37 inhibits anti-immunoglobulin-induced B cell activation and proliferation. *The Journal of Immunology*, 138(9):2793–2799, May 1987. Publisher: American Association of Immunologists.

[281] Sergey M. Kipriyanov, Olga A. Kupriyanova, Melvyn Little, and Gerhard Moldenhauer. Rapid detection of recombinant antibody fragments directed against cell-surface antigens by flow cytometry. *Journal of Immunological Methods*, 196(1):51–62, January 1996.

[282] U. E. Schaible, M. D. Kramer, K. Eichmann, M. Modolell, C. Museteanu, and M. M. Simon. Monoclonal antibodies specific for the outer surface protein A (OspA) of Borrelia burgdorferi prevent Lyme borreliosis in severe combined immunodeficiency (scid) mice. *Proceedings of the National Academy of Sciences*, 87(10):3768–3772, May 1990. Publisher: National Academy of Sciences Section: Research Article.

[283] Wei Ding, Xiaolin Huang, Xiaohua Yang, John J Dunn, Benjamin J Luft, Shohei Koide, and Catherine L Lawson. Structural identification of a key protective B-cell epitope in lyme disease antigen OspA11Edited by I. A. Wilson. *Journal of Molecular Biology*, 302(5):1153–1164, October 2000.

[284] Jagath R. Junutula, Helga Raab, Suzanna Clark, Sunil Bhakta, Douglas D. Leipold, Sylvia Weir, Yvonne Chen, Michelle Simpson, Siao Ping Tsai, Mark S. Dennis, Yanmei Lu, Y. Gloria Meng, Carl Ng, Jihong Yang, Chien C. Lee, Eileen Duenas, Jeffrey Gorrell, Viswanatham Katta, Amy Kim, Kevin McDorman, Kelly Flagella, Rayna Venook, Sarajane Ross, Susan D. Spencer, Wai Lee Wong, Henry B. Lowman, Richard Vandlen, Mark X. Sliwkowski, Richard H. Scheller, Paul Polakis, and William Mallet. Site-specific conjugation of a cytotoxic drug to an antibody improves the therapeutic index. *Nature Biotechnology*, 26(8):925–932, August 2008. Number: 8 Publisher: Nature Publishing Group.

[285] Hongyan Yuan, Ju Li, Gang Bao, and Sulin Zhang. Variable Nanoparticle-Cell Adhesion Strength Regulates Cellular Uptake. *Physical Review Letters*, 105(13):138101, September 2010.

[286] C. Ploner, R. Kofler, and A. Villunger. Noxa: at the tip of the balance between life and death. *Oncogene*, 27(1):S84–S92, December 2008. Number: 1 Publisher: Nature Publishing Group.

[287] Jingshan Tong, Peng Wang, Shuai Tan, Dongshi Chen, Zaneta Nikolovska-Coleska, Fangdong Zou, Jian Yu, and Lin Zhang. Mcl-1 Degradation Is Required for Targeted Therapeutics to Eradicate Colon Cancer Cells. *Cancer Research*, 77(9):2512–2521, May 2017. Publisher: American Association for Cancer Research Section: Therapeutics, Targets, and Chemical Biology.

[288] Thomas Tiller, Eric Meffre, Sergey Yurasov, Makoto Tsuiji, Michel C. Nussenzweig, and Hedda Wardemann. Efficient generation of monoclonal antibodies from single human B cells by single cell RT-PCR and expression vector cloning. *Journal of Immunological Methods*, 329(1):112–124, January 2008.

[289] Stian Foss, Maria Bottermann, Alexandra Jonsson, Inger Sandlie, Leo C. James, and Jan Terje Andersen. TRIM21—From Intracellular Immunity to Therapy. *Frontiers in Immunology*, 10, 2019. Publisher: Frontiers.

[290] Fabiola Cervantes-Gomez, Betty Lamothe, Jennifer A. Woyach, William G. Wierda, Michael J. Keating, Kumudha Balakrishnan, and Varsha Gandhi. Pharmacological and Protein Profiling Suggests Venetoclax (ABT-199) as Optimal Partner with Ibrutinib in Chronic Lymphocytic Leukemia. *Clinical Cancer Research*, 21(16):3705–3715, August 2015. Publisher: American Association for Cancer Research Section: Cancer Therapy: Preclinical.

[291] Nitin Jain, Michael Keating, Philip Thompson, Alessandra Ferrajoli, Jan Burger, Gautam Borthakur, Koichi Takahashi, Zeev Estrov, Nathan Fowler, Tapan Kadia, Marina Konopleva, Yesid Alvarado, Musa Yilmaz, Courtney DiNardo, Prithviraj Bose, Maro Ohanian, Naveen Pemmaraju, Elias Jabbour, Koji Sasaki, Rashmi Kanagal-Shamanna, Keyur Patel, Jeffrey Jorgensen, Naveen Garg, Xuemei Wang, Katrina Sondermann, Nichole Cruz, Chongjuan Wei, Ana Ayala, William Plunkett, Hagop Kantarjian, Varsha Gandhi, and William Wierda. Ibrutinib and Venetoclax for First-Line Treatment of CLL. *New England Journal of Medicine*, 380(22):2095–2103, May 2019. Publisher: Massachusetts Medical Society _eprint: https://doi.org/10.1056/NEJMoa1900574.

[292] Francisco J. Martinez-Veracoechea and Daan Frenkel. Designing super selectivity in multivalent nano-particle binding. *Proceedings of the National Academy of Sciences*, 108(27):10963–10968, July 2011. Publisher: National Academy of Sciences Section: Physical Sciences.

[293] Jared Francis Stefanick, David Thomas Omstead, Tanyel Kiziltepe, and Basar Bilgicer. Dual-receptor targeted strategy in nanoparticle design achieves tumor cell selectivity through cooperativity. *Nanoscale*, 11(10):4414–4427, March 2019. Publisher: The Royal Society of Chemistry.

[294] Xiaohe Tian, Stefano Angioletti-Uberti, and Giuseppe Battaglia. On the design of precision nanomedicines. *Science Advances*, 6(4):eaat0919, January 2020. Publisher: American Association for the Advancement of Science Section: Research Article.

[295] Nisha G Sosale, Kyle R Spinler, Cory Alvey, and Dennis E Discher. Macrophage engulfment of a cell or nanoparticle is regulated by unavoidable opsonization, a species-specific 'Marker of Self' CD47, and target physical properties. *Current Opinion in Immunology*, 35:107–112, August 2015.

[296] Pia L. Rodriguez, Takamasa Harada, David A. Christian, Diego A. Pantano, Richard K. Tsai, and Dennis E. Discher. Minimal "Self" Peptides That Inhibit Phagocytic Clearance and Enhance Delivery of Nanoparticles. *Science*, 339(6122):971–975, February 2013. Publisher: American Association for the Advancement of Science Section: Report.

[297] Ben Ouyang, Wilson Poon, Yi-Nan Zhang, Zachary P. Lin, Benjamin R. Kingston, Anthony J. Tavares, Yuwei Zhang, Juan Chen, Michael S. Valic, Abdullah M. Syed, Presley MacMillan, Julien Couture-Senécal, Gang Zheng, and Warren C. W. Chan. The dose threshold for nanoparticle tumour delivery. *Nature Materials*, pages 1–10, August 2020. Publisher: Nature Publishing Group.

[298] Shrey Sindhwani, Abdullah Muhammad Syed, Jessica Ngai, Benjamin R. Kingston, Laura Maiorino, Jeremy Rothschild, Presley MacMillan, Yuwei Zhang, Netra Unni Rajesh, Tran Hoang, Jamie L. Y. Wu, Stefan Wilhelm, Anton Zilman, Suresh Gadde, Andrew Sulaiman, Ben Ouyang, Zachary Lin, Lisheng Wang, Mikala Egeblad, and Warren C. W. Chan. The entry of nanoparticles into solid tumours. *Nature Materials*, 19(5):566–575, May 2020. Number: 5 Publisher: Nature Publishing Group.